UNIVERSITÄT DUISBURG ESSEN

Open-Minded

Anisotropic cobalt-based nanostructures: synthesis and characterization

Dissertation

Zur Erlangung des akademischen Grades

Doktor der Naturwissenschaften

an der Fakultät für Physik

der Universität Duisburg-Essen

vorgelegt von

Sara Liébana Viñas

aus

Zaragoza, Spanien

Duisburg, Dezember 2015

1 Gutachter: Prof. Dr. Michael Farle

2 Gutachter: Prof. Dr. Verónica Salgueiriño Maceira

Tag der mündlichen Prüfung: 29.01.2016

To my parents, who have taught me more than science.

To my sister, because we will always be "*una de dos*".

The most exciting phrase to hear in science, the one that heralds new discoveries, is not “Eureka!” but “That´s funny!”

Isaac Asimov

Abstract

Different types of cobalt-based magnetic nanoparticles have been designed to improve their performances in modern applications. For example, 3d transition metal-based magnetic nanowires are currently considered as potential candidates for rare-earth-free permanent magnets and for applications in catalysis. This thesis describes possible approaches for the design of optimized architectures on the nanoscale exploiting the combination of shape, magnetocrystalline and exchange anisotropy in 3*d*-metals. First, in a novel approach for the magnetic hardening, electroplated $Fe_{30}Co_{70}$ nanowires in anodic aluminum oxide templates with diameters of 20 nm and 40 nm (length 6 μm and 7.5 μm, respectively) are synthesized and thoroughly characterized by structural and magnetic techniques. A 3–4 nm thick, naturally formed ferrimagnetic FeCo oxide layer covering the tip of the FeCo nanowire increases the coercive field by 20% at T = 10 K. The increase of the coercive field is achieved by means of magnetic pinning by an antiferromagnet which suppresses vortex formation at the tips of the nanowires as suggested by micromagnetic simulations.

Second, $Co_{80}Ni_{20}$ nanorods with a mean diameter of 7 nm and a mean length of 53 nm have been synthesized by colloidal chemistry using the polyol process. Structural analysis shows crystalline rods with the crystallographic c-axis of the hexagonal close-packed (hcp) phase, i.e. the magneto-crystalline easy axis, parallel to the long axis of the $Co_{80}Ni_{20}$ alloy rods. Moreover, these are covered by a thin Co-rich oxidized face-centered cubic (fcc) shell. This shell promotes a larger hysteretic energy product by exchange anisotropy between the antiferromagnetic oxide shell and the ferromagnetic metallic core.

In a third study, cobalt oxide nanoparticles have been examined having a good catalytic response and additional magnetic properties. A new synthetic procedure has been developed to master the magnetic properties of cobalt oxide nanocrystals. 20 nm, 40 nm, and 85 nm edge length CoO-Co_3O_4 core-shell octahedra have been successfully synthesized by a thermal decomposition method. The particles exhibit sharp edges as well as almost atomically flat {111} facets. They consist of a CoO core and 2-4 nm thick Co_3O_4 shell. The interface between these two oxides is heavily strained and gives rise to ferromagnetism to at least 400 K, well above the antiferromagnetic ordering temperatures of both oxides.

Additional studies of different types of nanoparticles for innovative applications (e.g. hyperthermia, waste treatment, contrast agents) have been performed in the course of this thesis and summarized in the appendices II-IV.

Zusammenfassung

Verschiedene Arten Kobalt-basierter magnetischer Nanostrukturen wurden gezielt hergestellt, um ihre Eigenschaften in modernen Anwendungen zu verbessern. Zum Beispiel werden magnetische Nanodrähte bestehend aus 3d-Übergangsmetallen derzeit als potentielle Kandidaten für Permanentmagnete ohne seltene Erden und für Anwendungen in der Katalyse untersucht. Die vorliegende Dissertation schlägt mögliche Ansätze für das magnetische Härten vor, die eine Kombination aus Form-, magneto-kristalliner und Austauschanisotropie der 3d-Metalle ausnutzen. Zunächst ist eine neuartige Methode für das magnetische Härten von $Fe_{30}Co_{70}$ Nanodrähten untersucht worden. Der Durchmesser der in anodisierten Aluminiumoxid Templaten elektrochemisch gewachsenen Nanodrähte beträgt dabei 20 nm und 40 nm bei einer von Länge 6 µm und 7,5 µm. Detaillierte strukturelle und magnetische Untersuchungen ergaben dabei eine 3-4 nm dicke, natürlich gebildete ferrimagnetische FeCo Oxidschicht an den Enden der Nanodrähte. Diese erhöhen die Koerzitivfeldstärke um 20% bei T = 10 K. Diese Zunahme der Koerzitivfeldstärke wird erreicht durch magnetisches Pinnen, welches die Vortexbildung an den beiden Enden unterdrückt.

Andererseits sind $Co_{80}Ni_{20}$ Nanostäbchen mit einem mittleren Durchmesser von 7 nm und einer mittleren Länge von 53 nm kolloidal-chemisch mit einem Polyolprozess synthetisiert worden. Die Strukturanalyse zeigt kristalline Stäbchen mit einer kristallographischen Orientierung der c-Achse der hexagonalen dicht gepackten (hcp) Phase parallel zur langen Achse der $Co_{80}Ni_{20}$ Legierungsstäbchen. Weiterhin sind die Stäbchen mit einer dünnen, Co-reichen Oxidhülle mit kubisch-flächenzentrierten (fcc) Struktur ummantelt. Diese Hülle fördert ein größeres Energieprodukt der magnetischen Hysterese aufgrund des Auftretens der Austauschanisotropie zwischen der antiferromagnetischen Oxidhülle und dem ferromagnetischen Kern.

In einer dritten Studie wurden Kobaltoxid-Nanopartikel untersucht, die gleichzeitig gute katalytische und magnetische Eigenschaften zeigen. Ein neues Syntheseverfahren ist entwickelt worden, um die magnetischen Eigenschaften der Kobalt-Nanokristalle zu kontrollieren. CoO-Co_3O_4 Kern-Hülle-Oktaeder mit 20 nm, 40 nm und 85 nm Kantenlänge wurden erfolgreich durch ein thermisches Zersetzungsverfahren hergestellt. Die Partikel weisen scharfe Kanten sowie fast atomar glatte {111}–Facetten auf. Sie bestehen aus einen CoO-Kern und einer 2-4 nm dicken Co_3O_4 Hülle. Die Grenzschicht zwischen diesen beiden Oxiden ist stark verspannt, was zu ferromagnetischer Ordnung bis mindestens 400 K führt, die weit oberhalb der antiferromagnetischen Ordnungstemperatur der beiden Materialien liegt.

Darüber hinaus wurden weitere Untersuchungen an verschiedenen Arten von Nanopartikeln für andere Anwendungen (z.B. Hyperthermie, Abfallbehandlung, Kontrastmittel) im Rahmen dieser Dissertation durchgeführt. Diese sind in den Anhängen II-IV zusammengefasst.

List of Abbreviations

AAO	Anodic aluminum oxide
AFM	Atomic force microscopy(e)
bcc	Body centered cubic
DC	Direct current
EDX	Energy dispersive X-ray spectroscopy
EELS	Electron energy loss spectroscopy
ESCA	Electron spectroscopy for chemical analysis
FC	Field cooled
fcc	Face centered cubic
FFT	Fast Fourier transform
FW	Field warmed
HAADF	High-angle annular dark field
hcp	Hexagonal closed packed
HRTEM	High resolution transmission electron microscopy(e)
OT	Oxidized tips
OOT	Open oxidized tips
TEM	Transmission electron microscopy(e)
SAED	Selected area electron diffraction
SEM	Scanning electron microscopy(e)
SQUID	Super Quantum Interference Device
STEM	Scanning transmission electron microscopy(e)
UHV	Ultra-high vacuum
XPS	X-ray photoelectron spectroscopy
XRD	X-ray diffraction
ZFC	Zero field cooled

Contents

1 Scope and objectives

Magnetic nanostructures have attracted tremendous attention because of their unique and outstanding physical and chemical properties. The progress in (colloidal) chemistry over the last years led to a remarkable control of size and morphology. In particular, cobalt based nanocrystals -including metals as well as oxides- have shown great potential for many novel applications in information storage, building blocks for macroscopic magnets, catalysis and biomedical areas. Additionally, such size and shape-selected nanostructures serve as model systems for fundamental studies.

Permanent magnets play an important role and are widely spread in daily life-applications. In the last few years, there has been a large increase in the need for specialized magnets used for computers, vehicles, motors and renewable power generators. Nowadays most of the magnets used for technological applications contain rare-earth elements. $Nd_2Fe_{14}B$ and Sm_2Co_{17} compounds are most commonly used for hard magnets. The current alternative to rare-earth magnets are AlNiCo magnets and ceramic ferrites. However, these are either brittle and/or possess a lower energy product compared to their rare earth-containing counterparts. This fact in combination with the rare-earth shortage in Europe has stimulated intense effort towards new magnets matching price issues and sustainability.

To this end, 3d transition metals based magnetic nanowires/nanorods were suggested as possible candidates for substituting rare-earth magnets. The large saturation magnetization of these elements offers a very strong magnetic shape anisotropy when considering nanowires with a high aspect ratio. Additionally, they possess high Curie temperatures, which render the permanent magnet also suitable for technological applications at elevated temperatures. Among the 3d elements, pure metallic Fe or Ni nanorods do not have the potential to fulfil the needs of permanent magnets because of their low magnetocrystalline

anisotropy energy density. In contrast, hcp Co has about one order of magnitude larger magnetocrystalline anisotropy, which makes it a much better candidate for the production of permanent magnets. In this regard, FeCo alloys have been proposed since this binary alloy possesses the highest saturation magnetization among the 3d transition metals. Nonetheless, the magnetocrystalline anisotropy energy density of this alloy is one order of magnitude lower than the best rare-earth containing magnets. Thus, FeCo alloy must be tailored to compete with the existing magnets. Higher coercive fields can be achieved by manipulating the size and shape of FeCo at the nanoscale. For instance, the large saturation magnetization of this alloy offers a very strong magnetic shape anisotropy when considering nanostructures with a high aspect-ratio.

If the preparation technique or the synthetic method exerts control over the crystallographic orientation of the material along the nanowire geometry, one expects large coercive fields and high remanent magnetization stemming from the magnetocrystalline easy axis aligned parallel to the axis of the rod. Additionally, besides shape and magnetocrystalline contributions, exchange coupling to an antiferromagnetic material (exchange bias) can be used to increase the energy product of these nanostructures even further. Indeed, the magnetic anisotropy of nanoparticles increases by oxidizing the nanoparticles' surface. The oxidation of FeCo produces a mixed oxide that increase the coercive field, but only at low temperatures. In order to exploit such effects in these nanostructures but also optimize the performance of permanent magnets operating at ambient temperature, antiferromagnetic materials with significantly higher Néel temperature are needed while maintaining the large magnetocrystalline anisotropy energy density. In this regard, a good compromise between large magnetocrystalline anisotropy energy density and high Néel temperature in the antiferromagnetic shell is the admixture of nickel to cobalt.

Thus, two different elongated magnetic nanostructures are studied in this thesis, FeCo nanowires (chapter 3) and CoNi nanorods (chapter 4). The combination of shape, magnetocrystalline and exchange anisotropy is exploited in these nanostructures to improve their properties as novel rare-earh-free permanent magnets.

Although high aspect ratio nanostructures have been synthesized using a number of advanced nano-lithographic techniques, such as electron-beam or focused-ion-beam, fur-

ther up-scaling of these techniques for the production of large quantities remains a challenge. Consequently, there is a great interest in the development of new methodologies based on bottom-up approaches for the selective synthesis of anisotropically shaped nanostructures. Such techniques should include possibilities of materials diversity, low cost, and the potential for mass production and sustainability. In this line, one of the commonly adopted strategies for achieving shape control of cobalt-based nanostructures is through the use of templates (e.g. porous alumina membranes, carbon nanotubes, micelles). The material is synthesized in the interior of these cavities by different chemical methods. The electrodeposition technique offers the possibility of preparing periodically aligned high-aspect ratio nanostructures in template matrices. The polyol route is an alternative strategy for generating anisotropic nanostructures. It is based on the manipulation of the growth kinetics with the help of capping molecules (wet-chemistry). These organic molecules bind preferentially to certain crystal faces of the growing particle, thus introducing anisotropy into the particle geometry during growth.

The latter two techniques have been used for the preparation of high-aspect-ratio nanostructures studied in this thesis. FeCo nanowires are synthesized by electrodeposition in anodic aluminum oxide templates. The coercive fields of these nanowire arrays are generally smaller than the predicted values from model assumptions. Micromagnetic simulations reveal that this softening derives from the formation of a vortex and the nucleation of domain walls at the tips of the nanowires. Thus, the goal of the research presented in chapter 3 is the magnetic hardening of these nanowires by pinning the magnetization at the tips.

CoNi nanorods have been prepared by the colloidal route (polyol). The purpose here is to analyze the influence of the oxidized surface on the magnetic properties for the improvement of their performance for rare-earth-free permanent magnets based on 3*d* metal nanorods (chapter 4).

However, not only metallic nanostructures of these 3d transition metals are valuable in industrial applications. Transition metal oxide nanoparticles are also of high interest, mainly due to their chemical stability and magnetic properties. In particular, Co oxide nanoparticles have attracted special attention for applications in gas sensing or catalysis. The control in the synthesis of well-defined shapes and facets of Co oxide nanoparticles is essential for ultimate applications. For instance in catalysis the reactivity and and selectivity

of catalysts is strongly site-dependent, i.e. the chemistry of edge atoms significantly differs from atoms in the surface facets, due to the different number of dangling bonds. Thus, the main focus of the research presented in chapter 5 is the development of a new synthesis procedure to master the magnetic properties of cobalt oxide nanocrystals to possibly improve their performance as anode materials in lithium-ion batteries or in methane catalytic combustion reactions.

In summary, the overall goal of this Ph.D. dissertation is the design, the synthesis, and the thorough structural and magnetic characterization of new Co-based magnetic materials for modern applications.

The thesis is divided into the following chapters. The introductory chapter includes the theoretical background of the magnetism at the nanoscale, the principles of the chemical synthesis by wet-chemistry methods and the working principles of the measurement techniques that have been used. In the chapters presenting scientific results, an introduction into the topic is given and the motivation of the specific research is exposed. Secondly, the synthetic procedure is summarized. A thorough morphological, structural and chemical characterization is included. Afterwards, the magnetic properties of the nanoparticles are presented. Finally, the main conclusions of the thesis are highlighted.

2 Theoretical background

In this first chapter, the fundamental physical quantities that govern nanoscale magnetic systems are discussed as well as the mechanisms controlling the nucleation and growth of nanoparticles, characteristic of the synthesis in solution. Finally, a general overview of the characterization techniques employed to obtain the results presented in this PhD thesis is given.

2.1 Magnetic properties of nanoparticles

The present summary of the magnetic properties of nanoparticles has been prepared based on basic literature [1, 2, 3, 4, 5, 6, 7].

New magnetic phenomena can emerge at the nanometer scale if compared to bulk magnetism. The origin of the observed differences generally stems from:

(i) dimensions comparable to characteristic length scales of magnetic properties of the constituent material,

(ii) broken translation symmetry, which results in sites with reduced coordination number,

(iii) higher proportion of surface (or interface) atoms. The proportion of atoms that are on the surface atomic layer, whose electronic states are modified relative to interior layers, becomes significant. For example, in a 10 nm spherical particle, 10% of the atoms are in the surface layer.

But let´s start first understanding the origin of ferromagnetism. Magnetism fundamentally arises from the exchange interaction between neighboring electrons with overlapping wave functions situated at the *d* orbitals of different transition metals. The wave functions of the electrons have to be antisymmetric. In other words, there is no probability of finding two electrons with the same spin at the same point in space, and consequently they should have opposite spins (Pauli principle). The fundamental nature of the wave function thus tends to keep electrons with the same spin apart, which lowers their Coulomb energy. The system energy is therefore lower if the electrons have parallel spins, and the difference in energy between the parallel and anti-parallel alignments is the exchange energy. Indeed, this energy causes that intra-atomic electrons try to maintain parallel alignment of their spins (Hund's first rule).

The exchange interaction is effectively a correction to the Coulomb energy required by the anti-symmetric nature of the wave function and produces a difference in energy between the parallel and anti-parallel alignment of neighboring atomic spin moments. For two neighboring atoms with spins S_1 and S_2, the interaction can be represented by the energy term:

$$E_{exch} = -2JS_1 \cdot S_2 \qquad \textit{(Equation 2-1)}$$

where J is the exchange constant and can be either positive or negative, corresponding to parallel or antiparallel alignment. When the parallel alignment is favored ferromagnetism appears and alternatively, when the antiparallel alignment is favored the antiferromagnetism appears.

In response to the exchange energy, a magnetic material should be fully magnetized, with all the individual atomic moments aligned up with an applied field. This would cause the material to have maximum magnetostatic energy. The magnetostatic energy represents indeed the interaction energy of each dipole with the field generated by all the other dipoles integrated throughout the material [1]. However, magnetic materials tend to reduce this magnetostatic energy by a self-demagnetizing process (domain formation), so that this field is cancelled.

Both exchange interaction and magnetostatic energy compete. The exchange interaction is orders of magnitude stronger than the magnetic dipolar interactions between atoms. On the other hand, while dipolar interactions are long-range interactions, the exchange interaction only operates between atomic neighbors. Thus, there is a compromise that will minimize the energy relative to the totally magnetized state. A ferromagnetically ordered solid can reduce its magnetostatic energy by breaking up into a complex structure of domains. Thus, a single-domain structure (Figure 2-1(a)) has a much higher dipolar energy than any structure consisting of two domains of opposite magnetization (Figure 2-1(b)). Furthermore, the two-domain structure can lower its dipolar energy still further by producing additional domains, as shown in Figure 2-1 (c).

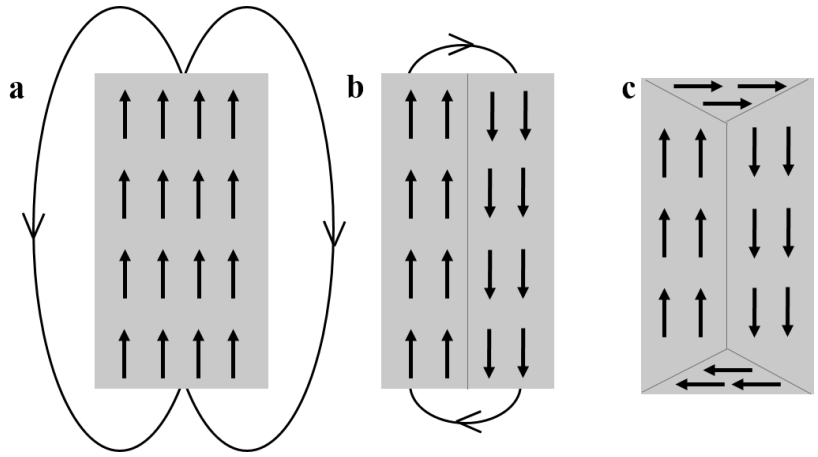

Figure 2-1. Schematics of the domains formation in a ferromagnetic material. (a) Uniformly magnetized ferromagnetic material, on which the magnetostatic energy becomes reduced by the formation of a domain with opposite magnetization (b). This two-domain structure can lower its dipolar energy further by producing additional domains (c). Note that the domain boundaries or domain walls are gradual and not as sharp as depicted in these sketches.

Minimization of the magnetostatic energy can be attained as the material forms as many domains as possible. However, every new domain introduces a boundary of oppositely aligned atomic spins, thereby increasing the exchange energy within the material. The energy balance works because only atoms at the boundary interact via the powerful exchange force whereas a much larger number of atoms benefits from the reduction in the dilute magnetostatic energy. In fact, the energy balance can be reached because the boundaries do not occur abruptly, from one atomic plane to the next. The formation of a domain structure relies on the minimization of the exchange energy of the boundary, lowered by spreading the reversal over many spins forming a domain wall with a particular thickness. The domain wall thickness is actually dictated by the competition between exchange and anisotropy energies (which will be described in section 2.1.1).

In bulk, there are three energy terms that play a role in the final magnetic configuration of the material: the exchange energy, the anisotropy energy and the magnetostatic energy. The average size of the magnetic domains is a function of these three parameters and as the volume of a piece of magnetic material is reduced the number of domains decreases. Eventually, the volume drops below a certain critical value, where it becomes energetically unfavorable to include another domain wall or, in other words, the uniformly magnetized state becomes the lowest energy configuration. Thus, a piece of magnetic material below the critical size stays permanently magnetized at close to its saturation magnetization. It may not have the full saturation magnetization in remanence, because of the canting of spins at the particle surface.

Thus, the single domain critical size is defined as the largest size that a ferromagnetic particle may have, beyond which it will be energetically more favorable to divide itself into two or more domains. This critical size varies depending on the material considered as well as the morphology. For spherical particles, it is given by the expression:

$$r_c = \frac{18\sqrt{AK_{eff}}}{\mu_0 M_s^2} \quad \textit{(Equation 2-2)}$$

where A is the exchange stiffness constant, K_{eff} is the effective magnetic anisotropy energy density constant, μ_0 is the magnetic permeability of vacuum and M_s is the saturation magnetization.

In the general case, one may assume that each magnetic nanocrystal may possess an uniaxial anisotropy axis, and as such, its magnetic anisotropy energy is given by:

$$E = K_{eff} V sin^2\theta \qquad \textit{(Equation 2-3)}$$

where K_{eff} is the effective anisotropy energy density constant, V is the particle volume and θ is the angle between the magnetization vector and the easy axis (see Figure 2-2). In this situation, there are two energy minima at $\theta = 0$ and $\theta = \pi$, which correspond to the parallel or antiparallel magnetization directions with respect to the easy axis, separated by an energy barrier which height is $K_{eff}V$. The energy landscape is represented in Figure 2-2.

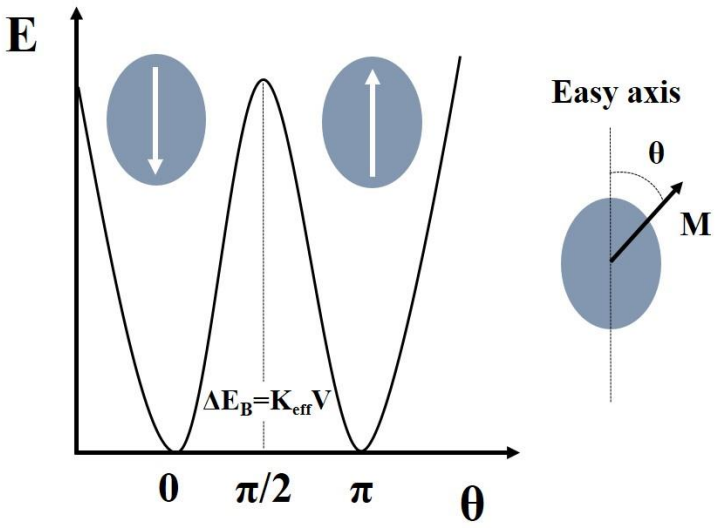

Figure 2-2. Magnetic energy landscape of a single domain nanoparticle with uniaxial anisotropy at zero magnetic field. The behavior is a function of the magnetization direction with respect to the easy axis (θ).

For small enough nanocrystals, the thermal energy may be sufficient to reverse the magnetization direction when $K_B T \gg K_{eff} V$. For all temperatures above the so-called blocking temperature, considering non-interacting nanocrystals, no-coercive field is observed in the magnetization curves. For these superparamagnetic systems, the fluctuation of the magnetization is described by a characteristic relaxation time (τ) given by the Néel-Brown model:

$$\tau = \tau_0 exp\left(\frac{K_{eff} V}{K_B T}\right) \qquad \textit{(Equation 2-4)}$$

where τ_0 is the natural lifetime.

In the theory of superparamagnetism it is assumed that the atomic magnetic moments are locked together by the exchange interaction and accordingly, they rotate coherently, so the magnetic behavior of the particle is described by a single magnetic moment (macrospin or superspin). This single magnetic moment has a magnitude of $\mu = \mu_{at} N$, where μ_{at} is the atomic magnetic moment and N is the number of atoms in the particle. A nanoparticle can thus be considered as a classical magnetic particle whose magnetic vector can point freely.

2.1.1 Magnetic anisotropy energy

The magnetic anisotropy induces the preferential magnetization orientation of a material in one particular direction of space; offering easy, intermediate and hard directions of magnetization. The easy axis is the energetically favorable direction of magnetization (minimum energy) while the hard axis is the magnetization direction where the energy reaches a maximum.

In bulk materials, the main sources of anisotropy are the magnetocrystalline anisotropy and magnetostatic energies. However, in nanosized materials, contributions of possible surface anisotropies have to be taken into consideration. Accordingly, the effective magnetic anisotropy energy is composed of different contributions:

$$\boldsymbol{K_{total} = K_{magnetocrystalline} + K_{shape} + K_{strain} + K_{surface} + K_{exchange}} \quad \textit{(Equation 2-5)}$$

Magnetocrystalline anisotropy energy ($K_{magnetocrystalline}$***)***: contribution related to the magnetic anisotropy, which preferentially directs the magnetization along a certain crystallographic direction in the material. Its origin is the spin-orbit interaction and the crystal symmetry of the sample. The simplest form of crystal anisotropy is the uniaxial anisotropy energy, which is given by:

$$E_{anis}^{uni} = K_2^u V sin^2\theta + K_4^u V sin^4\theta + higher\ orders \qquad \textit{(Equation 2-6)}$$

where K_2^u and K_4^u are the anisotropy constants, V is the particle volume and θ is the angle between the symmetry axis and the magnetization. Although higher order expansion coefficients can be large, in the literature the uniaxial anisotropy energy is often written as:

$$E_{uni} = K_u V sin^2\theta \qquad \textit{(Equation 2-7)}$$

where K_u is the effective uniaxial anisotropy energy density constant.

Shape anisotropy energy (K_{shape}***)***: contribution of anisotropy that arises directly from the shape of the material. A piece of magnetic matter with a high aspect ratio has an important shape anisotropy, displaying the so-called demagnetizing field. A demagnetizing field arises due to the appearance of surface charges (poles) and acts in opposition of the

magnetic induction formed within the materials when an external field is applied. As an example, the shape anisotropy energy of an ellipsoidal specimen is uniaxial and its energy can be expressed as:

$$E_{shape} = \frac{1}{2}\mu_0 V M_s^2 (N_X - N_Z) sin^2\theta \qquad \textit{(Equation 2-8)}$$

being V the volume of the particle, M_s the saturation magnetization, and N_X and N_Z the demagnetization factors relative to the *x* and *z* axes, respectively, and whose magnitude depends on the shape of the magnetic material. The sum of the demagnetizing factors in three orthogonal directions of a material has to be 1:

$$N_X + N_Y + N_Z = 1 \qquad \textit{(Equation 2-9)}$$

In the case of a system with uniaxial shape anisotropy (i.e. prolate ellipsoid) the magnitude of the demagnetizing field will be lower if the magnetization lies along the long axis. The demagnetizing factors in this case are:

$$N_Z(long\ axis) = \frac{1}{m^2-1}\left[\frac{m}{\sqrt{(m^2-1)}} ln\left(\frac{m+\sqrt{m^2-1}}{m-\sqrt{m^2-1}}\right) - 1\right] \qquad \textit{(Equation 2-10)}$$

$$when\ m >> 1,\quad N_X = N_Y = \frac{1}{2}\left[1 - \frac{ln(2m-1)}{m^3}\right] \qquad \textit{(Equation 2-11)}$$

where m represents the aspect ratio between the long and short axes of the ellipsoid. In the particular case of a cylinder with infinitive length, $N_Z = 0$ if the sample is magnetized across the long axis and $N_X = N_Y = 1/2$ if magnetized in perpendicular directions.

Strain anisotropy energy (K_{strain}): contribution stemming from a magnetostrictive effect. Its origin comes from a local change in atomic positions, altering the shape of the orbitals and consequently the spin-orbit interaction. This contribution to the magnetic anisotropy energy is described by:

$$E_{strain} = -\frac{3}{2}\lambda_s \sigma S cos^2\theta \qquad \textit{(Equation 2-12)}$$

where λ_s is the saturation magnetostriction, σ is the strain per area, S is the particle surface and θ is the angle between the magnetization and the strain axis.

Surface anisotropy energy ($K_{surface}$): contribution caused by the reduction of the coordination number of the atoms at the surface and the breaking of symmetry. It can be modified due to the expansion of the lattice spacing of atomic planes close to the surface. Surface anisotropy enhances the total anisotropy of small nanoparticles since, with decreasing particle size, the magnetic contributions from the surface increases. Hence, surface atoms give an important contribution to the effective anisotropy (K_{eff}), which in the case of spherical particles is given by:

$$K_{eff} = K_V + \frac{S}{V} K_S \qquad \textit{(Equation 2-13)}$$

where K_V and K_S are the volume and surface anisotropy constant, respectively, S is the surface $S = \pi d^2$ and V is the volume $V = \frac{\pi d^3}{6}$, (d-particle diameter) and thus, the previous expression can be written as:

$$K_{eff} = K_v + \frac{6}{d} K_s \qquad \textit{(Equation 2-14)}$$

Exchange anisotropy ($K_{exchange}$): contribution that arises from the magnetic interaction across an interface between two magnetic materials with different magnetic ordering (i.e. a ferromagnet in contact with an antiferromagnetic material). The magnetic anisotropy of a nanosized ferromagnet can become enhanced, for example by pinning its spins at the interface with an antiferromagnetic material. When a ferromagnetic-antiferromagnetic interface is cooled through the Néel temperature of the antiferromagnet, an unidirectional anisotropy or exchange bias is induced in the ferromagnet (provided that the Curie temperature of the ferromagnet is higher than the Néel temperature of the antiferromagnet), resulting in a shifted hysteresis loop. The coercive field H_c and the exchange bias H_{exch} fields of the hysteresis loops are calculated using equations:

$$H_C = \frac{(H_C^+ - H_C^-)}{2} \qquad \textit{(Equation 2-15)}$$

$$H_{exch} = \frac{(H_C^+ + H_C^-)}{2} \qquad \textit{(Equation 2-16)}$$

where H_C^+ (H_C^-) is the coercive field measured at positive (negative) applied magnetic field.

The presence of an antiferromagnet can even prevent the ferromagnetic moments from fluctuating due to thermal energy, as is the case for superparamagnetic particles. For that reason, exchange bias is seen nowadays as an effective means of overcoming the superparamagnetic limit typical of ferromagnetic nanoparticles.

2.2 Chemical synthesis

2.2.1 Colloidal chemistry

Over the last years, many different physical and chemical methods have been developed to synthesize magnetic nanoparticles. The physical methods are based on subdivision of bulk metals (known as "top-down" approach), including mechanical crushing/attrition or pulverization of bulk metal, laser ablation, arc discharge between metal electrodes, etc. The chemical methods are based on the reduction of metal ions or decomposition of precursors to obtain individual atoms, followed by aggregation or recombination of these atoms ("bottom-up" approach). Metal nanoparticles produced by physical methods are usually large in size and have wide size distribution, while nanoparticles prepared by chemical methods usually offer narrower size distributions.

Moreover, since colloidal nanocrystals are dispersed in solution, they are not bound to any solid support as it is the case for lithographically prepared nanoparticles or nanocrystals prepared by epitaxial growth. The direct advantage is that they can be produced in large quantities, which render colloidal chemistry one of the most useful method of synthesis in terms of their potential to be scaled up.

Another main advantage of this type of synthesis is the possibility to functionalize *in-situ* the nanostructures with ligands, not only to prevent agglomeration but also for other

purposes (for example, functionalization of nanoparticles with biological molecules that can perform tasks of molecular recognition to certain receptor molecules inside biological systems [8]). An extra benefit of this option of functionalization is that due to the existence of surfactants attached on the surface, these nanostructures can be used as building blocks to form macroscopic structures (superlattices) by self-assembly [9, 10, 11, 12].

Alternatively, it is well known that control over the nanocrystal morphology is a key parameter to finely tune the final properties and thus, a major aspect to take into account for their implementation into real devices. Colloidal chemistry has risen as the most reliable method to fulfill this demand, leading to an enormous variety of sizes and shapes of nanoparticles for almost any kind of material. Additionally, the synthesis can be done either in aqueous or non-aqueous solutions containing the soluble or suspended salts, making this technique suitable for biomedical sample preparation.

For all the advantages mentioned above, colloidal chemistry has been chosen as the method of synthesis of the nanostructures studied in this PhD thesis, with the exception of iron-cobalt nanowires that have been synthesized by electrochemical deposition (see section 3.2.1).

The growth mechanism of nanostructures in liquid remains nowadays an intricate and challenging question despite great achievements in the preparation of nanostructures. Although there are numerous examples of controlled synthesis of diverse nanostructures, morphology is not yet easy to predict. Generally speaking, in colloidal chemistry the formation of nanocrystals can be divided into two main processes: (i) nucleation initiated by a sudden increase of “monomer” concentration up to a supersaturation level, and (ii) subsequent growth of the seeds formed in the nucleation stage by adding “monomers”.

Despite the fact that mechanisms governing colloidal synthesis of nanoparticles (both nucleation and growth) are far from being completely understood, in the following a brief description of these mechanisms is presented.

2.2.2 Nucleation

Nucleation is the process whereby nuclei (seeds) act as templates for crystal growth. There are mainly two types of nucleation: homogeneous and heterogeneous. Homogeneous nucleation occurs when nuclei form uniformly throughout the parent phase by combining solute molecules in the absence of a solid interface. Heterogeneous nucleation however takes place at structural inhomogeneities (container surfaces, impurities, grain boundaries, dislocations, etc.). Additionally, heterogeneous nucleation can be induced through the in-situ formation of seed particles acting as foreign nuclei (usually noble metals). These seeds particles are formed *in-situ* by admixture of a suitable nucleating agent in the supersaturated solution, before the occurrence of the spontaneous nucleation step [13].

In this PhD work, heterogeneous nucleation has been used in the synthesis of CoNi nanorods. Ruthenium chloride was used as nucleation agent, since readily reduced in the conditions of reduction of cobalt and nickel precursors to form tiny metallic ruthenium particles. These very small Ru aggregates act as foreign nuclei sites for the subsequent growth of CoNi nanorods. The addition of this nucleating agent facilitates the formation of fairly monodisperse CoNi nanorods and with a better reproducibility (Chapter 4). In contrast, the synthesis of cobalt oxide octahedra (Chapter 5) was performed under homogeneous nucleation conditions.

The concepts of classical nucleation theory are discussed in some detail because they can be applied to describe the synthesis of nanoparticles in liquids. For more detail information refer to [14, 15].

The process of nuclei formation can be considered thermodynamically. The classical theory predicts that the total free energy cost (ΔG) of a nanoparticle is defined as the sum of the surface free energy and the bulk free energy [16]. For a spherical particle of radius r, the total free energy is given by:

$$\Delta G = \frac{4}{3}\pi r^3 \rho \Delta\mu + 4\pi r^2 \gamma \qquad \textit{(Equation 2-17)}$$

where γ represents the surface free energy, ρ is the density of the liquid and $\Delta\mu$ is the chemical potential difference between the bulk solid and the liquid. The first term of the

equation favors the growth of small nuclei since a bulk material is more stable than a supersaturated solution (less surface area), while the latter favors their dissolution due to the energy cost to create a solid-liquid interface. For a large enough radius the volume term begins to dominate the surface term, the nucleus becomes stable and may grow. In other words, homogeneous nucleation occurs because of a thermodynamic driving force, because the supersaturated solution is not stable in energy and the growth of these nuclei to form larger clusters is controlled by the competition between bulk (volume) and surface energy.

The crystal free energy, ΔG_v is dependent upon the temperature T, Boltzmann's constant K_B, the supersaturation of the solution S, and its molar volume v. Thus, ΔG_v is defined by:

$$\Delta G_v = \frac{-K_B T\, ln(S)}{v} \qquad \textit{(Equation 2-18)}$$

In fact, growth becomes favorable only when the nuclei reach a critical radius size (r_{crit}) at which the gain in bulk energy is dominating, which is defined by:

$$r_{crit} = \frac{-2\gamma}{\Delta G_v} = \frac{2\gamma v}{K_B T\, ln(S)} \qquad \textit{(Equation 2-19)}$$

The critical radius corresponds to the minimum size at which a particle can be stable in solution without being redisolved. The same is true for the particle´s free energy. A critical free energy is required to obtain stable particles within a solution.

For nucleation to occur, several experimental parameters can be varied. First of all, in the presence of active centers (impurities, walls, bubbles, drops, etc.) the energy barrier to overcome is globally decreased. Unlike homogeneous nucleation, in heterogeneous nucleation the nuclei are formed on the first surface of a foreign body. Moreover, in the homogeneous nucleation, changing parameters as supersaturation, temperature and surface free energy affect the nucleation step. The supersaturation is the parameter with the largest effect on nucleation rate. The surface free energy can be modified by surfactants through selected growth of high-energy crystal facets of the nuclei. More detailed information is given in section 2.2.3 [17].

Following the classical nucleation theory, Lamer and Dinegar proposed in the early

50's a complete mechanism for the formation of colloidal nanoparticles in solution. Though the initial model explained the formation of monodisperse sulphur colloids in ethanol, nowadays it is accepted as the general mechanism for the formation of any type of colloidal nanocrystals upon decomposition of the corresponding precursor in solution [18].

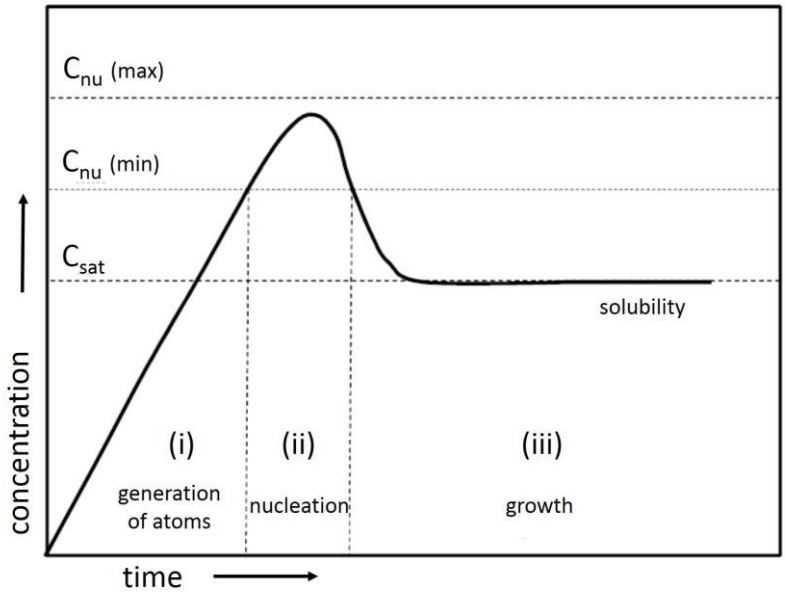

Figure 2-3. Plot of LaMer model that shows atomic concentration versus time. It illustrates the generation of metallic atoms in the solution, nucleation, and subsequent growth of colloidal nanoparticles in liquid media. Adapted from [18].

According to LaMer's plot for the crystal nucleation process (Figure 2-3) [18], the colloidal nanocrystal formation comprises the following steps: (i) the concentration of atoms steadily increases with time as the precursor is decomposed by heating, (ii) single atoms start to aggregate via self-nucleation as increasing the monomer concentration in the solution to a supersaturation level, called concentration of supersaturation; (iii) single atoms continuously aggregate into the existing nuclei which leads to gradual decrease in the monomer concentration. As long as the concentration of reactants is kept below the critical level, further nucleation is discouraged; (iv) with a continuous supply of atoms via ongoing precursor decomposition, the nuclei will grow into nanocrystals. Depending on different conditions, the nanocrystals can reach a very homogeneous size. If in this stage two nuclei coalesce (aggregate), it will lead to a loss in monodispersity.

For size and shape-monodisperse yield of nanocrystals, it is particularly important that nucleation occur rapidly and instantaneously. If nucleation proceeds over an extended

period, reactants are unevenly depleted from solution leading to variations in growth rate for seed particles formed at different reaction times.

On the other hand, the seed morphology can play a major role over the final shape of the nanoparticles, as it represents the first stage for the subsequent growth. Nuclei can take on a variety of shapes determined by the chemical potentials of the different crystallographic facets, which are in turn highly dependent on the reaction environment such as temperature and solute concentration. The crystalline phase of the nuclei can have a strong effect on the final nanocrystal shape as well. Xia and co-workers found out that the crystallinity of the seeds formed in the very early stage of the synthesis of silver nanoparticles was crucial for the final shape of the nanocrystals. Depending whether the seeds present single-crystal, single twinned or multiple twinned structures, different morphologies could be obtained like cubes, octahedrons, pentagonal rods or cuboctahedrons [19].

To go even deeper in the understanding of the driving forces beyond the nucleation of metallic nanoparticles, structural elucidation of subnanometric nuclei is of fundamental importance. In this line, Auer and Frenkel postulated in 2001 that the structure of nuclei in the primitive stages of the growth present a metastable random hexagonal close-packed configuration (rhcp) [20]. This arrangement corresponds to random stacking of fcc and hcp structures (possible due of the small free energy difference between them). In site of it, the experimental observation of the crystal structure of atomic nuclei before nanoparticle formation remains a big challenge to overcome.

2.2.3 Growth

After the formation of nuclei, the subsequent growth also strongly governs the final morphology of the nanocrystals. Generally, the nanocrystal growth can occur under two different regimes, either in a thermodynamically or kinetically controlled growth regime. The manipulation between thermodynamic and kinetic growth regimes is thus a critical factor in determining the final nanoparticle shape [21].

In thermodynamic equilibrium, the shape of a nanocrystal is obtained by minimizing the surface energy for a given volume according to Wulff's theorem [22, 23]. The preferred

structure of the seeds will be the one with the lowest interfacial free energy (γ), that is defined as the energy required for creating a unit area of "new" surface, which is given by:

$$\gamma = \frac{1}{2} N_b \varepsilon \rho_a \quad \textit{(Equation 2-20)}$$

where N_b is the number of broken bonds, ε is the bond strength and ρ_a is the density of surface atoms. For an fcc metallic nanoparticle {110}, {111} and {100} are the low-index crystallographic facets which are normally exposed at the surface, being $\gamma\{110\} < \gamma\{111\} < \gamma\{100\}$ their corresponding energetic sequence [17]. Therefore, for a growth process produced under thermodynamic conditions, these facets will grow by preferential adsorption of atoms on the facets with higher interfacial energy. This sequence is responsible for the predilection of truncated octahedrons as the most stable structures for small single crystalline seeds, presenting a shape close to a sphere and exposing the {111} and {100} facets.

In general, to promote a nanocrystal shape modification a kinetic growth regime is required, where the surface energy of crystallographic facets can be controlled. A good way to promote this surface stabilization implies the use of surfactants [24, 25]. Ligand molecules adsorb on the nanocrystal surface and can significantly alter the interfacial energies. A particular surfactant adheres selectively to a specific crystal facet, what is used to effectively lower the energy and slow the growth rate of that facet relative to others. Certainly, these organic molecules are chosen regarding their propensity to adhere to the surface of the growing material. This adhesion of surfactants on a nanoparticle surface is a dynamic process that allows the capping agents to exchange on and off the growing clusters to be indeed accessible for growth.

In particular, an effective strategy to generate well-defined anisotropic nanostructures during crystal growth is the use of a combination of ligands (two in most cases). One binds tightly to the nanocrystal surface, hindering growth, and the other is less tightly bound, permitting rapid growth. Sometimes, the formation of the intrinsic anisotropic nanocrystals is found to be a highly kinetics-driven process, which occurs far away from the thermodynamic equilibrium, and must be overdriven by high precursor monomer concentrations [26]. The surfactant size also plays a critical role, i.e. large molecules (bulkier surfactants) provide greater steric hindrance that slow the growth rate of "monomers" to the nanocrystal, resulting in smaller average nanocrystal size (see discussion of growth mechanism of

cobalt oxide nanocrystals in section 5.6).

Moreover, these ligand molecules provide an energetic barrier to counteract the van der Waals and magnetic attractions between nanocrystals, preventing the nanoparticles to form aggregates. The dispersion of fine particles in solution by different ligands has been studied intensively and a good review is provided in reference [27]. In addition, when the growth is stopped, the ligand molecules can be strongly bound to the surface of the nanocrystals, stabilizing them in a wide range of solvents. Accordingly, it offers a great synthetic flexibility in that different ligands can be exchanged having different functional groups or polarity.

To sum up, when nucleation and nanoparticle growth are controlled at the atomic level, well-defined anisotropic morphologies can be achieved. Control in the final nanoparticle morphology can be achieved by adding capping agents that selectively adsorb to specific crystal facets, modifying the growth rates in specific crystalline directions.

2.3 Characterization techniques

In this thesis, two main techniques have been used to characterize the nanocrystals: transmission electron microscopy (TEM) and Superconducting Quantum Interference Device (SQUID) magnetometry. TEM allows the direct observation of the nanoparticle morphology, crystalline structure and chemical composition while SQUID magnetometry allows measuring the magnetic properties of the samples. The structural characterization of all the samples is supported by X-rays techniques: X-ray photoemission spectroscopy (XPS) and X-ray diffraction (XRD). Morphological investigations were also supported by scanning electron microscopy (SEM) and atomic force microscopy (AFM).

The scope of this section is limited to the description of the basic principles and the experimental setups of TEM and SQUID magnetometry and it is not intended to provide a comprehensive review. The description of all other techniques is restricted to the particular experimental devices used to achieve the presented results.

2.3.1 Transmission electron microscopy

Morphological and structural properties of the nanoparticles were studied by means of high resolution transmission electron microscopy (HRTEM). The elemental analysis was conducted using TEM combined with energy dispersive X-ray (EDX) spectroscopy and energy-loss electron spectroscopy (EELS). The content of this section is based on references [28, 29, 30].

In this work; morphological, chemical composition and crystalline structure of nanoparticles were predominantly studied using FEI Tecnai F20 TEM and CM12 Philips TEM. The samples for TEM investigation were prepared by dropping few microliters of the nanoparticle solution onto amorphous carbon films supported on a copper grid and dried in ambient conditions.

A simplified ray diagram of a TEM consists of an electron source, a condenser lens system with aperture, the sample to analyze, an objective lens system with aperture, a projector lenses and a fluorescent screen imaging system. The schematic illustration of an electron microscope is presented in Figure 2-4.

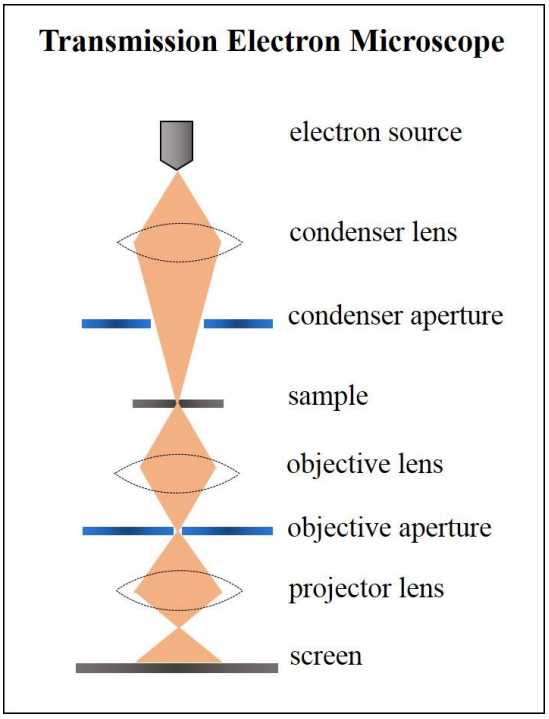

Figure 2-4. Simplified ray diagram of a TEM consisting of an electron source, a condenser lens system with aperture, a sample, an objective lens system with aperture, projector lenses and a fluorescent screen.

The electron source is either an electrically heated tungsten filament (CM12 Philips microscope) or a single-crystal LaB_6 cathode (TECNAI). The electrons are ejected from the gun by means of thermionic or field emission, respectively, and accelerated by the high voltage (100-300 kV). The electron gun emits electrons (electron beam) that are accelerated by the high potential and focused via the condenser lens system onto the sample in vacuum. When the electrons from the electron gun enter the sample, they are scattered as they pass through it, focused by the objective lens system, amplified by magnifying lenses, and finally they produce an image in the fluorescent screen.

When an accelerated electron enters the specimen it interacts with its atoms and a variety of signals are produced by electron-sample interactions (see Figure 2-5). The generated signals that derive from these interactions are collected and reveal information about the sample surface topography, chemical composition and crystalline structure.

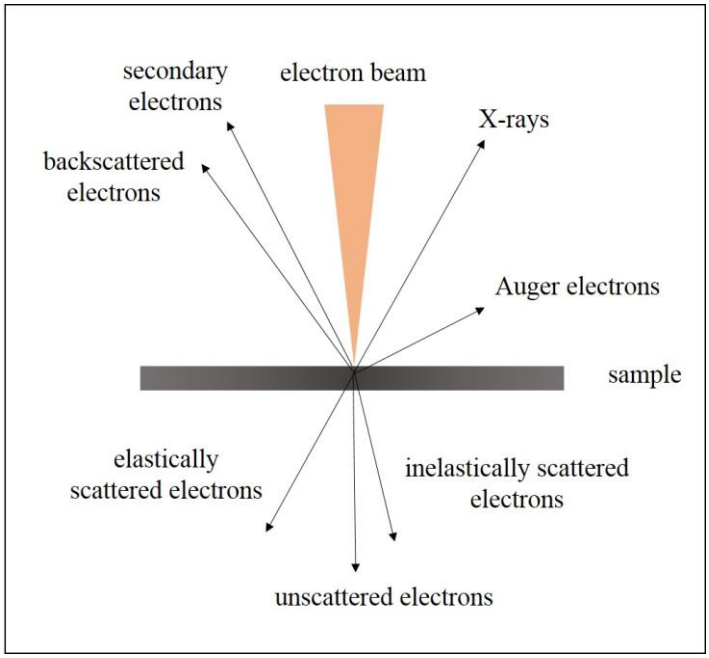

Figure 2-5. Electron-sample interactions in the TEM. The signals are generated when a high-energy electron beam interacts with a thin specimen. The directions shown for each signal do not necessarily represent the physical direction of the signal but indicate, in a relative manner where the signal is detected. Adapted from [29].

The main part of the electron beam transmitted by the sample consists of electrons that have not undergone any scattering. The beam also contains electrons that have been reflected or scattered (change in the trajectory) by the atoms of the sample, without losing

energy (elastic scattering). In addition to the directly transmitted and the diffracted electrons, there are other electrons in the beam that undergo inelastic scattering and lose energy by creating excitations in the specimen. A very important source of inelastic scattering occurs when the incoming electron induces as single-electron excitation in an atom. This might involve inner core atomic levels of atoms, such as inducing a transition from a lower level to a higher energetic level. This electronic excitation can decay via the return of excited electrons to their ground states, thereby producing secondary radiation, which often gives useful information about the sample. These types of transitions are utilized in various branches of electron spectroscopy.

The bright-field TEM images are produced by electrons scattered elastically through the small angles (so-called Bragg scattering). The bright-field contrast depends both on specimen material, its structure and orientation with respect to the beam. This kind of images are used for morphological and indirect structural characterization. Despite of other available modern techniques [31] the size distribution studies of the samples presented in this thesis have been done by measuring the two dimensional projection of nanoparticles in TEM bright field images with adequate magnification.

In contrast, the high-angle annular dark-field (HAADF) technique provides images produced by electrons scattered at high angles (4-11º). These electrons undergo the so-called Rutherford forward scattering, which is the consequence of interaction between the electrons and the atomic nuclei of the specimen. The scattering cross section, and thus the contrast in the HAADF images, is directly proportional to Z^2. In other words, HAADF contrast, also called Z-contrast, directly reflects the distribution of the different elements in the sample. In some cases, this technique is combined with scanning transmission electron microscopy (STEM) in which the electron beam is being focused down to a small spot (1 nm) and scanned through the sample.

Energy dispersive X-ray (EDX) spectroscopy was used to determine the chemical composition of the nanoparticles. When an incident electron of the electron beam hits an atom in the specimen, there is a probability of transferring its energy to the electron shell and ionize the atom. The ionized atom now has an electron vacancy in a certain shell. The electrons in outer levels will jump into this vacancy to restore the stationary state of the atom. During this process, X-ray radiation with an energy equal to the energy difference

between the levels is emitted. Each element has a unique electron shell structure, so the X-rays generated by the specimen are characteristic. Each type of atom produces several peaks in the spectrum corresponding to the transitions between different energy levels. By comparing the weighted integrated intensities of the peaks, the concentration ratio of the elements can be determined. EDX spectroscopy measurements performed in STEM mode also allow to determine the elemental distribution within the sample along a chosen line (so-called line scan) or to obtain a two dimensional elemental map.

Electron energy loss spectroscopy (EELS) utilizes the electrons that undergo inelastic scattering and lose energy after the interaction with the specimen. The amount of energy loss, measured using an electron spectrometer, provides as well information about the chemical composition of the sample.

To elucidate the crystalline structure of the sample, a diffraction pattern in the TEM is recorded. It shows concentric rings of scattering peaks corresponding to the various *d* spacing in the crystal lattice. The position and the intensities of the peaks are used for identifying the underlying crystalline structure (or phase) of the material.

Since conventional TEM images provides only the two-dimensional projections of the specimen, a method called 3D tomography is used to determine the three-dimensional morphology of cobalt oxide octahedra (results presented in section 5.5). This method consist of acquiring a series of TEM images by tilting the sample over a large tilt range, typically -70º to +70º, with an increment of 1°. After alignment of the projection images, the tilt series is combined into a 3D reconstruction of the original object through a mathematical algorithm [32, 33].

2.3.2 SQUID magnetometry

A SQUID (Superconducting Quantum Interference Design) magnetometer manufactured by Quantum Design (model MPMSXL) was used to study the magnetic properties of the powder samples. This instrument makes possible the study of the magnetization of relatively small samples (milligrams) at temperatures ranging from 5-390 K in fields up to 5 T. The SQUID magnetometer gives a quantitative measure of the magnetic moment,

measured either as a function of the temperature in a constant field or as a function of the applied field at constant temperature. This data is used to determine saturation magnetization, remanent magnetization, coercive field and transition temperatures (Curie Temperature T_C for ferromagnets or Néel temperature T_N for antiferromagnets).

The magnetometer system contains several different components including a computer operating system, a temperature control system, a sample transport system, a detection system, etc. The scope of this section is not to give a comprehensive review of the complete system and thus, only the superconducting-related parts will be discussed.

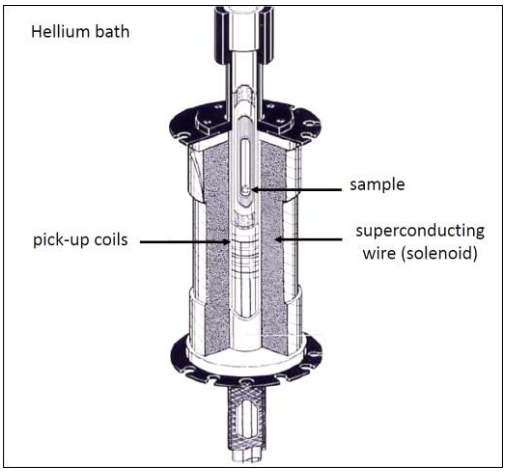

Figure 2-6. Sketch of SQUID magnetometer, showing the principal superconducting components and their location in the system, as well as the sample position.

Figure 2-6 shows a sketch of a SQUID magnetometer. The main components are:

- superconducting magnet that generates large magnetic fields,
- a superconducting detection coil which couples inductively to the sample,
- a Superconducting Quantum Interference Device (SQUID) connected to the detection coil,
- a superconducting magnetic shield surrounding the SQUID.

This magnetometry system employs a superconducting magnet wound in a solenoidal configuration. Superconducting magnets are made of materials with high critical fields (i.e. Nb_3Sn) that can sustain high current densities (zero resistance to the flow of DC electrical current), and therefore generate high magnetic fields when wound into a solenoid. The magnet is then constructed as a completely closed superconducting loop, allowing it to be

charged up to a specific current, then operated during a measurement in persistent mode without benefit of an external power supply.

Even though a SQUID magnetometer is the most sensitive device available for measuring magnetic fields, it does not detect directly the magnetic field from the sample. Instead, the sample moves through a system of superconducting detection coils that are connected to the SQUID with superconducting wires, allowing the current from the detection coils to inductively couple to the SQUID sensor.

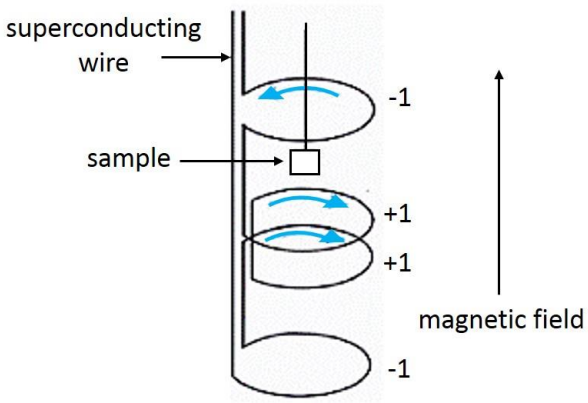

Figure 2-7. Schematic representation of the detection coil system. It consists of a superconducting wire wound in a set of three coils. Adapted from [34].

The detection coil is a single piece of superconducting wire wound in a set of three coils configured as a second-order (second-derivative) gradiometer, as shown in Figure 2-7. In this configuration, the upper coil is a single turn wound clockwise, the center coil comprises two turns wound counter-clockwise, and the bottom coil is a single turn wound clockwise. The coils are positioned at the center of the superconducting magnet outside the sample chamber such that the magnetic field from the sample couples inductively to the coils as the sample is moved through them. The radiometer configuration is used to reduce noise in the detection circuit caused by fluctuations in the large magnetic field of the superconducting magnet. The gradiometer coil set also minimizes background drifts in the SQUID detection system caused by relaxation in the magnetic field of the superconducting magnet. Ideally if the magnetic field is relaxing uniformly, the flux change in the two-turn center coil will be exactly canceled by the flux change in the single-turn top and bottom coils. On the other hand, the magnetic moment of a sample can still be measured by moving the sample through the detection coils because the counter wound coil set measures the local

changes in magnetic flux density produced by the dipole field of the sample.

These superconducting detection coils are connected to the SQUID with superconducting wires, allowing the current from the detection coils to inductively couple to the SQUID sensor. Then, the SQUID electronics produces an output voltage, strictly proportional to the current flowing in the SQUID input coil. Hence, the thin film SQUID device, which is located approximately some centimeters below the magnet inside a superconducting shield, essentially functions as an extremely sensitive current-to-voltage convertor. To measure even tiny magnetic flux, SQUIDs make use of a device called Josephson junctions. A Josephson junction is made up of two superconductors separated by a thin insulating layer through which electron pairs known as Cooper pairs can tunnel, creating an electrical current. The Cooper pairs on each side of the junction can be represented by a wave function similar to a free particle wave function. In the DC Josephson effect, a current proportional to the phase difference of the wave functions can flow in the junction in the absence of an applied voltage (the DC Josephson effect).

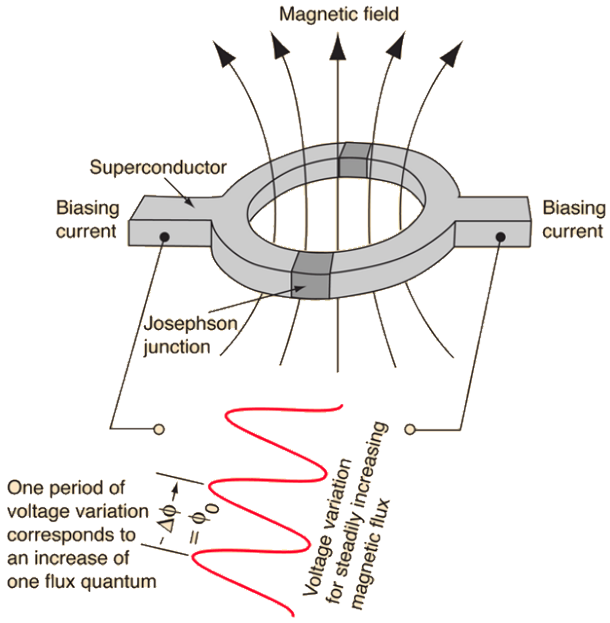

Figure 2-8. Schematic representation of a Superconducting Quantum Interference Device (SQUID), that makes use of Josephson junctions, where the electrons can tunnel through between the two superconductor regions creating an electrical current [35].

Because of the SQUID´s extreme sensitivity to fluctuations in magnetic fields, the sensor itself must be shielded both from fluctuation in the ambient magnetic field of the laboratory and from the large magnetic fields produced by the superconducting magnet.

Summarizing, the measurement is performed by moving the sample through the superconducting detection coils, which are located outside the sample chamber and at the center of the magnet. As the sample moves through the coils, the magnetic moment of the sample induces an electric current in the detection coils. Because the detection coils, the connecting wires, and the SQUID input coil form a closed superconducting loop, any change of magnetic flux in the detection coils produces a change in the persistent current in the detection circuit, which is proportional to the change in magnetic flux. Since the SQUID function is a highly linear current-to-voltage convertor, the variations in the current in the detection coils produce corresponding variations in the SQUID output voltage which are proportional to the magnetic moment of the sample. Excellent reviews of this characterization technique are [36, 37, 38, 39]. Further information on the magnetometry system and the measurements can be found in the MPMS User's manual and in the Application Notes and Technical Advisories available from *Quantum Design* Company [34].

2.3.3 Other techniques

A scanning electron microscope (SEM) was used to characterize the morphology and chemical composition of iron-cobalt nanowires (see chapter 3) and to check out the alignment of cobalt-nickel nanorods deposited on a substrate (see Appendix II). In scanning electron microscopy, a beam of accelerated high-energy electrons (keV) is focused at the surface of the specimen and scanned across it in a pattern of parallel lines. When the electrons strike the sample, they interact with the atoms and their kinetic energy is dissipated as a variety of signals produced by electron-sample interactions. The generated signals that derive from these interactions (like in the TEM) are collected so that, they can reveal information about the sample surface topography, chemical composition and crystalline structure. For instance, by scanning the sample and detecting the secondary electrons emitted from the atoms occupying the top surface, an image displaying the topography of the surface is created. The SEM is also capable of performing quantitative analysis of chemical composition of selected point locations on the sample. The interaction of the primary beam with atoms in the sample causes shell transitions which result in the emission of X-ray radiation with a certain energy characteristic of the parent element. Thus, the detection and measurement of these energies permits the elemental analysis (energy dispersive X-ray spectroscopy or EDX). For more extensive detailed information the reader is referred to

[28, 40].

Atomic force microscopy (AFM) was used as an additional technique to determine the surface morphology of the iron-cobalt nanowire sample. In contrast to other microscopy techniques, AFM probes the sample in three dimensions. Since SEM was not capable of providing information of the vertical dimension of the sample (z component, normal to the sample surface), AFM was used for mapping the surface topography (see section 3.3.2). AFM in the tapping mode operates by rasting a cantilever with a sharp tip across the sample surface. The tip-cantilever probe oscillates at the sample surface while the tip is scanned, thus, the tip lightly taps the sample surface while rastering (once in each oscillation cycle). The cantilever oscillation amplitude changes with sample surface topography and the topography image is obtained by monitoring these changes. For further reading, the reader is referred to [41, 42, 43].

X-ray photoelectron spectroscopy (XPS), also known as electron spectroscopy for chemical analysis (ESCA) is used to analyze the surface chemistry of CoNi nanorods (section 4.4) and CoO octahedral nanocrystals (section 5.4). It is a surface-sensitive analytical technique that provides information of both elemental composition of the sample and the chemical state of the elements within the material. XPS spectra are obtained by irradiating a solid surface in a UHV environment with a beam of X-rays while simultaneously measuring the kinetic energy and number of electrons that are emitted from the top few nanometers of the material being analyzed. The kinetic energy of these ejected electrons depends upon the photon energy of the X-rays and the binding energy of the electron (i.e., the energy required to remove the electron from the surface). The later depends on the element from which the electron is emitted and the orbital from which the electron is ejected. Thus, the energies and intensities of the photoelectron peaks enable the identification and quantification of all surface elements and corresponding chemical states [44, 45]. As mentioned in section 2.3.1, EELS spectroscopy provides similar information.

The structural characterization of several samples presented in this PhD thesis is supported by X-rays diffraction (XRD**)** technique (see sections 5.4). It relies on the dual wave/particle nature of X-rays to obtain information about the structure of crystalline materials and atomic spacing. The dominant effect that occurs when an incident beam of monochromatic X-rays interacts with a target material is the scattering of those X-rays from

atoms within the target material. In materials with regular structure (i.e. crystalline), the scattered X-rays undergo constructive and destructive interference, what is nothing else but the diffraction process. When the interaction of the incident rays with the crystalline sample produces constructive interference, the diffraction condition is satisfied and the X-ray diffraction process is described by Bragg´s law [2]. This law relates the wavelength of the electromagnetic radiation to the diffraction angle and the lattice spacing in a crystalline sample. The diffracted X-rays are then detected, processed and counted. In powder or polycrystalline materials, that are composed of many tiny crystallites randomly oriented in all possible orientations, all possible diffraction peaks and hence, all the interatomic distances can be detected by scanning the sample through a range of 2θ angles. The peak positions, intensities, widths and shapes, all provide important information about the structure of the material. Conversion of the diffraction peaks to *d*-spacings allows identification of the material with a set of unique *d*-spacings. Typically, this is achieved by comparison of *d*-spacings with standard reference patterns.

3 Iron-cobalt nanowires

All samples of nanowires discussed in this chapter have been produced by the group of Prof. Manuel Vázquez Villalabeitia in the Spanish National Research Council (CSIC: Consejo Superior de Investigaciones Científicas) in Madrid (Spain), at the ICMM. The research herein reported focuses on the magnetic hardening of $Fe_{30}Co_{70}$ nanowires (with average diameters of 20 nm and 40 nm and average lengths of 6 μm and 7.5 μm, respectively) by means of magnetic pinning at the tips of the nanowires, using anodic aluminum oxide (AAO) templates. In this regard, two different materials were studied as the capping layer: naturally formed FeCo oxide layer (ferrimagnetic material) and sputtered $Ni_{50}Mn_{50}$ alloy (antiferromagnetic material). The procedure of magnetic hardening is described in detail. Afterwards, the trend of the coercive field at different steps of the process measured by SQUID magnetometry is analyzed. The experimental findings are supported by micromagnetic simulations, which are also briefly summarized at the end of the chapter.

3.1 Introduction

Porous aluminum oxide (named Anodic Aluminum Oxide: AAO) membranes have become an ideal scaffold for the fabrication of aligned nanowires [46, 47, 48]. Anodization of aluminum foil at controlled conditions can produce regular patterns of cylindrical pores, with highly controllable pore diameter and good periodicity [49, 50, 51, 52, 53, 54]. Such a well-defined nano-architecture can be used as a template in the production of aligned magnetic nanowires by electrodeposition of magnetic materials in the interior of the pores.

As discussed in the section of scope and objectives, alternative magnetic materials that do not contain rare earth elements have been intensively investigated for permanent magnet applications. In this regard, 3*d* transition metals based magnetic nanowires were suggested as possible candidates [55]. The large magnetization of 3*d* elements offers a very strong magnetic shape anisotropy when considering nanowires with a high aspect ratio (*L*/*D*, where *L* and *D* are the length and the diameter of nanowires, respectively). Consequently, aligned ensembles of such nanowires will show a large coercive field and a high remanent magnetization, both parameters required for permanent magnets.

Moreover, these nanowires considered have one dimension (the diameter) smaller or comparable to the characteristic critical single domain size [56]; rendering very unfavorable multiple magnetic domain states, and consequently avoiding magnetic softening effects. In addition, 3*d* metals and their alloys have high Curie temperatures, which render the permanent magnet also suitable for technological applications at elevated temperatures.

Hence, it is undoubted that 3*d* transition metal based magnetic nanowires embedded in AAO membranes are good alternative candidates for high performance permanent magnet applications. Indeed, a large energy product of aligned pure Co and CoPt alloy nanowire assemblies has already been reported [55, 57, 58]. Moreover, magnetically hard nanowires aligned in porous anodic aluminum oxide (AAO) membranes have been discussed for applications in ultrahigh density magnetic storage devices [59], read-write recording heads [60] and magnetic field sensors [61].

According to the Slater-Pauling curve, binary FeCo alloys have the largest saturation magnetization among the 3*d* alloys yielding the largest shape anisotropy field H_A in high aspect-ratio nanowires [62, 63]. In addition, for a high performance permanent magnet a high packing density of magnetic nanowires is required. Close packing, however, leads to large magnetostatic interactions among nanowires, which significantly reduce the effective shape anisotropy field [64, 65]. For nanowire arrays in an AAO matrix the magnetostatic coupling between them depends on the volume fraction (porosity factor *P*) of the magnetic material in the template [66]. It has been shown [67, 68] that the effective anisotropy field H_D of nanowire arrays arising from shape anisotropy and dipolar coupling can be estimated by:

$$\mu_0 H_D = \frac{1}{2}\mu_0 M_s(1 - 3P) \qquad \textit{(Equation 3-1)}$$

From this equation it follows for $P = 1/3$ that the dipolar coupling between nanowires equals the shape anisotropy field and therefore a "hard axis-like" behavior in both directions parallel and perpendicular to the nanowire axis is observed [67]. Only a large magnetocrystalline anisotropy with the easy axis being aligned to the nanowires axis can overcome the effect of those magnetostatic interactions in highly packed nanowire arrays.

So far ideal single domain nanowires arranged in close-packed arrays have been considered. Experimentally it has been found that the coercive field of nanowire arrays is three times smaller than the shape anisotropy field, even with $P << 1/3$ [59]. Micromagnetic simulations have revealed that this softening in magnetic nanowires derives from the formation of a vortex and the nucleation of domain walls at their tips, with a subsequent depinning and propagation of domain walls along the length of the nanowire, which reduces H_C [69, 70, 71, 72]. These magnetic reversal modes strongly depend on sample properties, i.e. material and composition, crystalline structure, morphology (shape and size) and magnetocrystalline anisotropy [72]. In any case, the nucleation starts at the tips where the local demagnetizing field, which is almost parallel to the external field, has the largest value [69].

Accordingly, in this study, the exploitation of the interfacial exchange between ferromagnetic and antiferromagnetic or ferrimagnetic materials with high magnetocrystalline anisotropy is analyzed for the improvement of the performance of rare-earth-free permanent magnets based on 3*d* metal nanowires. The fact that domain wall nucleation occurs at the nanowires tips suggests that any pinning of the magnetization at this position will effectively increase the coercive field. Since it has been shown that in nanometer-sized FeCo and CoNi particles large magnetic anisotropies can be induced by oxidation of their surfaces [73, 74], it is therefore reasonable to think that the coercive field of nanowires can be increased by oxidizing their ends. Following this idea, nanowires tips were therefore released from the AAO membrane to form either a FeCo oxide layer (ferrimagnetic material) by natural oxidation or sputter an antiferromagnetic $Ni_{50}Mn_{50}$ layer, both tested independently as pinning layers. The gain in coercive field due to this interfacial exchange was analyzed in both cases.

3.2 Synthesis

3.2.1 Electrochemical method

Iron-cobalt nanowire arrays were synthesized using the electrochemical deposition method with an AAO template at room temperature. The mechanism behind the growth of the porous AAO nanostructure is out of the scope of this thesis and the reader is referred to the literature [49, 50, 51, 52, 53, 54, 75], which present an excellent overview of the state of the art of this technique and describe precisely the mechanism of formation of these templates.

A regular self-organized porous nanostructure can be formed when aluminum is anodized in acidic media. The anodization of aluminum is an electrochemical process that modifies the surface chemistry of the metal, via oxidation, to produce an anodic oxide layer. After a two-step anodization process, the resulting anodic aluminum oxide (AAO) membrane consists of a porous structure in which the pores are arranged in a highly ordered honeycomb-like nano-architecture. The pores are characterized by a high aspect ratio that favors their use as hollow templates in the production of align magnetic nanowires by electrodepositing the magnetic material inside.

Though many types of nanocomposites have been already fabricated using anodic porous alumina as a host material, in 1995 Masuda and Fukuda developed a process for fabricating a nanohole array in which the honeycomb structure of the anodic porous alumina is replaced through a two-step molding process [49]. After the first anodization, the cell arrangement of anodic porous alumina is usually very different from the ideally packed hexagonal columnar array. However, a second anodization step can produce porous alumina with a highly ordered cell configuration.

After this process, the anodic porous alumina has a close-packed array of columnar hexagonal cells with central, cylindrical, uniformly sized holes ranging from 6 to 200 nm in diameter [76]. Figure 3-1 (a) presents a sketch of the top view of these membranes.

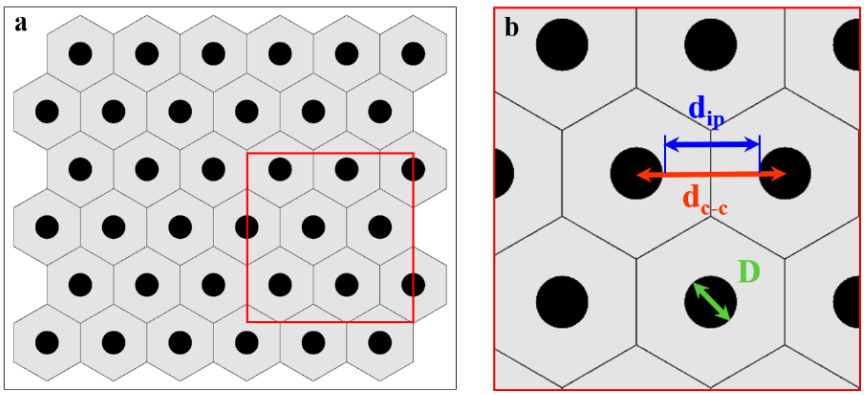

Figure 3-1. (a) Sketch of the top view of the AAO membrane after the second anodization with a magnified region shown in (b). d_{ip} in the interparticle distance, d_{c-c} is the distance from center to center of nanowires and D is the diameter of space where to grow the nanowires, and thus, the final diameter of the nanowires as well.

Geometrical characteristics of these membranes, such as pore diameter, periodicity and density distribution (see Figure 3-1) can be all controlled by tuning the experimental parameters (applied voltage, time of anodization, acid type, molarity, etc.) used during the production of these structures. For example, a wide variety of acids have been tested for the anodization process to address specific applications, from which it turned out that oxalic, phosphoric and sulfuric acid are suitable to manufacture nano-pores and tune the interpore distance. It is worth mentioning that the purity of aluminum foils used as starting materials have a direct bearing on the dissolution rate, which lastly has a significant impact on the morphology of the resulting nanostructures [77]. Thus, high purity aluminum foils are required.

In this thesis, the ordered templates were prepared by double anodization process from high purity (99.999%) aluminum foils. In order to study the size dependent magnetic properties of FeCo nanowires, two types of membranes were produced with 20 and 40 nm in diameter with the following specifications. The thickness (i.e., pore length) for both templates was kept to about 40 µm. For the template with pore diameter of 40 nm, anodization was carried out with oxalic acid electrolyte under 40 V constant voltage and keeping the temperature at 4 ± 0.5 ºC. First and second anodization processes lasted for 24 h and 20 h, respectively. The template with pore diameter of 20 nm was obtained using sulfuric aqueous solution as electrolyte, applying a constant voltage of 20 V and keeping the temperature in the range 0.5 ± 0.5 ºC. First and second anodization processes lasted for 16 h and 3 h, respectively. For both templates, an ordered hexagonal arrangement of the pores in AAO membranes was achieved as shown below in Figure 3-7 and sketched in Figure 3-2 (a).

After the formation of the pore membranes, residual Al and the alumina barrier layer at the bottom of foils were chemically etched. A thin 50 (100) nm thick gold layer for the 20 (40) nm pore membranes was subsequently sputtered to serve later as an electrode for the final electroplating of nanowires, as sketched in Figure 3-2 (b and c). Please note that the ratio of nanowires length and AAO membrane thickness (pore length) in the sketch is not representative for the nanowires under investigation.

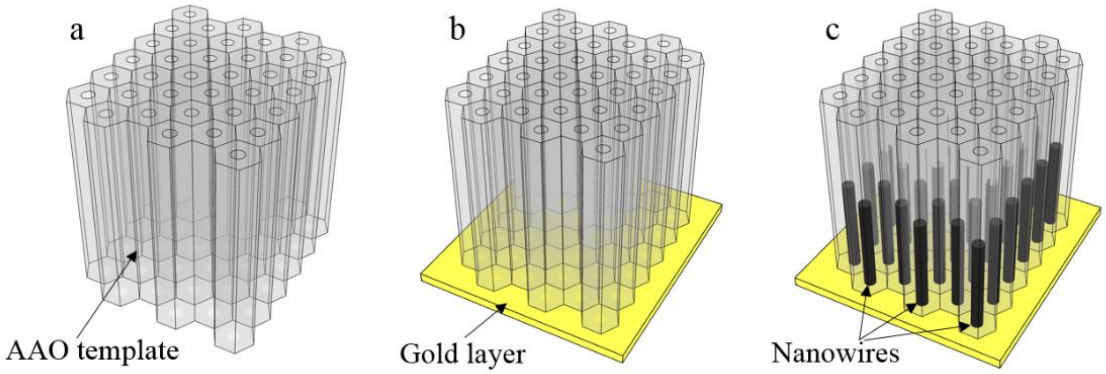

Figure 3-2. Sketch of the process of electroplating. (a) Drawing of the AAO structure with cylindrical holes arranged in a highly ordered honey-comb nano-architecture, which serve as template for the nanowire synthesis. (b) Deposition of a gold layer for electroplating (in yellow). (c) Schematics of nanowires electrochemically grown inside the pores of the AAO membrane.

$Fe_{30}Co_{70}$ alloy nanowires were grown into the nanopores of AAO templates by DC electrodeposition from sulphate-based electrolytes containing 0.12 M $CoSO_4 \cdot 7H_2O$ + 0.098 M $FeSO_4 \cdot 7H_2O$ + 0.16 M H_3BO_3 + 0.06 M $C_6H_8O_6$ at ambient temperature. The pH value was kept constant at 3.0 ± 0.2. Thus, two samples of $Fe_{30}Co_{70}$ alloy nanowires were prepared with average diameters of 20 and 40 nm.

3.2.2 Partial removal of the AAO membrane

For pinning the magnetic nanowires by ferri- or antiferromagnetic materials, the upper few tens of nanometers of the membrane were removed. Schematic representations shown in Figure 3-3 illustrate the strategy. At first, a small piece of each sample (Figure 3-3 (a)) was glued onto a silicon substrate for better stability. Each piece was glued upside down with the Au layer on topside using GE varnish (Figure 3-3 (b)). The samples are

glued in such way to reduce difficulties in the process of partial removal of the AAO membrane, which is actually a challenging issue and has not been described in the literature. Please note that the nanowires are 6-7 µm in length and the total pore length is about 40 µm, which means that only the bottom first few microns of the membrane pores (gold layer side) are filled with magnetic material during electroplating and more than 30 µm of the pores are still empty above (Figure 3-3 (a)). It is easier then to control the partial removal of the membrane when starting the process from the gold side, where only few nanometer of the membrane must be removed to have free-standing nanowires. If the partial removal of the membrane is carried out starting in the other side (opposed to gold layer), several micrometer should be removed to obtain free-standing tips, which would become much more complicated.

An aqueous solution of potassium iodine and iodine was used to remove the gold layer (Figure 3-3 (c)). With the aim of removing partially the AAO membrane, the sample was kept for 4 min at 60°C in the so-called orange solution, which is a mixture of phosphoric acid (H_3PO_4 : 6.9 wt.%) and chromic acid (H_2CrO_4 : 1.8 wt.%) [78]. The AAO membrane was etched several tens of nanometers as sketched in Figure 3-3 (d).

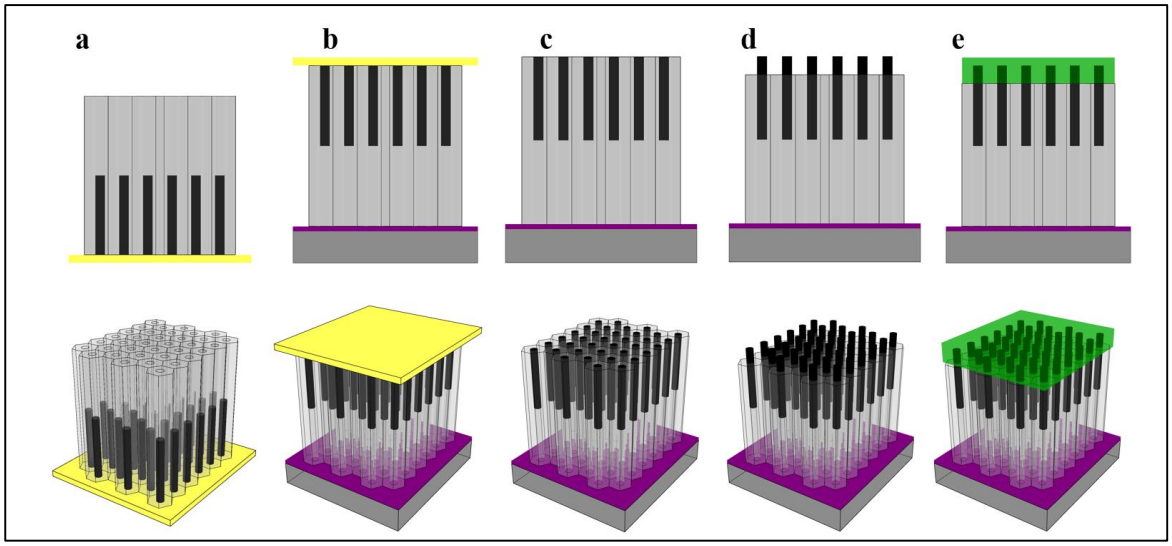

Figure 3-3. Schematic drawing of the process of the partial removal of the AAO membrane. Cross-sectional drawing are depicted in the first row with corresponding 3D perspective underneath. (a) Initial state of the samples of FeCo nanowires embedded in the AAO membrane. (b) Samples glued onto silicon substrate with Au layer (in yellow) on top, and used as an electrode during electrodeposition on top side. (c) Samples after removal of the gold layer. (d) Samples after partial removal of the AAO membrane, which leads to a self-standing opened nanowires tips exposed to air (to form naturally FeCo oxide layer), or alternatively, (e) samples after deposition of an antiferromagnetic NiMn capping layer (in green).

As a consequence, the nanowires remain aligned in the alumina membrane with a freestanding tip exposed to air, which causes the natural oxidation of their tips. This oxidation process leads to a magnetic hardening of the nanowires as discussed in detailed in the subchapter 3.4.

3.2.3 Sputtering of $Ni_{50}Mn_{50}$ on sample surface

After studying the effect of magnetic pinning of the nanowires with naturally formed FeCo oxide layer at the nanowires tips, a similar study was done using an antiferromagnetic NiMn layer. To accomplish this study, the sample with free standing nanowires (Figure 3-3 (d)) was introduced in a UHV-compatible plasma etching system, where the oxide layer was reduced by hydrogen plasma. Firstly, the hydrogen plasma was applied for 20 min at room temperature, with a pressure of $1.4 \cdot 10^{-1}$ mbar, DC bias voltage of -500 V and power of 50 W. Afterwards, a 30 nm $Ni_{50}Mn_{50}$ layer was deposited *in-situ* on the sample surface (see Figure 3-3 (e)) by radiofrequency sputtering for 35 min at a frequency of 13 MHz under an Ar^+ pressure of $2.8 \cdot 10^{-1}$ mbar. The dc-bias voltage was -400 V and the power was 50 W. The detailed structural and magnetic characterization of the samples accomplished at different stages of the magnetic hardening process follows in chapters 3.3 and 3.4.

3.3 Structural characterization

3.3.1 Scanning Electron Microscopy

Scanning Electron Microscopy (SEM) was used to characterize the morphology of the membranes and the nanowires synthesized. Figure 3-4 shows cross sectional SEM images of the FeCo nanowires sample glued onto the silicon substrate. Figure 3-4 (a) shows a low magnification image where the sample of 40 nm in diameter nanowires (appreciated as a nearly horizontal line with contrast variations in the middle of the image) is glued onto the silicon substrate (seen in white). Figure 3-4 (b) depicts a magnified image of the selected area marked in red in Figure 3-4 (a). Two different regions can be distinguished, illustrating that only few micrometers of the pores in the AAO membrane are filled with FeCo.

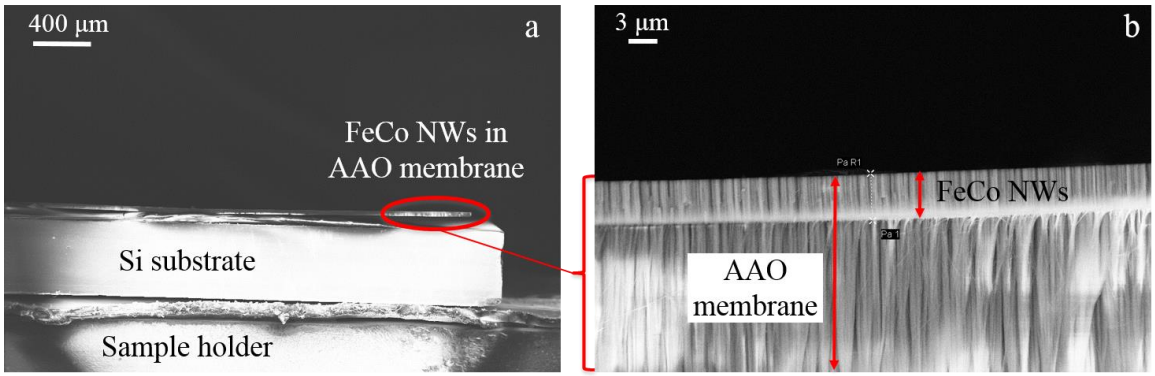

Figure 3-4. Cross-sectional SEM images of 40 nm in diameter nanowires sample glued onto a silicon substrate (a) and enlarged image of the selected area (b).

Lateral SEM images of FeCo nanowires samples of 40 nm and 20 nm in diameter before partial AAO removal are displayed in Figure 3-5 (a) and (b), respectively (sketched in Figure 3-3 (b)). In both cases, the images show that all pores have been filled homogeneously leading to high quality nanowires with constant diameter of 41 ± 2 and 20 ± 1.5 nm, correspondingly. The porosity value stays constant for both samples (P = 0.13) while the center-to-center distances are $d_{c\text{-}c}$ = 105 nm and 53 nm for the nanowires samples of 40 nm and 20 nm in diameter, respectively. Further details are given in Table 3-1.

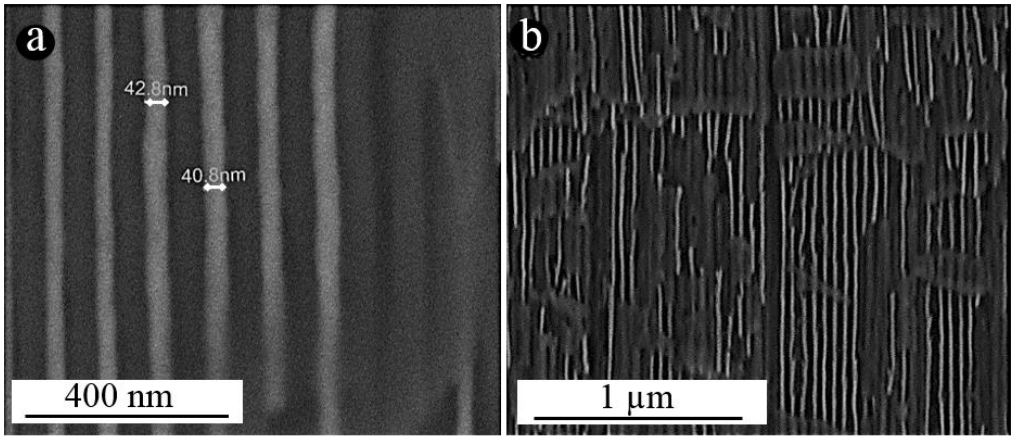

Figure 3-5. Cross-section SEM images of the FeCo nanowire sample with 40 (a) and 20 nm in diameter (b). All pores of the AAO membrane (dark) have been filled homogeneously with magnetic material forming nanowires (bright).

Table 3-1. Characteristic parameters of the synthesized $Fe_{30}Co_{70}$ nanowires.

Sample name	Diameter D [nm]	Distance $d_{c\text{-}c}$ [nm]	Length L [µm]	Aspect ratio L/D	Porosity factor P
20 nm	20 ± 1.5	53 ± 2	6	300	0.126
40 nm	41 ± 2	105 ± 2	7.5	188	0.130

The porosity value was calculated using the equation:

$$P = \frac{2\pi}{\sqrt{3}}\left(\frac{r}{d_{c-c}}\right)^2 \quad \textit{(Equation 3-2)}$$

where P is the porosity factor, r is the nanowires radius and $d_{c\text{-}c}$ is the distance from center to center of neighbouring nanowires [66].

The chemical composition of the FeCo nanowires was determined by quantitative Energy Dispersive X-Ray Spectroscopy (EDX), which confirmed an alloy composition of $Fe_{(30.6\pm0.5)}Co_{(69.4\pm0.6)}$ (See Figure 3-6).

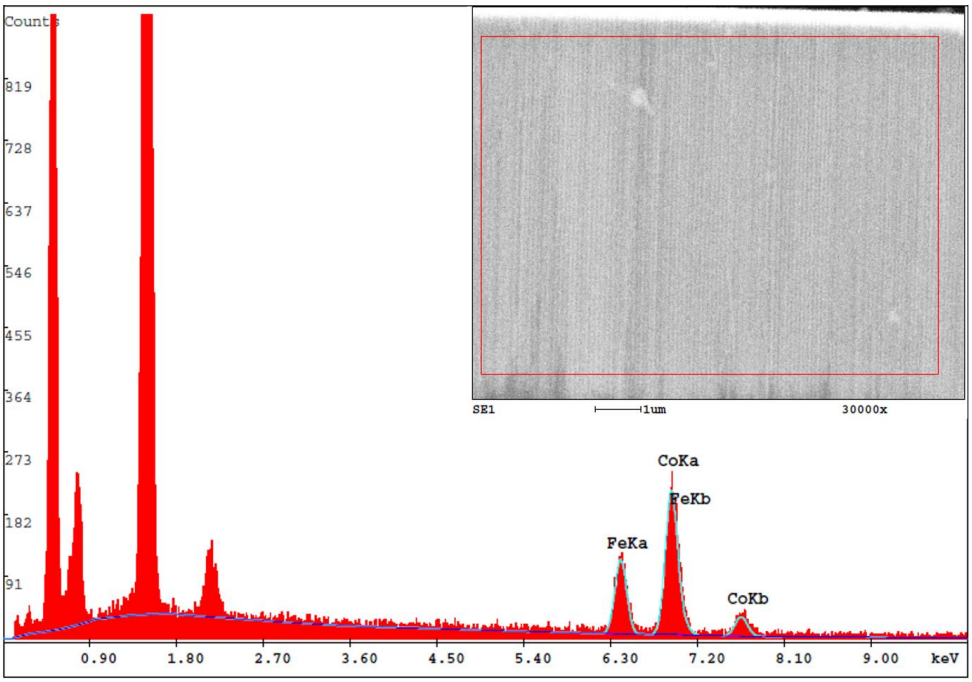

Figure 3-6. Energy dispersive X-ray spectrum of the 40 nm diameter nanowires sample performed on the area marked in the cross-sectional SEM image (inset), which confirm an allow composition of $Fe_{(30.6\pm0.5)}Co_{(69.4\pm0.6)}$.

The surface morphology of both samples at the different stages of the AAO removal process was imaged by SEM. Only the study of the 40 nm diameter sample is shown for simplification. A top view SEM image of the 40 nm diameter sample after the removal of the gold layer is shown in Figure 3-7 (a) and corresponds to the sketch represented in Figure 3-3 (c) viewed from the top perspective. The dark circular periodic structure corresponds to the nanowires embedded in the honey-comb nanostructured AAO membrane (light gray).

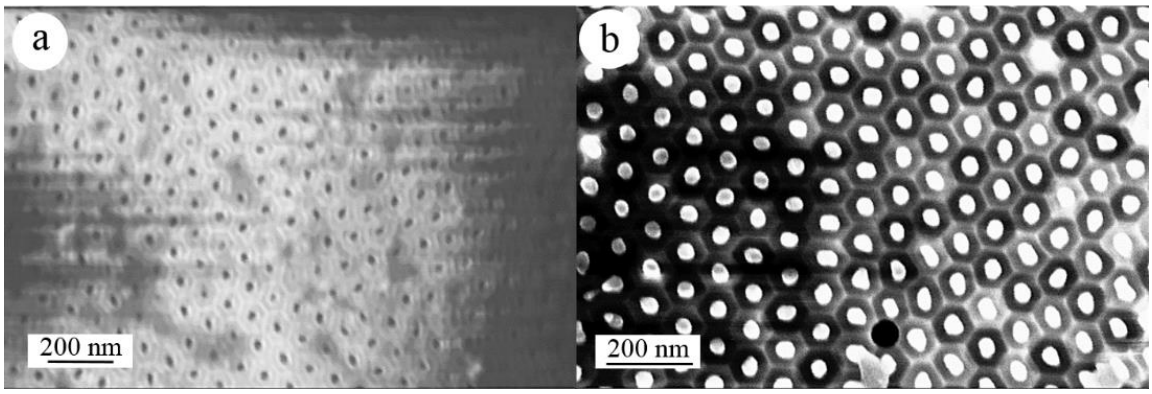

Figure 3-7. Top view SEM image of FeCo nanowires sample of 40 nm in diameter before (a) and after partial removal of the AAO membrane (b). The circular periodic structures are the nanowire tips, embedded in the AAO membrane, which is seen as a hexagonal structure. The varying background contrast is due to charging of the AAO substrate while scanning.

The result after the partial removal of the AAO membrane with orange solution is shown in Figure 3-7 (b) and corresponds to the sketched depicted in Figure 3-3(d). In this case, the bright circular periodic structures are the free standing nanowires tips and the darker background is the AAO membrane. The color inversion is due to the difference in height of the nanowires with respect to the AAO membrane and the number of electrons leaving the specific materials. Prior to the partial removal of the membrane (Figure 3-7 (a)), the nanowires tips present equal high level as the membrane. However, after removing partially the membrane (Figure 3-7 (b)), the nanowires tips are free standing for several tens of nanometers with respect to the AAO membrane surface. The varying background contrast of both images as well as the apparent elongation of some rod tips in panel (b) are due to charging of the AAO membrane while scanning.

3.3.2 Atomic Force Microscopy

The height of the nanowires free standing tips after the partial removal of the membrane was characterized by Atomic Force Microscopy (AFM). Figure 3-8 depicts the AFM measurement of the 40 nm nanowires sample (a) and the height profile corresponding to the line scan performed along the black line pointed with an arrow in AFM image (b). The color coded scale included in panel (a) represents the height of the free standing nanowires tips with respect to the AAO membrane surface and its analysis indicates that the partial removal of the template was successful. Accordingly, about 40-70 nm of the top side of the AAO membrane was etched.

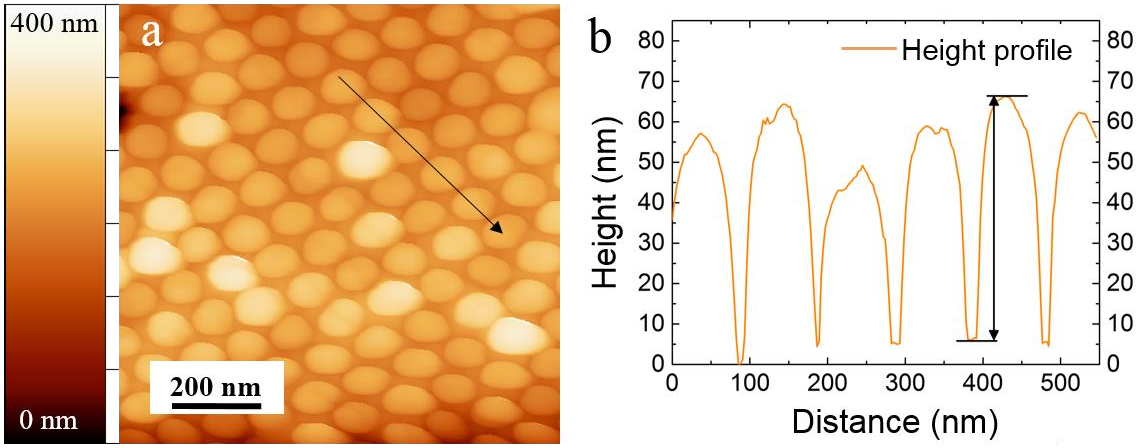

Figure 3-8. (a) AFM measurement of the 40 nm nanowires sample. (b) Height profile corresponding to the line scan performed along the line pointed with black arrow in (a). The color coded scale included in panel (a) represents the height of the free standing nanowires tips with respect to the AAO membrane surface. The apparent broadening of nanowire tip diameters to about 100 nm in panel (a) is an artefact caused by the dimensions of the AFM cantilever.

The three dimensional reconstruction of the sample surface as well as the statistical study of the free-standing tip height are presented in Figure 3-9 (a) and (b), respectively. A log normal function was used to fit the results and the statistical mean of free-standing nanowire tip length was found to be 56 nm with a statistical deviation of 13 nm. As a consequence, the nanowires remain aligned in the alumina membrane with a free standing tip between 40 and 70 nm long and exposed to air, undergoing consequently a natural oxidation process. The length of the free-standing tip of the 20 nm sample was estimated to be around 200-240 nm.

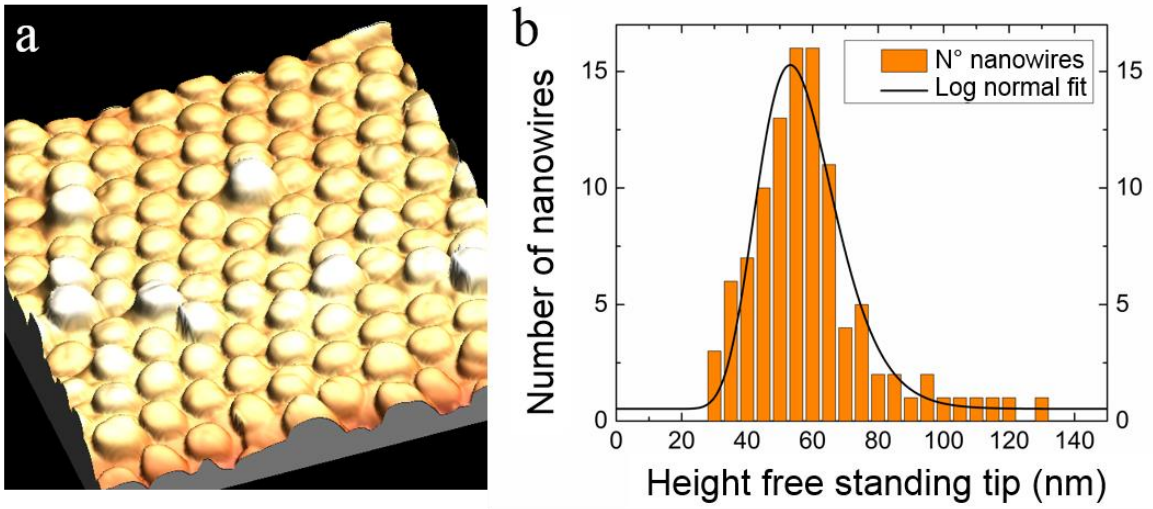

Figure 3-9. (a) 3D reconstruction of Figure 3-8 (a). (b) Histogram of the statistical analysis of the free-standing tip height of the nanowires compared to the AAO template surface.

The length variation of the exposed tips arises from (i) the sputtered gold layer with a certain thickness variation in the holes and (ii) the inhomogeneous etching process on the nanoscale regime. The apparent broadening of nanowire tip diameters to about 100 nm in the AFM image as compared to the SEM image of the identical sample (Figure 3-7 (b)) is due to the convolution of the sharp-edged sample surface and the pyramidal shaped AFM cantilever.

3.4 Magnetic characterization

The magnetic measurements were carried out using a Superconducting Quantum Interference Device (SQUID) magnetometer with temperature varying from 10 to 300 K and a maximum magnetic field of ± 2.0 T. The diamagnetic signals from the Si substrates and the glue were subtracted and all the data have been normalized to the saturation magnetization.

Hysteresis loops of both samples were measured at different steps of the synthetic process. Figure 3-10 shows hysteresis loops of the as-prepared 20 nm nanowires diameter sample (a) and 40 nm (b) with the external magnetic field applied parallel and perpendicular to the nanowire long axis at T = 300K.

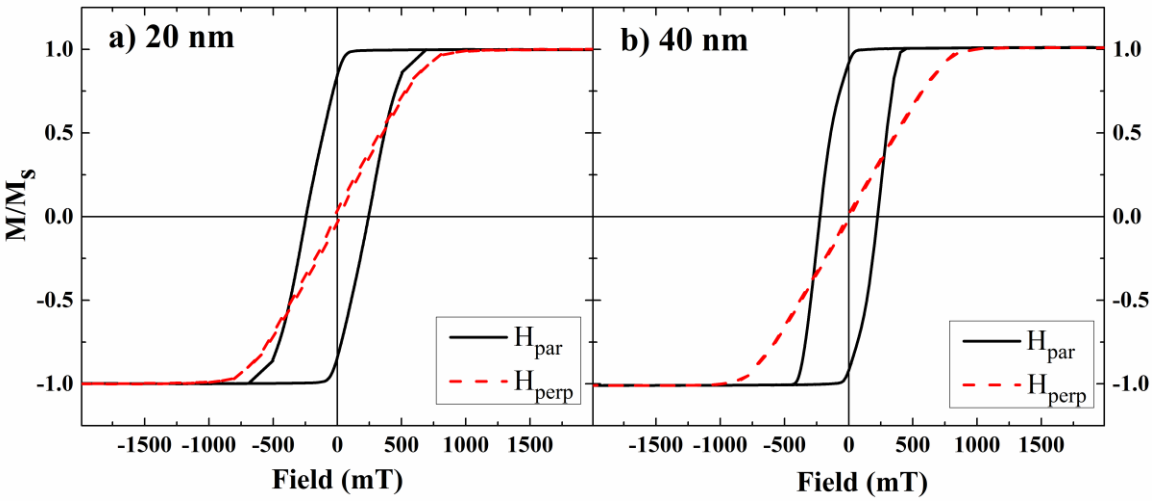

Figure 3-10. Hysteresis loops of nanowires of 20 nm (a) and 40 nm in diameter (b) measured at T = 300 K with the external magnetic field applied parallel (black) and perpendicular (red) to the nanowires long axis.

As expected considering the porosity factor P = 0.13 the magnetic anisotropy easy axis for both samples is parallel to the nanowire long axis, which is confirmed by the inspection of the hysteresis curves in Figure 3-10, being square-like shape when applying the field parallel to the nanowire axis and s-like shape when applying it perpendicularly. The saturation magnetization, M_s, coercive fields, H_C, and normalized remanent magnetization, M_r/M_s, for both samples are summarized in Table 3-2.

Table 3-2. Saturation magnetization M_s, normalized remanent magnetization M_r/M_s, and coercive field H_c obtained from SQUID magnetometry.

Diameter	M_s (MA/m)	M_r/M_s	$\mu_0 H_c$ (mT)
20 nm	1.5 ± 0.2	0.84 ± 0.02	240 ± 2
40 nm	1.6 ± 0.2	0.92 ± 0.02	220 ± 2

The estimation of the saturation magnetization, M_s, includes calculations of nanowires volume fraction in AAO templates. In the present $Fe_{30}Co_{70}$ alloy the bulk saturation magnetization is 1.7 MA/m ($\mu_0 M_s$ = 2.2 T), and it is fairly close to the saturation magnetization of both samples, 1.5 ± 0.2 MA/m and 1.6 ± 0.2 MA/m for 20 and 40 nm diameter nanowires samples, respectively. However, imperfections and vacancies may occur during the electrodeposition process of magnetic nanowires in the AAO template as well as flaws in the template itself. Thus, the difference between the calculated experimental and the literature values stems from the underestimation of the saturation magnetization due to these inhomogeneities in the electrodeposition process and not from the measurement techniques.

The measured coercive field of the 20 nm diameter sample is 240 ± 2 mT and for the sample of 40 nm in diameter is 220 ± 2 mT. It is worth to compare these experimental values with a simple theoretical approach. For the ideal case of an isolated cylindrical nanowire with the magnetocrystalline easy axis parallel to the nanowire axis and assuming coherent magnetization reversal the coercive field H_C of this system can be estimated by:

$$\mu_0 H_c = \mu_0 H_A + \mu_0 H_{MC} = (N_\perp - N_\parallel)\mu_0 M_s + \mu_0 H_{MC} \qquad \textit{(Equation 3-3)}$$

where H_{MC} denotes the magnetocrystalline anisotropy field, $N_\perp$ and $N_\parallel$ are the demagnetizing factors perpendicular and parallel to the nanowire axis, respectively. For nanowires with huge aspect ratio ($L/D >> 10$) the demagnetizing factors can be approximated by $N_\perp = ½$ and $N_\parallel = 0$ [79]. The magnetocrystalline anisotropy of *bcc* FeCo crystals is small, about 50 times smaller than the value of *hcp* Co [80]. Therefore, H_{MC} is very small as compared to H_A and the second term in equation (3-3) can be neglected. In this case, the coercive field of a FeCo nanowire may reach the value of $\mu_0 H_c = 1/2\ \mu_0 M_S = 1.1$ T, taking the bulk magnetization of $Fe_{30}Co_{70}$ (1.7 MA/m, $\mu_0 M_s = 2.2$ T).

For both diameters herein considered, the coercive field Hc is significantly smaller than the theoretical upper limit estimated from the shape anisotropy field, and it is reduces to approximately 20% in both cases. This fact indicates that domain wall nucleation and propagation determines the magnetic reversal process rather than coherent rotation.

In agreement with micromagnetic simulations [72], H_c is smaller for nanowires with larger diameter. The modeling, however, predicts a larger difference of the coercive fields of nanowires with D = 20 and 40 nm [69]. This large difference in the simulations is a consequence of the different mechanisms of magnetic reversal. Calculations showed that for these two different diameters the magnetic reversal mode usually changes from vortex (for d = 40 nm) to transverse domain walls (for d = 20 nm) [70, 71]. The domain wall nucleation and reversal types have the most significant influence on the coercive field of nanowires [70, 71, 81, 82]. In the two studied samples the difference in H_c is rather small (about 10%, see Table 3-2), suggesting that the magnetization reversal process in both samples is similar, and can most likely be described by vortex-like domain wall nucleation at the tips of the nanowires and its further propagation [82]. The reduced remanent magnetization M_r/M_s, for the 20 nm diameter sample is smaller than for 40 nm sample, opposing theoretical predictions [71]. These disagreements between the experimental findings and calculations can be explained by the fact that the nanowires in these two samples may possess a different magnetocrystalline anisotropy energy density.

To complete the magnetic characterization, low temperature magnetic properties were also recorded. The comparison of hysteresis loops of nanowires with non-oxidized tips (initial state) and open oxidized tips (OOT) (after partial removal of the membrane) is shown in Figure 3-11 for 20 nm (a) and 40 nm sample (b). The samples were measured at T = 10 K after field cooling (FC) in an external magnetic field of 2 T. The results obtained

from these low temperature measurements, including the normalized remanent magnetization, the coercive field and exchange bias field, are summarized in Table 3-3.

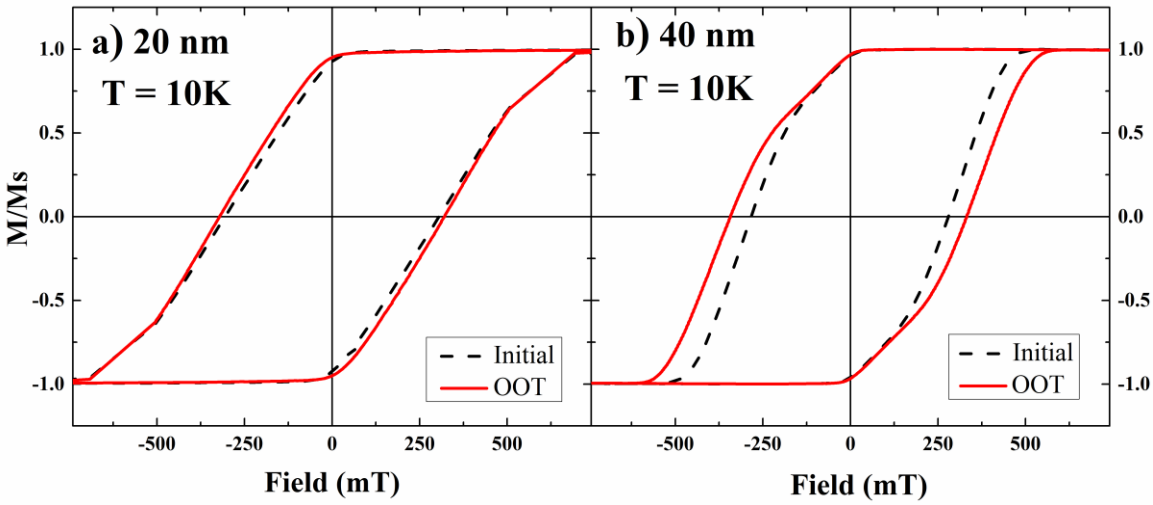

Figure 3-11. Hysteresis loops measured along the nanowire long axis at T = 10 K of 20 nm (a) and 40 nm (b) after field cooling in 2 T. The initial state is plotted in dashed black and after partial removal of the membrane (OOT: Opened Oxidized Tips) is presented in solid red. After releasing 40-70 nm of the surrounding AAO matrix and surface oxidation of the open tips the coercive field increases.

Table 3-3. Values obtained from hysteresis loops measured at 10 K for both samples, with 20 and 40 nm in diameter: normalized remanent magnetization, coercive field H_c and exchange bias field H_{ex} after cooling the sample in an external magnetic field of 2 T (Field Cooled).

Sample	20 nm		40 nm	
	T = 10 K(initial)	T = 10 K (OOT)	T = 10 K(initial)	T = 10 K (OOT)
M_r/M_s	0.92 ± 0.02	0.95 ± 0.02	0.96 ± 0.02	0.97 ± 0.02
$\mu_0 H_c$ [mT]	300 ± 2	320 ± 2	280 ± 2	340 ± 2
$\mu_0 H_{ex}$ [mT]	0 ± 2	0 ± 2	0 ± 2	6 ± 2

At T = 10 K, a larger normalized remanent magnetization is observed and the coercive field of both samples increases by 60 mT in comparison to the data at T = 300 K, both in the initial state. The increased coercive field at lower temperatures is due to the expected increase of the magnetocrystalline anisotropy with decreasing temperature [83, 84]. The hysteresis loops of the as prepared samples at T = 10 K are identical, independently whether

they were cooled at zero fields (ZFC) or at the field of 2 T (FC).

After partial removal of the membrane, the ambient temperature hysteresis loops of as prepared and OOT samples are almost identical too. However, both OOT samples have increased the coercive field at T = 10 K (See Figure 3-11 and Table 3-3). Additionally, the 40 nm diameter nanowires sample shows a slight shift of the hysteresis loop after field cooling in B = 2 T, indicating the presence of exchange bias. The coercive field H_c and exchange bias H_{exch} fields were calculated using Equations 2-15 and 2-16 respectively.

The exchange bias effect is explained by the presence of an interface between the metallic FeCo core and the oxidized shell presented at the tips of the nanowires. FeCo oxidation usually forms cobalt ferrites ($CoFe_2O_4$) [73], which are ferrimagnetic. However, the growth of Co-rich or Fe-rich oxide layers, both possessing large magnetocrystalline anisotropy, cannot be excluded here [74, 85]. For nanometer sized structures the efficiency of the exchange bias is proportional to the volume of the hard magnetic layer [86]. Consequently, a 3 nm passivating oxide layer has a larger effect on pinning the 40 nm nanowires as compared to 20 nm nanowires. Interestingly, similar to FeCo nanoparticles with $CoFe_2O_4$ shells [73] the pinning of 40 nm nanowires tips leads to a shift of hysteresis loop at FC measurements, and no shift for the zero field measurements (ZFC). The magnetic anisotropy of $CoFe_2O_4$ nanoparticles shows a extremely strong temperature dependence and decreases by two orders of magnitude with increasing temperature from 5 K to 300 K [87, 88]. This explains why we observe a remarkable increase of the nanowires coercive field after the tip opening at T = 10 K, and almost no effect of domain wall pinning at room temperature.

Since for most of the applications, room temperature permanent magnets are needed, one of the possible ways to increase the coercive field at 300 K is to use another material as a pinning layer, which possesses a higher magnetocrystalline anisotropy energy and also a high ordering temperature (higher than room temperature). Equiatomic NiMn alloy ($Ni_{50}Mn_{50}$) is a suitable candidate (T_N= 1070 K in bulk) has indeed been widely used as a pinning layer in exchange biased systems [89].

Accordingly, a thin film of $Ni_{50}Mn_{50}$ was sputtered on the top surface of the sample, with aligned freestanding tips, after reducing the oxide layer with hydrogen plasma in an Ultra-high Vacuum (UHV) chamber [90], as explained in detail in section 3.2.3. On this

way, the antiferromagnetic material is in direct contact with the ferromagnetic FeCo alloy nanowires, and can consequently act as a pinning material for the surface spins of the $Fe_{30}Co_{70}$ nanowires.

A detailed study of the process of the magnetic hardening was carried out. Figure 3-12 shows the hysteretic changes after each processing step illustrated in Table 3-4 .

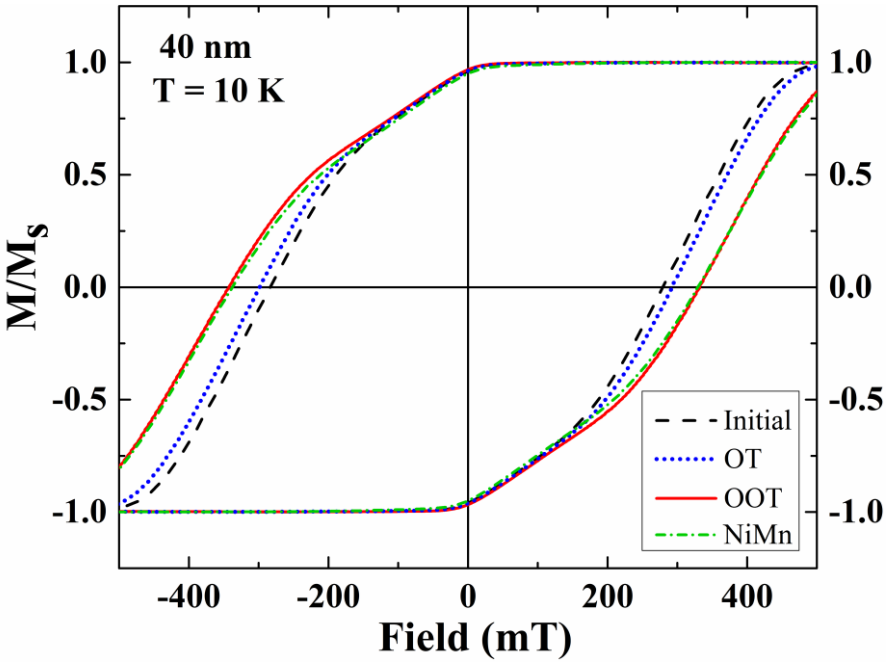

Figure 3-12. Hysteresis loops measured along the nanowires long axis at T = 10 K of 40 nm diameter sample after field cooling in 2 T. The initial state is plotted in dashed black, an intermediate state (after removal of gold layer) is presented dotted blue (OT), after partial removal of the membrane (OOT) is presented in solid red and after sputtering $Ni_{50}Mn_{50}$ alloy is presented in dash-dotted green. After removing the gold layer, the tips of nanowires oxidize at the surface (Oxidized tips: OT), which leads to a slight increase of H_c. After releasing 40-70 nm of the surrounding AAO matrix the coercive field increases further (Open Oxidized Tips: OOT). At this point the coercive field is limited by the natural oxidation of the other end tip inside the AAO. Therefore the coercive field does not depend any longer neither on the length of the "opened" end neither the material used as pinning layer ($Ni_{50}Mn_{50}$).

Micromagnetic simulations have shown that domain walls nucleate at the weaker tip of the nanowire (in this case the point of weakest pinning). Nanowires of the as prepared 20 (or 40 nm) sample (initial state, dashed black curve in Figure 3-12) have only one "free" tip, with an about 3 nm thick oxide layer formed in air [81, 85]. The second end is in contact with the Au layer, that is, protected from oxidation (Table 3-4 a). The domain wall nucleates at the tip in contact with the gold layer, as pointed out with a red arrow in Table 3-4 (column a - single nanowire).

Table 3-4. Summary of the magnetic hardening process at the different stages (columns), which includes a 3-dimensional sketch of the sample, a sketch of single nanowire and the increase of the coercive field with respect to the initial state. In all the sketches of the single nanowire, the different materials are indicated in different colors and correspond to gold (yellow), $Fe_{30}Co_{70}$ alloy (black), FeCo oxide (brown) and $Ni_{50}Mn_{50}$ alloy (green). The red arrows indicate where the domain wall nucleation starts.

	a	b	c	d
Stage of the process	Initial state	After removing Au layer	After removing partially the AAO membrane	After sputtering NiMn alloy
3D Sketch	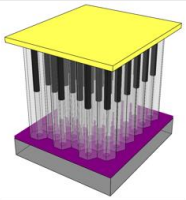	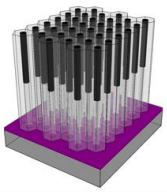	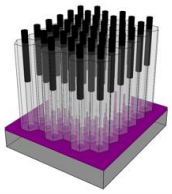	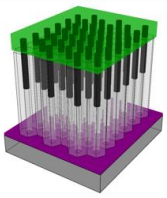
Single NW	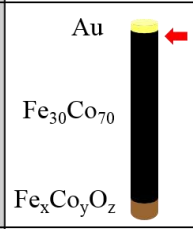	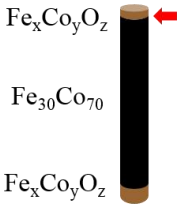	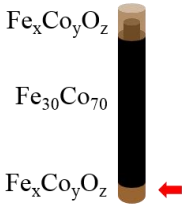	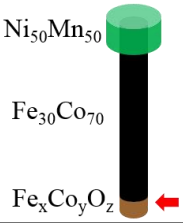
Increase of coercive field with repect to the initial state (mT)	—	12 ± 2	60 ± 2	60 ± 2

After removing the gold layer, these tips become partly oxidized leading to the slight increase of H_c of 12 mT (Table 3-4 - column b). The oxidation layer at this second tip is supposed to be thinner than the other one, due to the shorter exposure time to an oxygen-rich environment, rendering the tip weaker and favoring the domain wall to nucleate. This intermediate state is called in the following as oxidized tips (OT). After the 40-70 nm "opening" nanowire tips (named as OOT: opened oxidized tips), the increase of the coercive field is 60 mT with respect to the initial state, reaching a maximum value of 340 mT. At this stage of the process the domain wall nucleates at the other tip of the nanowire (initially oxidized end with the oxide thickness of about 3 nm), which determine the domain wall nucleation field (Table 3-4 - column c). The coercive field cannot be further increased and it does not depend any longer on the length of the "opened" end, and also of what material is pinning the other end (Table 3-4 - column d).

An alternative possibility to increase the coercive field is to increase the thickness of the oxide layer at the nanowires tips. It has been shown that the magnetic properties of these nanowires arrays are critically dependent of thermal treatment in oxygen atmosphere

[91]. To test this option and as a proof of principle, a post-oxidation step was also carried out. After partial removal of the AAO membrane, the 20 nm diameter sample was annealed at 300°C for 30 min in oxygen plasma inside a vacuum system, with a power of 50 W.

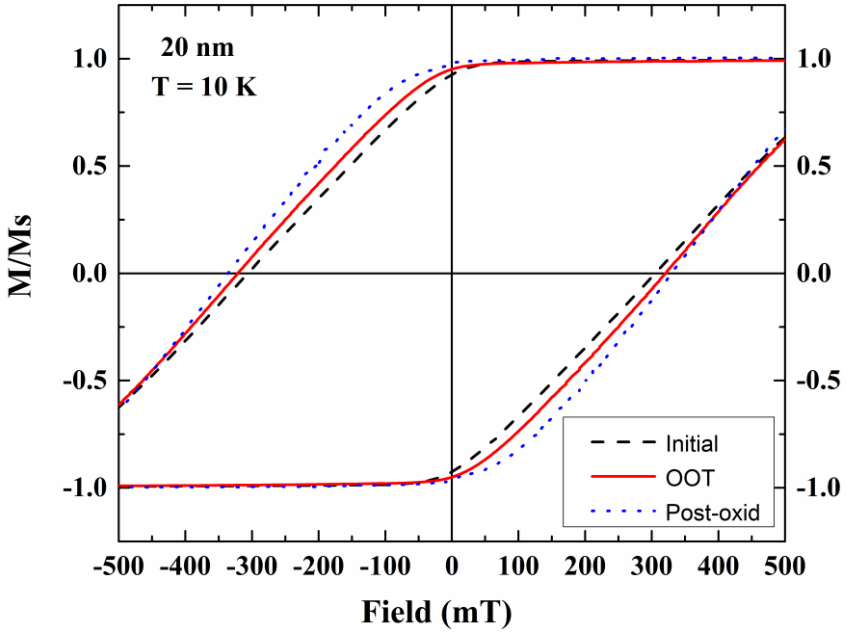

Figure 3-13. Hysteresis loops measured along the nanowires long axis at T = 10 K of the 20 nm diameter sample after field cooling in 2 T. The initial state is plotted in dashed black, after partial removal of the membrane (OOT) is presented in solid red and after post-oxidation process is presented in dash-dotted blue. After releasing approximately 200 nm of the surrounding AAO matrix the coercive field increases further (OOT). At this point the coercive field is limited by the natural oxidation of the other end tip inside the AAO. However, after the post-oxidation process the coercive field increases slightly.

Figure 3-13 shows the hysteretic changes after each processing step, including the initial state, after removing partially the AAO membrane (OOT) and after the post-oxidation treatment. The coercive field increases by 20 mT when removing partially the AAO membrane with respect to the initial state (300 mT). At this point the coercive field is limited by the natural oxidation of the tip inside the AAO, as discussed above. Moreover, after the post-oxidation process the coercive field increases further. After annealing the samples at 300°C, the coercive field increase by another 10 mT, reaching a final value of 330 mT and confirming the hypothesis of increasing the coercive field of these type of samples by annealing them with oxygen plasma. In this way, the oxidized layer becomes thicker and thus, more effective in pinning the ferromagnet (FeCo alloy).

In order to identify the effects of the oxide layers at the nanowires tips, the magnetic switching process was studied by micromagnetic simulations. Even though this study is

out of the scope of this PhD thesis, some remarkable conclusions can be pointed out. For further details, the reader is referred to [92]. The micromagnetic simulations were performed assuming similar characteristics to the samples studied (cylindrical shape, high aspect ratio, stoichiometry anisotropy constants, etc.). The tips of the nanowires were sealed with an antiferromagnetic capping layer with thicknesses varying between 3 nm and 7 nm. The main conclusions are:

1. The coercive field can be maximized by tuning the thickness of the capping layer, which has been proven experimentally increasing the oxide layer at the tip of the nanowires.
2. Magnetically harder caps potentially yield larger H_C.
3. The experimentally measured increase of the coercive field is explained by the presence of the oxide capping layers (iron cobalt oxides with a spinel structure and a composition between $Co_{1.1}Fe_{1.9}O_4$ and $Co_{0.8}Fe_{2.2}O_4$).
4. The antiferromagnetic capping layer is able to suppress the nucleation of domain walls at the nanowire tips and compensates the coercive field loss due to nucleation.

3.5 Conclusions

The magnetic hardening of FeCo nanowires by partial removal of the AAO membrane was successfully attained and suggests the possibility of improving the performance for rare-earth free permanent magnet applications.

The formation of an about 3 nm thick FeCo oxide layer at the FeCo (20 and 40 nm average diameter and aspect ratio >> 10) nanowire tips, increases both, the remanent magnetization and the coercive field by 20 % at T = 10 K. These findings experimentally confirm that magnetic nanowires, even with large aspect ratios (L/D above 100), become demagnetized via nucleation and depinning of domain walls at the nanowire tips. Micromagnetic simulations support the experimental findings and indicate that the measured gain of the coercive field can plausibly be explained by the presence of ferrimagnetic oxides as capping material and suppression of domain wall nucleation at the nanowires tips.

No further increase in the coercive field was achieved when the 40 nm diameter sample tips were coated by an antiferromagnetic NiMn layer, pointing out that the domain wall nucleate at the magnetically weaker nanowire tip. This fact indicates the importance of domain wall pinning at both tips of a magnetic nanowire. Moreover, the pinning efficiency is larger for larger nanowire diameters.

Such procedure of partial removal of the membrane may be extended to other electrodeposited nanowires in order to design and control their final magnetic properties. Furthermore, free-standing tips can be coated by materials with different properties (i.e. optically active) after releasing from the AAO matrix, consequently offering partially covered core-shell nanowires, as shown in [93, 94].

4 Cobalt-Nickel nanorods

$Co_{80}Ni_{20}$ nanorods have been synthesized by the polyol process, on which both morphology and stoichiometry have been optimized for the improvement of the magnetic properties. Thus, in this chapter, the method of synthesis is described concisely at first and the attained morphology is explained according to the growth mechanism. Then, the structure and magnetic properties of $Co_{80}Ni_{20}$ are analyzed in detailed. The TEM study shows that the rods are partially oxidized at the surface, forming $Co_{80}Ni_{20}$ core/oxide shell nanorods. These oxides form a passivating layer around the ferromagnetic core in ambient conditions and can consequently promote a larger hysteretic energy product by exchange anisotropy between an antiferromagnetic oxide shell and the ferromagnetic metallic core. At the end of the chapter, the present results on $Co_{80}Ni_{20}$ core/oxide shell nanorods are quantitatively compared with Co/CoO core−shell rods.

4.1 Introduction

As already discussed in the previous chapter, alternative materials which do not contain rare earth elements have been intensively investigated for permanent magnet applications, especially highly elongated nanomagnets like nanorods and nanowires [95, 96]. If the preparation technique or the synthetic method exerts control over the crystallographic orientation of the material along the nanorod geometry, one expects large coercive fields and high remanent magnetization stemming from the magnetocrystalline easy axis aligned parallel to the axis of the rod. Additionally, besides shape and magnetocrystalline contributions, any further increase of magnetic anisotropy, e.g., by exchange coupling to an antiferromagnetic material (exchange bias), will increase the energy product of the magnetic hysteresis of these nanostructures [97, 98]. Indeed, the idea of exploiting a combination of

shape, magnetocrystalline and exchange anisotropy in rare-earth free nanoscale anisotropic building blocks has been developed over the last decades and has received renewed attention over the last years [55, 99].

3*d* transition metal Fe or Ni nanorods do not have the potential to fulfil the needs of permanent magnets because of their low magnetocrystalline anisotropy energy density. In contrast, hcp Co has about one order of magnitude larger magnetocrystalline anisotropy energy density, which makes it a much better candidate for the production of permanent magnets [100]. Indeed, Co-based alloys may be tailored in a way comprising high magnetization, large magnetocrystalline anisotropy, and sufficient oxidation resistance by forming a thin surface oxide layer passivating the metallic core [101, 102]. Maurer and co-workers have reported the synthesis of Co nanorods with the magnetic easy axis (c-axis) aligned parallel to the long axis of the nanorods [103]. The presence of a thin CoO surface layer implies a two-fold advantage. Firstly, it protects the metallic Co core from further oxidation. Additionally, it creates an interface in which an interfacial exchange anisotropy contribution leads to an increase in the coercive field at low temperatures. However, with increasing temperature this magnetic hardening of the nanorods weakens and the gain in the coercive field vanishes above the Néel temperature of the antiferromagnet. Bulk CoO has a Néel temperature of T_N = 291 K [104], but it might be significantly reduced in thin nanostructures, leading to a vanishing exchange bias [105].

Thus, in order to exploit such effects for permanent magnets but operating at ambient temperature, materials with significantly higher Néel temperature are needed while maintaining the large magnetocrystalline anisotropy energy density. In this regard, a good compromise between large magnetocrystalline anisotropy energy density and high Néel temperature in the antiferromagnetic shell is the admixture of Ni, since NiO has a Néel temperature of T_N = 525 K in the bulk [104].

For all discussed above, highly elongated CoNi nanostructures were considered worthy to study. In general, magnetic nanoobjets of anisotropic shape can be prepared via confinement of the growth process inside anisotropic channels [106], via the use for example of unidirectional substrates such as carbon nanotubes [107, 108] or directly, via solution phase synthesis. Indeed, a variety of techniques have been used to synthesize CoNi nanowires and nanorods including template methods AAO [109], solvothermal routes [110,

111], chemical vapor deposition, in microemulsion [112], using microwave irradiation [113] and direct precipitation of anisotropic metal nanoparticles from solution (polyol) [114, 115, 116]. Among the latter chemical methods, precipitation in polyols appears as a very convenient method to prepare anisotropic ferromagnetic metal particles with well-defined morphological characteristics and an adjustable composition, thus tuning the magnetic properties as one wishes. It is also a quite simple process that requires low cost infrastructures. In order to produce anisotropic growth of this alloy in liquid-phase different surfactant must be added to induce different growth rates of the different crystallographic planes of the metal particles (see section 2.2.3).

The polyol process allows as well to produce bimetallic particles of these two ferromagnetic metals (Co and Ni) associated in various proportions. By varying the composition, one can expect nanoparticles with different magnetic properties, not only due to the influence of elemental composition upon saturation magnetization, but also due to the influence of the crystalline structure and of the surface oxidation upon volume and surface magnetocrystalline anisotropies respectively [117, 118, 68]. Toneguzzo, van Shooneveld and co-workers have studied these effects in detail [119, 120], and Brayner and co-workers have also produced CoNi alloy nanoparticles of tunable composition using alginate (biopolymer extracted from brown marine algae) as template [121].

For reasons below explained, the chosen Co:Ni stoichiometric ratio was 80:20. The magnetic properties of this $Co_{80}Ni_{20}$ bulk allow can be estimated as a percentage of the constituent elements, whose properties are presented in Table 4-1.

Table 4-1. Summary of the magnetic properties of Co and Ni elements in bulk, including the saturation magnetization (Ms), the mass magnetization at room temperature and at 0 K (σ_S), the atomic magnetic moment (μ_B) and the Curie temperature (Tc).

Element	M_S (T = 298 K) (kA/m)	M_S (T = 0 K) (kA/m)	σ_S (T = 298 K) (Am²/kg)	σ_S (T = 0 K) (Am²/kg)	μ_B	T_C (K)
Co^{hcp}	1400	1446	161,80	163,10	1,72	1388
Ni^{fcc}	485	510	55,09	58,57	0,606	627

Thus, bulk $Co_{80}Ni_{20}$ alloy has a saturation magnetization value of 1217 kA/m at 298 K and a mass bulk magnetization of 140.5 Am² / kg. The atomic magnetic moment per atom of the alloy is calculated to be 1.5 μ_B. This calculated value is consistent with the

theoretical value of the Slater-Pauling curve. The Curie temperature for CoNi alloys is also in between the T_C values of these two elements, being 1017.5 K for this particular alloy. In addition, the oxidation of both elements leads to the formation of CoO and NiO, respectively, which are antiferromagnetic below the Neel temperature ($T_{N(CoO)}$= 290 K and $T_{N(NiO)}$=520 K).

Interestingly, apart from high-aspect ratio nanostructures, many other shapes of CoNi have been reported including nanorings [122], spheres [123, 120], hollow spheres [124], nanowires [109], nanorods [115, 116], nanodumbbells [125, 115], nanotubes [126], dendrites [127], nanoleaves [128], flower-like structures [124], and thin films [129].

Summarizing this part, CoNi alloy possesses the characteristics of a good candidate material for permanent magnets with large values of remanence and coercive field and can be consequently considered as a potential replacement of the high-energy product rare-earth permanent magnets. Furthermore, it has been proven that nanocrystalline CoNi alloy possess resistance against corrosion, which might be an advantage for the final magnet applications in open environments [101, 102]. In this study, the exploitation of the interfacial exchange between ferromagnetic and antiferromagnetic or ferrimagnetic materials with high magnetocrystalline anisotropy is analyzed for the improvement of the performance of rare-earth-free permanent magnets based on 3*d* metal nanorods.

4.2 Synthesis

Viau, Fiévet and co-workers developed over the last decades a strategy for the synthesis of CoNi nanoparticles consisting in the thermal decomposition of cobalt and nickel acetate salts in liquid polyol. Monodisperse spherical metal particles with the mean diameter in the micrometer size range (1-2 µm) were obtained by homogeneous nucleation [130, 13]. The polyol acts simultaneously as the dispersing medium, the solvent, the reducing agent and the crystal growth medium for the metal particles. In the same medium, CoNi particles were obtained in the submicron size range when this spontaneous nucleation step was substituted by a heterogeneous nucleation [120, 131]. The mean particle size of the CoNi particles was decreased from 2 µm to 5 nm by seeding the solution with platinum,

which was formed in situ by adding K_2PtCl_4 in the reaction medium [120]. The Pt nanoclusters formed first serve in this situation as heterogeneous nucleation sites and facilitate the nucleation process of CoNi particles. A more detailed information of heterogeneous nucleation process and the role of the nucleating agent is given in subchapter 2.2.1.

However, despite of the heterogeneous nucleation, CoNi particles prepared by this method were generally isotropic or nearly spherical. In 2003, they first obtained anisotropic particles including platelets and diabolo-like particles by modifying this nucleation step [132]. To achieve these novel shapes, the nucleation agent, its concentration, and the basicity of the reaction media was modified. Ruthenium was chosen as the noble metal instead of platinum, and the amount of ruthenium seeds was found to be a key factor on controlling the morphology of the CoNi nanocrystals. This fact was also confirmed by other researchers [133, 134]. Under similar reaction conditions Gandha and co-workers report on the morphology control of CoNi particles by modifying the polyol reduction of cobalt acetate and nickel acetate using $RuCl_3$ as catalyst, varying the morphologies of the CoNi nanocrystals by varying the Ru/(Co+Ni) molar ratio. While no $RuCl_3$ was added in the reaction medium spherical particles were obtained, by increasing the molar ratio, dumbbell shaped and nanorods were achieved [134]. Ruthenium becomes a better choice for the growth of nanowires because it has the same crystalline structure as cobalt (hcp), whereas platinum crystallizes in a fcc phase. Indeed, Viau and co-workers proved that pure hcp ruthenium particles with sizes ranging from 1-4 nm were formed by reduction of ruthenium salt in liquid polyol at 160°C [135, 136].

In 2005 they also demonstrated, that the concentration of sodium hydroxide is an important parameter, also exerting control over the particle morphology [116]. For low hydroxide concentrations (0.05 mol/L), the particles presented a sea-urchin-like shape, with the characteristic needles more rod-like than wire-like morphology. When the sodium hydroxide concentration was increased (0.08 mol/L), the aspect ratio of the needles increased along. With a concentration of 0.15 mol/L, the wires appeared less agglomerated and when the concentration was 0.20 mol/L, a mixture of spherical particles and platelets was obtained [116]. In a comparable reaction, Rafique et al. demonstrate that hollow spheres, flower-like and nanoplate flowers of CoNi can be formed by varying the NaOH concentration [124].

In a latter publication (2007) Viau et al. put light into the growth mechanism of CoNi nanowires [115], demonstrating that the shape of the dumbbells strongly depends on the basicity; long dumbbells were obtained for the lowest NaOH concentration, and short dumbbells and diabolos for the highest. Moreover, within the particles, cobalt and nickel segregates in different areas. Nanodumbbells consist of a central column richer in cobalt capped with two terminal platelets richer in nickel, showing that the reduction rate of cobalt is higher than that of nickel.

Accordingly, they established that when the reduction of cobalt and nickel takes place, Co^{2+} and Ni^{2+} species are involved in an equilibrium between the solution and an unreduced solid phase, describing the mechanism of formation of these crystals as follows [137]:

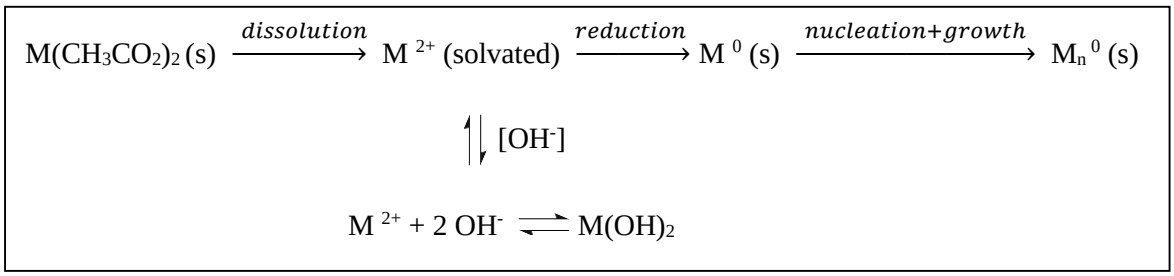

Figure 4-1. Mechanism of formation of cobalt-nickel nanorods. M stands for metal, where M = Co, Ni. The acetate precursors dissolve giving Co^{2+} and Ni^{2+} solvated species in solution, which are reduced to metallic Co and Ni by the polyol. The Co^0 and Ni^0 atoms will then form small nuclei, which grow to form the nanorods. The metal ions concentration in the reaction medium is controlled by the sodium hydroxide concentration through the precipitation of an intermediate solid phase (side reaction).

At first Ru^{3+} ($E°_{Ru3+/Ru0}$ = + 0.701 V) is initially reduced by 1,2-butanediol during the early stage of reaction so that Ru^0 nanoclusters or nanoparticles with hcp crystalline structure are formed. Simultaneously, the solid Co/Ni precursors dissolve progressively in the solvent. Then, on the basis of the catalysis of Ru^0, the Co^{2+} and Ni^{2+} solvated species are reduced by the polyol to Co^0 ($E°_{Co2+/Co0}$ = -0.28 V) and Ni^0 ($E°_{Ni2+/Ni0}$ = -0.25V) [138], and CoNi alloy with hcp phase will heterogeneously nucleate and grow on the surface of the Ru seeds. The metal ions concentration in the solution (unreacted Co^{2+} and Ni^{2+}) is controlled by the sodium hydroxide concentration through the precipitation of an intermediate solid phase, which acts as a reservoir for Co^{2+} and Ni^{2+} species. It is the dissolution of the intermediate solid phase what controls the solute species concentration and thus nucleation and growth steps, which occurs by a stepwise addition of monomeric entities of the solute [130].

To understand the role of the sodium hydroxide concentration and the different reactivity of cobalt and nickel, they focused their studies in analyzing the equilibrium between the Co^{2+} and Ni^{2+} ions in solution and the intermediate unreduced solid phase in the global reaction process. Strong differences between Co^{2+} and Ni^{2+} in solution were evidenced. They found that molecular complexes of Co^{2+} and Ni^{2+} are distinct, and while Co^{2+} forms an alkoxide, Ni^{2+} precipitates as hydroxyl-acetate. This is a proof of the difference in coordination chemistry of both species, from which stem the different dissolution rates and explain the different behavior of the two metals toward reduction and thus, the final segregation of elements within the nanoparticles.

This study is an example that manifests the importance of studying possible side reactions between different species in the medium during a chemical synthesis. A similar effect of in situ changes of the composition of the reaction medium on the structure and shape of nanocrystals has been evidenced by other researchers [139, 140]. For example, Comesaña-Hermo and co-workers have reported evidences of a side reaction between hexadecylamine and rhodamine B, which modifies the structure of the rhodamine molecule and has a direct consequence in the final shape of cobalt nanocrystals [139]. In comparison with the study of Viau and co-workers, the side reaction occurring in the reaction medium was not connected to the precursors but between two ligands.

Summarizing, various shapes of CoNi nanoparticles can be obtained resulting from different nucleation/growth processes, depending strongly on the cobalt/nickel composition, the sodium hydroxide concentration and the nucleating agent. An optimization process is therefore required in order to obtain bimetallic $Co_{80}Ni_{20}$ nanorods that retain a good interparticular homogeneity in composition. Taking into account that wire formation was observed within a narrow range of Ru/NaOH concentration ratio, $Co_{80}Ni_{20}$ nanorods were synthesized by the reduction of the metal precursors according to the recipe developed previously by Viau and co-workers [137, 116, 141, 115] with the following detailed experimental procedure. The composition of as-prepared CoNi nanocrystals was adjusted at $Co_{80}Ni_{20}$ by controlling the initial Co/Ni precursor ratio. In a typical synthesis, cobalt acetate tetrahydrate (4.8 mmol), nickel acetate tetrahydrate (1.2 mmol), sodium hydroxide (1.2 mmol) and ruthenium trichloride hydrate (0.15 mmol) were dissolved in 75 mL of 1,2-butanediol.

The solution containing all the reactants and the nucleating agent was heated up to 170°C (boiling point) while stirring and distilling the water off. Once the mixture reached this temperature, oleic acid (6 mmol) and trioctylphosphine (6 mmol) were added, keeping the solution at this temperature for 20 min. The solution turns black progressively when the reduction occurs. Water and volatile organic products generated by the overall reaction were distilled off while the polyol was refluxed. After cooling to room temperature the precipitate was collected by centrifugation and washed with absolute ethanol several times to remove residual organic components. Part of the sample was finally redispersed in tetrahydrofuran and another part was dried in air at 50ºC for magnetometry characterization.

4.3 Morphology

The morphology of the sample has been investigated by transmission electron microscopy. Figure 4-2 presents a set of typical TEM micrographs showing nanostructures mainly with an elongated shape, though two different morphologies (nanorods and spherical particles) can be clearly identified. As shown in Figure 4-2 (b) and (c), single nanorods show stronger contrast variations compared to the spherical particles, suggesting a polycrystalline structure. Figure 4-2 (d) shows a high resolution TEM image of the tip of a nanorod, which reveals a core-shell structure and a conical shaped head. An oxidized shell is expected to appear as a consequence of the inward oxidation of the initially synthesized metallic nanostructures by handling the sample under atmospheric conditions in the post-synthesis measurements. The conical shaped head of the rods is explained well by the influence of the growth rate on the particle shape. As explained in section 2.2.3, the shape is controlled by the growth rate, so the head formed at the end of the reaction grows under conditions of low supersaturation, which induces the growth perpendicular to the c-axis. Thus, wires are formed with high growth rates governed both by the large number of nuclei and by the adequate sodium hydroxide concentration. A high-enough concentration is necessary to allow the wire growth, though too high concentration can lead to very different shapes, such as platelets. This particular shape is probably the result of a lower growth rate at the end of the reaction, when the Co^{2+} and Ni^{2+} concentration falls (as a result of their reduction) so that the molar ratio $[OH^-]/[Co+Ni]$ increases.

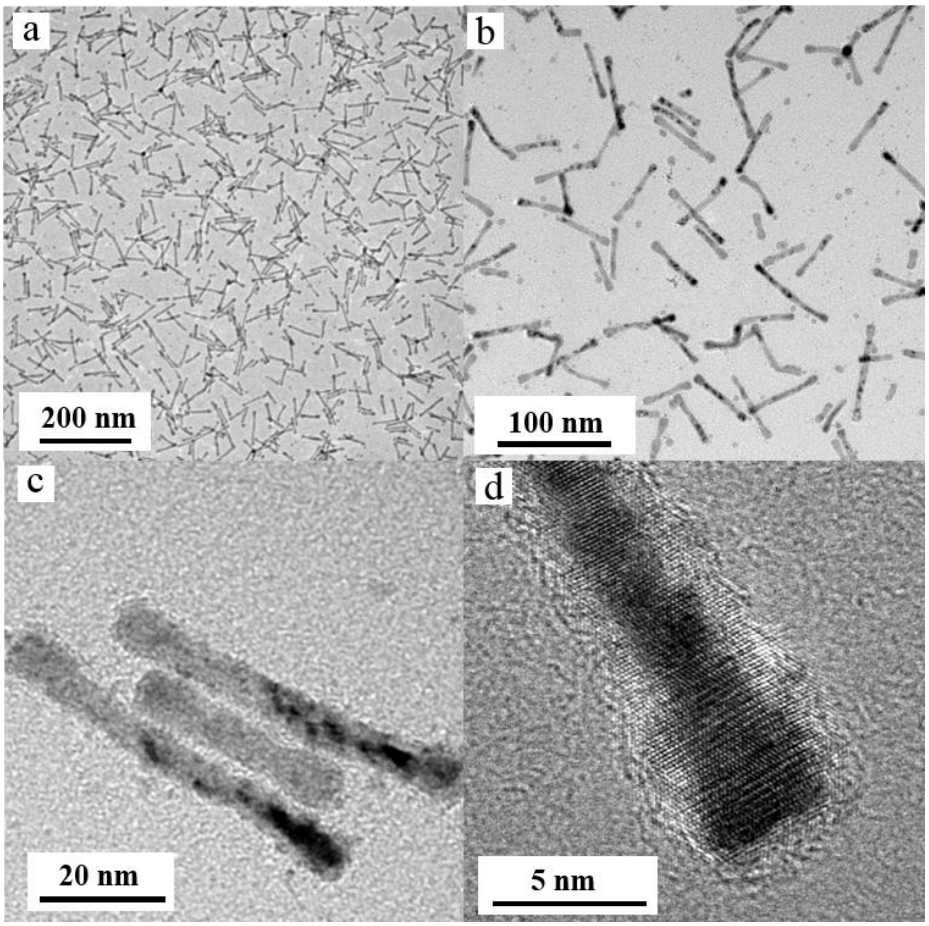

Figure 4-2. (a) and (b) Low magnification transmission electron microscopy images of $Co_{80}Ni_{20}$ particles showing nanostructures mainly with an elongated shape. (c) High resolution TEM image of the nanorods showing strong contrast variations. (d) HR-TEM image of the tip of a nanorod, which clearly reveal a core-shell structure.

The size (length) distribution of the nanocomposites displayed in Figure 4-3 (a) is bimodal. The two contributions arise from spherical nanoparticles (5-15 nm) and nanorods with the length varying from 20 nm to 80 nm, respectively. In addition to the overall size distribution, the aspect ratio of the nanorods defined as the ratio of length L to diameter D is shown in Figure 4-3 (b). A rather broad distribution of the aspect ratio varying from 3 to 15 is observed. The size distributions were fitted by log-normal functions and the resulting mean dimensions of the nanoparticles and nanorods are listed in Table 4-2. The obtained mean length (L) and diameter (D) of the nanorods are 52.5 nm and 6.5 nm, respectively, and the nanospheres diameter is d = 8.2 nm. Furthermore, the volume portion was determined to be 93 vol.% for the nanorods and 7 vol.% for the particles from the lognormal fits assuming cylinders and spheres, respectively. Thus, the magnetic properties are consequently assumed to be strongly governed by the nanorod morphology.

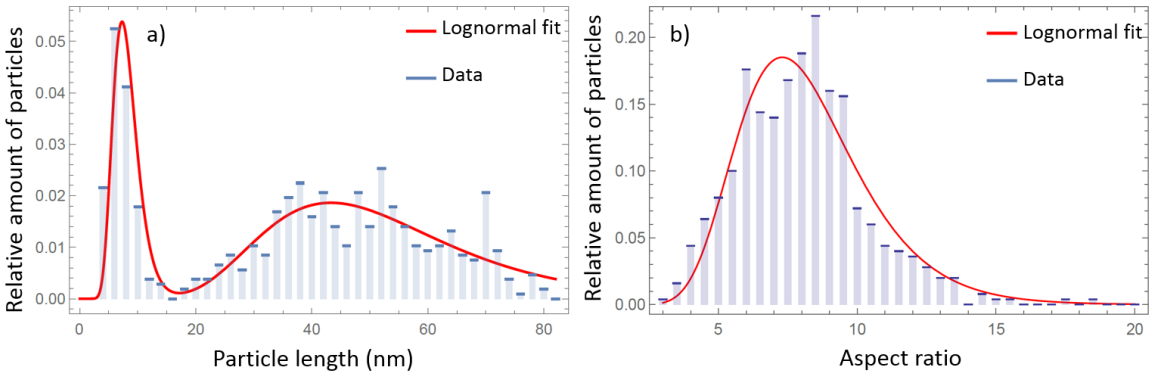

Figure 4-3. Size distribution diagrams with corresponding log-normal fit of the $Co_{80}Ni_{20}$ particles. (a) Particle length distribution. (b) Aspect ratio distribution of the nanorods. Fitting results of the log-normal distribution (red curve) are given in Table 4-2.

Table 4-2. Results of the morphological characterization by TEM. Size and aspect ratio distributions are determined for more than 300 CoNi nanorods and particles assuming lognormal distributions.

Nanorods 93 ± 2 vol.%			**Nanoparticles 7 ± 2 vol.%**
Length (L)	Diameter (D)	Aspect ratio (L/D)	Diameter (d)
52.5 ± 19.4 nm	6.5 ± 1.0 nm	8.2 ± 2.4	8.2 ± 2.3 nm

4.4 Structural and chemical characterization

The crystalline structure and chemical composition of the sample is characterized by energy-dispersive X-ray spectroscopy (EDX), electron powder diffraction and X-ray photoelectron spectroscopy (XPS). In addition to TEM investigations, XPS supplies information of the chemical environment of the investigated specimen.

The elemental concentration in CoNi nanorods has been measured by means of EDX spectroscopy in the transmission electron microscope.

Figure 4-4 shows the EDX spectrum acquired from a larger sample area containing hundreds of nanorods and nanospheres. The average composition of the sample is determined by the ratio of intensities of the different element peaks, revealing a Co:Ni elemental ratio of 4:1, very close to the ratio of the corresponding initial precursor concentration in

the starting solution. As expected for finely divided powders synthesized in a boiling solvent medium, the main impurities are carbon, oxygen and hydrogen. Carbon, as well as oxygen can originate from the presence of organic adsorbed species (either polyol or degradation products) or from a metallo-organic phase such as metal alkoxyde observed as an intermediate phase. Moreover, oxygen can originate from inorganic phases such as unreacted hydroxides or from oxygen captured from air, leading to a superficial oxidation of the finely divided metal particles. For these reasons, these parts of the spectrum are not shown.

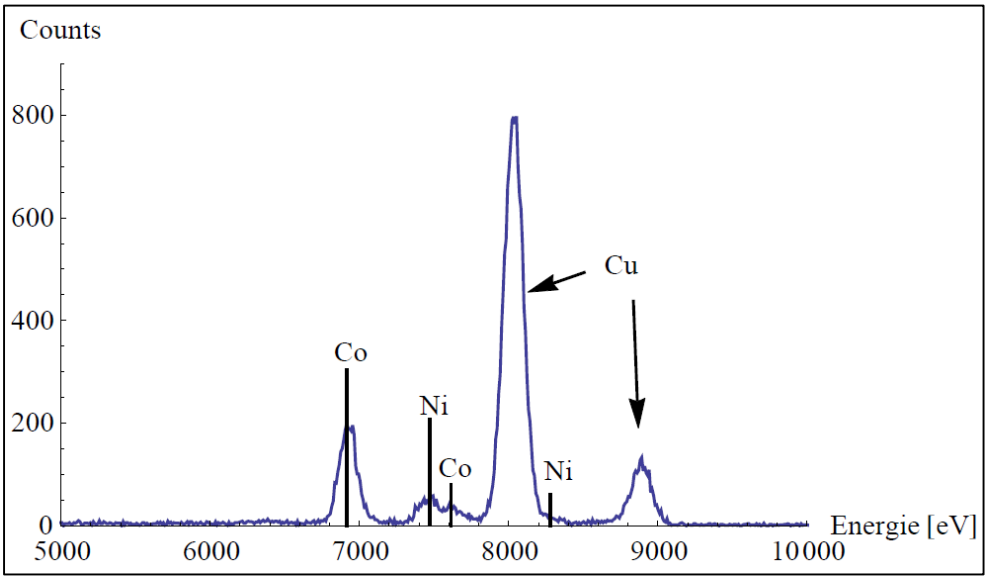

Figure 4-4. EDX spectrum of CoNi nanoparticles, showing the energy range between 5 and 10 KeV. The spectrum was acquired from a large sample area containing hundreds of nanorods and nanospheres, deposited on a carbon film supported copper TEM grid.

EDX spectra were also obtained from various points of individual nanostructures showing a relatively uniform distribution of Co and Ni within the particle core. Figure 4-5 illustrates a representative EDX line scan performed on individual nanorods, which confirms the presence of both Co and Ni within the whole nanostructure, including core and shell. Additionally, an amount of Ni becomes reduced when approaching the nanorod surface, if comparing the individual Co and Ni elemental intensities along the scan.

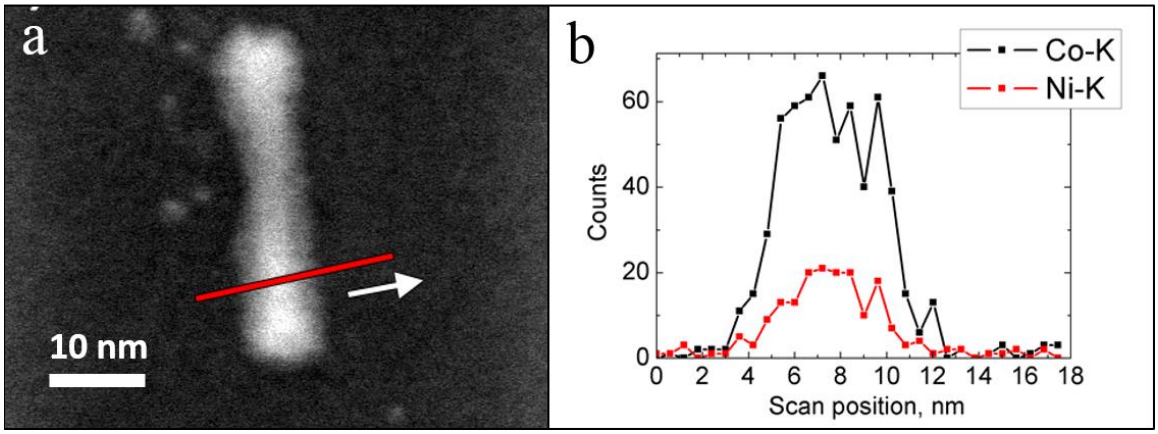

Figure 4-5. (a) High-angle annual dark-field scanning TEM (HAADF- STEM) image of the CoNi nanorod. (b) Line scan profiles of the characteristic X-ray Ni-K (red) and Co-K (black) lines as a function of the electron beam position along the path on the nanorod indicated with a red line in panel (a).

In addition to compositional information, XPS data also provide information on the chemical state of the elements in the near-surface region. However, the absolute binding energy of the $2p_{2/3}$ peak is not always very helpful in identifying the cobalt chemical environment, since relatively small shifts are reported to accompany oxidation of Co^{2+} and Co^{3+} [142].

The as-prepared $Co_{80}Ni_{20}$ nanorods were further characterized by XPS after deposition on Si/SiO_2 substrates. Note that the Ni content is small and, thus, spectra have a poor signal-to-noise ratio, and accordingly, herein the detailed discussion is restricted to the Co-2p XPS doublet. Figure 4-6 presents the Co-2p doublet of the specimen and two reference spectra. A binding energy of 781.8 eV was observed for the Co-$2p_{3/2}$ line and 797.8 eV for the Co-$2p_{1/2}$ line, making a doublet splitting of $\Delta = 16.0$ eV. Moreover, satellite peaks are observed towards higher binding energies. According to the NIST reference database [143] these observations suggest the formation of $Co(OH)_2$ on the particle surface, since CoO has slightly lower binding energies at a doublet splitting of $\Delta = 15.5$ eV. The reported values in the XPS database scatter by about ± 0.5 eV, and thus, an unambiguous proof of a certain chemical state is not possible here. On the other hand, when CoNi rods are exposed to air one may consider the formation of $Ni_xCo_{3-x}O_4$ ferrites with $0 < x < 1$. However, when comparing the spectra of the surface-oxidized CoNi rods with $NiCo_2O_4$ powder as a reference for ferrites [142], it is obvious that the satellite peaks are absent for the ferrite reference and the doublet separation (15.0 eV) is significantly smaller as compared to the CoNi rods (16.0 eV). Thus, the formation of ferrites can be excluded here. Further, we determined

from the total XPS line intensities the Co-to-Ni elemental ratio to 5.6 ± 1.5. The error bar arises from the poor signal-to-noise ratio of the Ni 2p spectrum. XPS predominantly probes the surface stoichiometry of the specimen, thus confirming the larger Co content in the oxide surface as suggested by the EDX line scans (cf. Figure 4-5).

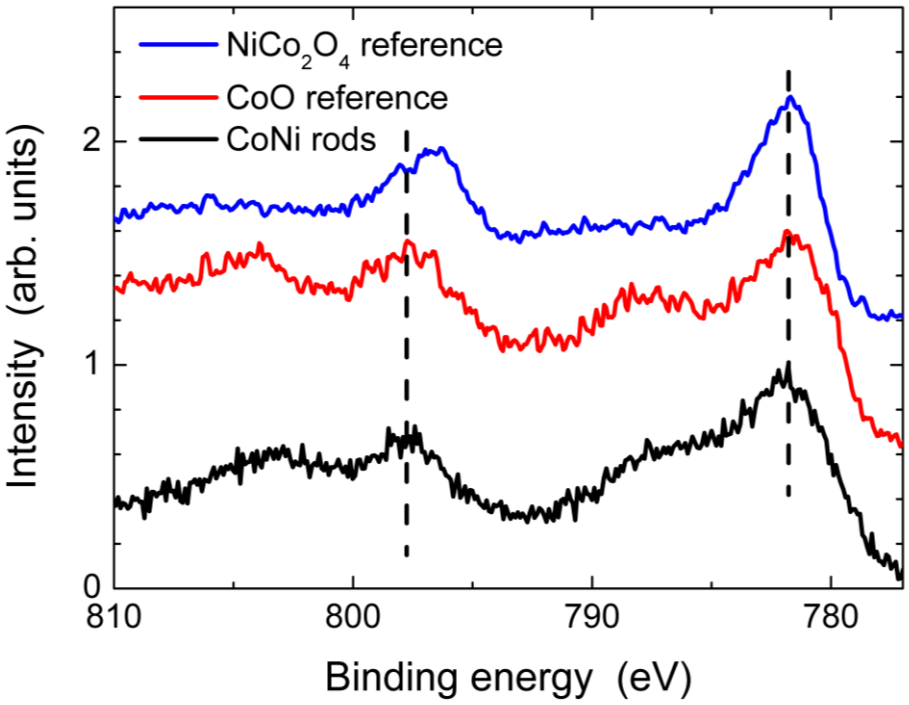

Figure 4-6. Co-2p XPS of the CoNi nanorods (black). Additionally, reference spectra of CoO (red) and $NiCo_2O_4$ (blue) powder samples are taken from the literature [143]. Vertical dashed lines indicate the peak positions of CoNi nanorods. The reference spectra were vertically shifted for clarity.

The structural analysis was carried out by means of high-resolution (HR)TEM and selected area electron diffraction (SAED). The analysis of SAED pattern (Figure 4-7) revealed that nanocomposites have an hcp structure with lattice parameters of a = 0.247 ± 0.006 nm, c = 0.400 ± 0.010 nm, corresponding to those in the bulk $Co_{80}Ni_{20}$ alloy (a = 0.250 nm, c = 0.407 nm) [144, 102]. Another diffraction ring labelled "oxide" was also found and most probably arises from an oxidized phase present in the nanoparticle surface (expected from sample handling). The exact type of oxide could not be determined, since the diffraction ring can be associated with different phases (NiO, CoO, Co_3O_4 or even the ternary oxide $Co_xNi_yO_z$).

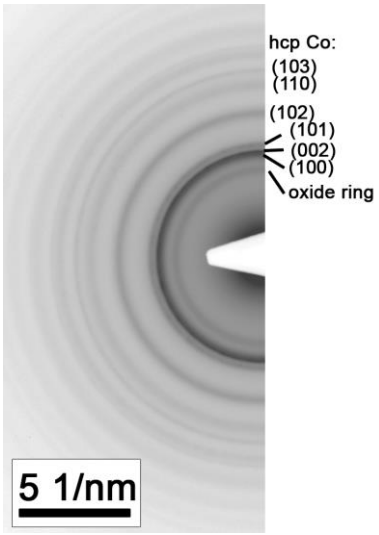

Figure 4-7. Selected area electron diffractogram of CoNi nanocomposites from a large sample area, revealing an hcp structure with an oxide phase.

Indeed, the presence of an hcp structure was expected considering the low reduction temperature (T = 170°C) and the Co/Ni elemental ratio (see phase diagram of the Co-Ni alloy system in Figure 4-8). The curie temperature of the alloy decreases continuously with increasing nickel content, from 1388 K for pure cobalt to 633 K for pure nickel [145].

Moreover, the hexagonal phase is favored by the high nucleation ratio as discussed in 4.2, and accordingly, under these synthetic conditions, anisotropic cobalt-nickel particles are favored.

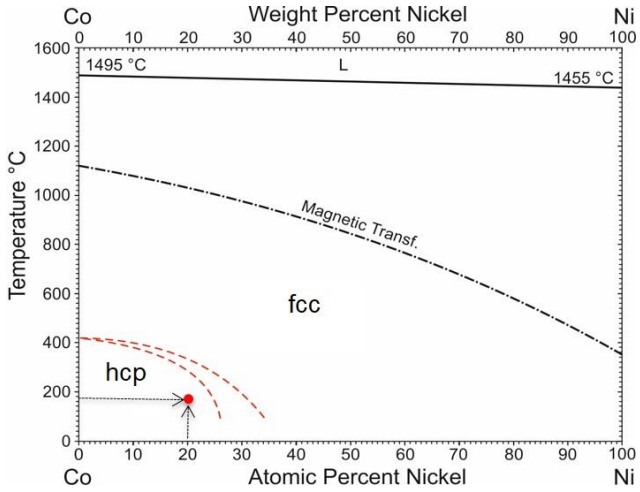

Figure 4-8. Phase diagram of the Co-Ni alloy system, showing the different crystal structures depending on the temperature and the chemical composition. The red point indicates the synthesis conditions of the CoNi nanoparticles. The black dot-dash line indicates the magnetic transition between ferromagnetic and paramagnetic regime while the continuous black line denotes the melting temperature for various compositions. The graph was modified according to [146].

More detailed information on the structure and composition of the CoNi nanorods can be obtained by analysis of the HRTEM images. Figure 4-9 (a) shows a typical HRTEM image of the center part of a CoNi nanorod. The contrast distribution indicates a core-shell structure with a single crystalline metallic core covered with a polycrystalline oxide shell.

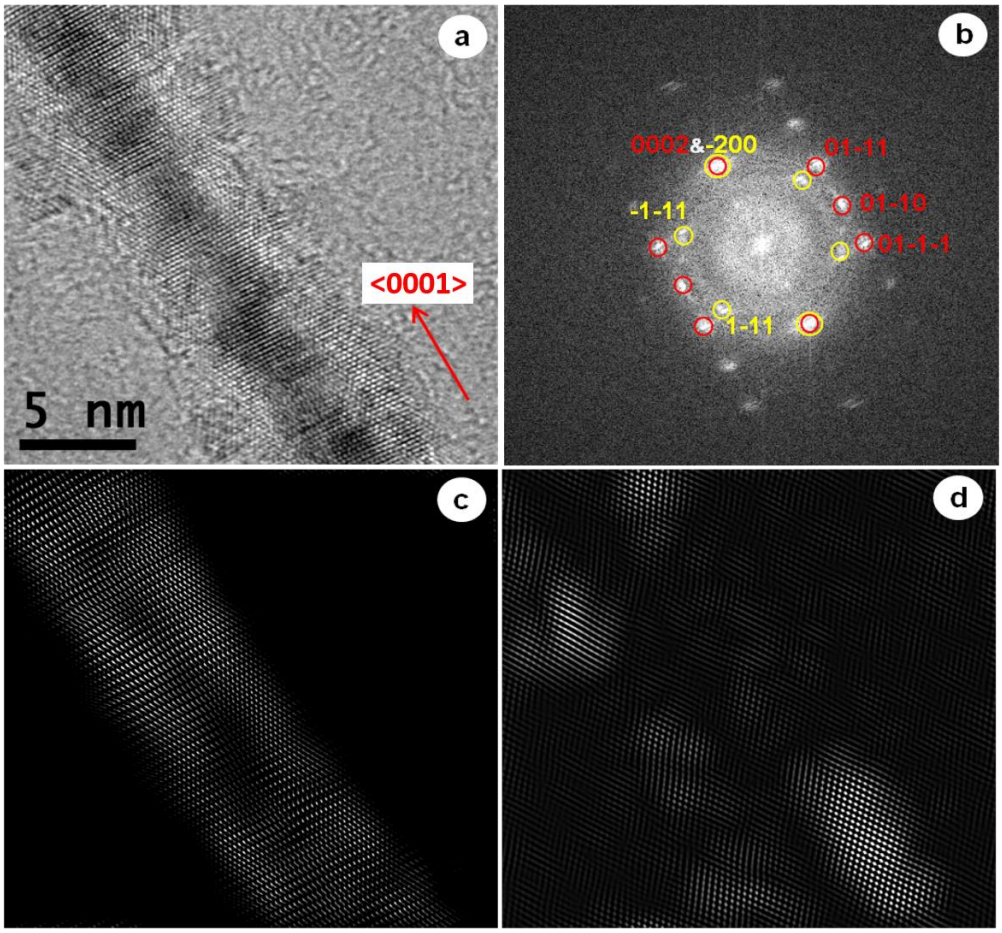

Figure 4-9. (a) HRTEM image of the center part of a CoNi nanorod with a clear core-shell contrast. (b) FFT pattern from the HRTEM image in panel (a). Red (yellow) circles mark spots arising from hcp (fcc) structure, respectively. Note that the hcp (0002) spot overlaps with the fcc (-200) spot. The hcp c-axis is parallel to the long axis of the nanorods as indicated in (a). The lower panels present structurally filtered images by choosing hcp (c) and fcc spots (d), respectively.

The fast Fourier transform (FFT) pattern of the image (Figure 4-9 (b)) consists of two sets of reflections. The red-encircled diffraction spots correspond to the hcp structure viewed along the [2-1-10] zone axis. The yellow-encircled reflection set is typical for the fcc structure imaged along the [011] direction. Thus, the diffraction pattern can be interpreted as the sum of overlapping hcp and fcc diffractions. The FFT pattern analysis yields the lattice constants a = 0.252±0.006 nm and c = 0.408±0.010 nm related to the hcp structure of $Co_{80}Ni_{20}$ [144, 102]. The lattice parameter of the cubic phase is found to be 0.417 ±

0.008 nm and can correspond to the lattice parameter of either CoO or NiO oxides [147]. Studies on the oxidation of Co-Ni alloys show that Co, due to the higher diffusivity of Co^{2+} ions in the oxide, segregates up to the surface [148, 149]. Moreover, the reduction potentials of Ni^{2+}, (E^0= - 0.25 V) and Co^{2+} (E^0= - 0.28 V) indicate the higher oxidation capability of the metallic cobalt compared to metallic nickel. Taking into account the expected oxidation behavior of Co-Ni and the corresponding experimental data from EDX and XPS, the possibility of the NiO oxide formation is therefore excluded here and most probably, a Co-rich fcc oxide shell was formed.

The HRTEM images in Figure 4-9 (c) and (d) are reconstructed from the FFT spot pattern (Figure 4-9 (b)) by filtering selected diffraction spots. Figure 4-9 (c) shows the inverse FFT image using only the red-encircled reflections, which correspond to the hcp structure. The reconstructed image shows a uniform distribution of the hcp structure within the rod while the reconstruction of the image using yellow-encircled fcc reflections in Figure 4-9 (d) shows a preferential allocation of this phase at the nanorod surface.

In summary, the CoNi rods have a core-shell structure that arises from a metallic hcp CoNi core covered with a 1-2 nm polycrystalline, strongly textured fcc Co-rich oxide shell. The shell thickness varies along the nanorods having a slighter largest thickness at the tips, as clearly reflected in the TEM images in Figure 4-10.

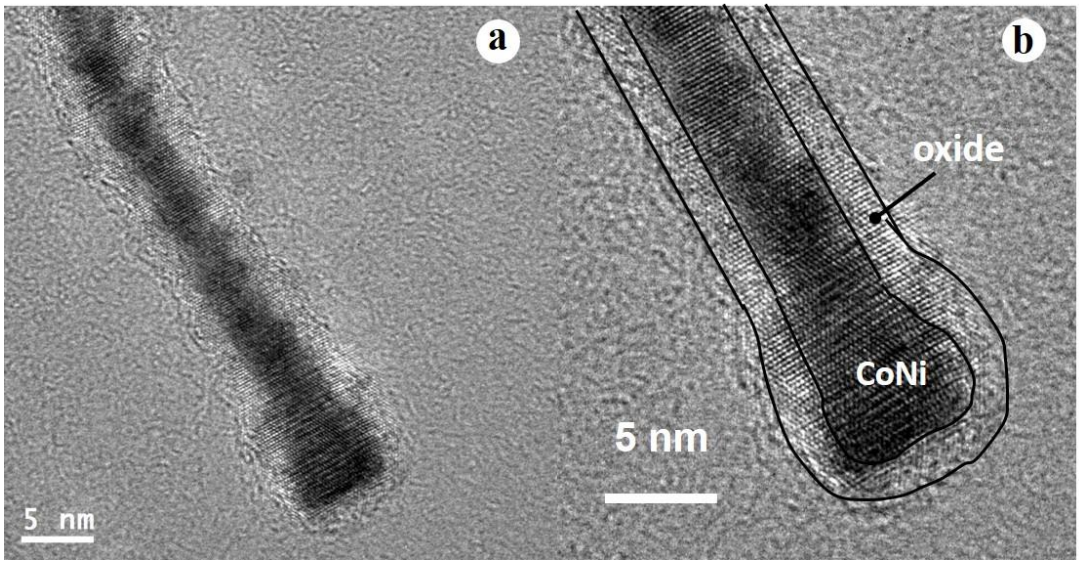

Figure 4-10. (a) HRTEM image of the nanorod with a magnified image of the nanorod tip (b), showing a clear contrast variation between the core and the shell. The black line delimitating the nanoparticle surface as well as the interface between core and shell is a guide to the eye.

Due to the hexagonal structure, the rod-like particles have a uniaxial anisotropy along the c-axis of the crystal lattice, which is the <0001> direction. From the previous studies accomplished by Viau and co-workers, it is known that the sodium hydroxide concentration used in the synthesis of these nanostructures forces the growth to occur preferentially along the <0001> direction of the crystal structure forming high aspect-ratio nanostructures, and hinders it to happen perpendicularly, as the case of platelets. This statement was verified and the hcp <0001> direction was found to be parallel to the long axis of the nanorod (see Figure 4-9 (a)) and coincides with the fcc <001> direction of the oxidized shell. This also suggests an epitaxial relation between the surface oxide layer and metal core, which is consistent with the fact that such shell was spontaneously formed by inward oxidation of pre-existing metallic particles to a considerable extent upon exposure to ambient conditions.

To study the degree of polycrystallinity, the nanorods were aligned on a carbon film supported cooper grid in the presence of an external magnetic field of 1.2 T, by magnetophoretic deposition [150, 151]. The nanorods aligned along the magnetic field direction as shown in Figure 4-11 (a) and an electron diffraction pattern was acquired from this area, the one shown in Figure 4-11 (b). The inhomogeneity of the diffraction rings indicates a strong <0001> texture along the long axis of the nanorods [152, 153].

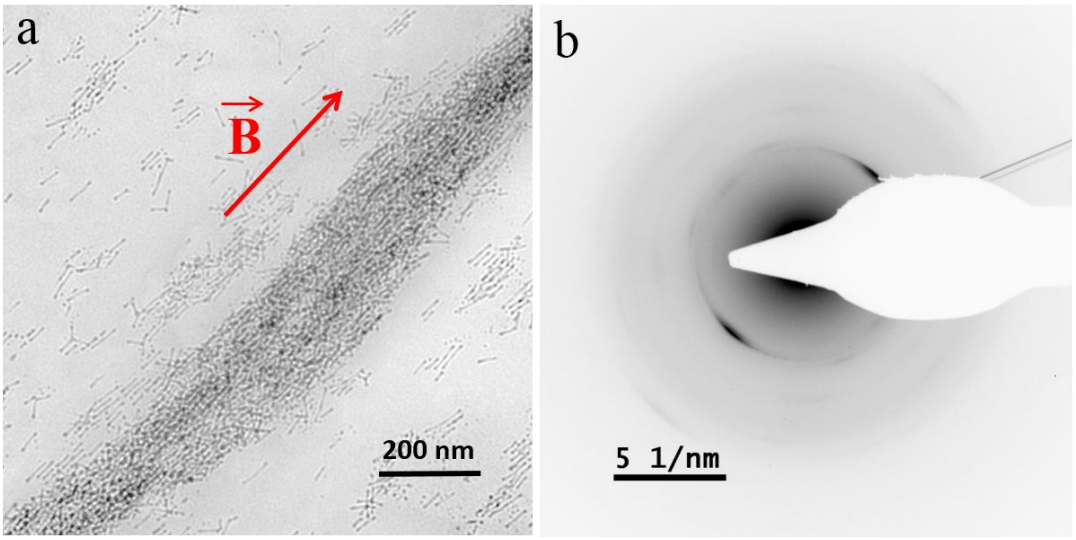

Figure 4-11. (a) TEM image of the CoNi nanorods deposited from the solution on a carbon film supported cooper grid in presence of an external magnetic field of 1.2 T, applied in the direction indicated by the red arrow. (b) Corresponding electron diffraction pattern.

4.5 Magnetic characterization

The magnetic characterization of dried powder fixed in a capsule was performed using a superconducting quantum interference device (SQUID) magnetometer. Magnetic hysteresis loops of dried powder of $Co_{80}Ni_{20}$ nanorods are measured in capsules in the temperature range 5 K – 350 K in external fields up to ± 4.5 T. In order to investigate the influence of the oxide surface layer on the magnetic properties, zero field cooling (ZFC) and field cooling (FC) hysteresis curves have been measured. For the field cooled (FC) measurements, a field of +4.5T was applied during cooling.

Representative ZFC hysteresis loops at different temperatures are shown in Figure 4-12. The sample has been carefully demagnetized at T = 350 K before cooling. The linear contribution observed in the measured loops derived from an antiferromagnetic/paramagnetic phase have been subtracted. It can be seen that all curves are symmetrical with respect to the origin. The saturation magnetization (M_s), the remanence magnetization (M_r), and the coercive field ($\mu_0 H_c$) are obtained from the graphs and summarized in Table 4-3. The positive and absolute negative values of the corresponding parameters have been averaged.

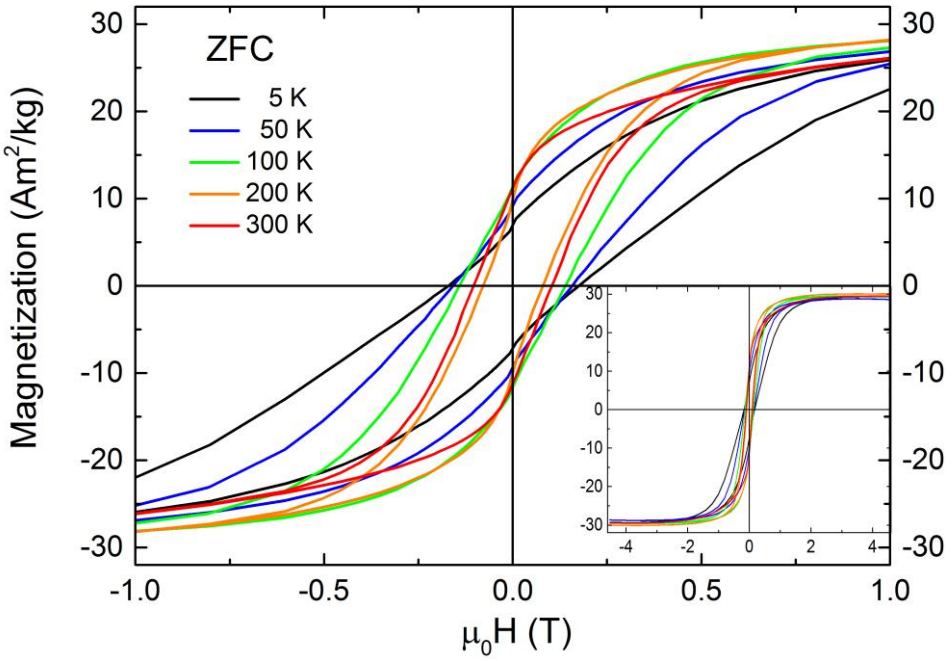

Figure 4-12. ZFC magnetic hysteresis loops of the $Co_{80}Ni_{20}$ nanorods powder sample recorded at different temperatures between 5 and 300 K. The sample has been carefully demagnetized at T = 350 K before cooling. The inset shows the complete hysteresis curves measured at applied magnetic fields of ± 4.5 T. The saturation magnetization remains fairly constant. However, with increasing temperature, the coercive field decreases, and the remanence increases.

Table 4-3. Characteristic parameters of the ZFC hysteresis curves of the $Co_{80}Ni_{20}$ nanorods at different temperatures, including the coercive field ($\mu_0 H_c$), saturation magnetization (M_s), the remanence magnetization (M_r), and the Mr to Ms ratio.

T (K)	$\mu_0 H_C$ (T)	M_s (Am^2/kg)	M_r (Am^2/kg)	M_r/M_s
5	0.17	29.08	7.09	0.24
25	0.17	28.16	7.88	0.28
50	0.16	29.11	9.26	0.32
75	0.15	28.84	10.47	0.36
100	0.14	29.59	11.53	0.39
150	0.10	29.84	11.79	0.39
200	0.08	30.04	9.94	0.33
250	0.15	28.25	12.55	0.44
300	0.10	28.92	11.23	0.39

Though the nanowires are clearly ferromagnetic at room temperature, the initial shape of the M(H) curve at 5K (see Figure 4-15) indicates the presence of different magnetic phases, a ferro(ferri)magnetic and an anti(para)ferromagnetic. In other words, the magnetic data verify the presence of both, pure metallic part and metal oxides in the sample.

For better visualization of the temperature dependence of M_s and M_r see Figure 4-13. Both parameters have an estimated error of 10%, which originates from an erroneous deduction of the slope of the non-ferromagnetic signal and certain uncertainty in reading the values. Taking into account the error bars, the saturation magnetization remains roughly constant, meaning that this data was acquired far below the curie temperature of the system [2]. The average saturation magnetization of the powder sample is 29.1 ± 0.7 Am^2/kg, which corresponds to 20% of the bulk value of $Co_{80}Ni_{20}$ alloy (140.46 Am^2/kg) [2]. This low magnetization is due to superficial oxidation of the nanorods and to the likely presence of organic matter remaining in the powders (surfactants: oleic acid and trioctylphosphine). The Co-rich oxide shell is antiferromagnetic and provides no net contribution to the magnetization. Indeed, supposing 80% of oxidation, taking into account the mean size values and assuming a perfectly cylindrical shape of the nanocrystal, the calculated oxide thickness of a nanorod was found to be 1.7 nm, which coincides with the thickness of the oxide layer measured in TEM images (see section 4.3). In contrast, the remanence magnetization

shows a slight temperature dependence. From 5 to 100 K, M_r increases linearly up to 40% as the temperature increases. Afterwards, the value oscillates between 10-12.5 Am²/kg.

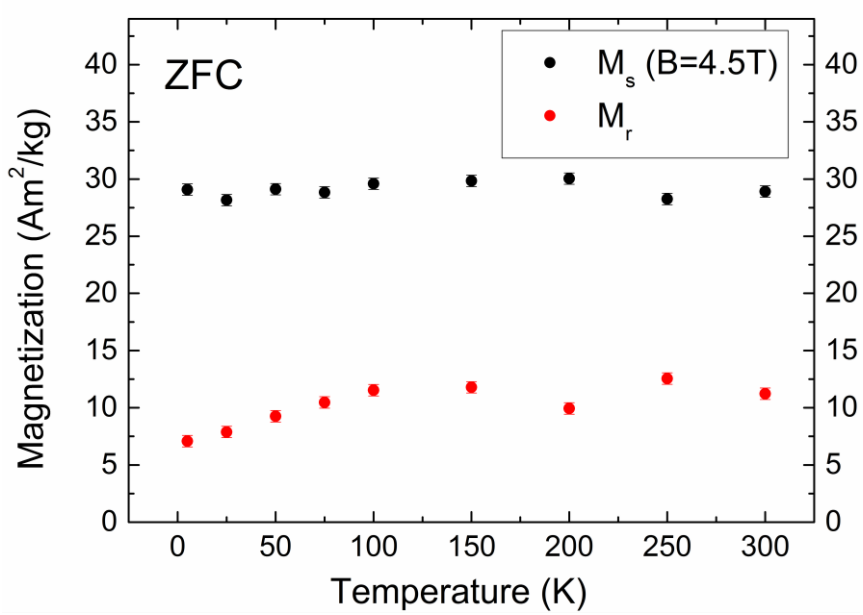

Figure 4-13. Temperature dependence of the saturation magnetization M_s and the remanence M_r is in the range between 5 and 300 K. The saturation magnetization (measured at 4.5T) remains approximately constant in the whole temperature range with an average value of 29.1 ± 0.7 Am² / kg. The remanence magnetization increases linearly between 5 and 100 K, and at higher temperatures oscillates between 10-12.5 Am²/kg. The error bar for both parameters is estimated to be 10% and it is slightly bigger as the dot size of the measurements points in the graph.

Representative FC-magnetization curves measured in the temperature range of 5-300 K are shown in Figure 4-14. A magnetic field of + 4.5 T was applied while cooling. It can be clearly seen that the hysteresis curves measured at lower temperatures are not symmetric with respect to the origin. This asymmetric "humming bird-like" shape of the hysteresis loop at low temperatures is generally attributed to a different magnetization reversal mechanism occurring in each branch rather than the uniform magnetization. Whereas a magnetic single-domain nanostructure with uniaxial magnetic anisotropy follows Stoner-Wohlfarth switching behavior, more complex magnetic nanostructures (i.e. hollow particles) may reverse in a rather inhomogeneous way [154]. Thus, the "humming bird-like" hysteresis is an indication of exchange coupling between two magnetic phases, an interfacial hard phase and a soft phase. Similar results were obtained by K. Simeonidis et al. in Co nanoparticles [155].

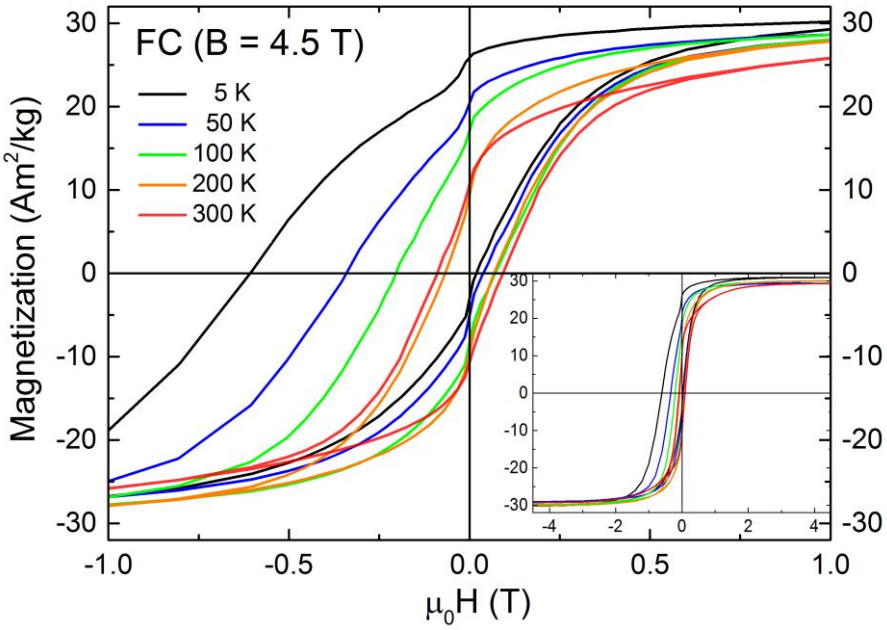

Figure 4-14. FC magnetic hysteresis loops of the $Co_{80}Ni_{20}$ nanorods powder after cooling from 350 K in an applied field of + 4.5 T. The inset shows the complete hysteresis curves measured at applied magnetic fields of ± 4.5 T. With decreasing temperature a higher shift towards negative fields and larger increase of the coercive field are observed (exchange bias).

To investigate the influence of the oxide surface layer on the magnetic properties, it is wise to compare the ZFC and FC hysteresis curves. Figure 4-15 presents both the ZFC and FC hysteresis loops at T = 5 K. The FC loop is shifted opposite to the cooling field direction (B = 4.5 T) indicating a FC-induced unidirectional magnetic anisotropy. The broadening of the FC hysteresis is due to an additional FC-induced uniaxial magnetic anisotropy. Besides, a vertical magnetization shift of +1.7% is found (cf. Figure 4-15 inset). The vertical shift is due to pinned magnetic moments that are not rotated by the applied field. In the FC process, a fraction of magnetic moments are tightly pinned to the antiferromagnetic lattice along the direction of the cooling field. As a result, the saturated magnetization in positive and negative magnetic field is different, which results in the vertical shift of the hysteresis loop. All three phenomena are well known for systems with ferromagnet/antiferromagnet interfaces due to interfacial exchange coupling between the magnetic moments of the ferromagnetic and antiferromagnetic regions (exchange bias effect) [156]. Thus, the Co-rich oxide layer as determined by TEM and XPS since antiferromagnetic increases the magnetic anisotropy of the nanorods at low temperatures.

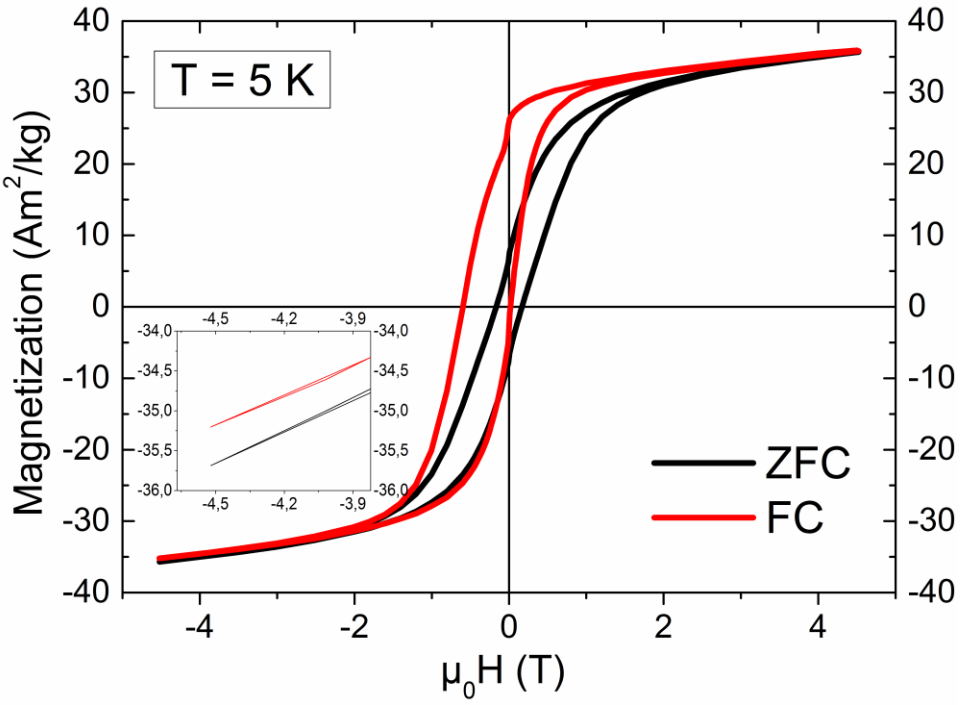

Figure 4-15. Magnetic hysteresis loops after cooling from 350 K to 5 K in zero field (ZFC) and in an applied field of 4.5 T (FC). The FC hysteresis has larger coercive field and a significant shift towards the negative field direction (exchange bias). The FC hysteresis loops is also shifted towards larger magnetization (see inset) indicating pinned magnetic moments.

Table 4-4. Characteristic parameters of the FC hysteresis curves of $Co_{80}Ni_{20}$ nanorods at different temperatures. $\mu_0 H_c^-$ and $\mu_0 H_c^+$ corresponds to the coercive field measured in the negative and positive branch of the field axis. The resulting coercive field ($\mu_0 H_C$) is calculated according to Eq. 2-15 and the exchange bias fields ($\mu_0 H_{exch}$) according to Eq. 2-16.

T (K)	$\mu_0 H_c^-$ (T)	$\mu_0 H_c^+$ (T)	$\mu_0 H_c$ (T)	$\mu_0 H_{exch}$ (T)
5	-0.61	0.02	0.31	0.29
25	-0.44	0.03	0.24	0.21
50	-0.34	0.05	0.20	0.15
75	-0.27	0.05	0.16	0.11
100	-0.20	0.07	0.14	0.07
150	-0.10	0.08	0.09	0.01
200	-0.07	0.07	0.07	0
250	-0.13	0.13	0.13	0
300	-0.09	0.09	0.09	0

The coercive field ($\mu_0 H_c$) and the exchange bias field ($\mu_0 H_{exch}$) for all the measured temperatures of the FC curves were calculated using equations Eq. 2-15 and 2-16 respectively. The results are listed in Table 4-4. A large exchange bias field $\mu_0 H_{exch}$ = 290 mT is

measured at 5 K. The FC coercive field $\mu_0 H_c^{FC}$= 305 mT is increased by 80% as compared to the ZFC value.

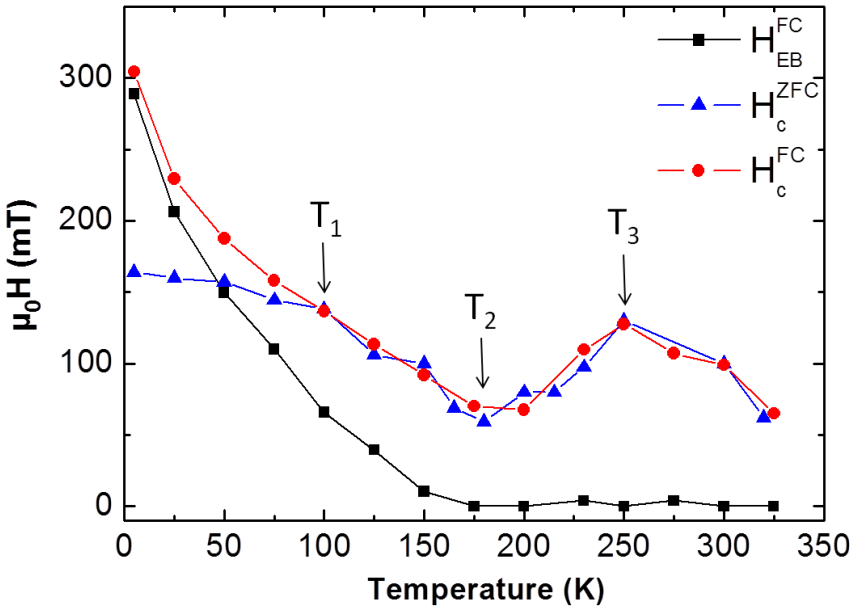

Figure 4-16. Coercive fields and exchange bias field as function of temperature after cooling the sample from 350 K to 5 K in zero field (ZFC) and 4.5 T (FC). The experiments were performed with increasing temperature.

The temperature dependence of the coercive field ($\mu_0 H_c$) after ZFC or FC, and the exchange bias field ($\mu_0 H_{exch}$) are displayed in Figure 4-16. The comparison of the coercive field values of ZFC and FC measurements (blue triangles and red dots) shows two different ranges. Above T_1 = 100 K both curves are congruent. Below T_1, $\mu_0 H_c$ of FC measurements increases sharply with decreasing temperature as compared to the ZFC values. This effect is due to the existence of an interface between ferromagnetic material and antiferromagnetic material, which causes the unidirectional and uniaxial anisotropy. The ferromagnetic material is the CoNi alloy that forms the core of the nanorods and the antiferromagnetic material is the Co-rich oxide shell that grows epitaxially on the surface by natural oxidation.

The exchange bias field $\mu_0 H_{exch}$ (black squares) gradually decreases from 290 mT at 5 K to vanish at T_2 = 175 K. The increase of the coercive field from 70 mT to 130 mT above T_2 up to T_3 = 250 K is even more important. This behavior has only been observed in few systems (films and nanorods) all having a related crystallographic growth between ferromagnet and antiferromagnet. For undirected oxide growth frequently observed for nanoparticles, nanorods, or films such intermediate increase of the coercive field is absent.

Before starting the detailed discussion of the temperature dependence of H_c, additional results on the thermomagnetic relaxation of the remanent magnetization M(t) as function of time are presented. These measurements give access to the so-called magnetic viscosity S [157]. After field cooling the sample from 350 K to the measuring temperature in an external field of 4.5 T, the time decay of the magnetization has been recorded at zero external magnetic field for temperatures in the 10 – 325 K range (Figure 4-17 (a)) [158].

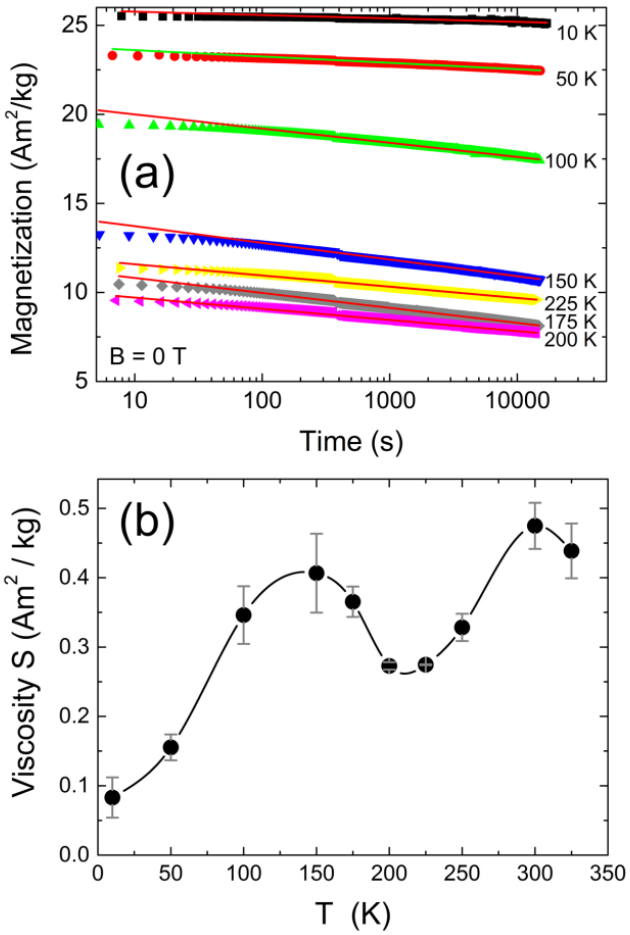

Figure 4-17. (a) Thermomagnetic relaxation of the remanent magnetization M(t) in logarithmic scale. All curves are measured at zero external magnetic field after cooling the specimen from 350 K to the indicated temperature in an external field of 4.5 T. Panel (b) shows the temperature dependence of magnetic viscosity S taken from a fit $M(t)=M_0-S(T)\ln(t/t_0)$ of the thermomagnetic relaxation curves. The spline function connecting the experimental points is a guide to the eye.

According to the model proposed by Street and Woolley [157] the distributions of size, crystallographic orientation and anisotropy in an ensemble of magnetostatically interacting particles lead to the logarithmic decay of the magnetization M in time t:

$$M(t) = M_0 - S(T)\, ln\left(\frac{t}{t_0}\right) \quad \textit{(Equation 4-1)}$$

where M_0 is the magnetization at $t_0 = 0$ s and S(T) is the magnetic viscosity describing the average decay of the magnetization with time. This viscosity model is suitable for the description of long-time relaxation at times t > 100 s, as it was observed in the present study (Figure 4-17 (a)). The linear slope in logarithmic scale corresponds to the magnetic viscosity S. It is worth mentioning that the remanent magnetization (as deduced from the viscosity measurements at $t = 10^4$ s) follows the identical temperature dependence as compared to the coercive field (Figure 4-16 and Figure 4-17). The temperature dependence of S is displayed in Figure 4-17 (b).

The magnetic viscosity S has a small value at low temperatures where the majority of nanorods and particles are thermally blocked and, therefore, magnetic relaxation is very weak. With increasing temperature S grows to a local maximum near 150 K, which is slightly below temperature T_2 in Figure 4-16, where a minimum of the coercive field was observed. Similar behavior has been reported for Co/CoO nanowires [103]. Above, S decreases to a local minimum at about T = 220 K, again slightly below the local maximum of the coercive field at T_3, before S rises to the highest observed values around ambient temperature. It is straightforward to understand these opposing trends of H_c and S dependencies with temperature, since the larger the stability of the magnetization (indicated here by a high H_c), the slower its decay with time (low S). The significant increase of S observed at higher temperatures (T > 220 K) can be related to the temperature variation of the different anisotropy contributions in the system [97]. However, the underlying mechanism for the formation of a local maximum of H_c and the local minimum of S cannot be explained with these observations alone.

In most exchange bias systems (films, nanorods, or nanoparticles) such an oscillatory temperature dependence of H_c was not observed. Some systems, i.e. highly textured MnF_2/Fe films [159], highly ordered Ni/NiO nanorods [160], or Co/CoO nanorods [103] exhibit an increase of H_c at an intermediate temperature while for spherical particles this behavior has not been observed yet. For MnF_2/Fe films Leighton et al. [159] found an enhancement of H_c at the Néel temperature of the antiferromagnetic MnF_2 only when the ferromagnetic Fe layer thickness is significantly larger as compared to the antiferromagnetic layer, thus making the ferromagnetic layer dominant upon reversal. They discussed this effect in the frame of the Stiles and McMichael model, in which competing anisotropy

energies of the ferromagnetic and antiferromagnetic layers are linked to specific crystallographic orientations [161]. Hsu et al. argued that in case of Ni/NiO nanorods spin frustration at the ferromagnetic/antiferromagnetic interface is important and H_c increases with increasing temperature as soon as the superparamagnetic blocking temperature of the antiferromagnetic shell is overpassed [160]. Nevertheless, Ni/NiO-coated carbon nanotubes working as nanowires and being spin-frustrated at the ferromagnet/antiferromagnetic interface do not show an increase of H_c at an intermediate temperature, likely because of the randomly oriented Ni/NiO nanostructures forming the magnetic coating of the carbon nanotubes [162].

For Co/CoO nanorods with an epitaxial relation of the Co core and the CoO shell, Maurer et al. obtained similar trends as presented here for the oxidized CoNi nanorods [103]. They observed a local minimum of $\mu_0 H_c = 450$ mT and a maximum of entropy at the temperature at which the exchange bias vanishes $T_2 = 100$ K, while H_C rises up to 600 mT at $T_3 = 200$ K [103]. In the CoNi system herein studied, very similar temperature dependencies of H_c and entropy appear, though shifted about 75 K towards higher temperatures. This can be assigned to the small Ni content in the shell leading to higher T_N and to a reduced effective magnetic anisotropy in the ferromagnetic core and the shell of CoNi nanorods. Maurer et al. discussed these observations in a three stage regime model: CoO grains in the shell are antiferromagnetic at low, become superparamagnetic at intermediate, and get paramagnetic at high temperatures.

Consequently, exchange bias is present until the superparamagnetic regime is reached ($T_2 = 175$ K in Figure 4-16). Any further temperature increase leads to a more superparamagnetic fluctuating grains. Thus, its influence on the ferromagnetic core decreases and the core magnetic moments at the interface can align easier along the long axis of the rods due to shape anisotropy. This leads to the higher squareness as indicated by the simultaneously increasing coercive field and remanent magnetization. Maurer et al. identified T_3 as T_N (cf. Figure 4-16), above which the influence of the antiferromagnetic shell vanishes, and H_c (S) decreases (increases) with temperature. In contrast to their argument, since in this case T_N is higher, these observations should be discussed within a temperature-dependent vectorial effective anisotropy model comprising at least the major anisotropy components, i.e. magnetic anisotropy of the ferromagnetic core and the antiferromagnetic

shell, and the interfacial exchange. Since the above anisotropy values are unknown or scatter significantly for nanoscale systems in the literature and the present study cannot deliver them precisely, the following discussion is on a qualitative level in conjunction with the structural results.

The magnetic easy axis of the ferromagnetic CoNi core is the nanorod long axis with collinear orientation of magnetocrystalline and shape anisotropies. The oxide shell grows quasi-epitaxial on the rods with one <001> direction parallel to the c-axis of the core. In bulk, CoO, and presumably also the present Ni-doped CoO have rock salt structure above and a monoclinic structure below T_N, with a large tetragonal distortion along the cube edges with c/a < 1 and a small deformation along <111>. This implies a pseudo-cubic structure with two CoO units per unit cell [163]. In the antiferromagnetic state the sublattice spins align collinear approximately in <110> directions of the pseudo-cubic structure [164]. Although significant additional stress at the interface can be expected for the CoNi nanorods, here, it is speculated that the spin orientation in the antiferromagnetic shell is similar and thus not collinear to the <100> direction and the c-axis of the ferromagnetic core.

This misalignment of ferromagnetic and antiferromagnetic spins at the interface certainly has a strong impact on the magnetic properties. Considering the stronger magnetic anisotropy of Co oxides, as compared to CoNi at low temperatures, likely, the interface spins are governed by the antiferromagnetic shell. From the fact that the Curie temperature of the CoNi core is much larger than T_N of the shell one may assume that the magnetic anisotropy contributions have strongly different temperature dependencies. Then the major source of magnetic anisotropy should switch from the antiferromagnetic shell to the ferromagnetic core upon rising temperature. Below T_1 = 100 K field-induced orientation of rotatable antiferromagnetic interfacial spins leads to the splitting of the coercive field after ZFC and FC. The temperature at which the exchange bias vanishes (T_2 = 175 K) is the temperature limit of pinned interface moments and above, antiferromagnetic moments get rotatable, contributing to the uniaxial anisotropy. For higher temperatures the influence of the antiferromagnetic moments gets weaker and, consequently, more and more interface spins align with the ferromagnetic core as suggested by the rising remanent magnetization up to T_3 = 250 K. The decrease at higher temperatures is presumably due the significant decrease of all anisotropy contributions in both, the core and the shell, even without reaching T_C and T_N in the present experiments.

Overall, one reasonable explanation of the magnetic hardening at intermediate temperatures is: (i) there is a certain degree of crystallographic order between core and shell and (ii) the magnetic easy axis of the ferromagnetic core (here c-axis and long axis of the rods) and the antiferromagnetic shell (here presumably monoclinic Co-rich oxide below T_N) are not collinear. These two conditions are fulfilled for the present study and all the examples discussed above. Thus, the ferromagnetic-antiferromagnetic core-shell nanorods represent a prototype system for investigating the influence of superparamagnetic fluctuations in exchange bias. Vice versa, for spherical particles with core-shell symmetry these conditions can hardly be matched, which is probably the reason why such behavior has not been observed so far.

4.6 Conclusions

$Co_{80}Ni_{20}$ nanorods with average length of 52.5 nm and 6.5 nm diameter were prepared as considering them a promising option for the production of permanent magnets, by exploiting the alignment of magnetocrystalline and shape anisotropy axes in conjunction with exchange bias. The stoichiometry has been chosen to exploit the highest magnetocrystalline anisotropy among the 3d-elements (hcp Co), the still large magnetization at low Ni content, and the good long-term stability of CoNi alloys. Structural, morphological, and chemical investigations revealed surface oxidized nanorods consisting of a metallic hcp CoNi core and a Co-rich oxide shell with a thickness of 1-2 nm. The crystallographic c-axis in the core is collinear with the long axis of the nanorods. Co-rich oxides have grown around the core with a defined crystallographic orientation, i.e. $\langle 0001 \rangle_{hcp} \parallel \langle 001 \rangle_{fcc}$. The magnetic characterization of this system shows strong unidirectional anisotropy at low temperatures after field cooling while the exchange bias vanishes at T = 175 K. Interestingly, in an intermediate temperature range 175 K < T < 250 K the coercive field rises by almost a factor of two, before it starts decreasing again for higher temperatures. This effect is discussed within a three range regime model suggested before, considering the superparamagnetic fluctuation of antiferromagnetic grains in the Co-rich oxide shell. Such behavior is expected only if the magnetic easy axes of the ferromagnetic core and the antiferromagnetic shell are not collinear.

5 CoO Octahedra

In this chapter, synthesis and structural as well as magnetic characterization of well-defined core-shell octahedral CoO-Co_3O_4 nanocrystals are discussed. These nanocrystals exhibit a remarkable room temperature ferromagnetic behavior well above the antiferromagnetic ordering temperature of both oxides. In order to understand this magnetic response, a detailed structural investigation on both, the atomic structure and composition of a single nanoparticle and their morphology is required. Therefore, in this chapter, first the synthetic procedure of cobalt oxide octahedral nanoparticles with tunable sizes is summarized, with the corresponding morphology studies of shape and size. Secondly, the structural and chemical composition of the nanoparticles are analyzed. Later on, the three dimensional morphology is discussed in the frame of a growth mechanism model and lastly, the magnetic characterization is presented and the origin of the ferromagnetic response briefly discussed.

5.1 Introduction

Transition metal oxide nanoparticles are significant due to their potential in a wide range of applications, mainly due to their chemical stability and magnetic properties. In particular, cobalt oxides nanoparticles have attracted special attention due to its applications in many fields such as gas sensors [165, 166], anodes of lithium batteries [167, 168, 169], catalysts [170], supercapacitors [171], magnetic data recording devices [172, 173], etc.

A significant feature of cobalt nanoparticles is their tendency to rapidly oxidize in atmospheric conditions even at room temperature. The oxidation of cobalt can lead to the

formation of three oxides: CoO (cobaltous oxide), Co_2O_3 (cobaltic oxide) and Co_3O_4 (cobaltous-cobaltic oxide). CoO is quite susceptible for further oxidation, especially in a finely divided form like in the case of nanoparticles. It can adsorb oxygen at room temperature up to the equivalent of Co_3O_4 on the crystal surface. On the contrary, Co_3O_4 is a stable, black crystalline compound with spinel structure.

It has been proven that both pure oxides CoO and Co_3O_4 are good candidates for their use as anode (negative-electrode) in lithium-ion batteries [174, 175, 176, 177]. In reference [176] nano-sized (387 nm edge length) and micron-sized (6.65µm) Co_3O_4 octahedrons were synthesized through a wet chemical method followed by thermal treatment. The electrochemical test revealed that the lithium storage property of Co_3O_4 materials as anode of lithium ion batteries depends strongly on their structure and particle size. The excellent electrochemical performance of the nanosized nanoparticles was attributed to the surface atomic arrangement of the {111} facets. The (111) planes of a fcc structure have a more accesible surface structure than (100) and (110) planes, which can be related to more active sites for the diffusion of lithium ions. Thus, Co_3O_4 nanooctahedra enclosed by eight {111} facets facilitate the diffusion of lithium ions and enhance the performance when used as anode of lithium ion battery. This conclusion is also supported in reference [178].

Furthermore, control in the synthesis of well-defined shapes and facets of Co oxides nanoparticles is essential for ultimate applications. For instance, in catalysis, the reactivity and selectivity of catalysts depend upon the different arrangement manner of surface atoms and the number of dangling bonds of different crystal planes [179]. In this regard, the study done by Yadong Li and co-workers [180] is an example of the importance of controlling the shape and outer facets of a cobalt oxide crystal. They have shown the different yield in methane catalytic combustion using Co_3O_4 nanoparticles with different shapes: nanosheets, nanobelts and nanocubes. They have found that the well-defined outer {112} crystal planes of the nanosheets present higher catalytic activity than the {011} and {001} outer planes of the nanobelts and nanocubes. These results indicate therefore the significance of tuning the shape of crystals.

As discussed in chapter 2.2, the reactivity of materials depends on theirs physical properties. In order to fulfill the requirement for various technical applications of Co oxides nanoparticles, it is rather important to control various factors such as size, composition,

crystallinity, morphology and well-defined shapes of these nanocrystals.

Cobalt oxide nanoparticles have been synthesized by different methods including thermal decomposition [181, 182], gas vapor condensation [183], solvothermal methods [184], coprecipitation [185] and sol–gel methods [185, 186], among others. In the thermal decomposition method, cobalt carbonyl ($Co_2(CO)_8$) has been often used as the precursor [187]. However, this compound is strongly toxic and relatively expensive. To avoid these disadvantages, other precursors have been used, such as cobalt hydroxide [188], cobalt (II) acetate tetrahydrate [181], cobalt (II) acetylacetonate [189] or cobalt oleate [190].

Other shapes of cobalt oxides crystals have been achieved as well, such as cubic [191], spheres [192, 193, 194], tetragonal nanocrystals [187, 192], tetrapods [195], hexagonal pyramid-shaped [182], pencil-shaped [190], flower-like [196, 197], nanobelts [178], nanorings [198], nanoplates and nanorods [199] among others. The latter case is a study of Peng and co-workers which is indeed a good example of how optical and catalytic properties vary with the crystal shape and dimensions of nanocrystals. One of the main conclusions of their study is that nanoplated shapes with basal planes corresponding to {001} facets, present better catalytic activity than nanorods for hydrogen generation.

For reasons above discussed, the design of a new method for the synthesis of cobalt oxide octahedron-shaped nanoparticles with tunable size, as well as determining precisely the physical and chemical properties of these nanocrystals is the main focus of the research presented in this chapter.

5.2 Synthesis

Park and co-workers developed several years ago a simple and reproducible strategy for the synthesis of hexagonal and cubic CoO nanocrystals consisting in the thermal decomposition of a single molecular precursor $Co(acac)_3$ (cobalt acetylacetonate) in oleylamine at 200 ºC [182]. They managed to isolate cubic and hexagonal phases of CoO by changing the synthetic conditions. Additionally, they were able to control the size and shape of the CoO nanocrystals by changing the precursor concentration. When the molar ratio between the organometallic precursor and the solvent was set to be 1:200 or 1:100, rod-

shaped and pyramid-shaped (respectively) CoO nanocrystals were formed. Molar ratio of 1:50 led to a pyramid-shaped nanoparticles with larger crystals, which indicates however that the hexagonal pyramid shape was favored by the abrupt decomposition of precursor at higher concentration.

In the same work, the isolation of the cubic CoO phase was also achieved by variations in the reaction temperature. It was suggested that oleylamine-substituted cobalt complex formed by prolonged heating at 135ºC (prior to increase the temperature up to 200ºC), was the key factor to obtain cubic seeds and consequently fcc CoO final product. Although the reaction mechanism leading from Co^{3+} to Co^{2+} ($Co(acac)_3 \rightarrow CoO$) and the source of oxygen were not clearly understood, oleylamine was assumed to be the reducing agent and the acetylacetonate ligand was thought to be the source of oxygen to form CoO [182]. Chen and co-workers [200] also stated that the oxygen for the formation of CoO nanocrystals should originate from the decomposition of acetylacetonate cobalt precursor because the reaction was conducted with rigorous exclusion of other oxygen sources.

The excellent results obtained by Park and co-workers concerning the phase-, shape- and size- controlled synthesis of CoO nanocrystals, served as a precedent to advance this line of inquiry. Thus, the work presented in this chapter is the result of that effort and all the CoO nanoparticles were synthesized varying and optimizing the thermal decomposition process initially proposed by Park et al. Indeed, adapting this method of synthesis, CoO octahedron-shaped nanoparticles were obtained. Particularly in this chapter, a detailed study of three samples of CoO nanocrystals with 20, 40 and 85 nm average edge length is presented.

The samples of 40 and 85 nm average edge length CoO nanooctahedra were synthesized using the hot-injection thermodecomposition method. The precursor solution, which consist of Co (II) acetate tetrahydrate (2.66 and 4 mmol, respectively) dissolved in 5 mL of absolute ethanol, was added into a mixture of trioctylamine (25 mL, 57.18 mmol) and oleic acid (5.12 and 8 mmol) at 170 ºC. The mixture was kept at this temperature for 30 min in order to let the ethanol evaporates. After that, the temperature was increased at the rate of 3 °C/min until 300 °C. The system was left to reflux (at T = 300 ºC) for two hours. 20 nm average edge length CoO nanooctahedra were similarly synthesized but dissolving cobalt acetate tetrahydrate (2 mmol), oleic acid (8 mmol), oleylamine (20 mmol) and TOPO (0.2

mmol) in a mixture of trioctylamine (5 mL) and octyl ether (15 mL), and then heating to reflux (at T = 300 ºC) for six hours. Once cooled to room temperature, the nanostructures were separated by centrifugation, washed several times with ethanol and finally stored in absolute ethanol as well.

The observation of a color change in the reaction mixture is a good indicator of the progress of the reaction. The initial precursor solution consisting of Co (II) acetate tetrahydrate dissolved in absolute ethanol is pink as shown in Figure 5-1 (a). When this solution is added to the hot liquid mixture of solvents, the blend takes on a yellowish tone (Figure 5-1 (b)). As the reaction progresses, the color of the reaction mixture changes gradually from yellow to dark brown as shown in Figure 5-1 (b) and (c). Park and co-workers also obtained a final brown solution when preparing cubic CoO nanocrystals [201]. However, they observed that the final solution was green when preparing nanoparticles with a hexagonal crystalline structure from similar synthetic conditions. They attributed this differentiation of hexagonal and cubic phases to the presence of water because cubic nanocrystals were only formed when water was added to the reaction. In agreement with the observation of Park and co-workers [201], the experimentally obtained final solution was also brown (Figure 5-1 (c)), indicating that most probably the formed nanocrystals have a cubic structure. In the present case, the presence of water in the reaction blend is attributed to the degree of hydration of reagents used in the synthesis (i.e. cobalt acetate tetrahydrate).

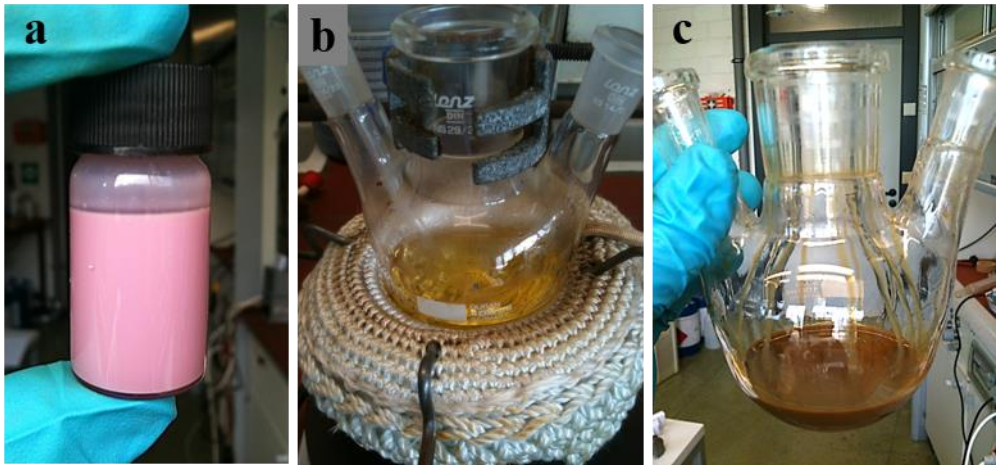

Figure 5-1. (a) Initial precursor solution consisting of Co (II) acetate tetrahydrate dissolved in absolute ethanol. (b) Reaction blend after the hot injection addition of precursor solution into a mixture of solvents at 170°C. (c) Final reaction product after cool down to room temperature.

5.3 Morphology

CoO nanocrystals have been characterized by means of transmission electron microscopy (TEM). A typical TEM overview image of the as-synthesized cobalt oxide nanocrystals is shown in Figure 5-2. Low magnification bright-field TEM image in Figure 5-2 (a) display the 2D projections of theses nanocrystals supported on a carbon film. The projected morphologies display well-defined geometrical shapes such as square, rectangle, hexagon and rhombus, which can be derived from an octahedral shape depending on the orientation of each nanoparticle as depicted in Figure 5-2 (b). These morphologies closely resemble the TEM images acquired at higher magnification shown in Figure 5-2 (c). Derived from TEM studies, the different geometries were matched to different zone axis (depicted in panel (b)), which is described in section 5.4.

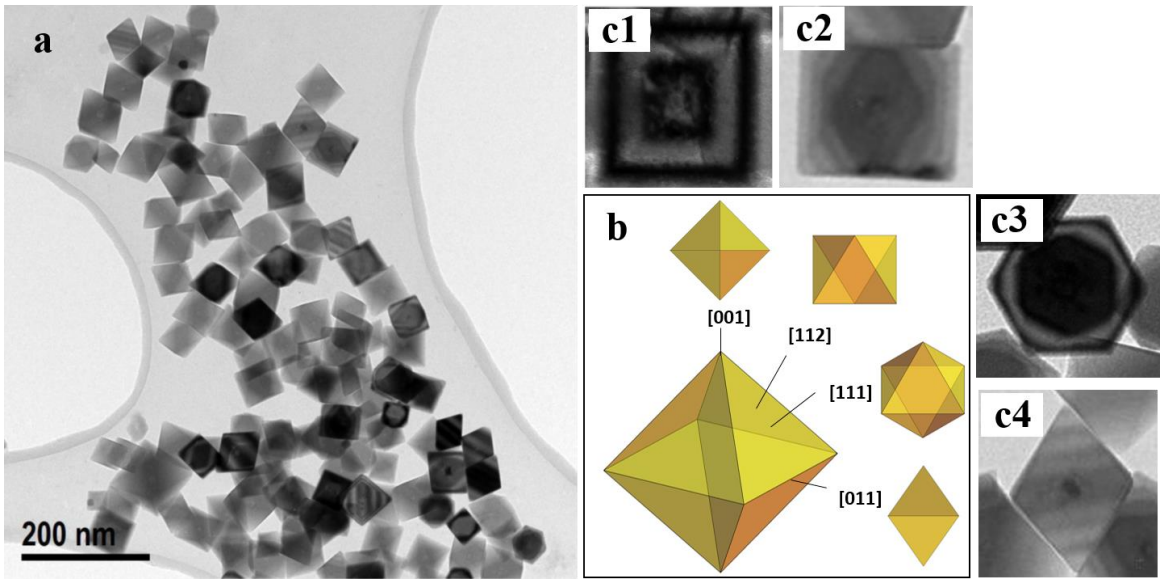

Figure 5-2. (a) Bright-field TEM micrograph of the Co oxide nanoparticles. (b) Schematic drawing of an octahedron in perspective and its 2D projections, with indication of the main zone axes. (c) Particles projections correspond to that of an octahedron.

For an overview of the size and polydispersity of the different synthesized samples, statistical measurements of the nanocrystals were performed. The TEM overview images of the as-synthesized cobalt oxide nanocrystals with corresponding size distributions are shown in Figure 5-3. The average edge length of the octahedron-shaped nanocrystals were determined to be 19.4 ± 2.7 nm (a), 40.9 ± 9.3 nm (b) and 85.3 ± 8.3 nm (c). The graphs plotting the size distribution analysis including the lognormal fit parameters are in Figure 5-3 (d), (e) and (f), respectively.

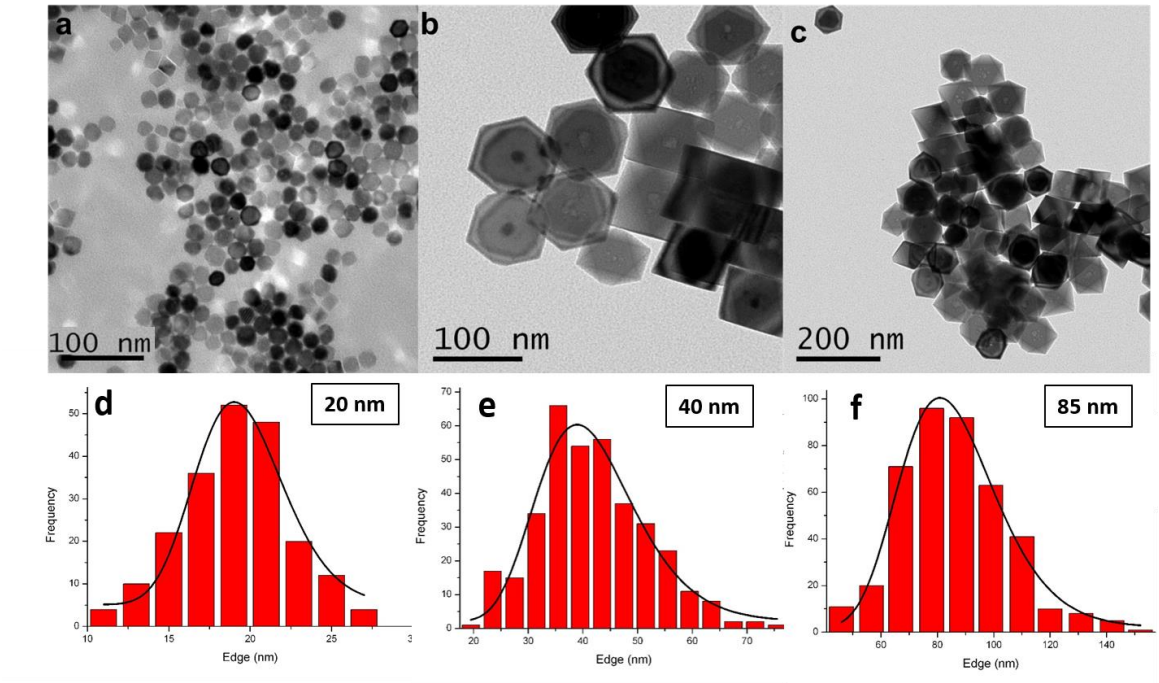

Figure 5-3. TEM overview images of the octahedron-shaped nanocrystals with 20 (a), 40 (b) and 85 (c) nm as average edge length with corresponding size distribution (d), (e) and (f) underneath.

Because different orientations of the nanooctahedra might lead to misunderstanding in the estimation of the particle size, the average edge length (ℓ) was measured taking into account only the direct projection of the octahedron edge, as illustrated in Figure 5-4.

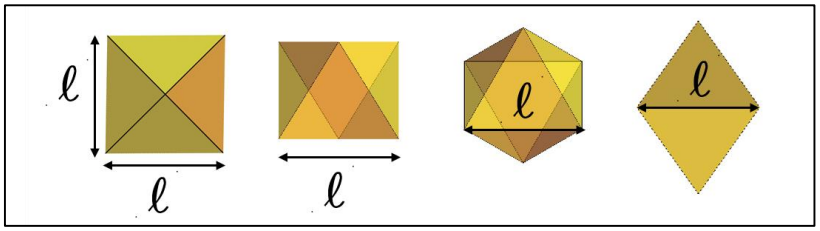

Figure 5-4. 2D projections of the cobalt oxide nanocrystals, including the measured average edge length depending on the displayed projection in the TEM image.

5.4 Structural and chemical characterization

The crystalline structure and chemical composition of all the three samples was characterized by X-ray photoelectron spectroscopy (XPS), X-ray diffraction (XRD), selected

area electron diffraction (SAED) and electron energy loss spectroscopy (EELS).

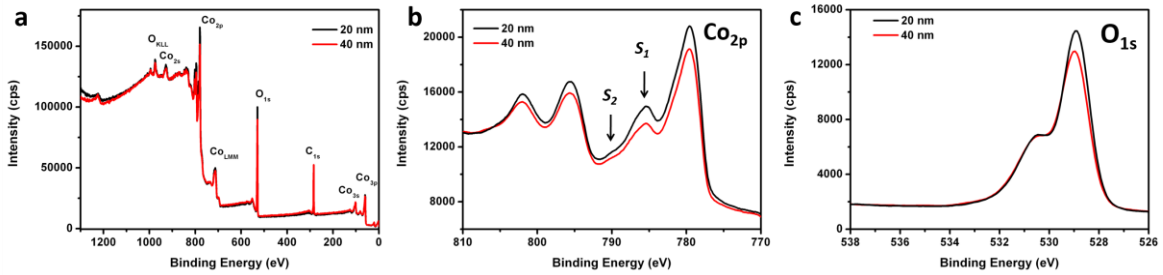

Figure 5-5. X-ray photoelectron (XPS) spectra of nanocrystals with 20 and 40 nm average length, black and red lines, respectively.

Figure 5-5. X-ray photoelectron (XPS) spectra of nanocrystals with 20 and 40 nm average length, black and red lines, respectively. In each spectrum, the main peaks can be indexed to Co 2p, O 1s and C 1s regions. The presence of carbon is likely explained by the existence of an organic layer (capping molecules) on the surface of nanocrystals.

Figure 5-5 (b) presents the Co 2p region including two broad sets of signals. The binding energies are 782 eV for the $2p_{3/2}$ line and 798 eV for the $2p_{1/2}$ line. The doublet splitting is $\Delta = 16$ eV. According to the NIST reference database [143], these observations possess many similarities to CoO and $Co(OH)_2$, confirming the presence of Co^{2+}. Within the resolution of XPS, the presence of metallic Co (Co^0) can be excluded (778.0 eV). In addition, satellite features of this region allow distinguishing cobalt oxidation states, which are highly related to the energy gaps between the Co 2p main peak and satellite peaks. The spectra of the Co-2p doublet include two distinguishable satellite peaks shifted by ~6 (S_1) and ~9 eV (S_2) with respect to the Co $2p_{3/2}$ main peak. The relative intensities of these peaks (S_2 is rather weak but still discernible) indicate that Co^{2+} is the predominant species and some Co^{3+} is also present. Figure 5-5 (c) shows the O 1s signals, centered at 531.7 eV. As the Co 2p and O 1s core levels binding energies of cobalt oxides and hydroxides are in the same range, the spectra confirm again the absence of metallic cobalt [202].

A representative XRD pattern of the octahedron-shaped nanocrystals is shown in Figure 5-6 (black line). All the reflection peaks are characteristic of a standard face-centered cubic (fcc) phase, which corresponds to rock salt CoO crystalline lattice. All the reflection peaks of 2θ at 36.5, 42.4, 61.4, 73.7 and 77.5 can be assigned respectively to the scattering

from the {111}, {200}, {220}, {311} and {222} planes of the CoO cubic structure. No other phases such as the hexagonal CoO wurzite (blue line) or the Co_3O_4 spinel types, previously reported on nanocrystals [182, 191, 190, 189], are discernible.

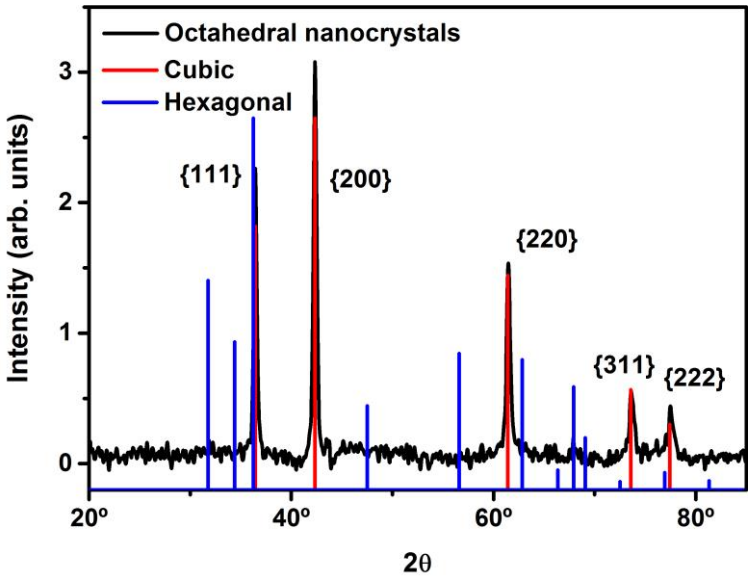

Figure 5-6. XRD pattern of the octahedron-shaped nanocrystals (black) along with two reference samples, cubic CoO crystal (red) and hexagonal CoO (blue).

The sharp diffraction peaks indicate that the as-synthesized CoO particles possess a good crystallinity, while the qualitatively broadening of the peaks with respect to the bulk CoO congener indicate that the nanoparticles are in the nanometer size regime [203, 204, 205]. The resulting relative intensities of the {200} and {111} diffraction peaks is higher than the tabulated value (1.36 instead of 1.19), which indicates that the nanostructures are abundant in {100} planes, likely due to an accelerated growth along the <100> directions [206].

Since the magnetic response of the sample (Subchapter 5.7) can not be explained by the existence of a pure CoO phase as inferred from the XRD data analysis, selected area electron diffraction (SAED) method was applied as an additional technique to determine the nanocrystals structure. Figure 5-7 (a) shows a typical electron diffraction obtained by selecting an ensemble of nano-octahedra of 4 μm in diameter (see inset) and can be indexed according to a cubic structure with a = 4.02 Å, which corresponds to rock-salt structure of CoO. Figure 5-7 (b) shows the integrated intensity profile of these electron diffraction rings. This intensity profile was further analyzed by second derivative to identify the reflection

peaks, which basically matches the CoO and Co_3O_4 phases. However, additional peaks marked with white arrows in the diffraction pattern and black arrows in the 2nd derivative profile seem to not match either CoO or Co_3O_4 phases. This feature corresponds to a double reflexion peak.

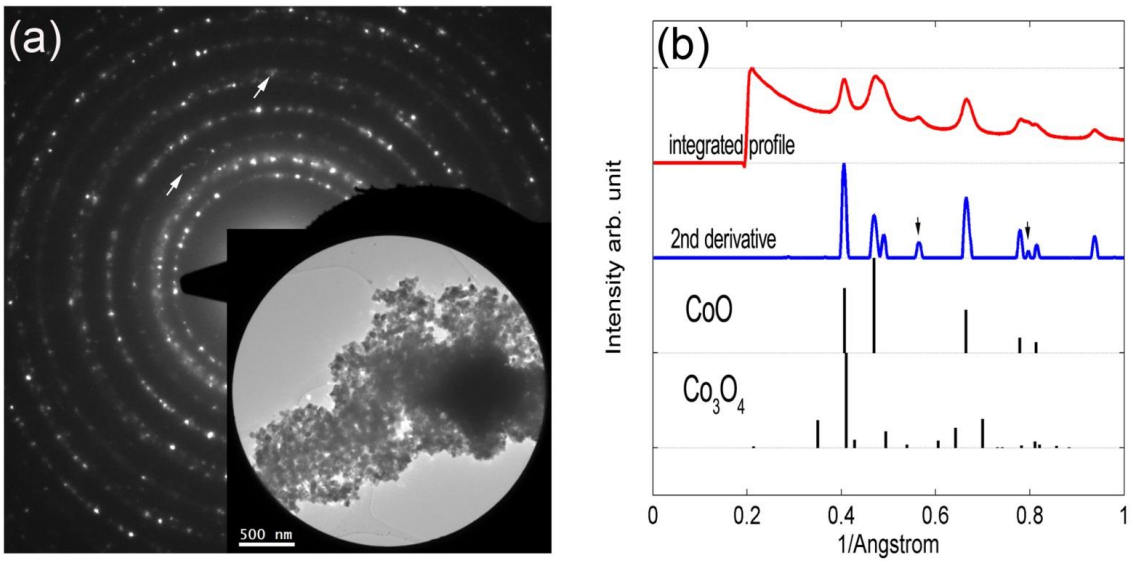

Figure 5-7. (a) SAED pattern of an ensemble of nanooctahedra shown in inset. (b) Integral intensity profile of these electron diffraction rings.

In contrast with the information provided by the x-ray diffraction pattern, in which no other phase than pure CoO was identified, SAED pattern reveals two different crystal lattices. This discrepancy is probably due to the high scattering sensitivity in electron diffraction. The scattering strength due to multiple scattering of x-ray photon with matter is 3-4 orders of magnitude weaker than the scattering strength of electron (with energy of kilovolts) with matter [207].

Indeed, contrast differences were observed in the low-magnification bright-field TEM images (Figure 5-8 (a)) which indicate evidence of a change in the nature of different areas within the NP, pointing towards the existence of a core-shell structure. A dash-line curve is included in the figure as a guideline for the eye denoting the interface boundaries of the core-shell contrast variations.

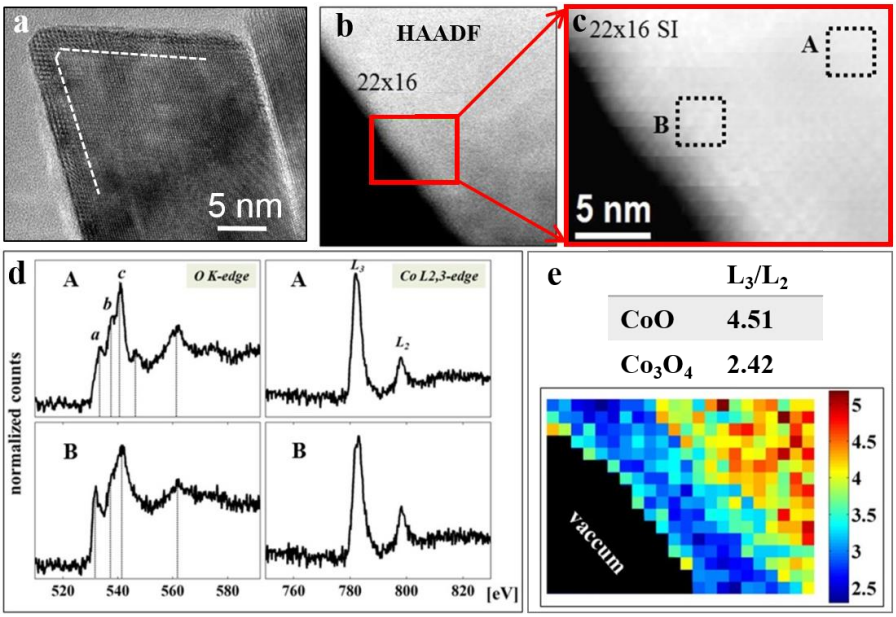

Figure 5-8. STEM-EELS mapping of the CoO/Co_3O_4 interface of a single cobalt oxide octahedron. (a) Bright-field TEM image of a typical octahedra oriented along the [110]-zone axis, displaying contrast variations as delineated by dash-curves. (b) STEM-EELS spectrum image (SI) acquired with 22x16 pixels, at 80 kV using a probe size of 1 nm and magnified area (c) near the crystal surface. (d) Background-subtracted EEL spectra obtained from the core (A) and shell (B) regions indicated in (c). (e) Map of the ratio of the L edge intensities Co $I(L_3)/I(L_2)$ determined from the spectrum acquire at different position (b). A ratio of 4.5 (red) and 2.4 (blue) is typical for Co in CoO and Co_3O_4, respectively. These values are adapted from [208].

In order to provide atomically resolved structural information, spatially resolved electron energy loss spectroscopy (EELS) was performed in scanning transmission electron microscopy (STEM) mode.

In EELS, the L ionization edges of transition-metal elements usually display sharp peaks at the near edge region, known as white lines. For transition metals with unoccupied 3d states, i.e. cobalt, the transition of an electron from 2p state to 3d levels leads to the appearance of these white lines. Numerous EELS experiments have shown that a change in the valence state of 3d element cations introduces a dramatic change in the ratio of intensities of these white lines [209, 210, 211, 212]. Thus the L_3/L_2 intensity ratio in the Co $L_{2,3}$-edges, is a fingerprint that can be used for identification of different ionization states of cobalt.

Since the spectroscopy analysis of the white line intensity is feasible for a region selected by the electron beam, different areas of the sample have been analyzed separately (core and shell). Figure 5-8 (b) shows a high-angular annular dark-field (HAADF) image

of the edge of the octahedron. Figure 5-8 (c) depicts a magnified area near the crystal surface, in which a core region (A) and shell region (B), are marked with black dashed squares. Figure 5-8 (d) shows background-subtracted typical EEL spectra at the O K-edge and Co $L_{2,3}$-edges obtained from the core (A) and shell (B) regions indicated in (c). It can be seen that the L_2 edge in the shell region (B) is higher than that in the core (A).

In order to quantify the Co L_3/L_2 ratios acquired from the core-shell particle with high spatial resolution, every EEL spectra in the spectrum image (SI) dataset have been analyzed using a second-derivative method [213], in order to calculate an L_3/L_2 ratio map. As shown in Figure 5-8 (e), the core region of the particle exhibits a higher L_3/L_2 ratio of 4-5, whereas the shell region exhibits a lower L_3/L_2 ratio of 2-3.5, which is typical for Co in CoO and Co_3O_4, respectively [208, 214].

The O K-edge can also provide information about the oxidation states of cobalt. For the O K-edge, peaks labelled as *a*, *b*, and *c* in in Figure 5-8 (d) arise from the electronic transitions from O 1s → 2p states hybridized with unoccupied Co 3d, 4s, and 4p orbitals, respectively. Characteristics features in these peaks (relative intensities and energies) are also commonly used as fingerprint for discriminating Co oxide phases [208, 214]. In O K-edge spectra, a high intensity in pre-peak *a* acquired from the shell region (B) is indicative of a Co_3O_4 phase. In contrast, the O K-edge acquired from the core region (A), in which the intensity of pre-peak *a* is much lower, is typical for CoO. [208, 214]

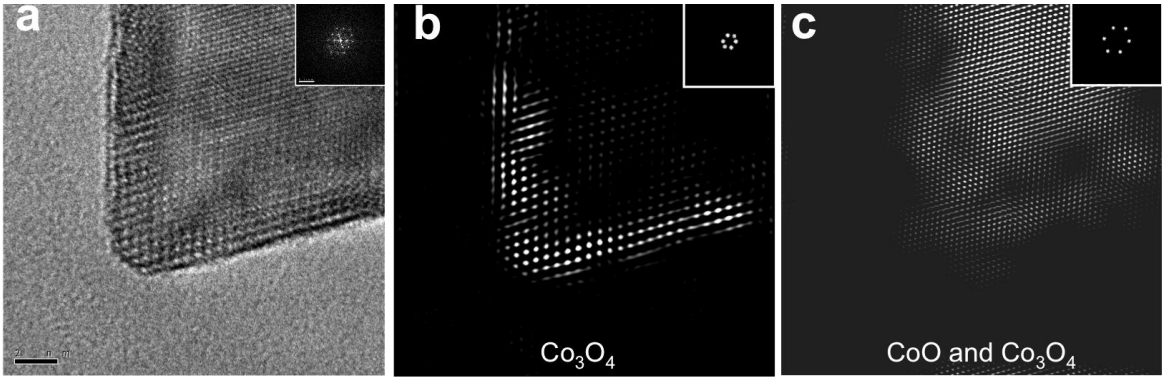

Figure 5-9. HRTEM image (scale bar: 2nm) of an octahedral nanocrystal showing core and shell areas with different contrast (a). Fourier filtering of the image (a); using frequencies that correspond only to Co_3O_4 planes (b) and using frequencies that correspond both to Co_3O_4 and to CoO (c). Insets demonstrate the Fourier transform of each of the images.

To fully demonstrate the existence of a core-shell structure with different crystalline lattices, Fourier transform filtering analysis was performed. The result is shown in Figure 5-9. The panel on the left (a) shows a low magnification bright-field TEM image of an octahedron that exhibits bright-dark patched contrast. Because the particles present a nearly perfect octahedron shape and are oriented along their zone axes, the contrast variation arises from changes in scattering condition due to the core/shell structural overlay. This feature is the so called Moiré effect and appears when two dissimilar lattices overlay or rotate,one respect to the other. Nevertheless, the distinct CoO(core)-Co_3O_4(shell) contrast is clearly revealed.

The Fourier filtered images are shown in Figure 5-9 (b) and (c). Figure 5-9 (b) shows an image that is the result of the Fourier filtering of the TEM image in Figure 5-9 (a), using the spots or frequencies that are exclusive for the Co_3O_4, while in panel (c) the filtering was done using the spots that are due both to Co_3O_4 and CoO. This provides convincing evidence for the presence of two different lattices, CoO in the core region and Co_3O_4 in the shell.

In summary, the combination of TEM imaging and spectroscopy confirm the existence of a thin 2-4 nm thickness spinel-like Co_3O_4 structure on a surface of cubic CoO core. This fact is in concordance with the possible surface oxidation mentioned in the introduction of this chapter. Pure CoO is difficult to obtain by a simple chemical route since this approach typically produces CoO with small amount of metallic Co or Co_3O_4 (due to surface oxidation) [215].

Detailed analysis of HRTEM images provided additional information about the structure and composition of the nanooctahedra. A combination of the high- resolution imaging and SAED pattern makes possible the elucidation of the relationship between the crystallographic orientations of the nanocrystals according to the octahedron shape.

Figure 5-10 includes HRTEM images with enlarged views of the octahedron edges. The regions marked by the red squares in the insets show the imaged area on the octahedron. These HRTEM images were acquired on the edges of the nanoparticles and show well-defined lattice fringes with the interplanar spacing of the (111) planes resolved at 2.46 Å. Upon careful inspection of the limiting surfaces of octahedra, it was found that these

nanocrystals present really smooth {111} facets of the cubic structure, demonstrating planar boundaries ordered up to the surface. No planar defects such as twin boundaries or stacking faults are seen.

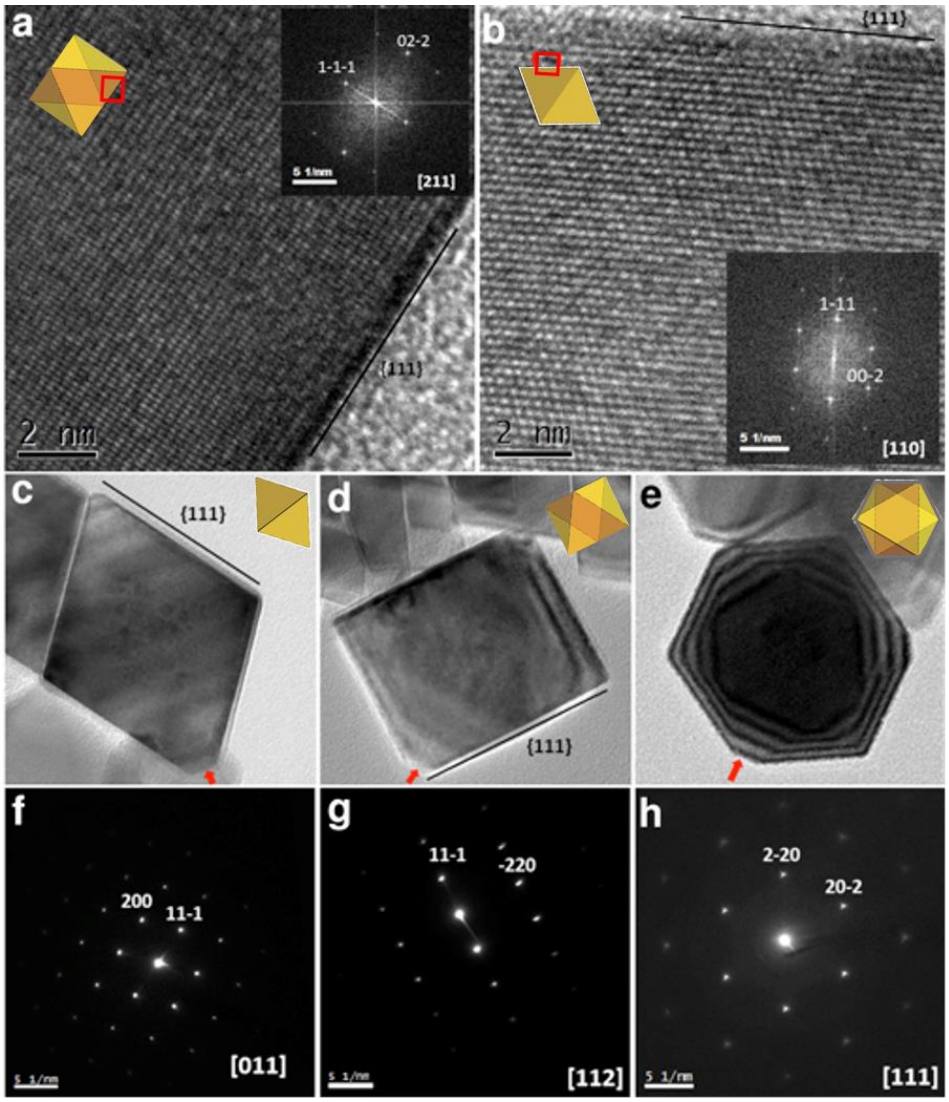

Figure 5-10. HRTEM images of the cobalt oxide octahedra showing the planes ordered up to the surface (top) and three main projections. HRTEM images of octahedra at their sides in the [211] and [110] zone axis respectively (a and b), and the corresponding digital diffractogram in the inset. Three different projections of the octahedra in the [011], [112] and [111] zone axis (sketches in yellow correspond to projection schemes of an octahedron model in the same corresponding axis (c, d and e). Corresponding SAED patterns obtained from the very same single octahedron showed in the upper images, in plane rotation of the diffraction patterns were compensated (f, g and h).

Figure 5-10 (c-e) includes different 2D-projections of the octahedra and their corresponding Fourier transform pattern (f-h), from which the analysis reveals the corresponding crystalline zone axis. Drawings of the projections of a regular octahedron in the various

zone axes have been included, in correspondence with scheme in Figure 5-2 (b). In Figure 5-10 (c) and (d) it is included as well the views of the {111} facet in section, because it is parallel to the electron beam in this orientation of the octahedra. The selected area electron diffraction (SAED) patterns (Figure 5-10 (f-h)) obtained from the very same corresponding single octahedron shown in the upper images (Figure 5-10 (c-e)) show a set of spots that can be indexed as different Bragg planes of cubic CoO. These projections look like a rhombus, a rectangle, or a hexagon and correspond to the [011], [112], and [111] zone axis, respectively. The sharp diffraction spots in these patterns indicate that the octahedra are single crystals, which is in agreement with the result of XRD analysis.

As revealed in the HRTEM images of octahedral with different orientations, the sharp surfaces can actually show truncated tips, marked with red arrows in Figure 5-10 (c-e), and magnified in Figure 5-11.

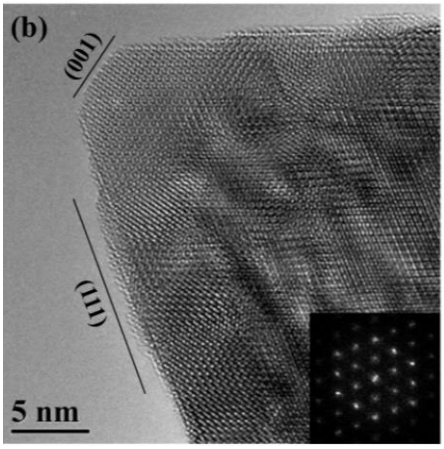

Figure 5-11. HRTEM image of a tip of an octahedral nanoparticle, showing distinct CoO-core and Co_3O_4-shell lattice. The inset shows the Moiré pattern due to the overlay of two crystalline lattices.

The presence of bevels (truncated tips) in octahedron-shaped nanocrystals was observed by Liz-Marzán and co-workers [216]. They considered that this feature might be due to the presence of water in the reaction mixture. Zhang et al. [200] also sustain that water plays a critical role as regarding shape and size of CoO nanocrystals, which evolve from spherical into more quasi-cubic shapes when water was added into their reaction medium. These quasi-cubic shapes are also wounded by {111} facets and bevels (though not mentioned by the authors) [200]. Xu et al. [176] also succeeded in synthesizing 387 nm Co_3O_4 nanocrystals with similar bevels, but they did not analyze this feature either.

Summarizing the structural analysis, X-ray powder diffraction revealed that the major constituent of these nanocrystals is CoO with rock salt structure and confirmed the absence of metallic cobalt (Co^0). X-ray photoemission spectroscopy (XPS) measurements confirm the presence of two different magnetic phases in agreement with the HRTEM results, which reflected the CoO-Co_3O_4 core-shell structure of the nanoparticles. These crystalline cobalt oxide octahedra have eight (111) crystal facets stabilized in air by a thin Co_3O_4 skin, which is formed naturally by surface oxidation in air, and is thermodynamically more stable than CoO. The flatness of the outer facets is outstanding and indicates the excellent crystallinity of the nanoparticles.

5.5 3D morphology: perfect octahedra

To unambiguously confirm the octahedral shape and precisely reconstruct the 3D morphology, electron tomography was used in combination with high-angle annular dark field (HAADF) scanning transmission electron microscopy (STEM) imaging. This method consists of acquiring a series of TEM images by tilting the sample over a large tilt range, with an increment of 1°. After alignment of the projection images, the tilt series is combined into a 3D reconstruction of the original object using a mathematical algorithm [32, 33]. The reconstructed morphology is summarized in Figure 5-12.

Figure 5-12 (a) shows a pair of corresponding images of projected 2D and reconstructed 3D image of a chain of cobalt oxide octahedra, confirming the 3D octahedral shape. One chosen octahedron is color coded and oriented along 2 major axes, [001] and [110] as shown in Figure 5-12 (b) and (c), respectively, together with octahedron schematics. A good match is found with the low-magnification images along the corresponding directions showed in Figure 5-2 (c). The reconstructed 3D structure that is volume-rendered (and consequently mass-dependent) enables us to measure the edges and angles of the individual octahedron-shaped particles. The dihedral angles between (101) and (110) facets is 70.1° and the angle between (111) and (110) facets is 117°. The analysis reveals the almost ideal octahedron shape with equal edge lengths. According to the perfect octahedron shape, exact {111} crystallographic facets terminated on the eight facets of the octahedron emerge, as determined both by diffraction and high-resolution imaging.

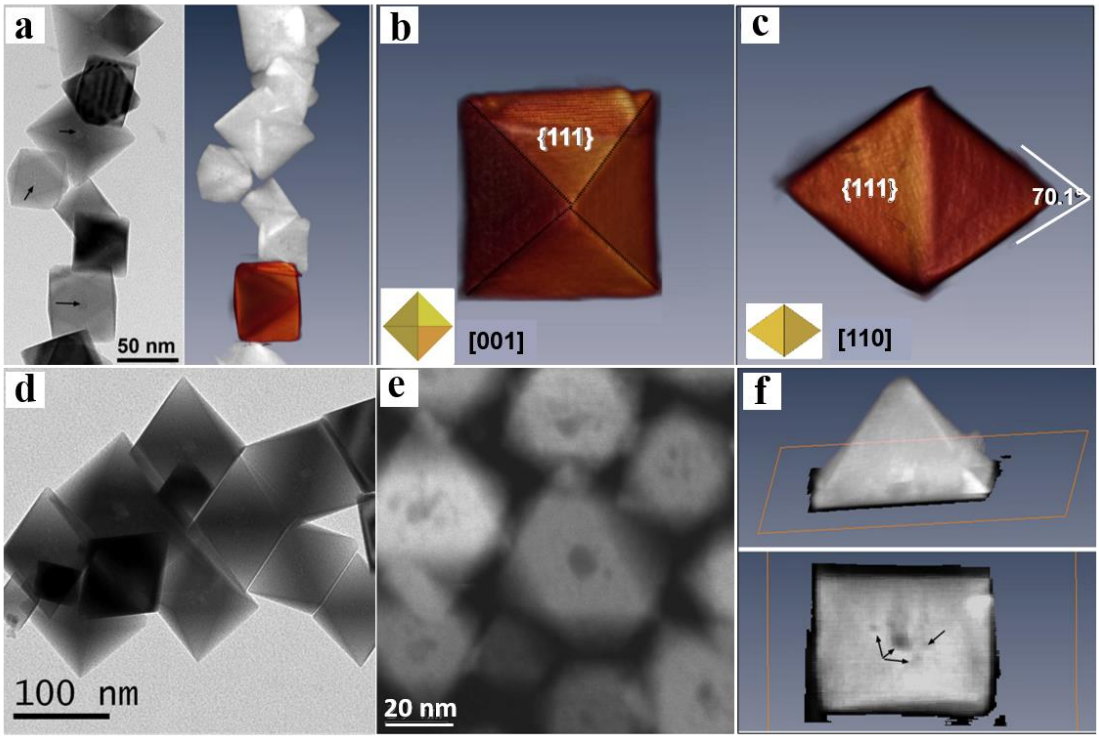

Figure 5-12. HRTEM (a) and 3D reconstruction images (a right, b, and c) of perfectly shaped CoO octahedra. (d) Bright field TEM in which you can see difference in contrast in the center of the octahedrons. (e) STEM-HAADF image proving that most of the nano-octahedral have a large void surrounded by some smaller. (f) Oblique slicing 3D reconstruction image through an octahedron confirming the presence of voids in the inner part of these particles.

In most of bright field TEM images a difference in contrast in the center of the nano-crystals can be appreciated (Figure 5-3 (b)). The HAADF STEM image shown in Figure 5-12 (e) confirms that the contrast difference is due to difference in thickness of the nano-crystal. The presence of holes at the surface of the crystals can be discarded because HRTEM and TEM images do not display any similar feature even when imaged the facets in section as shown in Figure 5-10. Moreover, to confirm the presence of voids in the inner part of these particles, oblique slicing through an octahedron-shaped particle was per-formed, as shown in Figure 5-12 (f). The oblique slicing along octahedron [001] zone-axis revealed indeed the presence of several voids inside the octahedron located around a main and centered cavity of 5-10 nm diameter (indicated by black arrows in (f)). The explanation of this feature is included in subchapter 5.6.

From the above complementary analysis, we can conclude that while the 2D mor-phologies display well-defined geometrical shapes deriving from a projected octahedron, the tomographic results undoubtedly settle the 3D octahedral-shape and internal partially hollow structure.

5.6 Growth mechanism

From the comprehensive structural and compositional information from the cobalt oxide nanocrystals discussed above and in order to explain the octahedron shape, the voids observed and the final core-shell structure attained, we have performed a systematic work going through every step of the synthetic process, in order to understand the mechanism involved.

As explained in subchapter 2.2, a general synthetic process to produce nanoparticles by colloidal chemistry methods consists on a single short burst of nucleation followed by a slower growth of these nuclei formed to reach the final size of the nanoparticles. This mechanism generally fits a scheme on which there is a main chemical reaction that supplies "monomers" of the sought material, reaching a critical level above its equilibrium solubility so that a burst of nucleation occurs. As monomers condense into nuclei and then contribute to the nanoparticle growth, their concentration becomes highly decreased or even depleted and different processes such as Ostwald ripening can begin. In this kind of processes, variables such as temperature and metal-precursor-to-surfactant ratio, exert control over the nanoparticle size and shape.

Thus, in order to understand the synthetic process for the production of these octahedron-shaped nanoparticles, one needs to pay attention to the decomposition of the metal precursor-surfactant complex and the use of a coordinating ligand that directs the growth.

From the point of view of the reaction, in comparison to previous work by Park and co-workers who synthesized CoO nanoparallelepipeds with rod and pyramidal shape from a similar reaction mentioned above [182], our method is different in terms of:

- the nucleophilic attack between the acetate (from precursor) and the amine groups (from solvent molecules),
- the growth of the nanoparticles (using oleic acid as a ligand),
- the solvent that reaches a much higher refluxing temperature,
- addition of the precursor at high temperature (hot injection).

All these aspects favor the production of perfectly shaped octahedral, so let´s analyze them in detail. Compared to the previous work done by Park and co-workers, in the present

study cobalt acetate tetrahydrate in trioctylamine has been used instead of cobalt acetylacetonate in oleylamine [182] or benzylamine [191]. However, the reaction mechanism postulated by Park et al. in their studies and the analogous mechanism proposed by Niederberger et al. [217], can also apply here. Trioctylamine nucleophilically attacks the carboxylic groups of the acetates causing a bimolecular nucleophilic substitution, termed SN_2, which leads to the formation of covalent bonds between cobalt and oxygen atoms [218].

The degree of amine substitution is an important factor in the reaction of these compounds. An increasing of the number of alkyl groups on the amine nitrogen leads to a change the strength of the nucleophilic attack. Higher number of alkyl group gives more electronic charge to the nitrogen making the amine more nucleophilic. However, it also increases the steric disruption, which is unfavorable for the nucleophilic attack. Both phenomena counteract the inductive donor properties of the nitrogen as a nucleophilic atom. Acetate is indeed a good ligand for this process since it is weakly bonded to the metal ion and implies low steric hindrances, which facilitates the mentioned nucleophilic attack. It is difficult and out of scope of this thesis to estimate precisely the difference between the nucleophilic attack between the trioctylamine and cobalt acetate and the previously reported nucleophilic attack of cobalt acetylacetonate in oleylamine, but it will definitely modify the reaction kinetics.

It is worth to mention the fact that amines can not only act as solvents or surfactants, but can even become mild reducing agents in high temperature solution phase synthesis of metal and metal oxide nanoparticles [219]. Such properties are certainly correlated to the specific nature of the target nanomaterial and to the reaction conditions. In the presence of stronger reducing agents, the role of amines is limited to act as a surfactant and/or solvent. However, when the concentration of amines is higher, these compounds can act as reducing agents. For example, pure oleylamine was able to reduced metal oxide fcc-CoO nanoparallelepipeds into pure fcc-Co hollow nanoparallelepipeds [220] and pure cobalt polypod-like structures were also synthesized using oleylamine as reducing agent and cobalt acetate as metal precursor [221]. Magnetite nanocrystals were also produced using oleylamine as reducing agent, stabilizer and co-solvent with benzyl ether, using iron (III) acetylacetonate as metal source [222]. Bimetallic nanoparticles were also produced by this method. For example, monodispersed MPt (M=Fe, Co, Ni, Cu, Zn) nanoparticles where produced by

co-reduction of the metal acetylacetonates with oleylamine at 300°C [223] and FeCo nanoparticles were synthesized by reduction decomposition of iron (III) and Co (II) acetylacetonates in a mixture of oleylamine and oleic acid and 1,2-hexadecanediol.

Though trioctylamine molecules present in the reaction medium can act as a mild reducing agent, the released Co^{2+} ions keep this oxidation state in the final product. In case of reaching the metallic Co^{0} oxidation state, the atoms would easily turn back into Co^{2+} ions due to the oxygen-rich environment favored by the (open-air) reflux. Trioctylamine may however prevent at some extend the further oxidation of these ions to reach the Co^{3+} oxidation state.

In other words, both molecules involved in the main reaction, electrophilic (acetate) and nucleophilic molecule (amine), have been substituted with respect to the corresponding ones used in the mentioned previous studies. Consequently, the nucleophilic attack has been modified, thus altering the kinetic control of the reaction, which plays an important role in the size- and shape-control of the final product as explained in chapter 2.2.

The second key factor that has been modified is the use of an extra capping agent. In this study, oleic acid is used as a stabilizing or capping agent controlling the growth by changing the surface energy of certain crystallographic faces and thus promoting the shape modification of the nanocrystals. The oleic acid molecule, as an amphiphilic compound, possess both hydrophilic (polar) and hydrophobic/lipophilic (apolar) properties (see Figure 5-13). The hydrophilic part of the molecule is a carboxylic group (-COOH), which is negatively charged and coordinates to the surface of the nanoparticles. Certainly, oleic acid is known as a surfactant that binds tightly to the metal nanoparticles surface. The lipophilic group is a large hydrocarbon chain that extends within the solvent and thus determines the stability of the nanoparticles in solution. More detail discussion is given later on.

In this study, the presumably selective adsorption of the oleic acid molecules on the surface of the nanoparticles have directed the growth, ending up with octahedron-shaped particles with eight {111} surface facets since no octahedral shaped nanoparticles were obtained in its absence.

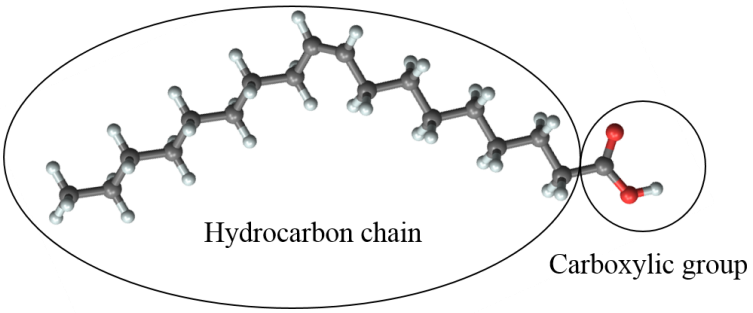

Figure 5-13. Schematics of the oleic acid molecule, which possesses a carboxylic group (-COOH, negatively charged) that coordinates to the nanoparticle surface and a hydrocarbon chain that extends within the solvent and determines the stability of the nanoparticles in solution. The atoms depicted in grey are carbon atoms, the white atoms corresponds to hydrogen and the red ones to oxygen.

Paying attention to the oleic acid molecules; we can consider the negatively charged functional group as electron donating to coordinate to the electron-poor metal atoms at the nanocrystal surface (Co^{2+}). Different crystallographic facets of ionic crystals have different spatial atomic distribution and therefore different polarizabilities. As a consequence, the –COOH groups from the oleic acid can selectively stabilize the (111) planes of the cubic rock salt structure of CoO (containing Co^{2+} cations only) because electrostatically the interaction with the charged {111} facets is favored in comparison to the uncharged {100} facets (containing both Co^{2+} cations and O^{2-} anions). On the other hand, oleic acid is able to modify the free energies of the different crystallographic facets. When oleic acid selectively adheres to {111} facets it decreases their energy and slows down their growth. As studied in reference [17] the surface energy (γ) corresponding to different crystallographic facets follow the sequence: $\gamma\{111\} < \gamma\ \{100\} < \gamma\ \{110\}$, being the {111} facets the ones with lowest surface energy. Facets with higher energy like {100} will grow faster, leading to nanocrystals that are terminated by slow-growing low-energy facets {111}. In other words, oleic acid controls the formation of densely packed {111} outer facets of CoO rock salt structure.

One more parameter that has been changed is the solvent where the reaction takes place. The solvent determines the refluxing temperature and thus the reaction temperature. Comparing with references [191, 201], in which benzylamine was used as a solvent (with a boiling point of 185 °C), we have used trioctylamine that reaches a much higher refluxing temperature (300 °C).

The last parameter that has been changed in comparison with the previous studies was the addition of the precursor at high temperature. In order to favor the production of

nanoparticles with narrow size distributions, it is desirable that nucleation and growth stages take place subsequently in time, situation that can be favored by injecting the precursors into the solvent at high temperature and forcing the chemical process to reach the supersaturation of the monomer in a very short period of time. This process is known as hot injection procedure. The study done by Shukla et al. [26] is a clear example of the significance of the temperature at which the cobalt precursor is added to the reaction mixture on the final cobalt nanoparticle shape. When the cobalt precursor is added at 100 ºC, disk-shaped nanoparticles were obtained. However, when the temperature of injection was 150 ºC, spherical nanoparticles were formed.

Summarizing, these main variations introduced in the synthesis procedure has a drastic impact in the shape of the nanoparticles, leading to an octahedral shape. In the literature there are many other examples of octahedron-shaped nanoparticles of different materials. Fe_3O_4 nanooctahedra (48 nm edge length) were synthesized by thermolysis of iron oleate in the presence of tetraoctylammonium bromide [216], Mn_3O_4 octahedra were produced using a simple hydrothermal method under the help of polyethylene glycol as a reductant and shape-directing agent. WO_3 octahedra with edge lengths 200-400 nm were also synthesized by a solvothermal route with the assistance of urea [224]. Indeed, pure CoO nanooctahedra have been produced using the same metal precursor, cobalt acetate tetrahydrate, in oleylamine [170] and in anhydrous ethanol using polyethylene glycol as surfactant [181]. Pure Co_3O_4 octahedral were also obtained using cobalt chloride in ethylene glycol [176].

Besides changes in nanoparticle shape, size is another key factor that determines the properties of the nanoobjets and thus theirs potential application. The size of the octahedrons can be tuned by changing multiple parameters. Empirically, it was found out that concentration of the precursor in the solution is the key factor to change the size between 40 and 80 nm edge length. When the reaction is carried out using 2.66 mmol of cobalt acetate tetrahydrate, nanoparticles with 40 nm are obtained. However, when 4 mmol are used, the final octahedrons are 80 nm in size.

With the aim of decreasing the size of the CoO octahedrons even further, different (extra) reagents were added. It is known that the combined effects of several surfactants can be much more profound than those of individual contributions [225]. As an example,

Shao and co-workers have controlled the particle size using various surfactant combinations [188]. They prepared cobalt nanoparticles in the presence of various surfactants: oleylamine, trioctylphosphine and oleylamine and trioctylphosphine, oleylamine and oleic acid. These additional surfactants resulted in a decrease in the average particle size from about 200 to 8 nm [188].

Accordingly, the same idea was applied here to reduce the size of the CoO-Co_3O_4 octahedra. For that, trioctylphosphine oxide and oleylamine were added to the reaction mixture as additional surfactants, which cause the reduction of particle size down to 20 nm average edge length. The fact that small sizes were obtained can be mainly attributed to the trioctylphosphine oxide [221]. This surfactant is a high-boiling point molecule with a patulous long chain structure, which provides greater steric hindrance. Consequently, the presence of this capping agent affects the nucleation step, creating a higher amount of nuclei and thus rendering to smaller nanoparticle size.

Summarizing, from the point of view of the chemical reaction, the successful control in terms of size and shape stems directly from the change in the nucleophilic attack and the temperature at which the reaction take place. The dynamic surface solvation process established at this organic – inorganic interface plays also a decisive role.

In order to understand deeply the mechanism involved in the formation and growth of these nanoparticles, the evolution of the morphology and crystallinity of the nanocrystals was closely monitored during the course of a synthesis by ex-situ examination with TEM of the intermediate-products, extracted from the same synthetic batch at different times.

This extra synthesis was done as follows: a mixture of trioctylamine (25 mL) and oleic acid (2.82 mL) was heated up to 180°C using magnetic stirring. Then the precursor solution (4 mmol of Co (II) acetate tetrahydrate dissolved in 5 mL of absolute ethanol) was added drop by drop and the mixture was kept for 30 min at this temperature in order to let the ethanol evaporates. After that, the temperature was increased at the rate of 3°C/min until 300°C. During this time, the color of the reaction mixture changes gradually from yellow to dark brown as explained in subchapter 5.2. The system was left for refluxing for 6 hours at 300°C. Aliquots from the reaction mixture were collected at different times for TEM analysis (0 min, 10 min, 30 min, 1 h, 2 h, 3 h, 4 h and 6 h). Series of snapshots of

nanostructures from the different extracted aliquots is shown in Figure 5-14 (5-15), together with their corresponding electron diffraction patterns and the result of the size distribution analysis.

Time	TEM image (1)	Electron diffraction (2)	Size distribution (3)
a **0 min**	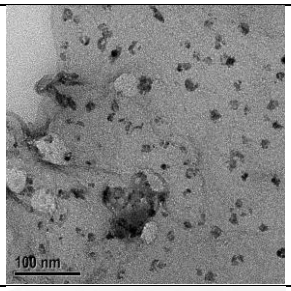		**E_L= 10.4 ± 0.7 nm**
b **10 min**	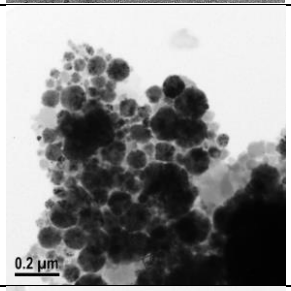		**E_L (1)= 115.8 ± 0.1 nm** **E_L (2)= 49.1 ± 0.8 nm**
c **30 min**	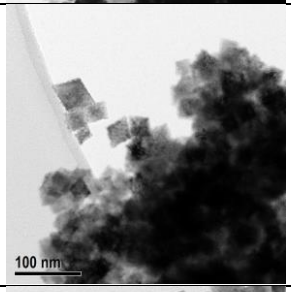	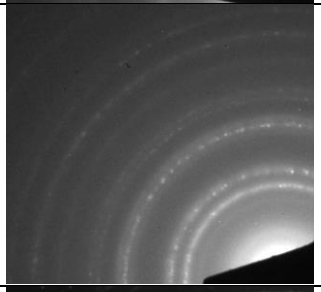	**E_L (1)= 28.0 ± 0.3 nm**
d **1 h**	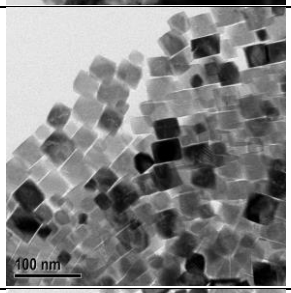		**E_L (1)= 38.3 ± 0.3 nm** **E_L (2)= 20.4 ± 0.5 nm**
e **2h**	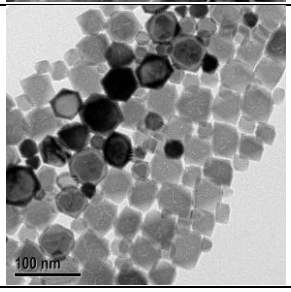	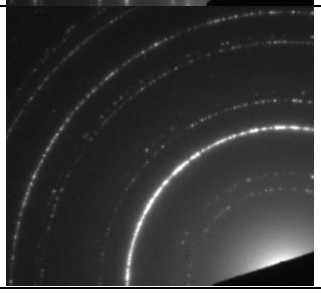	**E_L (1)= 48.4 ± 0.2 nm** **E_L (2)= 25.1 ± 0.4 nm**

Figure 5-14. Growth of octahedral nanoparticles. Image array of bright-field TEM images and electron diffraction patterns of the particles with different reaction duration time. (a 1-3) 0 minutes. (b 1-3) 10 minutes. (c 1-3) 30 minutes. (d 1-3) 1 hour. (e 1-3) 2 hour.

Time	TEM image (1)	Electron diffraction (2)	Size distribution (3)
f **3 min**	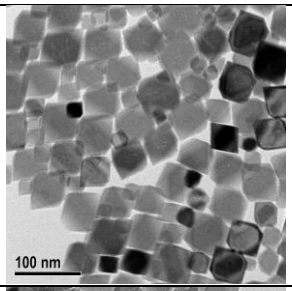	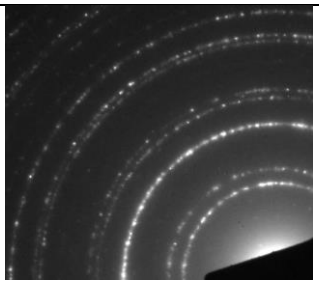	**E_L (1)= 50.4 ± 0.2 nm** **E_L (2)= 28.0 ± 0.5 nm**
g **4 min**	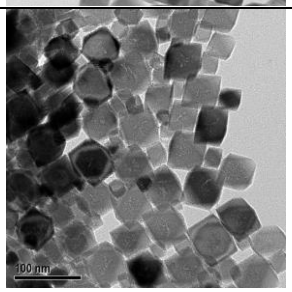		**E_L (1)= 54.7 ± 0.1 nm** **E_L (2)= 27.0 ± 0.3 nm**
h **6 min**	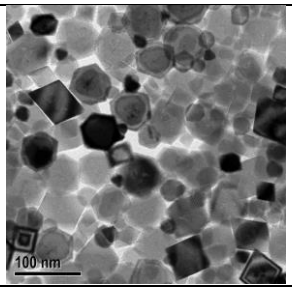	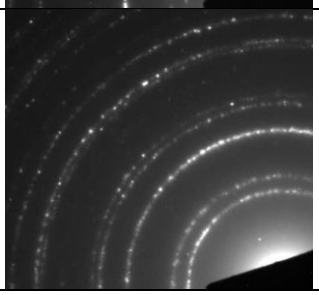	**E_L (1)= 54.6 ± 0.2 nm** **E_L (2)= 26.3 ± 0.5 nm**

Figure 5-15. Growth of octahedral nanoparticles. Image array of bright-field TEM images and electron diffraction patterns of the particles with different reaction duration time. (f 1-3) 3 hours. (g 1-3) 4 hours. (h 1-3) 6 hours.

In the early stages, that is, before the thermal decomposition process (0 min, Fig. (a 1-3)), small precipitates of 10 nm with irregular shapes are formed. The absence of rings in the diffraction pattern indicates that they are not crystalline. After 10 min of reaction (Fig. (b 1-3)), hundreds of fine nanoparticles aggregate to form larger spherical nanoparticles with bimodal distribution of sizes around 49 and 116 nm in diameter. The diffraction pattern indicates the formation of crystallites. At a reaction time of 30 min (Fig. (c 1-3)) nanoparticles with a preoctahedral shape appear, likely as a consequence of the continuous assembly of small crystallites, as clearly seen in Figure 5-16. After 1 hour of reaction (Fig. (d 1-3)), an Ostwald ripening process seems to come into play, since bigger particles have grown at the expense of smaller ones.

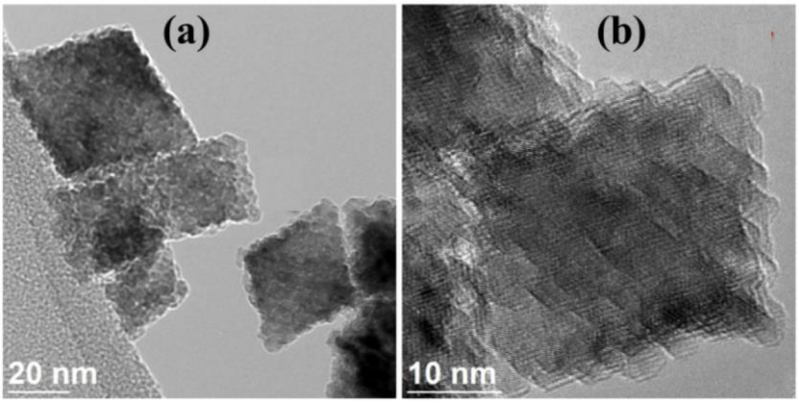

Figure 5-16. Bright-field TEM images of cobalt oxide nanoparticles at the intermediate stage of 60 min of reaction, showing small crystallites self-assemble into an octahedral-shape.

In the mean time, the relatively high temperature of the reflux (300 °C) can facilitate the diffusion of atoms and provide enough thermal energy for the particles to recrystallize, leading to the formation of the observed single-crystal octahedra. Nevertheless, the size distribution is bimodal and crystalline octahedra with average edge length of around 38 and 20 nm are formed. Between 1 and 4 hours of reaction, both population of octahedra grow up to ~ 55 and 27 nm respectively. After 6 h of reaction, the growth stop and the octahedron attain the final size and shape. For all the intermediate products, their corresponding electron diffraction patterns suggest the sequential growth and progressive crystallinity perfection. This growth process resembles the one proposed by Papirer and co-workers who reported a constant number of growing particles during the entire synthetic process [226]. In contrast to the other three reported samples of cobalt oxide octahedral with 20, 40 and 85 nm in average edge length, which possess a relative narrow size distribution, the product of the latter synthesis is more polydisperse, which can be explained through a slower for the larger particles and faster growth process of the small particles, as suggested by Reiss [227].

To put it briefly, these results indicate that the growth of single-crystalline octahedra can be attributed to cooperation of two principal mechanisms: oriented aggregation and Ostwald ripening. Accordingly, small crystallites aggregate and then, the resulting aggregates fuse into a single crystal, via Ostwald ripening [228, 229]. These results demonstrate the importance of the oleic acid in the reaction since it avoids a fast and random aggregation of small crystallites and tailor subsequently the morphology according to a certain crystal plane for crystal growth.

Paying attention to the general description of synthesis of nanoparticles in solution,

the mechanism of formation of the cobalt oxide nanooctahedra is described as follows: the main chemical reaction is based on the thermal decomposition of cobalt (II) acetate tetrahydrate, used as metal-precursor to provide the –Co–O– "monomer". When the concentration of –Co–O– "monomers" reach the supersaturation level, monomers form assembles so that nucleation starts. The subsequent growth of these nuclei, which takes place by the addition of more monomers, is controlled by the present oleic acid molecules in solution, ending up with an octahedron-shaped nanoparticles.

However, the structural characterization have shown a core-shell structure with a CoO core and Co_3O_4 shell, pointing to further oxidation of the nanoparticle surface to Co_3O_4 at ambient conditions, which is indeed the most thermodynamically stable phase [215]. The surface oxidation of CoO nanoparticles to Co_3O_4 has been investigated previously by Soriano et al. [230]. They have shown that the surface of CoO nanoparticles appears oxidized up to Co_3O_4 and annealing in ultrahigh vacuum reduces the surface of the nanoparticles to the CoO. Chaudret and co-workers monitored the progress of the oxidation reaction with temperature [194]. They found out that the CoO rock salt structure remains, mainly after heat treatment at 95ºC for 24 hours. However, when the CoO nanoparticles were heated at 130ºC for 14 days, the pure spinel oxide Co_3O_4 is reached. A study by Manouchehri et al. have on the other hand demonstrated the result of partial oxidation of as-prepared CoO nanoparticles to form CoO-Co_3O_4 [231]. Similar behavior is observed in the present case of CoO-Co_3O_4 octahedra and thus, a core-shell growth model can be derived, involving an initial growth of CoO clusters mediated by surfactants, which self-assemble forming octahedral nanocrystals, and the subsequent formation of Co_3O_4 shell that result from continuing oxidation of pre-formed CoO core at ambient conditions.

Oxidation is a common nanoparticle conversion chemical reaction. Several theories explain the oxidation of metals. Among them Cabrera-Mott theory [232, 233, 234, 235, 236], Wagner theory [237], and the logarithmic rate expression of Jia [238], can be emphasized. Cabrera-Mott theory is the most widely applied theory to explain the oxidation of nanoparticles but in principle it is only valid to explain the low-temperature oxidation of a thin oxide layer up to ~ 3 nm and relies upon several assumptions that limit its scope. Beyond this initial oxidation and at sufficiently high temperatures, oxidation can also proceed according to other diffusion mechanisms. Furthermore, the mechanism of initial oxidation does not depend on size, which is actually experimentally observed in the samples herein

studied (20, 40 and 85 nm average edge length) since the oxide layer in all the samples has the same thickness (~ 2-4 nm).

In the Cabrera-Mott theory, the first stage of oxidation involves adsorption of the oxygen molecule on the metal surface. This is considered to involve dissociation and at least partial ionization of oxygen followed by the incorporation of oxygen into the metal surface. The initial oxidation is completed when a continuous thin layer of stable oxide is formed. Then, it is assumed that electrons from the inner region of the nanoparticle can rapidly tunnel through the oxide layer to ionize the oxygen at the outer surface. This ionization creates a strong electric field across the oxide film, which drives cation diffusion outwards. The Cabrera-Mott model predicts that the oxidation to be very fast first to then slow down significantly as the oxide layer grows thicker, because the electrical field depends inversely on the layer thickness.

For all mentioned above, Cabrera-Mott theory can be applied here to explain the formation of the Co_3O_4 shell on the CoO surface forming the CoO-Co_3O_4 nanocrystals. The oxide-I/oxide-II system can be seen as an analogy of the metal/oxide system (described in Cabrera-Mott theory) with differences in terms of the oxidation states of the constituents.

Another structural feature worth to analyze in these nanocrystals is the presence of many small voids inside the octahedral nanoparticles and located around a main and centered cavity (5-10 nm in diameter). To determine unambiguously the reason for the presence of voids inside the octahedra is out of the scope of this work but nevertheless, some notes can be pointed out. Several theories can be applied to describe nanostructural changes in nanoparticles that accompany oxidation and the resulting formation of voids inside nanoparticles. As mentioned, the oxidation conditions and nanoparticle properties (composition, size, shape) give rise to different regimes of oxidation behavior and determine the composition and structure of intermediates and the final product, such as whether voids form and how they are arranged.

The Kinkendall effect has been usually used to explain the formation mechanism of hollow structures, where the outward diffusion of metal cations from the core is faster than the simultaneous inward diffusion of reactive species into the nanoparticles, resulting in

void formation [239, 240, 241]. In other words, the void formation is the result of the imbalance of diffusion rates. This effect was initially described for nanoscale systems by Alivisatos et al., whom studied how Co nanoparticles react with oxygen, sulphur, and selenium and the influence of these reactions in particle morphology [242, 243]. In such cases, the reaction of colloidal cobalt and molecular sulphur produced similar multiple void formation within each nanocrystals as observed herein in the cobalt oxide nanooctahedra, and attributed to the low vacancies mobility. Further increase in the temperature and/or longer reaction time would lead to coalescence of voids [242].

Other void formation mechanisms have been suggested [244, 245, 246, 247], such as the one by Zhang and co-workers, who proposed a surface-energy-driven mechanism as responsible for the formation of hollow iron based nanooctahedra [245]. In the initial stage of particle formation, concaved nanooctahedra are formed with high surface-energy faces. These octahedra have an average side length of 150 nm and they are composed of many small crystallites of 10 nm in diameter. The surface of the sample can be visualized as an octahedron with a trigonal pyramid excavated at the center of each fac. They suggested that over time and as the reaction proceeds, an inside-out formation process (solid evacuation) takes place to reduce their high surface energy. In this process, the inner small crystallites dissolve, migrate out, and redeposite on the octahedral frame, leading to the formation of hollow octahedral nanostructures with an average edge of 240 nm and flat surfaces.

The galvanic replacement process is an alternative option for producing hollow nanostructures. Even though these reactions have been initially limited to the chemical transformation of metallic nanostructures [248, 249, 250], galvanic exchange reactions in metal oxide nanocrystals have been demonstrated as well [251]. These reactions involve a corrosion process that is driven by the difference in the electrochemical potentials of two metallic species. In these reactions, metal nanoparticles react with noble metal salts, taking advantage of a redox reaction that favors the reduction and deposition of the noble metal (alloying) and the oxidation and dissolution of the template metal (dealloying), thus creating a hollow interior. Notable results have been reported from the Hyeon group [251], who demonstrated that a galvanic replacement reaction can occur in oxide nanocrystals too. Indeed, they have demonstrated that Mn_3O_4 square prism-shaped nanocrystals can be completely transformed into hollow γ-Fe_2O_3 nanocages by using an iron (II) perchlorate solution.

In the case herein studied, we have discarded all the mentioned options but the Kirkendall effect, which is considered the cause of the presence of voids in the octahedra.

The small voids mentioned are only present in the samples of 40 and 85 nm in average edge length but not in the 20 nm edge length octahedra. The main difference in the synthetic procedure of the two first samples compared to the one of the 20 nm average edge length octahedral nanoparticles, is the hot-injection issue already described, in which the cobalt precursor was injected into the hot mixture solution of solvent and surfactants. This is the key to understand the presence of voids only in the bigger 40 and 85 nm particles, since implies that the reaction was completed under a kinetic instead of thermodynamic control, so that voids are formed.

In a kinetically controlled process, an organometallic intermediate phase would match the premises for creating some kind of porosity using a chemical gradient, because according to Smigelkas and Kirkendall solid diffusion in a concentration gradient occurs through a vacancy exchange mechanism [252]. Since the diffusion coefficient of the two species (the intermediate organometallic compound and the CoO) is different, the net directional flow of vacancies results in the formation of pores, with the outward diffusion of the core material, likely the intermediate organometallic compound trapped during the growth process inside the CoO lattice, being faster than the CoO inward diffusion. Likewise, this process is slightly thermally activated as well. The creation of atomic vacancies by their outward diffusion of the organometallic compound will lead to vacancy clusters inside the nanoparticles and due to the limited volume, will eventually condense to form small voids. Gösele and co-workers claimed a general fabrication route for hollow nanostructures provided that the Kirkendall effect should be generic [253, 254, 255], and Dilger et al. reported a similar case for the synthesis of aerogel-like ZnO with organometallic methylzinc methoxyethoxide and ZnO [256]. Mourdikoudis et al. and Chernavskii and co-workers also observed the void formation in cobalt oxide supported on cobalt nanoparticles [221, 257, 258].

In the whole synthetic process it can be reasonably point out the formation of voids once the CoO nanoparticles were formed but before becoming oxidized when exposed to atmospheric conditions for adopting the core/shell morphology.

To put it briefly, this section can be summarized as following. Based on the structural

and chemical analysis of the samples and taking into consideration many criteria, including the reaction synthesis, progress of crystal growth at intermediate stages of the process and final attained morphology, the mechanism of formation and growth of these crystals has been proposed. The successful control in terms of size and shape of the octahedral nanocrystals stems directly from the dynamic surface solvation established at this organic – inorganic interface at the reaction conditions, which have been modified as compared to previous work, in combination with Ostwald ripening process of initially formed crystals. The formation of Co_3O_4 on the nanoparticles surface is described as the result of the partial oxidation of CoO at ambient conditions and can be understood in terms of Cabrera-Mott theory, while the presence of voids inside the crystals are a consequence of the Kirkendall effect.

5.7 Ferromagnetism at room temperature

After cooling, the dispersed particles did not show a tendency to stick on the magnet which was used for stirring. However, when a NdFeB magnet was placed in the surroundings (in touch with the sample vial), these nominally antiferromagnetic nanoparticles moved in magnetic field gradients at room temperature, indicating their rather ferromagnetic character well above the magnetic ordering temperatures of both present oxides: CoO (with a Néel temperature of T_{N1} = 291 K) and Co_3O_4 (T_{N2} = 40 K).

To study their magnetic response in detail, a superconducting quantum interference device (SQUID) magnetometer was used. The data were acquired from dried powders of nanoparticles fixed in a gelatin capsule.

Figure 5-17 shows the magnetization curves of the 20, 40, and 85 nm octahedral particles as a function of the applied magnetic field recorded at 300 K. The shape of the M(H) curves clearly indicates the presence of different magnetic phases. The linear increase of the magnetization with increasing field above 1 T, and the unsaturated magnetization at magnetic fields up to 5 T are a response of paramagnetic and also antiferromagnetic phases. The two present oxides in the nanoparticles, CoO and Co_3O_4, are expected to give such linear field-dependent magnetic response. But surprisingly, all three samples show an irreversible magnetization point and a well-defined hysteresis at 300 K (see panel (b)), veri-

fying the ferri- or ferromagnetic response above the magnetic ordering temperatures (paramagnetic regime) of CoO and Co_3O_4. Moreover, based on the chemical synthesis route and on preliminary structural and chemical analysis, the presence of metallic cobalt as the origin for the observed ferromagnetism can be excluded.

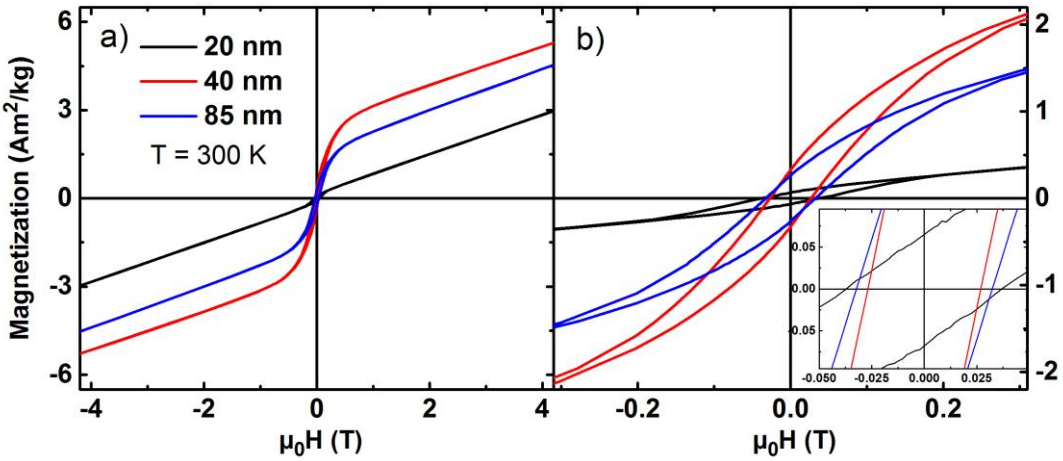

Figure 5-17. Magnetization of the 20 (black), 40 (red) and 85 nm (blue) samples as a function of the applied field at 300 K (a) along with a magnified area around the origin (b and inset in b).

Coercive fields of $\mu_0 H_C$ = 370, 290, and 320 mT are measured for 20, 40, and 85 nm samples, respectively. The error bar is 10%. The intrinsic magnetization was determined by extrapolation of the linear part of the M(H) curve to zero field and the saturation magnetization of the samples are 0.165 $A \cdot m^2/kg$ (20 nm) 2.4 $A \cdot m^2/kg$ (40 nm) and 1.6 $A \cdot m^2/kg$ (85 nm). For the different samples, the slope of the M(H) curve, that is the mass susceptibility, is the same (8-9·10^{-7} m^3/kg) within the error bar indicating that the contribution of the antiferromagnetic and/or paramagnetic phase is size independent. It is seen that the room temperature saturation magnetization as well as the coercive field do not increase along with average particle size.

The nonmonotonous values of coercive field as increasing size can stem from the different contributions of magnetic anisotropy present in these nanocrystals (Eq. 2-5), such as surface anisotropy (changing monotonously) and magnetostriction effects (changing nonmonotonously), which vary with the octahedron average edge length. With increasing size, the configuration of magnetic domains as well as the domain reversal mechanism, which determine the effective coercive field, can change in the nanocrystals and thus cannot be predicted by simple arguments. Similar nonmonotonic behavior is observed in this PhD

thesis, in the study of FeCo nanowires (chapter 3), where theoretical simulations were accomplished in the literature to predict the domain reversal mechanism. The nonmonotonic change determination of this magnetic response with particle size is out of the scope of this thesis.

Another clear evidence for the room temperature ferromagnetic response of the samples is provided by the zero-field cooled (ZFC) and the field-cooled (FC) magnetization as a function of temperature from 5 up to 370 K for the 20 and 40 nm samples, as shown in Figure 5-18.

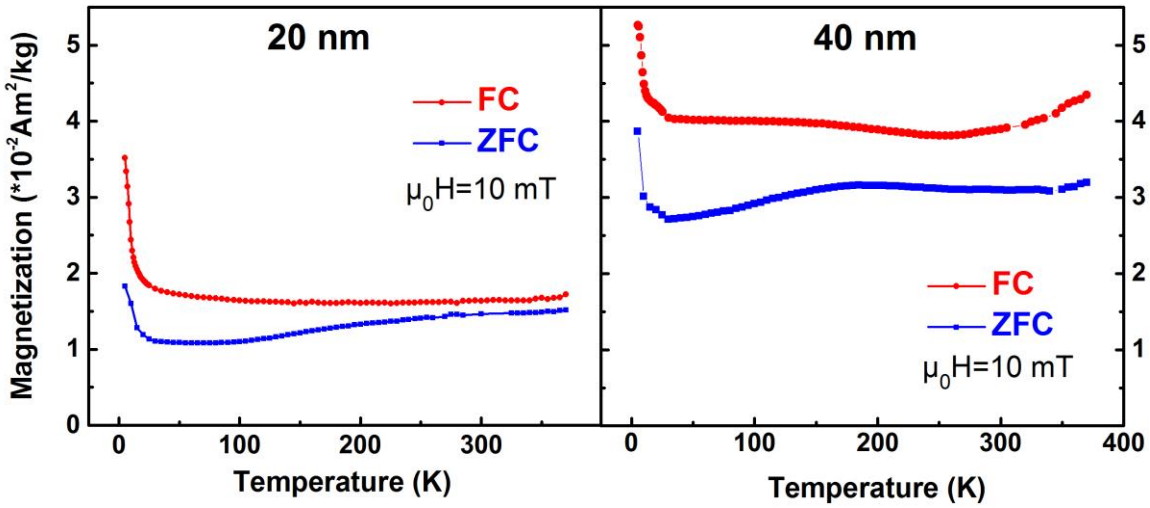

Figure 5-18. Temperature dependence of ZFC-FC (blue-red) magnetization of the 20 nm (left) and 40 nm (right) samples. The measuring and cooling field is 10 mT.

For the ZFC measurements, the sample was cooled without an external magnetic field from 370 to 5 K, then a magnetic field of 10 mT was applied and the magnetization of the sample was measured with increasing temperature. For FC measurements, the sample was cooled in a magnetic field of 10 mT from 370 to 5 K, and then the magnetization was measured at 10 mT with increasing temperature. A distinct difference between ZFC and FC magnetization is observed in the whole measured temperature range, which is a characteristic feature of the presence of a ferromagnetic phase in the system. No evidence for superparamagnetism such as a maximum in the temperature dependence of the magnetization is observed when measured in a low field of 10 mT.

Nevertheless, the temperature dependence of the high-field susceptibility (Figure 5-19), determined by the slope of M(H) curves, in fields between 2 and 3 T shows a characteristic maximum at T = 285 K (indicated in the graph by a vertical grey dotted line),

really close to the Néel temperature of bulk CoO for all three samples, although shifted to lower values when decreasing the average particle size. These differences can be justified considering the different surface/volume ratio of the samples and hence the role of the surface. These temperature dependent magnetic data confirm the presence of the antiferromagnetic CoO and no obvious maxima near the Néel temperature of Co_3O_4 (T_{N2} = 40 K) are observed.

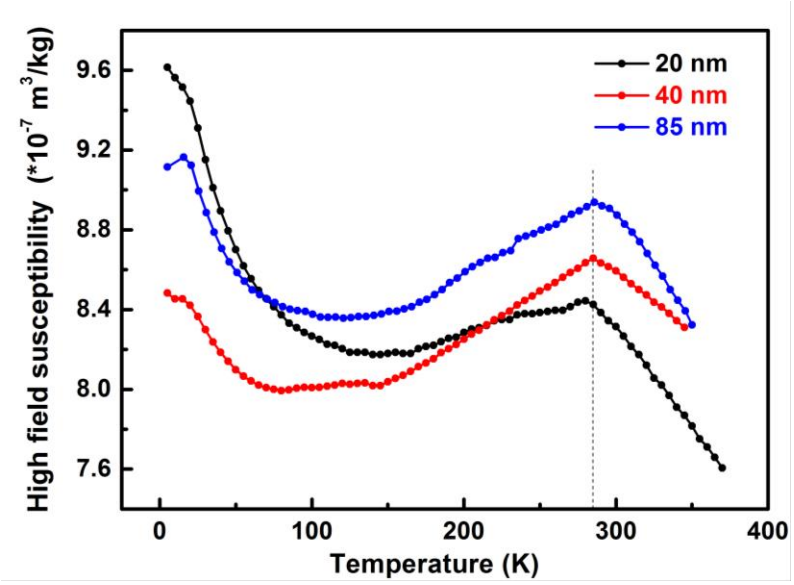

Figure 5-19. Temperature dependence of the high-field magnetic mass susceptibility of the 20, 40 and 85 nm sample. The three samples shows a characteristic maximum at T ~ 285 K (dashed line helps for the eye). The dash lines indicate the Neel temperature T_N around 290 K, which is the typical T_N for bulk CoO.

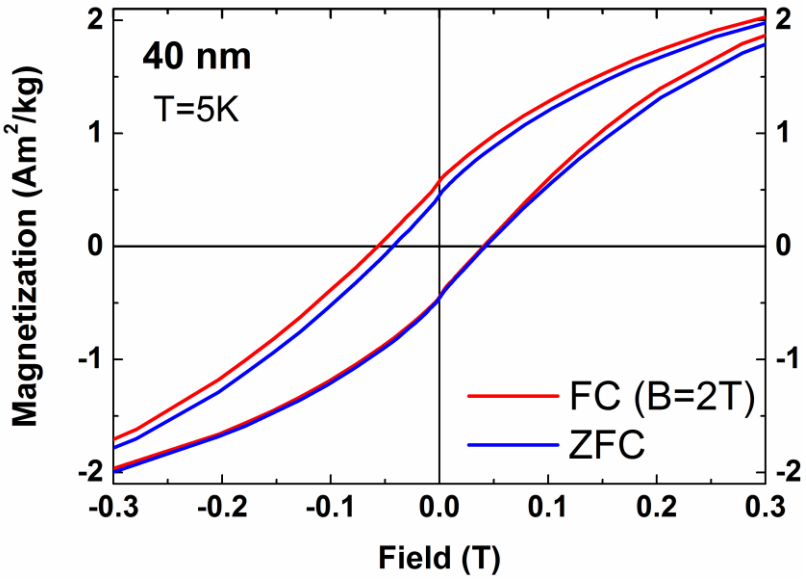

Figure 5-20. ZFC (blue) and FC (red) hysteresis loops of 40 nm sample at 5K. For the FC hysteresis loop, the sample was cooled in a magnetic field of 2 T.

Another unambiguous proof for the existence of an interface between a ferromagnetic and antiferromagnetic components is the observation of an exchange bias field H_{EB} at lower temperatures seen as the horizontal and vertical shift of the hysteresis curves after field cooling (FC) compared to the ZFC loop (Figure 5-20), along with the coercive field enhancement. This unidirectional anisotropy arise from interfacial magnetic moment pinned between antiferromagnetic and ferromagnetic components.

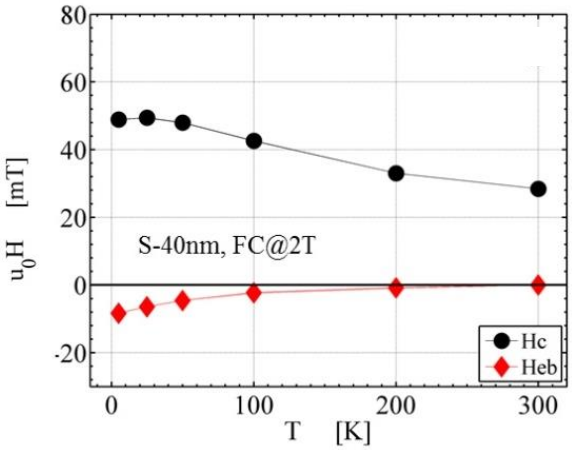

Figure 5-21. Temperature dependence of coercive field (FC) and exchange bias field of the 40 nm sample. For the FC hysteresis loop, the sample was cooled in a magnetic field of 2 T.

To trace the exchange bias effect, several hysteresis curves were measured at different temperatures and the temperature dependence of the coercive field and exchange bias field was evaluated. Figure 5-21 shows the temperature dependence of the coercive field and exchange bias field for the 40 nm sample. The temperature-dependence of the exchange bias field (red) shows that the exchange bias is prominent at temperatures at least 100 K and vanishes above the Néel temperature of CoO (T_{N1} = 291 K), while the coercive field is still larger than about 30 mT. Therefore, it is reasonable to suggest that the ferromagnetic component is adjacent to the CoO core forming a ferromagnetic-antiferromagnetic interface.

The coercive field dependence shows a maximum near or below T = 50 K in all the three cases, fairly close to the Néel temperature of Co_3O_4. Larger coercive fields are exhibited by the 20 nm average edge octahedral, compared to the 40 nm and 85 nm samples likely due to the increased surface-to-volume ratio as decreasing size.

The reduced mass normalized saturation magnetization M_S measured for the 40 nm

octahedra (2.60 Am^2/kg at 300 K) in comparison to the 85 nm octahedra (1.58 Am^2/kg at 300 K) indicates that a surface or interface contribution is the origin the ferromagnetic response.

The origin of a ferromagnetic response in a temperature range where the two constituents bulk phases are paramagnetic is not understood yet.

Néel in 1961 suggested that small antiferromagnetic nanoparticles should exhibit superparamagnetism or weak ferromagnetism [259]. He proposed a model for antiferromagnetic nanoparticles based on the presence of two sublattices, one with spins up and another with spins down at the surface. Any imbalance in the number of spins at the surface is the origin of a net magnetic moment in "antiferromagnetic" nanoparticles below the ordering temperatures. Naturally, the magnetic behavior of CoO nanoparticles was widely studied in the next half a century but the origin of room temperature ferromagnetic response for the CoO nanostructures still controversial. Indeed, since then large magnetic moment in antiferromagnetic nanoparticles have been observed [260, 261, 262, 263]. However, it also exhibits anomalous magnetic properties such as large coercivities and loop shifts up to several tens of mT. This behavior is difficult to understand in terms of 2-sublattice antiferromagnetic ordering which is accepted for bulk materials. According to Kodama et al. [264], the reduced coordination of the surface spins in nanoparticles might result in a stabilization of multi-sublattice configurations with respect to the classical 2-sublattice one. These additional sublattices disturb the otherwise compensated antiferromagnetic bulk structure and lead to numerous effects including hysteresis and shift of hysteresis loops [264].

However and in most cases, researchers impute the presence of ferromagnetism to the existence of uncompensated surface spins on the nanoparticle surface [265, 200, 184, 186]. Wdowik et al. have stated that cation vacancies can account for the ferromagnetic properties of CoO based on first principle calculations [266]. Dutta et al. studied the ferromagnetic property of pure CoO nanoparticles after annealing the precursor under nitrogen atmosphere and they attributed the present of ferromagnetism to anionic vacancies uncompensated surface spins [267]. Moreover, Yang and co-workers also support that the ferromagnetism of vacuum-annealed CoO nanoparticles is due to oxygen vacancies at the surface and the ferromagnetic response intensity is proportional to the concentration of oxygen vacancies [268]. Following this line, the uncompensated magnetic moments in the ~ 4 nm

thick antiferromagnetic Co_3O_4 surface layer could be assumed as a likely source of the observed ferromagnetism but the CoO-Co_3O_4 core-shell nanooctahedra possess a hetero-interface between these two phases. Thus, the origin of a quasi-two-dimensional long-range ferromagnetic order persisting in a temperature range where the antiferromagnetic CoO and Co_3O_4 bulk phases are paramagnetic is not explained by these statements.

The interesting question arises if ferromagnetic order can be stabilized between two simple antiferromagnets like CoO and Co_3O_4, both of which are antiferromagnets with ordering temperatures of 291 K [269] and 40K [270], respectively. Interestingly, a lamellar ferromagnetic order at intergrowths of antiferromagnetic hematite (Fe_2O_3) and para/antiferromagnetic ilmenite ($FeTiO_3$) has been reported [271, 272]. In the later references, the charge imbalance at the interface between two oxides (often accompanied by local distortions) can induce charge transfer processes and change the bond-angles between ions, which causes the ferromagnetic response. These effects modify the competing ferromagnetic and antiferromagnetic interactions (superexchange and double exchange) in antiferromagnets as described by the so called Goodenough-Kanamori-Anderson rules [273].

To put light in this fact and by making use of the geometrical relationship between the rock salt-spinel crystal structures and the octahedral morphology, the expected magnetization of ferromagnetic single and double surface or interface layer of Co^{2+} ions have been calculated for the sample of 40 nm octahedrons. The calculated and experimental saturation magnetization values are in good agreement for the single layer approach, confirming that the ferromagnetism is associated with the interface [274].

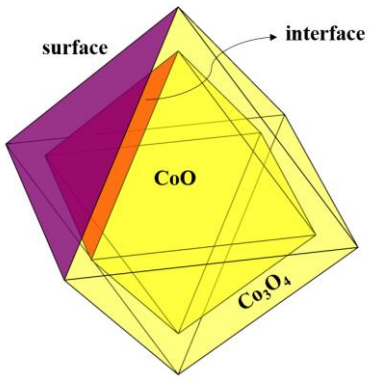

Figure 5-22. Sketch of a well-defined regular octahedron with highly symmetrical shape and sharp edges as well as smooth surfaces limited by {111} facets (purple). They are composed of several tens nm-sized CoO core and 2-4 nm thick Co_3O_4 shell in contact by an interface (orange).

Thus, the detailed interfacial structure is of particular interest in order to clarify even further the origin of the ferromagnetism. The exact atomically identified interface is difficult to obtain partly due to the intricate HRTEM imaging formation that is highly depending on focus and aberration parameters, and partly due to the core-shell structure of overlapping CoO and Co_3O_4 giving rise to Moiré pattern as shown in Figure 5-11 and sketch in Figure 5-22.

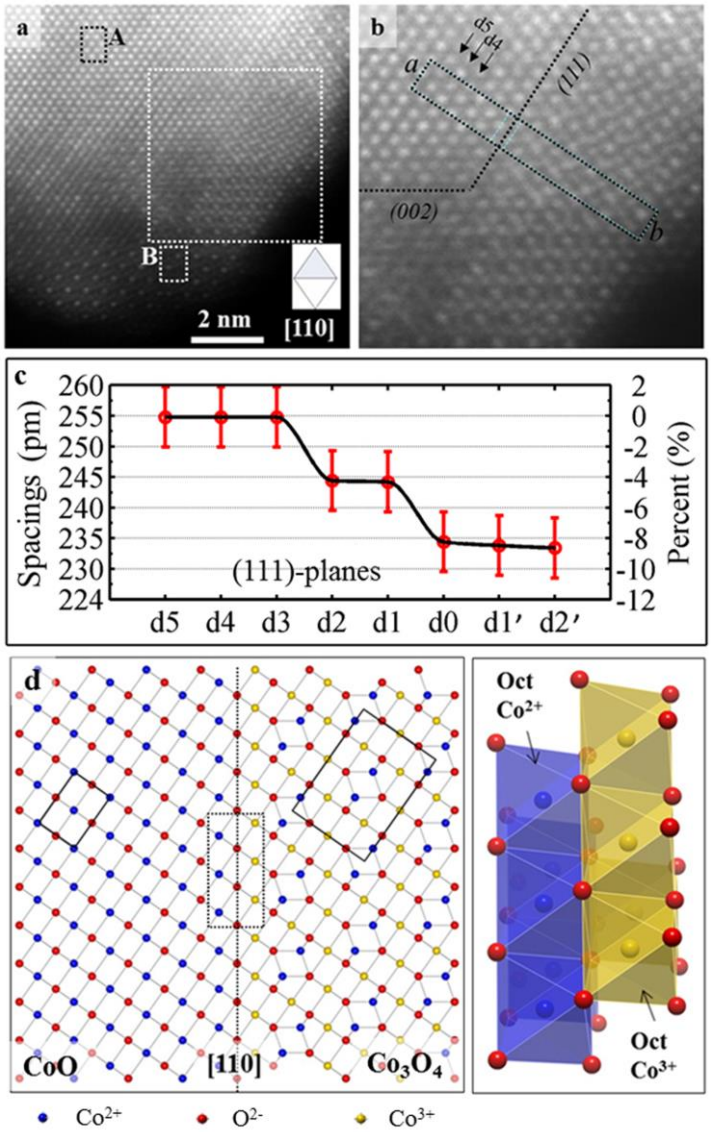

Figure 5-23. (a) Atom-column-resolved STEM-HAADF image of a single octahedral cobalt oxide nanocrystal edge. The core region (A) and the shell region (B) exhibit contrast characteristic of [1-10]-oriented CoO and Co_3O_4 respectively. (b) Enlargement of the interfacial area. (c) Measured (111) lattice plane spacings as a function of spacing number near the interface. ''d0'' denotes the spacing indicated by the dashed line in b. (d) Atomic model showing an epitaxial (111) interface structures between CoO and Co_3O_4 viewed along [110]. A (111)-type common plane of oxygen ions is indicated by a dashed line. The unit cells of [110]-oriented CoO and Co_3O_4 are outlined by solid boxes. The interfacial oxygen plane is connected to octahedral Co^{3+} ions in Co_3O_4 and to octahedral Co^{2+} ions in CoO. The interfacial Co-O configurations are shown in the form of Co-O polyhedra.

Nevertheless, one can approximate the interface with the change in lattice patterns measuring the intensity variation in high resolution HAADF images (Figure 5-23 (a) and (b)). The rectangular *a-b* area shown in Figure 5-23 (b) was selected for intensity profile analysis and indicates a clear intensity variation that reflects structure and chemistry differences across the interface boundaries. By using the CoO core as a reference, the variations of the (111) plane lattice spacing in the CoO-Co_3O_4 have been measured (Figure 5-23 (c)). The measurements revealed a progressive decrease in lattice spacing from the core to the surface by such as 8%, suggesting the presence of large strain in the interface region. The Co_3O_4 plane spacing is bulk-like and stays unchanged (235 pm) [208]. In other words, the CoO spacing is strongly compressed at the interface and relaxes towards the core within three to four layers compared to its respective bulk value.

Based on the obtained detailed atomistic information provided from the thorough TEM analysis concerning the epitaxial formation of (111) Co_3O_4 shell on CoO, the atomic structure of the CoO-Co_3O_4 (111) interface was reconstructed as shown in Figure 5-23 (d).

Density functional theory calculations with an on-site Coulomb repulsion parameter were performed to calculate the lattice spacing at the interface of both oxides. Even though this work is out of the scope of this thesis, it is worth to mention the main conclusions (see ref. [274]). It was suggested that it is possible to achieve long-range ferromagnetic order with a high Curie temperature when the Co^{2+} cations occupying the octahedral sites couple with the Co^{2+} cations occupying the tetrahedral sites on both sides of the epitaxial interface. In other words, occurrence of magnetic order even above the high Néel temperature of the antiferromagnets can be attributed to the charge transfer process of Co^{3+} to Co^{2+} at the (111) CoO-Co_3O_4 interface, which modify the relative strengths of the inherent ferromagnetic double exchange and antiferromagnetic superexchange.

5.8 Conclusions

A new synthetic procedure has been develop to synthesize CoO-Co_3O_4 core-shell polyhedra. On the basis of all the morphological, chemical and structural information, the particles are indeed well-defined regular octahedral with highly symmetrical shape and exhibit sharp edges as well as smooth surfaces limited by {111} facets. They are composed of several tens nm-sized CoO core and 2-4 nm thick Co_3O_4 shell. A core-shell growth model

has been proposed, which involves an initial nucleation of CoO clusters, subsequent growth mediated by the oleic acid capping agent and final rearrangement to reach the octahedral shape, which then become oxidized to Co_3O_4 when exposed to the atmosphere. A long range ferromagnetic response was observed in all the samples up to 400 K, which was attributed to the interface between the crystalline ~ 4 nm thick spinel-type Co_3O_4 surface layer and the crystalline CoO (rock salt structure). It was proven that the epitaxial interface forms at the eight (111) facets is heavily strained, and it was suggested that a charge transfer process (partial reduction) of Co^{3+} to Co^{2+} at the CoO-Co_3O_4 interface is the origin of the experimentally observed ferromagnetic phase. Finally, due to the attained morphology, these nanoparticles could be good candidates as anode materials in lithium-ion batteries or might be useful as well for methane catalytic combustion reactions.

6 General conclusions

In the course of this dissertation, new cobalt-based magnetic nanostructures have been synthesized to improve their performance. In chapter 3 and 4, two different systems have been studied in detail for the enhanced performance of rare-earth-free permanent magnets based on 3*d* metal nanowires. For a higher magnetic energy product, the materials and growth modes have been designed to reach a high effective magnetic anisotropy energy density. This goal is reached by exploiting the shape anisotropy of highly elongated nanostructures and aligning the easy axis determined by the magnetocrystalline and the exchange anisotropy parallel to the wire axis.

This novel approach for magnetic hardening was successfully applied to $Fe_{30}Co_{70}$ nanowires electroplated in an anodic aluminum oxide template. It turned out that the partial removal of the template leads to surface oxidized tips. This ferrimagnetic FeCo oxide layer suppresses the vortex formation and domain wall nucleation at the tips, leading to an increase of the coercive field (up to 20% at T=10 K). In agreement with micromagnetic simulations, these findings experimentally confirm that the magnetization reversal in magnetic nanowires, even with large aspect ratios, occur through nucleation at the tip and domain wall propagation. Interestingly, the coercive field does not rise when only one tip of the nanowires is coated with ferri- or antiferromagnets, verifying that a domain wall nucleates at the magnetically weaker tip. Both tips of the magnetic nanowires must be covered with an antiferromagnet material for an effective growth of the energy product.

In the second study, $Co_{80}Ni_{20}$ nanorods with average length of 53 nm and diameter of 7 nm were successfully prepared to judge their potential in permanent magnet applica-

tions. The stoichiometry has been chosen to exploit the highest magnetocrystalline anisotropy among the 3d-elements, the still large magnetization at low Ni content, and the good long-term stability of CoNi alloys. The rods possess a core-shell morphology consisting of a metallic hcp CoNi core and a fcc Co-rich oxide shell (1-2 nm thick). This shell has grown epitaxially on the surface of the metallic core by natural oxidation, forming a passivating layer.

The related crystallographic growth between the ferromagnetic core and the antiferromagnet shell has a strong impact on the magnetic properties. An infrequent temperature dependence of the surprisingly high coercive field ($\mu_0 H_C$ = 0.3 T at T = 5 K) is observed. After monotonous decreases, the coercive field increases again at the intermediate temperature range (175 K < T < 250 K) and reaches a local maximum at 250 K. This behaviour has only been observed in systems with a directed oxide growth and clearly reflects the high structural quality of the prepared nanorods. Its origin is the relative (mis)alignment of the ferromagnetic and antiferromagnetic spins at the interface that decreases with increasing temperature and vanishes above the superparamagnetic blocking temperature of the shell grains. These results prove that a strong magnetic hardening is promoted by exchange anisotropy due to the alignment of anisotropy axes of the ferromagnetic core and the antiferromagnetic shell.

In comparison with a previous study on Co/CoO core-shell rods, the admixture of Ni to the system shifts the Néel temperature of the antiferromagnet by nearly 100 K, close to ambient temperature. Thus, this strategy demonstrates that the admixture of Ni to pure Co nanorods, not only improves the corrosion resistance but also enhances the critical temperature close to ambient temperature. Further fine tuning would lead to nanorods with optimized properties at 300 K.

In chapter 5, cobalt oxide nanoparticles have been studied for considering them as good anode materials in lithium-ion batteries, gas sensors, or catalysts in methane combustion reactions. A new synthetic procedure has been developed to master the magnetic properties of cobalt oxide nanocrystals. The precise control of the synthesis parameters leads to CoO-Co_3O_4 core-shell nanoparticles with highly symmetrical octahedral shape terminated by {111} facets. This study illustrates that the precise control of the synthesis parameters in colloidal chemistry can lead to well-defined morphologies with sharp edges and nearly

atomically flat surfaces, what is essential for ultimate applications.

These nanocrystals are composed of a CoO core of several tens of nm and a 2-4 nm thick Co_3O_4 shell. Interestingly, the interface between these two oxides is heavily strained and gives rise to a long-range ferromagnetic order at the interface up to at least 400 K, well above the antiferromagnetic ordering temperature of both oxides. This unusual behaviour is attributed to the charge transfer process (partial reduction) of Co^{3+} to Co^{2+} at the (111) CoO-Co_3O_4 interface, which modifies the relative strengths of the inherent ferromagnetic double exchange and antiferromagnetic superexchange. This research illustrates the potential of finding new magnetic phenomena at the nanoscale.

7 Appendix

Appendix I: Alignment of CoNi rods

The magnetic properties of $Co_{80}Ni_{20}$ nanorods as powdered sample have been described in section 4.5. Although the main focus is the structural and magnetic characterization of the anisotropic nanoparticles, an extra effort was carried out to align these nanorods in a matrix. The aim in this kind of experiment is to study if the magnetic properties can be optimized by aligning these rods in a composite material, in a way to study potential applications using them as building units in rare-earth free bonded magnets [275]. A higher magnetic ordering is caused by the dipole-dipole interaction between the individual rods [276], and the process of alignment as well as the magnetic properties attained in these ensembles, are briefly discussed in this appendix.

Two different approaches were carried out in order to form aligned $Co_{80}Ni_{20}$ nanorods ensembles: two- and three-dimensional alignment. In both cases, the alignment of the magnetic nanoobjects was induced by the application of a homogeneous magnetic field [277], which causes the interaction of every individual nanorod dipole moment.

In the two-dimensional approach, the nanorods have been aligned on 4 x 4 mm boron-doped silicon substrates by magnetophoretic deposition [150, 151]. The field was generated by an electromagnet applying a uniform magnetic field of 1.2 T. Different process parameters have been optimized, including the type of substrates, field strength, concentration of the particle solution, type of solvent as well as the amount of solution dropped on the substrate. For further details, see [278]. Figure 7-1 (a) shows a SEM image of $Co_{80}Ni_{20}$ nanorods, aligned on a silicon substrate by magnetophoretic deposition. It can be seen that the nanorods align along the applied magnetic field direction to a great extent. Panel (b) shows a bright-field TEM image of the CoNi nanorods sample deposited on a carbon coated TEM grid under similar experimental conditions.

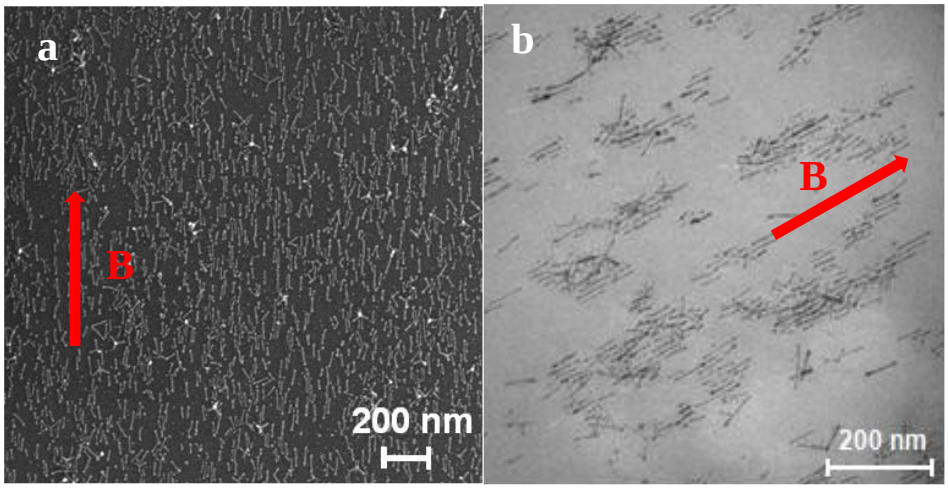

Figure 7-1. (a) SEM image of nanorods on a silicon substrate after magnetophoretic deposition. It can be seen that the nanorods align along the applied field direction to a great extent (marked in red). (b) Bright-field TEM image of aligned nanorods deposited on a carbon coated TEM grid under similar experimental conditions.

To obtain a three-dimensional aligned nanorods assembly, the rods have been aligned in an organic matrix inside a gelatin capsule. Tetracosane was chosen as a matrix because of the long alkane hydrocarbon with the structural formula of $C_{24}H_{50}$ and the low melting point of about 50°C. To align the nanorods, a small fraction of the colloidal solution is mixed with liquid tetracosane in the gelatin capsule. The sample is then introduced in a SQUID magnetometer and the temperature was rise up to 75°C to melt the tetracosane. Afterwards, an applied magnetic field of 5 T was applied to align the nanorods in the matrix and the temperature decreased progressively while keeping the magnetic field constant. Tetracosane recrystallizes as a brittle white solid that presumably contains aligned rods in its interior.

The magnetic properties of both samples were characterized by SQUID magnetometry. The ZFC hysteresis curve (T = 10 K) of aligned CoNi rods on silicon substrate (two-dimensional nanocomposite) is shown in Figure 7-2. The external magnetic field was applied in-plane and in the same direction of the applied magnetic field during alignment process, thus corresponding with the nanorods easy axis. The diamagnetic signal from the Si substrates is subtracted. A coercive field of 230 mT is found at 10 K and the Mr/Ms ratio increase to 0.58 with respect to the powder sample (0.28).

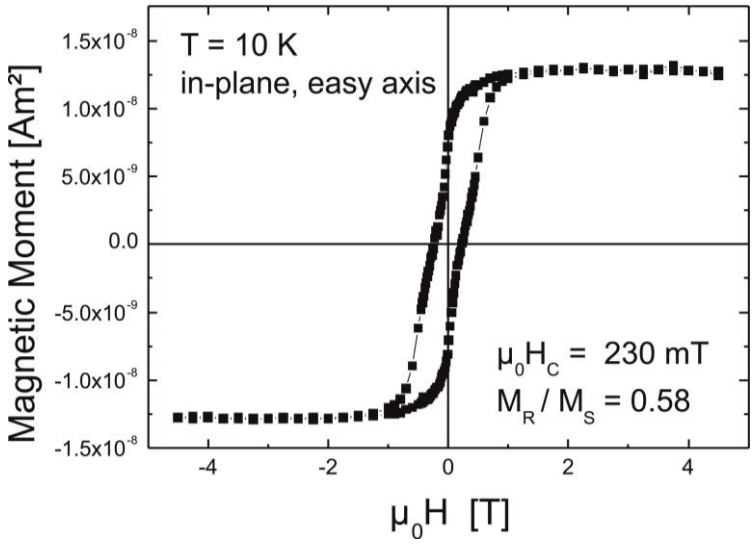

Figure 7-2. ZFC hysteresis loop of CoNi nanorods aligned on a silicon substrate acquired at 10K. The external magnetic field was applied in-plane and in the same direction of the applied magnetic field during alignment process, thus corresponding with the nanorods easy axis. The diamagnetic signals from the Si substrates is subtracted.

The direct comparison of the normalized ZFC magnetization curves of aligned particles in the tetracosane matrix (three-dimensional ensemble) and the powder sample at 300 K is shown in Figure 7-3. The nanorods are three-dimensionally aligned in tetracosane and measured parallel to the applied field in the SQUID magnetometer. The diamagnetic signal steaming from the nature of tetracosane was subtracted.

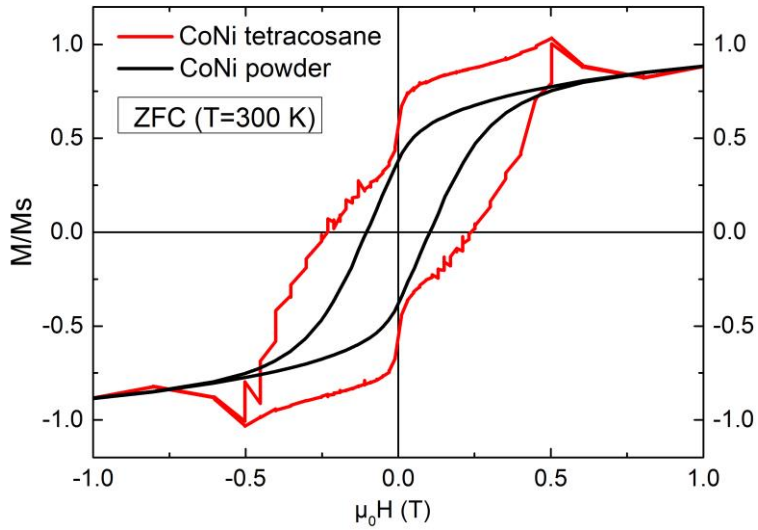

Figure 7-3. Comparison of the normalized ZFC magnetization curves of the aligned nanorods in the tetracosane matrix (red) and the powder sample (black) at 300 K. The coercive field of the aligned particles in the matrix is 2.5 times larger than the corresponding in the powder, where the rods are randomly oriented. The remanence in the composite is also nearly 1.5 times larger compared to the powder sample.

The magnetic properties of the three samples are compared, that is the powder sample, the CoNi nanorods aligned on a silicon substrate (2D alignment) and the rods aligned in tetracosane matrix (3D alignment). The coercive field and Mr/Ms ratio obtained from the ZFC hysteresis curves at 5 and 300 K are listen in Table 7-1.

Table 7-1. Characteristic parameters of the ZFC hysteresis curves acquired at 5 K and 300 K of the powder sample, the CoNi nanorods aligned on a silicon substrate (2D alignment) and the rods aligned in tetracosane matrix (3D alignment). Listed are the coercive field (μ_0Hc) and the remanence to saturation magnetization ratio (Mr/Ms).

	Mr/Ms (T=5K)	**μ_0Hc (T) (T=5K)**	**Mr/Ms (T=300K)**	**μ_0Hc (T) (T=300K)**
Powder	0.24	0.17	0.38	0.10
2D alignment	0.58	0.23	-	-
3D alignment	0.38	0.30	0.54	0.24

The Mr/Ms ratio is an indication of the alignment degree. The larger the ratio is, the more particles are parallel to each other in the matrix and also aligned parallel to the applied magnetic field of the magnetometer. When comparing the Mr/Ms ratio of the three samples at 5 K, the value increases more than double in the 2D alignment (Mr/Ms=0.58) compared to the powder sample (Mr/Ms=0.24). The Mr/Ms ratio also increases in the 3D alignment but only reaching a value of 0.38, which indicates that the alignment of the rods on the substrates was more successful that in the tetracosane matrix. This might be explained considering a process of agglomeration of nanorods in certain areas of the tetracosane matrix, on which consequently the degree of relative alignment is partially lost. A detailed analysis of the order in the matrix could be carried out by means of transmission electron microscopy. Here, however, the sample preparation for TEM investigations was not possible due to the brittle behavior of the tetracosane matrix. For further investigation, polymethylmetacrylate polymer may become a suitable matrix, due to its great stability and easy handling. Moreover, at both temperatures, the coercive field of the aligned nanorods on the substrate as well as in the tetracosane matrix is bigger than that of the powder sample (see values in Figure 7-1), due to dipolar interactions between the rods.

In summary, the alignment of nanorods either in two- or three-dimensional geometry improves the magnetic properties (higher coercive field and Mr/Ms ratio) of the sample, which is desired for potential permanent magnet applications. To optimize the system for ultimate applications, further optimization needs to be done.

Appendix II: Iron cubes

Iron oxide nanoparticles have attracted tremendous attention in the last decades due to the widely use as catalysts [279], for the treatment of waste water [280], hyperthermia mediators [281] and contrast agents [282].

As explained in section 2.2, the shape of the nanoparticles can have a huge effect on the final properties they can display. Therefore, special attention can be paid to fabrication of nanosystems with concave surface and consequent negative curvature and/or high-index surface structures, that are proven to have enhanced catalytic performance [283]. The intrinsic high surface energy renders rather difficult the growth of these nanostructures and consequently, only few cases have been reported and actually rather limited to metallic systems. Recently manganese ferrite concaved structures have been obtained with a fairly good catalytic performance [284]. Thus, the presence of high index facets in iron oxides nanoparticles could possibly improve the catalytic perfomance of these crystals. For that reason, novel shaped iron oxide nanoparticles have been synthesized and the results are briefly discussed in this appendix.

Iron oxide magnetite nanocrystals were synthesized according to a modified procedure to produce cubes developed by Hyeon and co-workers [285], consisting in the thermal decomposition of an iron stearate precursor in the presence of oleic acid and sodium oleate. The introduced modifications in the synthesis method permit to attain different morphologies. Iron oxide cubic nanoparticles, with the cubes truncated at the apexes (rombicubooctahedrons) or with eight pods grown from the apexes in the <111> directions (concave cubes) were obtained. Figure 7-4 shows bright field TEM images of both samples.

As an example of the work that has been done with these nanocrystals, the structural and magnetic properties of the concaved cubes are summarized in the following.

Figure 7-5 includes the TEM analysis of this type of nanoparticles. Figure 7-5 (a) includes a bright-field TEM image of the concaved cubic iron oxide nanoparticle offering an overview of size and shape. Figure 7-5 (b) includes a HAADF-TEM image showing the presence of small hollow cavities randomly oriented inside the nanocrystals. Figure 7-5 (c) includes a TEM image of one of these nanoparticles with a sketch that corresponds to the

projection scheme of a cube model in the same orientation (close to the [111] zone axis) and showing consequently an almost hexagonal shape. Figure 7-5 (d) includes a HRTEM image of the edges of a cube, showing the {001} facet (indicated by the dotted line) with corresponding Fourier transform in the inset.

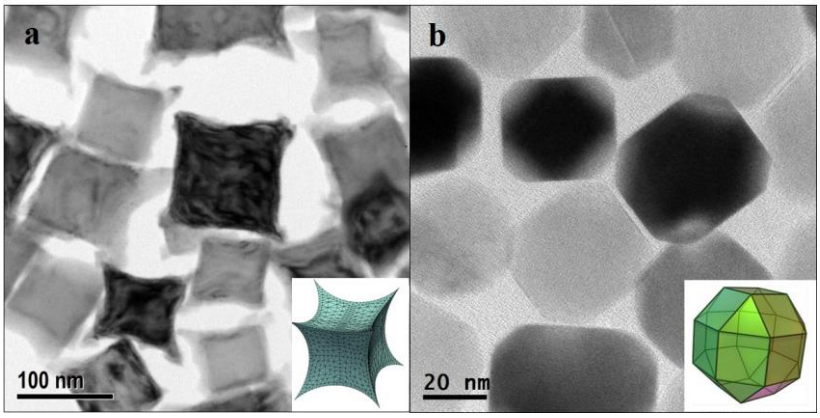

Figure 7-4. Bright field TEM micrographs of iron oxide concave cubes (a) and cuboctahedrons (b). Note the different scale bars. Insets depict schematics representations of the three-dimensional nanoparticles shapes obtained by computer reconstruction of the two dimensional projections in the TEM images.

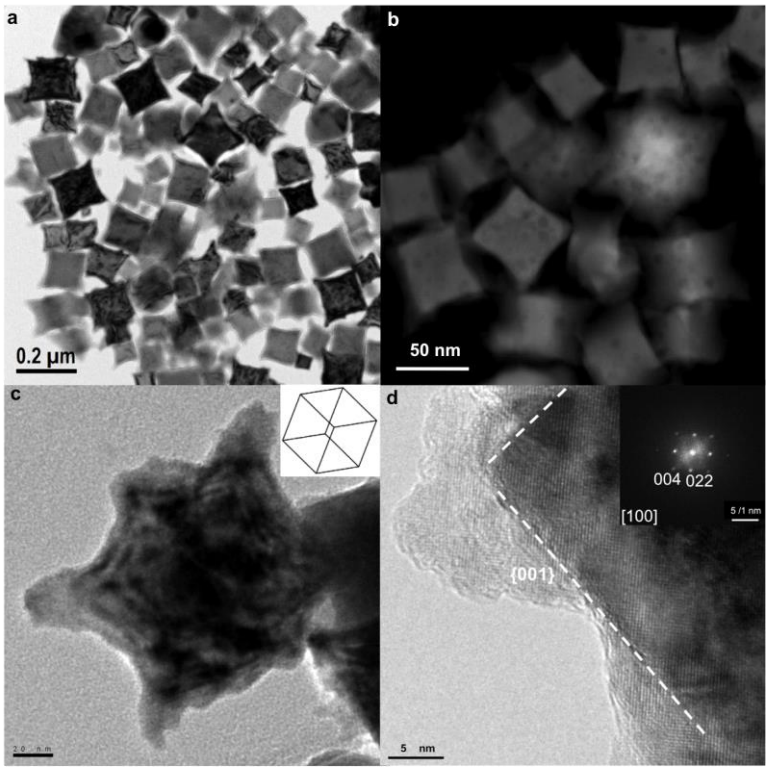

Figure 7-5. TEM images of the spiked cubic-shaped iron oxide nanoparticles (a), HAADF-STEM image showing voids distributed all over the cubic core of the nanoparticles (b), a cube-shaped nanoparticle close to the [111] zone axis orientation showing an almost hexagonal shape and a pod growing in each corner (c), the inset depicts thee approximated position of the cube, and (d) HRTEM image of the corner of a cube showing the {001} facet as the nearby average face of the magnetite cube (inset: FT that demonstrates a [100] zone axis with the (004) planes parallel to the cube edge) and the (022) planes of magnetite.

XRD pattern of these nanoparticles in powder (not shown) reflects the presence of different phases of iron oxides such as magnetite, maghemite and even hematite.

Magnetic measurements were performed on a powder sample using a SQUID magnetometry. Figure 7-6 shows the hysteresis curves of the concave cubic-shaped nanoparticles at two different temperatures, 5 K and 300 K. The hysteresis loops show two main contributions, one responsible for the large magnetization values and open hysteresis due to the ferromagnetic magnetite, and a second linear contribution antiferromagnetic responsible for the non-saturation of the magnetization at high field values.

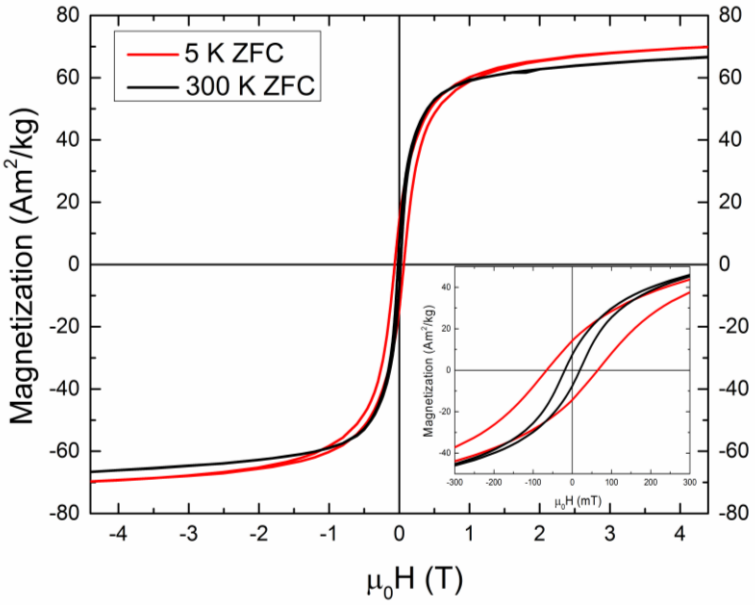

Figure 7-6. (a) M-H hysteresis loops of the concave cubic-shaped nanoparticles recorded at 5 and 300 K. Inset shows the magnification around zero field. The sample was carefully demagnetized before cooling to 5K.

Another indication of the anti(para)magnetic phase is seen in Figure 7-7, which shows the comparison of the ZFC and FC hysteresis loops at 5 K. The FC loop is shifted to the left and not symmetric with respect to the origin, indicating the exchange bias effect. To elucidate the origin of the ferri/antiferromagnetic interface that gives rise to the exchange bias effect at low temperatures, further structural and magnetic characterization is currently on progress.

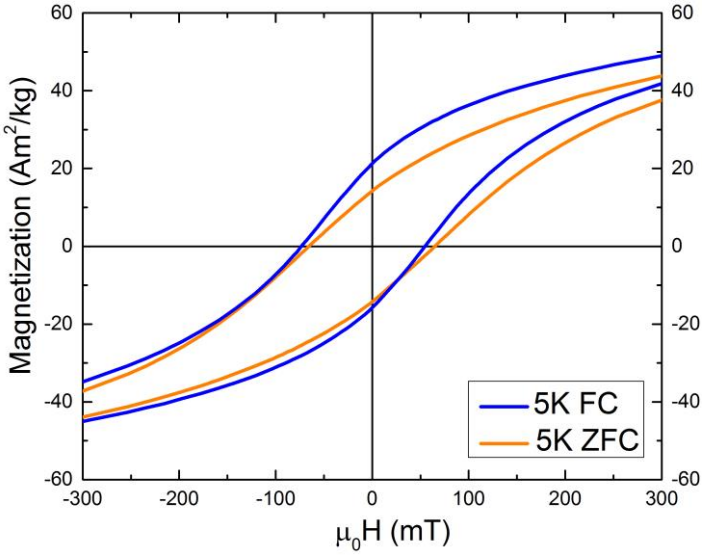

Figure 7-7. Comparison of the ZFC and FC hysteresis curves of concave cubic nanocrystals acquired at 5K. The magnetic field applied while cooling for the FC measurement was 4.5 T. The FC hysteresis has larger coercive field (exchange bias).

Appendix III: Ferrites for hyperthermia

Since magnetic nanoparticles can be easily conjugated with biologically important constituents such as DNA, peptides, and antibodies, it is possible to construct versatile nano-bio hybrids particles, which simultaneously possess magnetic and biological functions for biomedical diagnostics and therapeutics. In this context, magnetic nanoparticles are of immerse current interest because of their possible use as hyperthermia carriers for killing carcinomas or metastatic sarcomas.

Magnetic particle hyperthermia is an anti-cancer therapeutical scheme able to deliver severe thermal shocks to targeted cancer sites. In an external AC magnetic field magnetic nanoparticles produce heat via mechanisms strongly interconnected with their morphological, structural and magnetic profile. In addition to the established usage of iron oxide magnetic nanoparticles in biomedicine spinel ferrites are nowadays proposed as alternatives for magnetic particle hyperthermia mediators, MRI contrast agents or drug carriers [286].

In an attempt to combine hard with soft magnetic features and simultaneously introduce biocompatibility, two alternative synthetic procedures were followed, each one comprising two stages. The first synthetic procedure initiated by Co-ferrite or Mn-ferrite nanoparticles followed a typical thermal decomposition route in an organic environment resulting in typical sizes < 10 nm. At a second stage, magnetite synthesis was attempted, using Co-ferrite or Mn-ferrite as seeds, resulting in nanoparticles of < 15 nm in diameter. The goal was to form a Fe_3O_4 shell around the intrinsically toxic ferrite nanoparticles, providing internal nanoscale magnetic interfaces and suitable biocompatible coverage as well. A second independent synthetic procedure based on the aqueous co-precipitation of proper salts was also attempted to obtain similar mixed ferrite systems with an additional biocompatible shell of citric acid.

Structural and morphological features were revealed by XRD and TEM studies while EDX mapping unraveled the stoichiometry of the nanoparticle (see Figure 7-8). SQUID magnetometry indicated that mixed ferrite systems have significant coercive field and high magnetization values, appearing as the result of the exchange interaction between a magnetically “harder” with a magnetically “softer” phase at the *intra*-particle interface (Figure 7-9). These features are readily seen also in magnetic particle hyperthermia experiments

where the superior behavior of mixed ferrite systems may be directly exploited (Figure 7-10).

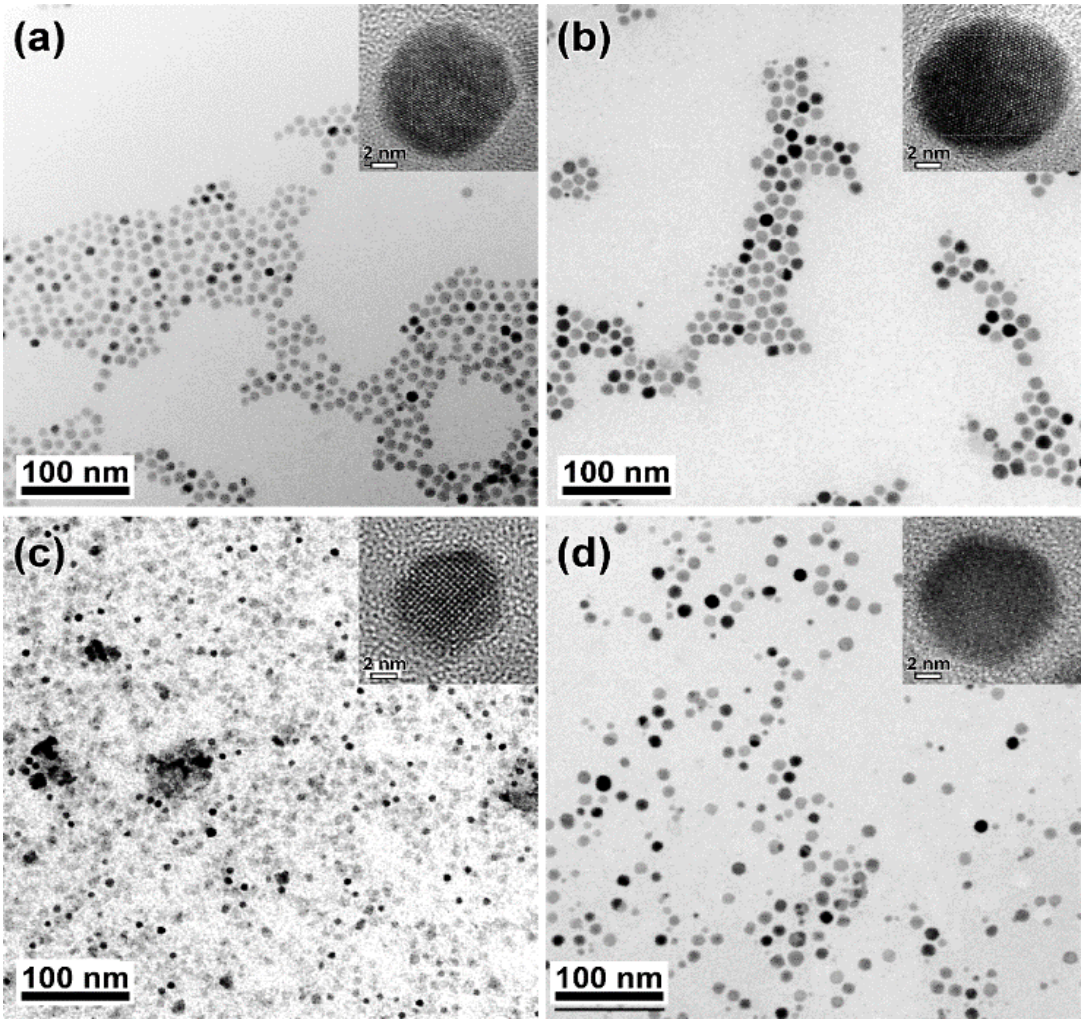

Figure 7-8. TEM images of single (a) and magnetite-coated $MnFe_2O_4$ (b) nanoparticles. Corresponding images for single (c) and magnetite-coated $CoFe_2O_4$ (d) nanoparticles. Insets show high-resolution images of individual nanoparticles.

Summarizing, magnetically-coupled core-shell ferrite nanoparticles with improved heating efficiency while maintaining a less toxic behavior for biological systems were produced. This latter reason of reducing the cytotoxicity of the nanopraticles led us to use magnetite was used as a coating layer onto spherical $MnFe_2O_4$ and $CoFe_2O_4$ nanoparticles, introducing simultaneously high heating performance and biocompatibility. The core-shell nanoparticles were synthesized in a two-step synthetic route to study the effect of interface coupling in exchange anisotropy and the potential to work as efficient magnetic hyperthermia mediators.

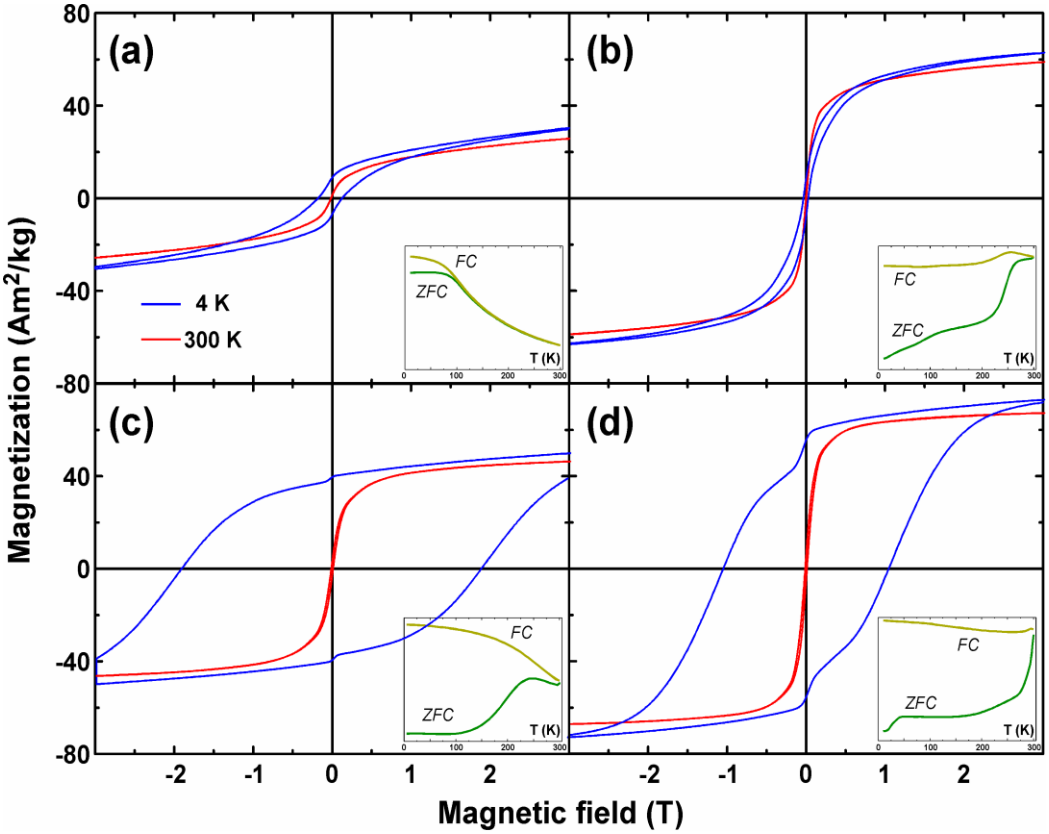

Figure 7-9. Magnetic hysteresis loops of single (a) and magnetite-coated (c) $MnFe_2O_4$ nanoparticles, single (b) and magnetite-coated (d) $CoFe_2O_4$ nanoparticles at 4 and 300 K. Corresponding ZFC-FC curves under 50 Oe were included as insets.

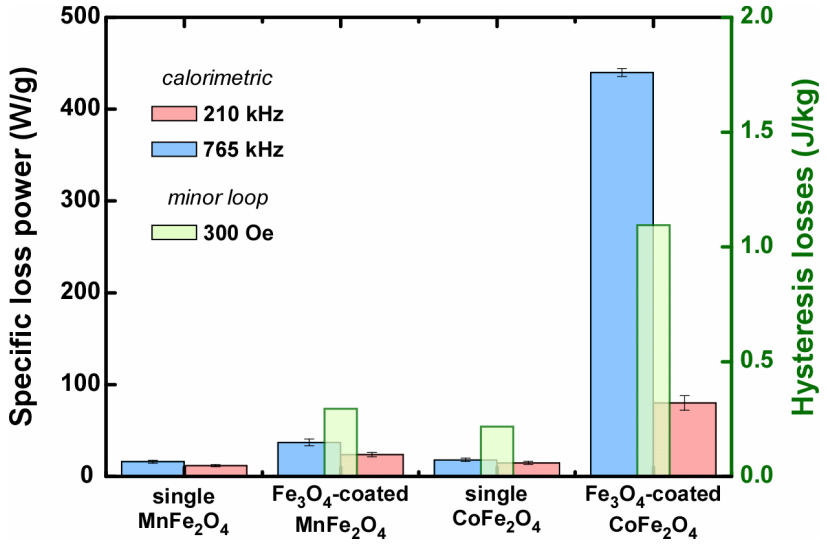

Figure 7-10. SLP values for the studied samples in comparison to hysteresis losses estimated by minor loops. Calorimetric measurements were performed in 4 mg/mL particle dispersions under a 300 Oe AC field at 210 and 765 kHz.

Appendix IV: FeMn nanoparticles

CoNi nanorods were thought as appropriate building blocks for bonded magnets. However, the increase in coercive field due to the exchange bias effect is limited to a very low temperature range. Since for ultimate applications, it is desirable to have permanent magnets working at room temperature (or higher), one strategy to increase the coercive field of a ferromagnetic material is to deposit on the surface an antiferromagnet, that pin the magnetic moment at the interface, causing the coercive field to increase. Following this idea and in order to increase the coercive field of the $Co_{80}Ni_{20}$ nanorods even further, an antiferromagnet can be placed on their outer surface.

In order to obtain such a combination of magnetic materials, that is, aligned CoNi nanorods embedded in an antiferromagnetic three-dimensional matrix, the following strategy was proposed. Antiferromagnetic nanoparticles can indeed be prepared and mixed with the CoNi rods, such that the nanoparticle mixture will be introduced in a furnace, for compaction and annealing of the ferro/antiferromagnetic composite. Prior to this, the CoNi nanorods should be aligned by a high magnetic field in the presence of a reducing atmosphere (to reduce the oxidized layer of the rods), otherwise the direct ferro/antiferromagnetic interface will not be formed. In such a way, a three dimensional arrangement of aligned CoNi nanorods embedded in an antiferromagnetic matrix will be obtained.

With this objective in mind, the FeMn alloy was chosen for the production of the antiferromagnetic nanoparticles, since being an antiferromagnetic material with a high Néel temperature (above room temperature) and high magnetocrystalline anisotropy. However, due to the high chemical reactivity of Mn, the fabrication of FeMn nanoparticles by wet-chemistry methods or electrodeposition is extremely difficult. The laser ablation method offers the possibility of fabricating novel nanostructures with metastable phases and shapes, which could not be achieved by any other technique. Thus, this technique was selected for producing $Fe_{50}Mn_{50}$ nanoparticles.

After the synthesis of these nanoparticles by laser ablation of a commercial FeMn target in tetrahydrofuran, detailed structural and chemical characterization was performed.

The bright-field TEM micrographs of Fe-Mn nanoparticles acquired at two different

magnifications are presented in Figure 7-11. These images demonstrate a broad size distribution (panel a) and a core-shell structure (panel b). Moreover, TEM analysis reveals a non-homogeneous inter- and intra-particle element distribution. Accordingly, from the structural point of view, the sample consists of two fractions, one consisting of small particles of manganese monoxide and another fraction consisting of larger particles with the Fe-Mn alloy core and $FeMn_2O_4$ oxide shell. The latter fraction constitutes 92 % of sample volume and accordingly will determine the magnetic properties of the particle ensemble.

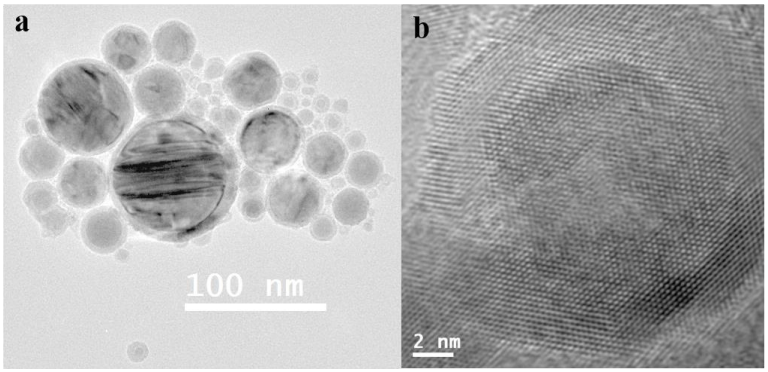

Figure 7-11. (a) Bright-field TEM micrograph of FeMn particles with a large size distribution. (b) High-resolution TEM image of a Fe-Mn nanoparticle showing a clear crystalline core-shell structure.

Magnetic hysteresis loops of the FeMn nanoparticles as dried powder were measured in the temperature range of 5-300 K in external fields up to 4.5 T. Figure 7-12 shows hysteresis loops measured at different temperatures.

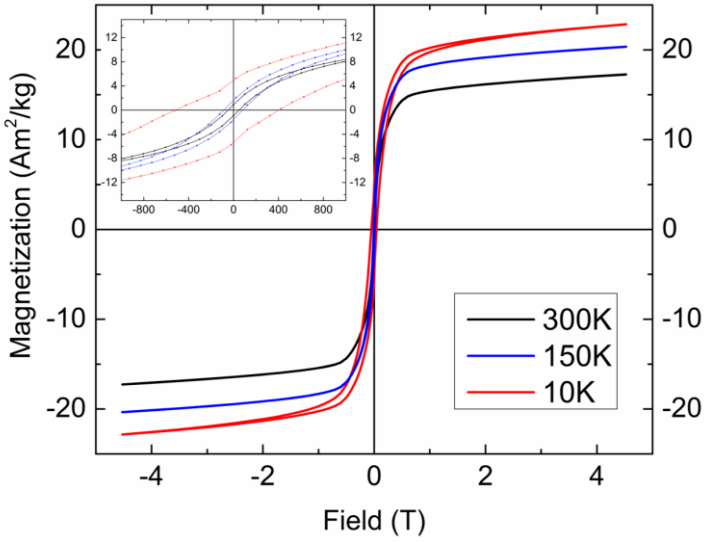

Figure 7-12. Hysteresis loops at different temperatures. Inset: magnification around zero field.

Though the FeMn nanoparticles show a ferromagnetic response even at 300 K, but with a rather low magnetization, since it is an antiferromagnetic phase, possible reasons to explain such ferromagnetic signal must be investigated. These reasons may be related to stoichiometry changes, demixing of FeMn, elemental segregation and oxidized shell $FeMnO_x$. In view of all that, one can assume that the observed magnetic behavior of these nanoparticles can be predominantly governed by the ferromagnetic $FeMn_2O_4$ oxide shell phase.

Summarizing, the detailed structural and chemical characterization reveal the presence of an inverted antiferromagnetic/ferromagnetic core/shell FeMn/$FeMn_2O_4$ nanoparticles. These type of structures are becoming the subject of increasing interest due to the related exchange bias properties, that are superior compared to the classical core/shell structure (ferro/antiferromagnet) due to the higher crystallinity of the antiferromagnetic component for being at the core.

The FeMn nanoparticles by themselves became an interesting subject of research and several synthesis parameters are being currently studied to optimize the properties of these nanocrystals. Thus, the scientific effort was shifted to understand deeply the structural and magnetic properties of the FeMn nanoparticles and the preparation of the CoNi/FeMn composite for permanent magnet applications have been postponed.

Bibliography

[1] C. Binns, *Nanomagnetism: fundamentals and applications,* Poland (2014)

[2] C. Kittel, Introduction to solid state physics, 7th ed., New York, John Wiley & sons, p. 446-450 (2006)

[3] B. D. Cullity and C. D. Graham, *Introduction to magnetic materials*, Hoboken, New Jersey (2009)

[4] J. Stöhr and H. C. Siegmann, *Magnetism, from fundamentals to nanoscale dynamics,* Berlin and Heidelberg (2006)

[5] R. C. O´Handley, *Modern magnetic materials, principles and applications,* New York (2000)

[6] N. W. Ashcroft and N. D. Mermin, *Solid state physics,* New York (1976)

[7] M. Farle, Magnetic nanoparticles (Magnetism goes Nano), Jülich, Forschungszentrum Jülich GmbH, C4 (2005)

[8] W. Wu, Q. He and C. Jiang, Magnetic iron oxide nanoparticles: synthesis and surface functionalization strategies, *Nanoscale Res. Lett.*, **3**, 397-415, (2008)

[9] E. V. Shevchenkok, D. V. Talapin, N. A. Kotov, S. O´Brien and C. B. Murray, Structural diversity in binary nanoparticle superlattices, *Nature*, **439**, 55-59, (2006)

[10] J. Park, E. Kang, S. U. Son, H. M. Park, M. K. Lee, J. Kim, K. W. Kim, H.-J. Noh, J. Park, C. J. Bae, J.-G. Park and T. Hyeon, Monodisperse nanoparticles of Ni and NiO: synthesis, characterization, self-assembled superlattices, and catalytic applications in the suzuki coupling reaction, *Adv. Mater.*, **17**, 4, 429-434, (2005)

[11] K. J. M. Bishop, C. E. Wilmer, S. Soh and B. A. Grzybowski, Nanoscale forces and their uses in self-assembly, *Small*, **5**, 14, 1600-1630, (2009)

[12] X. Teng and H. Yang, Effects of surfactants and synthethic conditions on the sizes and self-assembly of monodisperse iron oxide nanoparticles, *J. Mater. Chem.*, **14**, 774-779, (2004)

[13] F. Fievet, J. Lagier, B. Blin, B. Beaudoin and M. Figlarz, Homogeneous and heterogeneous nucleations in the polyol process for the preparation of micron and submicron size metal particles, *Solid State Ion.*, **32/33**, Part 1, 198-205, (1989)

[14] N. T. K. Thanh, N. Maclean and S. Mahiddine, Mechanisms of nucleation and growth of nanoparticles in solution, *Chem. Rev.*, **114**, 7610-7630, (2014)

[15] M. A. Watzky and R. G. Finke, Transition metal nanocluster formation kinetic and mechanistic studies. A new mechanisms when hydrogen is the reductant: slow, continuous nucleation and fast autocatalytic surface growth, *J. Am. Chem. Soc.*, **119**, 10382-10400, (1997)

[16] G. Schmid, *Nanoparticles, from theory to application*, Weinheim (Germany) (2004)

[17] Y. Xia, Y. Xiong, B. Lim and S. E. Skrabalak, Shape-controlled synthesis of metal nanocrystals: simiple chemistry meets complex physics?, *Angew. Chem. Int. Ed. Engl.*, **48**, 1, 60-103, (2009)

[18] V. K. LaMer and R. H. Dinegar, Theory, production and mechanism of formation of monodispersed hydrosols, *J. Am. Chem. Soc.*, **72**, 4847-4854, (1950)

[19] Y. Xia, X. Xia, Y. Wang and S. Xie, Shape-controlled synthesis of metal nanocrystals, *MRS Bulletin*, **38**, 335-344, (2013)

[20] S. Auer and D. Frenkel, Prediction of absolute crystal-nucleation rate in hard-sphere colloids, *Nature*, **409**, 1020-1023, (2001)

[21] S. G. Kwon and T. Hyeon, Kinetics of colloidal chemical synthesis of monodisperse spherical nanocrystals, *in Nanoscale materials in chemistry, 2nd ed.*, Hoboken, NJ, USA, John Wiley & Sons, Inc., (2009)

[22] C. Burda, X. Chen, R. Narayanan and M. A. El-Sayed, Chemistry and properties of nanocrystals of different shapes, *Chem. Rev.*, **105**, 1025-1102, (2005)

[23] S. Polarz, Shape matters: anisotropy of the morphology of inorganic colloidal particles-synthesis and function, *Adv. Func. Mater.*, **21**, 3214-3230, (2011)

[24] Y. Yin and A. P. Alivisatos, Colloidal nanocrystal synthesis and the organic-inorganic interface, *Nature*, **437**, 664-670, (2005)

[25] N. Ortiz and S. E. Skrabalak, On the dual roles of ligands in the synthesis of colloidal metal nanostructures, *Langmuir*, **30**, 6649-6659, (2014)

[26] N. Shukla, E. B. Svedberg, J. Ell and A. J. Roy, Surfactant effects on the shapes of cobalt nanoparticles, *Mater. Lett.*, **60**, 1950-1955, (2006)

[27] M. J. Rosen, *Surfactants and interfacial phenomena*, New York (1989)

[28] I. M. Watt, *The principles and practice of electron microscopy, 2nd. ed.*, Cambridge: (1997)

[29] D. B. Williams and C. B. Carter, *Transmission electron microscopy: a textbook for material science*, New York (1996)

[30] J. W. Edington, *Practical electron microscopy in materials science*, Herndon (India) (1976)

[31] T. R. Gordon, B. T. Diroll, T. Paik, V. V. T. Doan-Nguyen, E. A. Gaulding and C. B. Murray, Characterization of shape and monodispersity of anisotropic nanocrystals through atomistic X-ray scattering simulation, *Chem. Mater.*, **27**, 7, 2502-2506, (2015)

[32] S. Bals, B. Goris, T. Altantzis, H. Heidari, S. V. Aert and G. V. Tendeloo, Seeing and measuring in 3D with electrons, *C. R. Phys.*, **15**, 140-150, (2014)

[33] P. Midgley and M. Weyland, 3D electron microscopy in the physical sciences: the development of Z-contrast and EFTEM tomography, *Ultramicroscopy*, **96**, 413-431, (2003)

[34] M. McElfresh, Quantum Design International, Purdue University, http://www.qd-international.com/

[35] Department of physics, University of Wuppertal, http://hydrogen.physik.uni-wuppertal.de/hyperphysics/hyperphysics/hbase/solids/squid.html

[36] H. Weinstock, *SQUID sensors: fundamentals, fabrication and applications*, Dordrecht (The Netherlands) (1996)

[37] J. Clarke and A. Braginski, *The SQUID handbook*, Weinheim (2004)

[38] K. Gramm, L. Lundgren and O. Beckman, SQUID magnetometer for magnetization measurements, *Physica Scripta*, **13**, 2, 93, (1976)

[39] G. Aviv, *SQUIDs- superconducting quantum interference devices*, Experimental physics course, Be'er-Sheva, Israel, (2008)

[40] W. C. Nixon, The general principles of scanning electron microscopy, *Phil. Trans. Roy. Soc. Lond. B.*, **261**, 45-50, (1971)

[41] E. Meyer, Atomic force microscopy, *Prog. Surf. Sci.*, **41**, 1, 3-49, (1992)

[42] S. Magonov, Surface characterization of materials at ambient conditions by scanning tunneling microscopy and atomic force microscopy, *Appl. Spect. Rev.*, **28**, 1, 1-121, (1993)

[43] G. Binnig, C. F. Quate and C. Gerber, Atomic force microscope, *Phys. Rev. Lett.*, **56**, 9, 930, (1986)

[44] D. A. Skoog, F. J. Hooler and T. A. Nieman, *Principles of instrumental analysis*, New York (1997)

[45] J. F. Watts, X-ray photoelectron spectroscopy, *Vacuum*, **45**, 6-7, 653-671, (1994)

[46] D. C. Pinto-Leitao, *PhD thesis: Micro and nano patterned magnetic structures*, Porto (2010)

[47] W. Li, J. Zhang, T. Shen, G. A. Jones and P. J. Grundy, Magnetic nanowires fabricated by anodic aluminum oxide template - a brief review, *Science China*, **54**, 7, 1181-1189, (2011)

[48] C. Lu and Z. Chen, Anodic aluminum oxide-based nanostructures and devices, *in Encyclopedia of Nanoscience and Nanotechnology*, Lexington, Kentucky, USA, American Scientific Publishers, 2011, p. 235-259 (Vol. 11)

[49] H. Masuda and K. Fukuda, Ordered metal nanohole arrays made by a two-step replication of honeycomb structures of anodic alumina, *Science*, **268**, 1466-1468, (1995)

[50] G. E. J. Poinern, N. Ali and D. Fawcett, Progress in nano-engineered anodic aluminum oxide membrane development, *Materials,* **4**, 487-526, (2011)

[51] J. H. Yuan, F. Y. He, D. C. Sun and X. H. Xia, A simple method for preparation of through-hole porous anodic alumina membrane, *Chem. Mater.,* **16**, 1841-1844, (2004)

[52] W. Lee, R. Ji, U. Gösele and K. Nielsch, Fast fabrication of long-range ordered porous alumina membranes by hard anodization, *Nat. Mater.,* **5**, 741-747, (2006)

[53] J.-H. Zhou, J.-P. He, G.-W. Zhao, C.-X. Zhang, J.-S. Zhao and H.-P. Hu, Alumina nanostructures prepared by two-step anodization process, *Trans. Nonferrous Met. Soc. China*, **17**, 82-86, (2007)

[54] Y. Li, Z. Y. Ling, S. S. Chen and J. C. Wang, Fabrication of novel porous anodic alumina membranes by two-step hard anodization, *Nanotechnology,* **19**, 225604, (2008)

[55] T. Maurer, F. Ott, G. Chaboussant, Y. Soumare, J.-Y. Piquemal and G. Viau, Magnetic nanowires as permanent magnet materials, *Appl. Phys. Lett.,* **91**, 172501, (2007)

[56] X. Liu, H. Kanda and A. Morisako, The effect of underlayers on FeCo thin films, *J. Phys.: Conf. Ser.,* **266**, 012037, (2011)

[57] K. Gandha, K. Elkins, N. Poudyal, X. Liu and J. P. Liu, High energy product developed from cobalt nanowires, *Scientific Reports,* **4**, 5345, (2014)

[58] Y. Dahmane, L. Cagnon, J. Voiron, S. Pairis, M. Bacia, L. Ortega, N. Benbrahim and A. Kadri, Magnetic and structural properties of electrodeposited CoPt and FePt nanowires in nanoporous alumina templates, *J. Phys. D: Appl. Phys.,* **39**, 4523-4528, (2006)

[59] C.-L. Xu, H. Li, G.-Y. Zhao and H.-L. Li, Electrodeposition of ferromagnetic nanowire arrays on AAO/Ti/Si substrate for ultrahigh-density magnetic storage devices, *Mater. Lett.,* **60**, 2335-2338, (2006)

[60] S. S. P. Parkin, M. Hayashi and L. Thomas, Magnetic domain-wall racetrack memory, *Science,* **320**, 190, (2008)

[61] B. Cox, D. Davis and N. Crews, Creating magnetic field sensors from GMR nanowire networks, *Sensors and actuators A,* **203**, 335-340, (2013)

[62] K. Gandha, P. Tsai, G. Chaubey, N. Poudyal, K. Elkins, J. Cui and J. P. Liu, Synthesis and characterization of FeCo nanowires with high coercivity, *Nanotechnology*, **26**, 075601, (2015)

[63] S. Chikazumi, *The Physics of Ferromagnetism, p. 125,* New York (1997)

[64] I. Panagiotopoulos, W.Fang, F. Ott, F. Boué, K. Ait-Atmane, J.-Y. Piquemal and G.Viau, Packing fraction dependence of the coercivity and the energy product in nanowire based permanent magnets, *J. Appl. Phys.,* **114**, 143902, (2013)

[65] R. Skomski, Y. Liu, J. Shield, G. Hadjipanayis and D. Sellmyer, Permanent magnetism of dense-packed nanostructures, *J. Appl. Phys.,* **107**, 09A739, (2010)

[66] K. Nielsch, J. Choi, K. Schwirn, R. B. Wherspohn and U. Gösele, Self-ordering regimes of porous alumina: the 10% porosity rule, *Nano Lett.,* **2**, 7, 677-680, (2002)

[67] A. Encinas-Oropesa, M. Demand, L. Piraux, I. Huynen and U. Ebels, Dipolar interactions in arrays of nickel nanowires studied by ferromagnetic resonance, *Phys. Rev. B,* **63**, 104415, (2001)

[68] V. Vega, T. Böhnert, S. Martens, M. Waleczek, J. M. Montero-Moreno, D. Görlitz, V. M. Prida and K. Nielsch, Tuning the magnetic anisotropy of Co-Ni nanowires: comparison between single nanowires and nanowire arrays in hard-anodic aluminum oxide membranes, *Nanotechnology,* **23**, 465709, (2012)

[69] R. Hertel and J. Kirschner, Magnetization reversal dynamics in nickel nanowires, *Physica B,* **343**, 206-210, (2004)

[70] P. Toson, W. Wallisch, A. Asali and J. Fidler, Modelling of packed Co nanorods for hard magnetic applications, *EPJ Web of Conferences,* **75**, 03002, (2014)

[71] Y. P. Ivanov, M. Vázquez and O. Chubykalo-Fesenko, Magnetic reversal modes in cylindrical nanowires, *J. Phys. D: Appl. Phys.,* **46**, 485001, (2013)

[72] Y. P. Ivanov, D. Trabada, A. Chuvilin, J. Kosel, O. Chubykalo-Fesenko and M. Vázquez, Crystallographically driven magnetic behaviour of arrays of monocrystalline Co nanowires, *Nanotechnology,* **25**, 475702, (2014)

[73] Z. Turgut, N. T. Nuhfer, H. R. Piehler and M. E. McHenry, Magnetic properties and microstructural observations of oxide coated FeCo nanocrystals before and after compaction, *J. Appl. Phys.,* **85**, 4406-4408, (1999)

[74] K. N. Collier, N. J. Jones, K. J. Miller, Y. L. Qin, D. E. Laughlin and M. E. McHenry, Controlled oxidation of FeCo magnetic nanoparticles to produce faceted FeCo/ferrite nanocomposites for rf heating applications, *J. Appl. Phys.*, **105**, 07A328, (2009)

[75] C. Cheng and A. H. W.Ngan, Modelling and simulation of self-ordering in anodic porous alumina, *Electrochim. Acta,* **56**, 27, 9998-10008, (2011)

[76] C. T. Sousa, D. C. Leitao, M. P. Proenca, J. Ventura, A. M. Pereira and J. P. Araujo, Nanoporous alumina as templates for multifunctional applications, *Appl. Phys. Rev.,* **1**, 031102, (2014)

[77] H. Masuda and K. Fukuda, Ordered metal nanohole arrays made by a two-step replication of honeycomb structures of anodic alumina, *Science,* **268**, 1466, (1995)

[78] G. Hu, H. Zhang, W. Di and T. Zhao, Study on wet etching of AAO template, *Appl. Phys. Research,* **1**, 2, (2009)

[79] D. J. Sellmyer, M. Zheng and R. Skomski, Magnetism of Fe, Co, and Ni nanowires in self-assembled arrays, *J. Phys.: Condens. Matter,* **13**, R433-R460, (2001)

[80] M. Farle, Ferromagnetic resonance of ultrathin metallic layers, *Rep. Prog. Phys.*, **61**, 755-826, (1998)

[81] C. Bran, Y. P. Ivanov, J. Garcia, R. P. d. Real, V. M. Prida, O. Chubykalo-Fesenko and M. Vazquez, Tuning the magnetization reversal process of FeCoCu nanowire arrays by thermal annealing, *J. Appl. Phys.*, **114**, 043908, (2013)

[82] C. Bran, Y. P. Ivanov, D. G. Trabada, J. Tomkowicz, R. P. d. Real, O. Chubykalo-Fesenko and M. Vazquez, Structural dependence of magnetic properties in Co-based nanowires: experiments and micromagnetic simulations, *IEEE Trans. Mag.*, **49**, 4491, (2013)

[83] E. Callen and H. B. Callen, Magnetostriction, forced magnetostriction, and anomalous thermal expansion in ferromagnets, *Phys. Rev.*, **139**, A455 (1965)

[84] H. B. Callen and E. Callen, The present status of the temperature dependence of magnetocrystalline anisotropy, and the l(l+1)2 power law, *J. Phys. Chem. Solids*, **27**, 1271-1285, (1966)

[85] N. J. Jones, K. L. McNerny, A. T. Wise, M. Sorescu, M. E. McHenry and D. E. Laughlin, Observations of oxidation mechanisms and kinetics in faceted FeCo magnetic nanoparticles, *J. Appl. Phys.*, **107**, 09A304, (2010)

[86] U. Ebels, J.-L. Duvai, P. E. Wigen, L. Piraux, L. D. Buda and K. Ounadjela, Ferromagnetic resonance studies of Ni nanowire arrays, *Phys. Rev. B*, **64**, 144421, (2001)

[87] S. Yoon, Temperature dependence of magnetic anisotropy constant in cobalt ferrite nanoparticles, *J. Magn. Magn. Mater.*, **324**, 2620-2624, (2012)

[88] A. Franco and V. Zapf, Temperature dependence of magnetic anisotropy in nanoparticles of $Co_xFe_{(3-x)}O_4$, *J. Magn. Magn. Mater.*, **320**, 709-713, (2008)

[89] S. Mao, N. Amin and E. Murdock, Temperature dependence of giant magnetoresistance properties of NiMn pinned spin valves, *J. Appl. Phys.*, **83**, 6807, (1998)

[90] U. Wiedwald, L. Han, J. Biskupek, U. Kaiser and P. Ziemann, Preparation and characterization of supported magnetic nanoparticles prepared by reverse micelles, *Beilstein J. Nanotechnol.*, **1**, 24-47, (2010)

[91] L. Cao, X. Qiu, J. Ding, H. Li and L. Chen, The effects of composition and thermal treatment on the magnetic properties of $Fe_{100-x}Co_x$ nanowire arrays based on AAO templates, *J. Mater. Sci.*, **41**, 2211-2218, (2006)

[92] S. Liébana-Viñas, R. Salikhov, C. Bran, E. M. Palmero, M. Vazquez, B. Arvan, X. Yao, P. Toson, J. Fidler, M. Spasova, U. Wiedwald and M. Farle, Magnetic hardening of $Fe_{30}Co_{70}$ nanowires, *Nanotechnology*, **26**, 41, 415704, (2015)

[93] J.-L. Sun, X. Zhao and J.-L. Zhu, Metal-insulator transition in Au-NiO-Ni dual Schottky nanojunctions, *Nanotechnology*, **20**, 455203, (2009)

[94] Q. Zhou, g. meng, Q. Huang, C. Zhu, H. Tang, Y. Quian, B. Chen and B. Chen, Ag-nanoparticles-decorated NiO-nanoflakes grafted Ni-nanorod arrays stuck out of porous AAO as effective SERS substrates, *Phys. Chem. Chem. Phys.,* **16**, 3686, (2014)

[95] L. I. Mendelsohn, F. E. Luborsky and T. O. Paine, Permanent magnet properties of elongated single domain iron particles, *J. Appl. Phys.*, **26**, 1274, (1955)

[96] F. E. Luborsky, Development of elongated particle magnets, *J. Appl. Phys. ,* **32**, 3, 171S-183S, (1961)

[97] B. Kuerbanjiang, U. Wiedwald, F. Haering, J. Biskupek, U. Kaiser, P. Ziemann and U. Herr, Exchange bias of Ni nanoparticles embedded in an antiferromagnetic IrMn matrix, *Nanotechnology,* **24**, 455702, (2013)

[98] M. Artus, S. Ammar, L. Sicard, J. Y. Piquemal, F. Herbst, M. J. Vauly, F. Fievet and V. Richard, Synthesis and magnetic properties of ferrimagnetic $CoFe_2O_4$ nanoparticles embedded in an antiferromagnetic NiO matrix, *Chem. Mater.,* **20**, 4861-4872, (2008)

[99] F. E. Luborsky, L. I. Mendelsohn and T. O. Paine, Reproducing the properties of Alnico permanent magnet alloys with elongated single-domain cobalt-iron particles, *J. Appl. Phys.*, **28**, 344-3514, (1957)

[100] J. M. D. Coey, *Magnetism and Magnetic materials,* Cambridge (2009)

[101] B. Bakhit and A. Akbari, Nanocrystalline Ni-Co alloy coatings: electrodeposition using horizontal electrodes and corrosion resistance, *J. Coat. Technol. Res.,* **10**, 285-295, (2013)

[102] M. Srivastava, V. E. Selvi, V. K. W. Grips and K. S. Rajam, Corrosion resistance and microstructure of electrodeposited nickel cobalt alloy coatings, *Surf. Coat. Technol.,* **201**, 3051-3060, (2006)

[103] T. Maurer, F. Zighem, F. Ott, G. Chaboussant, G. Andre, Y. Soumare, J. Y. Piquemal, G. Viau and C. Gatel, Exchange bias in Co/CoO core-shell nanowires: role of antieferromagnetic superparamagnetic fluctuations, *Phys. Rev. B,* **80**, 064427, (2009)

[104] J. Nogués and I. K. Shuller, Exchange anisotropy, *J. Magn. Magn. Mater.*, **192**, 2, 203-232, (1999)

[105] M. Spasova, U. Wiedwald, M. Farle, T. Radetic, U. Dahmen, M. Hilgendorff and M. Giersig, Temperature dependence of exchange anisotropy in monodisperse cobalt nanoparticles with a cobalt oxide shell, *J. Magn. Magn. Mater.,* **272**, 1508-1509, (2004)

[106] M. V. Chernysheva, N. A. Sapoletova, A. A. Eliseev, A. V. Lukashin, Y. D. Tretyakov and P. Goernert, Formation of ordered cobalt nanowire arrays in the mesoporous silica channels, *Pure Appl. Chem.,* **78**, 9, 1749-1757, (2006)

[107] L. Guan, Z. Shi, H. Li, L. You and Z. Gu, Super-long continuous Ni nanowires encapsulated in carbon nanotubes, *Chem. Commun.*, 1988-1989, (2004)

[108] I. Alexandrou, D. K. H. Ang, N. D. Mathur, S. Haq and G. A. J. Amaratunga, Encapsulated nanowires formed by nanotube-assisted oriented attachment, *Nano Lett.*, **4**, 11, 2299-2302, (2004)

[109] S. Talapatra, X. Tang, M. Padi, T. Kim, R. Vajtai, G. V. S. Sastry, M. Shima, S. C. Deevi and P. M. Ajayan, Synthesis and characterization of cobalt-nickel alloy nanowires, *J. Mater. Sci.*, **44**, 2271-2275, (2009)

[110] M. J. Hu, B. Lin and S. H. Yu, Magnetic field-induced solvothermal synthesis of one-dimensional assemblies of Ni-Co alloy microstructures, *Nano. Res.*, **1**, 303-313, (2008)

[111] L.-P. Zhu, H.-M. Xiao and S.-Y. Fu, Surfactant-assisted synthesis and characterization of novel chain-like CoNi alloy assemblies, *Eur. J. Inorg. Chem.,* **25**, 3947-3951, (2007)

[112] D.-E. Zhang, X.-M. Ni, X.-J. Zhang and H.-G. Zheng, Synthesis and characterization of Ni-Co needle-like alloys in water-in-oil microemulsion, *J. Magn. Magn. Mater.*, **302**, 2, 290-293, (2006)

[113] T. Yamauchi, Y. Tsukahara, K. Yamada, T. Sakata and Y. Wada, Nucleation and growth of magnetic Ni-Co (core-shell) nanoparticles in a one-pot reaction under microwave irradiation, *Chem. Mater.*, **23**, 75-84, (2011)

[114] Q. Liu, X. Guo, T. Wang, Y. Li and W. Shen, Synthesis of CoNi nanowires by heterogeneous nucleation in polyol, *Mater. Lett.*, **64**, 11, 1271-1274, (2010)

[115] D. Ung, Y. soumare, N. Chakroune, G. Viau, M. J. Vaulay, V. Richard and F. Fievet, Growth of magnetic nanowires and nanodumbbells in liquid polyol, *Chem. Mater.*, **19**, 8, 2084-2094, (2007)

[116] D. Ung, G. Viau, C. Ricolleau, F. Warmont, P. Gredin and F. F. Fievet, CoNi nanowires synthesized by heterogeneous nucleation in liquid polyol, *Adv. Mater.*, **17**, 338-344, (2005)

[117] L. G. Rivas, M. Vazquez, J. Escrig, S. Allende, D. Altbir, D. C. Leitao and J. P. Araujo, Magnetic anisotropy in CoNi nanowire arrays: analytical calculations and experiments, *Phys. Rev. B*, **85**, 035439, (2012)

[118] W. O. Rosa, L. G. Vivas, K. R. Pirota, A. Asenjo and M. Vázquez, Influence of aspect ratio and anisotropy distribution in ordered CoNi nanowire arrays, *J. Magn. Magn. Mater.*, **324**, 3679-3682, (2012)

[119] M. M. v. Schooneveld, C. Campos-Cuerva, J. Pet, J. D. Meeldijk, J. v. Rijssel, A. Meijerink, B. H. Erné and F. M. F. d. Groot, Composition tunable cobalt-nickel and cobalt-iron alloy nanoparticles below 10 nm synthesized using acetonated cobalt carbonyl, *J. Nanopart. Res.*, **14**, 991, (2012)

[120] P. Toneguzzo, G. Viau, O. Acher, F. Guillet, E. Bruneton, F. Fievet-Vincent and F. Fievet, CoNi and FeCoNi fine particles prepared by the polyol process: physico-chemical characterization and dynamic magnetic properties, *J. Mater. Sci.,* **35**, 3767-3784, (2000)

[121] R. Brayner, M.-J. Vaulay, F. Fiévet and T. Coradin, Alginate-mediated growth of Co, Ni, and CoNi nanoparticles: influence of the biopolymer structure, *Chem. Mater.,* **19**, 1190-1198, (2007)

[122] M.-J. Hu, Y. Lu, S. Zhang, S.-R. Guo, B. Lin, M. Zhang and S.-H. Yu, High yield synthesis of bracelet-like hydrophilic Ni-Co magnetic alloy flux-closure nanorings, *J. Am. Chem. Soc.,* **130**, 35, 11606-11607, (2008)

[123] S. Panday, B. S. S. Daniel and P. Jeevanandam, Synthesis of nanocrystalline Co-Ni alloys by precursor approach and studies on their magnetic properties, *J. Magn. Magn. Mater.,* **323**, 2271-2280, (2011)

[124] M. Y. Rafique, L. Pan, W. S. Khan, M. Z. Iqbal, H. Qiu, M. H. Farooq, M. Ellahi and Z. Guo, Controlled synthesis, phase formation, growth mechanism, and magnetic properties of 3-D CoNi alloy microstructures composed of nanorods, *Cryst. Eng. Comm.,* **15**, 5314, (2013)

[125] G. Viau, C. García, T. Maurer, G. Chaboussant, F. Ott, Y. Soumare and J.-Y. Piquemal, Highly crystalline cobalt nanowires with high coercivity prepared by soft chemistry, *Phys. Status Solidi A,* **206**, 4, 663-666, (2009)

[126] X.-Z. Li, X.-W. Wei and Y. Ye, Template electrodeposition to cobalt-based alloys nanotube arrays, *Mater. Lett.,* **65**, 5, 578-580, (2009)

[127] K.-L. Wu, X.-W. Wei, X.-M. Zhou, D.-H. Wu, X.-W. Liu, Y. Ye and Q. Wang, $NiCo_2$ alloys: controllable synthesis, magnetic properties, and catalytic applications in reduction of 4-nitrophenol, *J. Phys. Chem. C,* **115**, 16268-16274, (2011)

[128] H. Li, J. Liao, Y. Feng, S. Yu, X. Zhang and Z. Jin, Controlled synthesis of three-dimensional CoNi microstructures composed of single crystal CoNi nanoleaves, *Cryst. Eng. Comm.,* **14**, 2974-2980, (2012)

[129] N. Bahlawane, P. A. Premkumar, Z. Tian, X. Hong, F. Qi and K. Kohse-Höinghaus, Nickel and nickel-based nanoalloy thin films from alcohol-assisted chemical vapor deposition, *Chem. Mater.,* **22**, 1, 92-100, (2010)

[130] G. Viau, F. Fiévet-Vincent and F. Fiévet, Nucleation and growth of bimetallic CoNi and FeNi monodisperse particles prepared in polyols, *Solid State Ion.,* **84**, 259-270, (1996)

[131] G. Viau, P. Toneguzzo, A. Pierrard, O. Acher, F. Fiévet-Vincent and F. Fiévet, Heterogeneous nucleation and growth of metal nanoparticles in polyols, *Scripta Mater.,* **44**, 8-9, 2263-2267, (2001)

[132] N. Chakroune, G. Viau, C. Ricolleau, F. Fiévet-Vincent and F. Fiévet, Cobalt-based anisotropic particles prepared by the polyol process, *J. Mater. Chem.,* **13**, 312-318, (2003)

[133] Y.-M. Lee, C.-W. Park, H.-K. Choi, B.-H. Koo and C.-G. Lee, Effect of nucleating agents on synthesis of CoNi alloy particles via polyol process, *Met. Mater. Inter.*, **14**, 1, 117-121, (2008)

[134] K. Gandha, N. Poudyal, Q. Zhang and J. P. Liu, Effect of $RuCl_3$ on morphology and magnetic properties of CoNi nanowires, *IEEE Trans. Magn.*, **49**, 7, 3273-3276, (2013)

[135] G. Viau, R. Brayner, L. Poul, N. Chakroune, E. Lacaze, F. Fiévet-Vincent and F. Fiévet, Ruthenium nanoparticles: size, shape, and self-assemblies, *Chem. Mater.*, **15**, 2, 486-494, (2003)

[136] F. Fiévet, Fine particles: synthesis, characterization, and mechanism of growth, *in Surfactant Sci. Ser.*, New York, Ed. T. Sugimoto, Marcel Dekker, p. 460 (Vol. 92) (2000)

[137] Y. Soumare, J. Y. Piquemal, T. Maurer, F. Ott, G. Chaboussant, A. Falqui and G. Viau, Oriented magnetic nanowires with high coercivity, *J. Mater. Chem.*, **18**, 5696-5702, (2008)

[138] W. M. Haynes, *CRC Handbook of chemistry and physics, 93rd Edition*, Boca Raton (Florida) (2012-2013)

[139] M. Comesaña-Hermo, R. Estivill, D. Ciuculescu, Z.-A. Li, M. Spasova, M. Farle and C. Amiens, Effect of a side reaction involving a structural changes of the surfactants on the shape control of cobalt nanoparticles, *Langmuir*, **30**, 15, 4474-4482, (2014)

[140] N. Liakakos, B. Cormary, X. Li, P. Lecante, M. Respaud, L. Maron, A. Falqui, A. Genovese, L. Vendier, S. Koïnis, B. Chaudret and K. Soulantica, The big impact of a small detail: cobalt nanocrystal polymorphism as a result of precursor addition rate during stock solution preparation, *J. Am. Chem. Soc.*, **134**, 43, 17922-17931, (2012)

[141] T. Maurer, *Ph. D. Thesis: Magnetism of anisotropic nano-objects: magnetic and neutron studies of* $Co_{1-x}Ni_x$ *nanowires*, Universite de Paris-Sud, France (2010)

[142] J.-G. Kim, D. L. Pugmire, D. Battaglia and M. Langell, Analysis of the $NiCo_2O_4$ spinel surface with Auger and X-ray photoelectron spectroscopy, *Appl. Surf. Sci.*, **165:1**, 70-84, (2000)

[143] *X-ray Photoelectron Spectroscopy Database, http://srdata.nist.gov/xps*, National Institute of Standards and Technology, Gaithersburg, 2012.

[144] A. Taylor, Lattice parameters of binary nickel cobalt alloys, *J. Inst. Met.*, **77**, 585-594, (1950)

[145] K. Hirano, R. P. Agarwala, B. L. Averbach and M. Cohen, Diffusion in cobalt nickel alloys, *J. Appl. Phys.*, **33**, 3049, (1962)

[146] T. Nishizawa and K. Ishida, *The Co-Ni (Cobalt-Nickel) system*, Bulletin of alloy phase diagrams, 390-395, (1983)

[147] R. W. G. Wyckoff, *Crystal structures*, New York, p. 85, vol. 1, (1963)

[148] D. P. Whittle, F. Gesmudo, B. D. Bastow and G. C. Wood, The formation of solid-solution oxides during internal oxidation, *Oxid. Met.*, **16**, 159-174, (1981)

[149] Y. T. Law, T. Dintzer and S. Zafeiratos, Surface oxidation of NiCo alloy: a comparative X-ray photoelectron spectroscopy study in a wide pressure range, *Appl. Surf. Sci.*, **258**, 1480-1487, (2011)

[150] M. Hilgendorff and M. Giersig, The preparation of ordered colloidal magnetic particles by magnetophoretic deposition, *J. Phys. D: Appl. Phys.*, **32**, 22, L111-L113, (1999)

[151] J. L. Katza, Y. Xing and R. Cammarata, Magnetophoretic deposition of nanocomposites, *J. Mater. Res.*, **14**, 12, 4457-4459, (1999)

[152] L. Tang and D. E. Laughlin, Electron diffraction patterns of fibrous and lamellar textured polycrystalline thin films, *J. Appl. Cryst.*, **29**, 4, 411-418, (1996)

[153] L. Tang, Y. Feng, L.-L. Lee and D. E. Laughlin, Electron diffraction patterns of fibrous and lamellar textured polycrystalline thin films. II. Applications, *J. Appl. Cryst.*, **29**, 4, 419-426, (1996)

[154] D. Goll, A. E. Berkowitz and H. N. Bertram, Critical sizes for ferromagnetic spherical hollow nanoparticles, *Phys. Rev. B*, **70**, 184432, (2004)

[155] K. Simeonidis, C. Martinez-Boubeta, O. Iglesias, A. Cabot, M. Angelakeris, S. Mourdikoudis, I. Tsiaoussis, A. Delimitis, C. Dendrinou-Samara and O. Kalogirou, Morphology influence on nanoscale magnetism of Co nanoparticles: experimental and theoretical aspects of exchange bias, *Phys. Rev. B*, **84**, 144430, (2011)

[156] J. Nogués and I. K. Schuller, Exchange bias, *J. Magn. Magn. Mater.*, **192**, 203-232, (1999)

[157] R. Street and J. C. Woolley, A study of magnetic viscosity, *Proc. Phys. Soc. A*, **62**, 562-572, (1949)

[158] S. Liébana-Viñas, U. Wiedwald, A. Elsukova, J. Perl, B. Zingsem, A. S. Semisalova, V. Salgueiriño, M. Spasova and M. Farle, Structure-correlated exchange anisotropy in oxidized $Co_{80}Ni_{20}$ nanorods, *Chem. Mater.*, **27**, 4015-4022, (2015)

[159] C. Leighton, M. R. Fitzsimmons, A. Hoffmann, J. Dura, D. F. Majkrzad, M. S. Lund and I. K. Schuller, Thickness-dependent coercive mechanisms in exchange-biased bilayer, *Phys. Rev. B*, **65**, 064403, (2002)

[160] H. C. Hsu, C. C. Lo and Y. C. Tseng, Competing magnetic interactions and interfacial frozen-spins in Ni-NiO core-shell nanorods, *J. Appl. Phys.*, **111**, 063919, (2012)

[161] M. D. Stiles and R. D. McMichael, Model for exchange bias in polycrystalline ferromagnetic-antiferromagnet bilayers, *Phys. Rev. B*, **59**, 5, 3722-3733, (1999)

[162] V. Salgueiriño-Maceira, M. A. Correa-Duarte, M. Bañobre-López, M. Grzelczak, M. Farle, L. M. Liz-Marzán and J. Rivas, Magnetic properties of Ni/NiO nanowires deposited onto CNT/Pt nanocomposites, *J. Adv. Funct. Mater.*, **18**, 616-621, (2008)

[163] W. Jauch and M. Reehuis, Eelectron density distribution in paramangetic and antiferromagnetic CoO: a gamma-ray diffraction study, *Phys. Rev. B,* **65**, 125111, (2002)

[164] W. Jauch, M. Reehuis, H. J. Bleif and F. Kubanek, Crystallographic symmetry and magnetic structure of CoO, *Phys. Rev. B,* **64**, 052102, (2001)

[165] H. Che, A. Liu, J. Hou, J. Mu, Y. Bai, S. Zhao, X. Zhang and H.He, Solvothermal synthesis of hierarchical CoO flower-like microspheres for superior ethanol gas sensing properties, *J. Mater. Sci.: Mater. El.*, **25**, 7, 3209-3218, (2014)

[166] B. Geng, F. Zhan, C. Fang and N. Yu, A facile coordination compound precursor route to controlled synthesis of Co_3O_4 nanostructures and their room-temperature gas sensing properties, *J. Mater. Chem.*, **18**, 4977-4984, (2008)

[167] G. X. Wang, Y. Chen, K. Konstantinov, J. Yao, J.-H. Ahn, H. K. Liu and S. X. Dou, Nanosize cobalt oxides as anode materials for lithium-ion batteries, *J. Alloys Compd.*, **340**, L5-L10, (2002)

[168] G. X. Wang, Y. Chen, K. Konstantinov, M. Lindsay, H. Liu and S. X. Dou, Investigation of cobalt oxides as anode materials for Li-ion batteries, *J. Power Sources*, **109**, 142-147, (2002)

[169] P. Poizot, S. Laruelle, S. Grugeon, L. Dupong and J.-M. Tarascon, Nano-sized transition-metal oxides as negative-electrode materials for lithium-ion batteries, *Nature*, **407**, 496-499, (2000)

[170] A. Lu, Y. Chen, J. Jin, G.-H. Yue and D.-L. Peng, CoO nanocrystals as a highly active catalyst for the generation of hydrogen from hydrolysis of sodium borohydride, *J. Power Sources*, **220**, 391-398, (2012)

[171] K. Deori, S. K. Ujjain, R. Ki, Sharma and S. Deka, Morphology controlled synthesis of nanoporous Co_3O_4 nanostructures and their charge storage characteristics in supercapacitors, *ACS Appl. Mater. Interfaces*, **5**, 10665-10672, (2013)

[172] V. Skumryev, S. Stoyanov, Y. Zhang, G. Hadjipanayis, D. Givord and J. Nogués, Beating the superparamagnetic limit with exchange bias, *Nature*, **423**, 850-853, (2003)

[173] J. B. Tracy, D. N. Weiss, D. P. Dinega and M. G. Bawendi, Exchange biasing and magnetic properties of partially and fully oxidized colloidal cobalt nanoparticles, *Phys. Rev. B,* **72**, 064404, (2005)

[174] J.-S. Do and C.-H. Weng, Preparation and characterization of CoO used as anodic material of lithium battery, *J. Power Sources*, **146**, 482-486, (2005)

[175] H. C. Choi, S. Y. Lee, S. B. Kim, M. G. Kim, M. K. Lee, H. J. Shin and J. S. Lee, Local structural characterization for electrochemical insertion-extraction of lithium

into CoO with X-ray absorption spectroscopy, *J. Phys. Chem. B*, **103**, 36, 9252-9260, (2002)

[176] G.-L. Xu, J.-T. Li, L. Huang, W. Lin and S.-G. Sun, Synthesis of Co_3O_4 nano-octahedra enclosed by {111} facets and their excellent lithium storage properties as anode material of lithium ion batteries, *Nano Energy*, **2**, 394-402, (2013)

[177] W.-Y. Li, L.-N. Xu and J. Chen, Co_3O_4 nanomaterials in lithium-ion batteries and gas sensors, *Adv. Funct. Mater.*, **15**, 5, 851-857, (2005)

[178] Y. Wang, H. Xia, L. Lu and J. Lin, Excellent performance in lithium-ion battery anodes: rational synthesis of $Co(CO_3)_{0.5}(OH)_{0.11}H_2O$ nanobelt array and its conversion into mesoporous and single-crystal Co_3O_4, *ACS Nano*, **4**, 3, 1425-1432, (2010)

[179] K. Zhou and Y. Li, Catalysis based on nanocrystals with well-defined facets, *Angew. Chem. Int. Ed.*, **51**, 602-613, (2012)

[180] L. Hu, Q. Peng and Y. Li, Selective synthesis of Co_3O_4 nanocrystal with different shape and crystal plane effect on catalytic property for methane combustion, *J. Am. Chem. Soc.*, **130**, 16136-16137, (2008)

[181] Y. Ye, F. Yuan and S. Li, Synthesis of CoO nanoparticles by esterification reaction under solvothermal conditions, *Mat. Lett.*, **60**, 3175-3178, (2006)

[182] W.-S. Seo, J.-H. Shim, S.-J. Oh, E.-K. Lee, N.-H. Hur and J.-T. Parkin, Phase- and size-controlled synthesis of hexagonal and cubic CoO nanocrystals, *J. Am. Chem. Soc.*, **127**, 6188-6189, (2005)

[183] G. P. Glaspell, P. W. Jagodzinski and A. Manivannan, Formation of cobalt nitrate hydrate, cobalt oxide, and cobalt nanoparticles using laser vaporization controlled condensation, *J. Phys. Chem. B*, **108**, 9604-9607, (2004)

[184] M. Ghosh, E. V. Sampathkumaran and C. N. R. Rao, Synthesis and magnetic properties of CoO nanoparticles, *Chem. Mater.*, **17**, 9, 2348-2352, (2005)

[185] K. Sinkó, G. Szabó and M. Zrínyi, Liquid-phase synthesis of cobalt oxide nanoparticles, *J. Nanosci. Nanotechnol.*, **11**, 1-9, (2011)

[186] L. Zhang, D. Xue and G. Gao, Anomalous magnetic properties of antiferromagnetic CoO nanoparticles, *J. Magn. Magn. Mater.*, **267**, 111-114, (2003)

[187] J. S. Yin and Z. L. Wang, Ordered self-assembling of tetrahedral oxide nanocrystals, *Phys. Rev. Lett.*, **79**, 13, 2570-2573, (1997)

[188] H. Shao, Y. Huang, H.-S. Lee, Y.-J. Suh and C.-O. Kim, Cobalt nanoparticles synthesis from $Co(CH_3COO)_2$ by thermal decomposition, *J. Magn. Magn. Mater.*, **304**, e28-e30, (2006)

[189] A. S. Risbud, L. P. Snedeker, M. M. Elcombe, A. K. Cheetham and R. Seshadri, Wurzite CoO, *Chem. Mater.*, **17**, 4, 834-838, (2005)

[190] K. An, N. Lee, J. Park, S. C. Kim, Y. Hwang, J.-G. Park, J.-Y. Kim, J.-H. Park, M. J. Han, J. Yu and T. Hyeon, Synthesis, characterization, and self-assembly of pencil-shaped CoO nanorods, *J. Am. Chem. Soc.*, **128**, 9753-9760, (2006)

[191] K. M. Nam, J. H. Shim, D.-W..Han, H. S. Kwon, Y.-M. Kang, Y. Li, H. Song, W. S. Seo and J. T. Parkin, Synthesis and characterization of wurtzite CoO, rocksalt CoO, and spinel Co_3O_4 nanocrystals: their interconversion and tuning of phase and morphology, *Chem. Mater.*, **22**, 4446-4454, (2010)

[192] Y. Zhang, J. Zhu, X. Song and X. Zhong, Controlling the synthesis of CoO nanocrystals with various morphologies, *J. Phys. Chem. C*, **112**, 5322-5327, (2008)

[193] M. Salavati-Niasari, F. Davar, M. Mazaheri and M. Shaterian, Preparation of cobalt nanoparticles from [bis(salicylidene)cobalt(II)]-oleylamine complex by thermal decomposition, *J. Magn. Magn. Mater.*, **320**, 575-578, (2008)

[194] M. Verelst, T. O. Ely, C. Amiens, E. Snoeck, P. Lecante, A. Mosset, M. Respaud, B. J. M and B. Chaudret, Synthesis and characterization of CoO,Co_3O_4, and mixed Co/CoO nanoparticules, *Chem. Mater.*, **11**, 2702-2708, (1999)

[195] Y. Zhang, X. Zhong, J. Zhu and X. Song, Alcoholysis route to monodisperse CoO nanotetrapods with tunable size, *Nanotechnology*, **18**, 195605, (2007)

[196] Z. Chen, A. Xu, Y. Zhang and N. Gu, Preparation of NiO and CoO nanoparticles using M^{2+}-oleate (M=Ni, Co) as precursor, *Curr. Appl. Phys.*, **10**, 967-970, (2010)

[197] Y. Zhu, Y. Wang, Y. Shi, J. I. Wong and H. Y. Yang, CoO nanoflowers woven by CNT network for high energy density flexible micro-supercapacitor, *Nano Energy*, **3**, 46-54, (2014)

[198] S. Kundu, A. J. Nelson, S. K. McCall, T. v. Buuren and H. Liang, Shape-influenced magnetic properties of CoO nanoparticles, *J. Nanopart. Res.*, **15**, 1587, (2013)

[199] A. Lu, Y. Chen, D. Zeng, M. Li, Q. Xie, X. Zhang and D.-L. Peng, Shape-related optical and catalytic properties of wurtzite- type CoO nanoplates and nanorods, *Nanotechnology*, **25**, 035707, (2014)

[200] H. Zhang and X. Chen, Controlled synthesis and anomalous magnetic properties of relatively monodisperse CoO nanocrystals, *Nanotechnology*, **16**, 2288-2294, (2005)

[201] J. H. Shim, K. M. Nam, W. S. Seo, H. Song and J. T. Park, The role of water for the phase-selective preparation of hexagonal and cubic cobalt oxide nanoparticles, *Chem. Asian J.*, **6**, 1575-1581, (2011)

[202] J. Yang, H. Liu, W. N. Martens and R. L. Frost, Synthesis and characterization of cobalt hydroxide, cobalt oxyhydroxide, and cobalt oxide nanodiscs, *J. Phys. Chem. C*, **114**, 111-119, (2010)

[203] B. E. Warren, *X-ray diffraction*, New York (1990)

[204] B. D. Cullity and S. R. Stock, *Elements of X-ray diffraction*, Michigan (1978)

[205] B. D. Cullity, Elements of X-ray Diffraction, New Jersey, Prentice-Hall (2001)

[206] N. Wang, X. Cao, L. Guo, S. Yang and Z. Wu, Facile synthesis of PbS truncated octahedron crystals with high simmetry and their large-scale assembly into regular patterns by a simple solution route, *ACS Nano,* **2**, 2, 184-190, (2008)

[207] C. Poole and F. J. Owens, *Introduction to nanotechnology,* USA (2003)

[208] Y. Zhao, T. E. Feltes, J. R. Regalbuto, R. J. Meyer and R. F. Klie, In situ electron energy loss spectroscopy study of metallic Co and Co oxides, *J. Appl. Phys.*, **108**, 063704, (2010)

[209] Z. Wang, J. Bentley and N. Evans, Valence state mapping of cobalt and manganese using near-edge fine structures, *Micron,* **31**, 355–362, (2000)

[210] D. H. Pearson, C. C. Ahn and B. Fultz, White lines and d-electron occupancies for the 3d and 4d transition metals, *Phys. Rev. B*, **47**, 8471-8478, (1993)

[211] Z.-. L. Wang, J.-S. Yin, W.-D. Mo and Z.-J. Zhang, In-situ analysis of valence conversion in transition metal oxides using electron energy-loss spectroscopy, *J. Phys. Chem. B,* **101**, 35, 6793-6798, (1997)

[212] Z. Wang, J. Yin and Y. Jiang, EELS analysis of cation valence states and oxygen vacancies in magnetic oxides, *Micron,* **31**, 571-580, (2000)

[213] G. A. Botton, C. C. Appel, A. Horsewell and W. M. Stobbs, Quantification of the EELS near-edge structures to study Mn doping in oxides, *J. Microsc.*, **180**, 211, (1995)

[214] Z. Zhang, Surface effects in the energy loss near edge structure of different cobalt oxides, *Ultramicroscopy,* **107**, 598-603, (2007)

[215] R. Metz, J. Morel, H. Delalu, S. Ananthakumar and M. Hassanzadeh, Direct oxidation route from metal to ceramic: study on cobalt oxide, *Mater. Res. Bull.*, **44**, 10, 1984-1989, (2009)

[216] A. Shavel, B. Rodríguez-González, J. Pacifico, M. Spasova, M. Farle and L. M. Liz-Marzán, Shape control in iron oxide nanocrystal synthesis, induced by trioctylammonium ions, *Chem. Mater.*, **21**, 1326-1332, (2009)

[217] N. Pinna, G. Garnweitner, M. Antonietti and M. Niederberger, A general nonaquesous route to binary metal oxide nanocrystals involving a C-C bond cleavage, *J. Am. Chem. Soc.,* **127**, 5608-5612, (2005)

[218] N. Fontaiña-Troitiño, B. Rivas-Murias, B. Rodríguez-González and V. Salgueiriño, Exchange bias effect in CoO@Fe_3O_4 core-shell octahedron-shaped nanoparticles, *Chem. Mater.*, **26**, 5566-5575, (2014)

[219] S. Mourdikoudis and L. M. Liz-Marzán, Oleylamine in nanoparticle synthesis, *Chem. Mater.*, **25**, 1465-1476, (2013)

[220] K. M. Nam, J. H. Shim, H. Ki, S.-I. Choi, G. Lee, J. K. Jang, Y. Jo, M.-H. Jung, H. Song and J. T. Park, Single-crystalline hollow face-centered-cubic cobalt

nanoparticles from solid face-centered-cubic cobalt oxide nanoparticles, *Angew. Chem. Int. Ed.*, **47**, 9504-9508, (2008)

[221] S. Moudikoudis, K. Simeonidis, I. Tsiaoussis, C. Dendrinou-Samara, M. Angelakeris and O. Kalogirou, Impact of synthesis parameters on structural and magnetic characteristics of Co-based nanoparticles, *J. Nanopart. Res.*, **11**, 477-1484, (2009)

[222] Z. Xu, C. Shen, Y. Hou, H. Gao and S. Sun, Oleylamine as both reducing agent and stabilizer in a facile synthesis of magnetite nanoparticles, *Chem. Mater.*, **21**, 1778-1780, (2009)

[223] Y. Yu, W. Yang, X. Sun, W. Zhu, X.-Z. Li, D. Sellmyer and S. Sun, Monodispersed MPt (M=Fe, Co, Ni, Cu, Zn) nanoparticles prepared from a facile oleylamine reduction of metal salts, *Nano Letters*, **14**, 2778-2782, (2014)

[224] Z.-G. Zhao, Z.-F. Liu and M. Miyauchi, Nature-inspired construction, characterization, and photocatalytic properties of single-crystalline tungsten oxide octahedra, *Chem. Commun.*, **46**, 3321-3323, (2010)

[225] W. Bu, Z. Chen, F. Chen and J. Shi, Oleic acid/oleylamine cooperative-controlled crystallization mechanism for monodisperse tetragonal bipyramid $NaLa(MoO_4)_2$ nanocrystals, *J. Phys. Chem. C*, **113**, 12176-12185, (2009)

[226] E. Papirer, P. Horny, H. Balard, R. Anthore, C. Petipas and A. Martinet, The preparation of a ferrofluid by decomposition of dicobalt octacarbonyl: II. Nucleation and growth of particles, *J. Colloid Interface Sci.*, **94**, 220, (1983)

[227] H. Reiss, The growth of uniform colloidal dispersions, *J. Chem. Phys.*, **19**, 474, (1951)

[228] P. W. Voorhees, The theory of Ostwald ripening, *J. Stat. Phys.*, **38**, 1-2, 231-252, (1985)

[229] B. Jia and L. Gao, Growth of well-defined cubic hematite single crystals: oriented aggregation and Ostwald ripening, *Cryst. Growth Des.*, **8**, 4, 1372-1376, (2008)

[230] L. Soriano, M. Abbate, A. Fernández, A. R. González-Elipe, F. Sirotti and J. M. Sanz, Oxidation state and size effects in CoO nanoparticles, *J. Phys. Chem. B*, **103**, 6676-6679, (1999)

[231] I. Manouchehri, P. Kameli and H. Salamati, Facile synthesis of Co_3O_4/CoO nanoparticles by thermal treatment of ball-milled precursors, *J. Supercond. Nov. Magn.*, **24**, 1907-1910, (2011)

[232] N. Cabrera and N. F. Mott, Theory of oxidation of metals, *Rep. Prog. Phys.*, **12**, 163, (1949)

[233] N. F. Mott, The theory of the formation of protective oxide films on metals-III, *Trans. Faraday Soc.*, **43**, 429-434, (1947)

[234] C. M. Wang, D. R. Baer, L. E. Thomas, J. E. Amonette, J. Antony, Y. Quiang and G. Duscher, Void formation during early stages of passivation: Initial oxidation of iron nanoparticles at room temperature, *J. Appl. Phys.,* **98**, 094308, (2005)

[235] N. F. Mott, Oxidation of metals and the formation of protective films, *Nature,* **145**, 996-1000, (1940)

[236] R. Nakamura, D. Tokozakura, H. Nakajima, J.-G. Lee and H. Mori, Holow oxide formation by oxidation of Al and Cu nanoparticles, *J. Appl. Phys.,* **101**, 074303, (2007)

[237] C. Wagner, Beitrag zur Theorie des Anlaufvorgangs (Theory of the tarnishing process), *Zeitschrift für Physikalische Chemie, Abteilung B: Chemie der Elementarprozesse, Aufbau der Materie,* **B21**, 25-41, (1933)

[238] S. Jia, C.-H. Hsia and D.-H. Son, In situ study of room-temperature oxidation kinetics of colloidal Co nanocrystals investigated by Faraday rotation measurement, *J. Phys. Chem. C,* **92**, 115, (2011)

[239] A. Cabot and V. F. Puntes, Vacancy coalescence during oxidation of iron nanoparticles, *J. Am. Chem. Soc.,* **129**, 34, 10358-10360, (2007)

[240] H. Khurshid, W. Li, V. Tzitzios and G. C. Hadjipanayis, Chemically synthesized hollow nanostructes in iron oxides, *Nanotechnology,* **22**, 265605, (2011)

[241] H. J. Fan, U. Gösele and M. Zacharias, Formation of nanotubes and hollow nanopartciels based on Kirkendall and diffusion processes: a review, *Small,* **3**, 10, 1660-1671, (2007)

[242] Y. Yin, C. K. Erdonmez, A. Cabot, S. Hughes and A. P. Alivisatos, Colloidal synthesis of hollow cobalt sulfide nanocrystals, *Adv. Funct. Mater.,* **16**, 1389-1399, (2006)

[243] Y. Yin, R. M. Rioux, C. K. Erdonmez, S. Hughes, G. A. Somorjai and A. P. Alivisatos, Formation of hollow nanocrystals through the nanoscale Kirkendall effect, *Science,* **304**, 711-714, (2004)

[244] B. D. Anderson and J. B. Tracy, Nanoparticle conversion chemistry: Kirkendall effect, galvanic exchange, and anion exchange, *Nanoscale,* **6**, 12195-12216, (2014)

[245] Z. Zhang, Y. Chen, X. Xu, J. Zhang, G. Xiang, W. He and X. Wang, Well-defined metal-organic framework hollow nanocages, *Angew. Chem.,* **126**, 439-443, (2014)

[246] S. Peng and S. Sun, Synthesis and characterization of nonodisperse hollow Fe_3O_4 nanoparticles, *Angew. Chem.,* **119**, 4233, (2007)

[247] W. Wu, S. Xiao, S. Zhang, H. Li, X. Zhou and C. Jiang, One-pot reaction and subsequent annealing to synthesis hollow spherical magnetite and maghemite nanocages, *Nanoscale Res. Lett.,* **4**, 8, 926-931, (2009)

[248] V. Bansal, H. Jani, J. D. Plessis, P. J. Coloe and S. K. Bhargava, Galvanic replacement reaction on metal films: A one-step approach to create nanoporous surfaces for catalysis, *Adv. Mater.*, **20**, 717-723, (2008)

[249] Y. Sun and Y. Xia, Mechanistic study on the replacement reaction between silver nanostructures and chloroauric acid in aquous medium, *J. Am. Chem. Soc.*, **126**, 12, 3892-3901, (2004)

[250] S. Shukla, A. Priscilla, M. Banerjee, R. R. Bhonde, J. Ghatak, P. Satyam and M. Sastry, Porous gold nanospheres by controlled transmetalation reaction: a novel material for application in cell imaging, *Chem. Mater.*, **17**, 20, 5000-5005, (2005)

[251] M. H. Oh, T. Yu, S. Yu, B. Lim, K. Ko, M.-G. Willinger, D.-H. Seo, B. H. Kim, M. G. Cho, J.-H. Park, K. Kang, Y.-E. Sung, N. Pinna and T. Hyeon, Galvanic replacement reactions in metal oxide nanocrystals, *Science*, **340**, 964, (2013)

[252] A. D. Smigelskas and E. O. Kirkendall, Zinc diffusion in alpha brass, *Trans. AIME*, **171**, 130-142, (1947)

[253] H. J. Fan, M. Knez, R. Sholz, D. Hesse, K. Nielsch, M. Zacharias and U. Gösele, Influence of surface diffusion on the formation of hollow nanostructures induced by the Kirkendall effect: the basic concept, *Nano Lett.*, **7**, 4, 993-997, (2007)

[254] H. J. Fan, M. Knez, R. Scholz, K. Nielsch, E. Pippel, D. Hesse, M. Zacharias and U. Gösele, Monocrystalline spinel nanotube fabrication based on the Kirkendall effect, *Nat. Mater.*, **5**, 627-631, (2006)

[255] K. N. Tu and U. Gösele, Hollow nanostructures based on the Kirkendall effect: design and stability considerations, *Appl. Phys. Lett.*, **86**, 093111, (2005)

[256] S. Dilger, C. Lizandara-Pueyo, M. Krumm and S. Polarz, Hierarchical zinc oxide materials with multiple porosity prepared by ultrafast temperature gradient chemical gas-phase synthesis, *Adv. Mater.*, **24**, 543-548, (2012)

[257] P. A. Chernavskii, G. V. Pankina, V. I. Zaikovskii, N. V. Peskov and P. Afanasiev, Formation of hollow spheres upon oxidation of supported cobalt nanoparticles, *J. Phys. Chem. C*, **112**, 9573-9578, (2008)

[258] N. Doan, K. Kontturi and C. Johans, Direction oxidation of cobalt nanoparticles with the capping ligand, *J. Colloid Interface Sci.*, **350**, 126-131, (2010)

[259] L. Néel, Superparamagnetism of very small antiferromagnetic particles, *Comptes Rendus*, **252**, 4075, (1961)

[260] L. Zhang and D. Xue, Preparation and magnetic properties of pure CoO nanoparticles, *J. Mater. Sci. Lett.*, **21**, 1931-1933, (2002)

[261] M. Feygenson, A. Kou, L. E. Kreno, A. L. Tiano, J. M. Patete, F. Zhang, M. S. Kim, V. Solovyov, S. S. Wong and M. C. Aronson, Properties of highly crystalline NiO and Ni nanoparticles prepared by high-temperature oxidation and reduction, *Phys. Rev. B*, **81**, 014420, (2010)

[262] S. A. Makhlouf, H. Al-Attar and R. Kodama, Particle size and temperature dependence of exchange bias in NiO nanoparticles, *Solid State Commun.*, **145**, 1-4, (2008)

[263] N. J. O. Silva, A. Millán, F. Palacio, M. Martins, T. Rindade, I. Puente-Orench and J. Campo, Remanent magnetization in CoO antiferromagnetic nanoparticles, *Phys. Rev. B*, **82**, 094433-094440, (2010)

[264] R. H. Kodama, S. A. Makhlouf and A. E. Berkowitz, Finite size effects in antiferromagnetic NiO nanoparticles, *Phys. Rev. Lett.*, **79**, 1393, (1997)

[265] X. He and H. Shi, Synthesis and anomalous magnetic properties of hexagonal CoO nanoparticles, *Mater. Res. Bull.*, **46**, 1692-1697, (2011)

[266] U. D. Wdowik and K. Parlinski, Electronic structure of cation-deficient CoO from first principles, *Phys. Rev. B*, **77**, 115110-115112, (2008)

[267] D. P. Dutta, G. Sharma, P. K. Manna, A. K. Tyagi and S. M. Yusuf, Room temperature ferromagnetism in CoO nanoparticles obtained from sonochemically synthesized precursors, *Nanotechnology*, **19**, 245609-245615, (2008)

[268] G. Yang, D. Gao, Y. Shi, Y. Zhang, J. Zhang, J. Zhang and D. Xue, Room temperature ferromagnetism in vacuum-annealed CoO nanospheres, *J. Phys. Chem. C*, **114**, 21989-21993, (2010)

[269] W. L. Roth, Magnetic structures of MnO, FeO, CoO and NiO, *Phys. Rev.*, **110**, 1333-1341, (1958)

[270] W. L. Roth, The magnetic structure of Co_3O_4, *J. Phys. Chem. Solids*, **25**, 1-10, (1964)

[271] P. Robinson, R. J. Harrison, S. A. McEnroe and R. B. Hargraves, Lamellar magnetism in the haematite-ilmenite series as an explanation for strong remanent magnetization, *Nature*, **418**, 517-520, (2002)

[272] H. S. Nabi, R. J. Harrison and R. Pentcheva, Magnetic coupling parameters at an oxide-oxide interface from first principles: Fe_2O_3-$FeTiO_3$, *Phys. Rev. B*, **81**, 214432, (2010)

[273] W. Geertsma and D. Khomskii, Influence of side groups on 90 degrees superexchange: a modification of the 'Goodenough-Kanamori-Anderson rules, *Phys. Rev. B. Conds. Matter*, **54**, 3011-3014, (1996)

[274] Z.-A. Li, N. Fontaiña-Troitiño, A. Kovács, S. Liébana-Viñas, M. Spasova, R. E. Dunin-Borkowski, M. Müller, D. Doennig, R. Pentcheva, M. Farle and V. Salgueiriño, Electrostatic doping as a source for robust ferromagnetism at the interface between antiferromagnetic cobalt oxides, *Sci. Rep.*, **5**, 7997, (2015)

[275] W. Fang, I. Panagiotopoulos, F. Ott, F. Boué, K. Ait-Atmane, J.-Y. Piquemal, G. Viau and F. Dalmas, Optimization of the magnetic properties of aligned Co nanowires/polymer composites for the fabrication of permanent magnets, *J. Nanopart. Res.*, **16**, 2265, (2014)

[276] J. S. Miller and M. Drillon, Magnetic ordering due to dipolar interaction in low dimensional materials, *in Magnetism: molecules to materials IV,* Weinheim, Wiley-VCH (2003)

[277] A. Hannour, D. Vincent, F. K. A. Tchangoulian, S. Neveu and V. Dupuis, Self-biased cobalt ferrite nanocomposites for microwave applications, *J. Magn. Magn. Mater.*, **353**, 29-33, (2014)

[278] J. Perl, *Master thesis: Magnetische eigenschaften von chemisch synthetisierten CoNi nanostäbchen,* Duisburg (2013)

[279] P. Li, D. E. Miser, S. Rabiei, R. T. Yadav and M. R. Hajaligol, The removal of carbon monoxide by iron oxide nanoparticles, *Appl. Catal. B*, **43**, 2, 151-162, (2003)

[280] J. M. Perez, Iron oxide nanoparticles: a hidden talent, *Nat. Nanotechnol.*, **2**, 535-536, (2007)

[281] S. Laurenta, S. Dutzb, U. O. Häfelib and M. Mahmoudi, Magnetic fluid hyperthermia: focus on superparamagnetic iron oxide nanoparticles, *Adv. Colloid Interface Sci.*, **166**, 1-2, 8-23, (2011)

[282] Z. Zhao, Z. Zhou, J. Bao, Z. Wang, J. Hu, X. Chi, K. Ni, R. Wang, X. Chen, Z. Chen and J. Gao, Octapod iron oxide nanoparticles as high-performance T2 contrast agents for magnetic resonance imaging, *Nat. Commun.,* **4**, 2266, (2013)

[283] K. Zhou and Y. Li, Catalysis based on nanocrystals with well-defined facets, *Angew. Chem.*, **51**, 3, 602-613, (2012)

[284] P. Y. Lee, H. S. Teng and C. S. Yeh, Preparation of superparamagnetic $Mn_{(x)}Fe_{(1-x)}O$ nanoparticles from low-index-facet cubes to high-index-facet concave structures and their catalytic performance in aqueous solution, *Nanoscale*, **5**, 16, 7558-7563, (2013)

[285] D. Kim, J. Park, K. An, N.-K. Yang, J.-G. Park and T. Hyeon, Synthesis of hollow iron nanoframes, *J. Am. Chem. Soc.,* **129**, 5812-5813, (2007)

[286] M. Angelakeris, Z.-A. Li, M. Hilgendorff, 1, K. Simeonidis, D. Sakellari, M. Filippousi, H. Tian, G. V. Tendeloo, M. Spasova, M. Acet and M. Farle, Enhanced biomedical heat-triggered carriers via nanomagnetism tuning in ferrite-based nanoparticles, *J. Magn. Magn. Mater.,* **381**, 179-187, (2015)

Acknowledgements

No one who achieves a PhD thesis success does so without the help of others. I take this opportunity to gratefully acknowledge the contributions of a vast number of people, who make it possible. They all deserve my respect and gratitude.

First and foremost I would like to express my sincere gratitude to my supervisors, Prof. Dr. Michael Farle at the University of Duisburg-Essen (Germany) and Prof. Dr. Verónica Salgueiriño at the University of Vigo (Spain). Veronica brought me into the world of colloidal chemistry and encourages my interest in science. Her explanations about nanochemistry were priceless. The patience of Michael in teaching a chemist the world of nanoscale magnetism during tutorials is really exemplary. I am privileged to have them as supervisors in this venture. Michael and Verónica, thanks for your guidance, for providing motivation and most important, for having faith in me.

I am truly thankful to Prof. Dr. Rolf Möller and Priv. Doz. Dr. Markus Gruner, at the University of Duisburg-Essen, whom accepted to be a member of the committee.

The work presented here would not have been possible without the invaluable help provided by Priv. Doz. Dr. Ulf Wiedwald and Dr. Marina Spasova. I am obliged to them for sharing with me their encyclopedic knowledge of magnetism at the nanoscale, as well as deep explanations of measurement techniques. I was incredibly impressed by their scientific interest and great enthusiasm. Special thanks to Dr. Wiedwald for his input correcting manuscripts, abstracts and all sort of official documents.

I am indebted to Dr. Ruslan Salikhov, Prof. Dr. Mehmet Acet, Dr. Detlef Spoddig and Dr. Ralf Meckenstock for their explanations and discussions of my results during seminar sessions and late evenings as well. Dr. Salikhov guided me in the study of the iron-cobalt nanowires.

Without the input of nanoparticle imaging techniques the correlation of structure and magnetism would not have been possible. Dr. Zi-An Li, Dr. Anna Elsukova and Dr. Benito Rodríguez González are gratefully acknowledged for TEM image acquisition. Behnaz Arvan and Xiang Yao are acknowledged for the SEM and AFM images acquisition, respectively. It was my pleasure to work with them.

Deserving of special mention is Horst Zähres, who was there whenever I needed support in the chemistry lab or solving technical problems with the TEM, and that happened countless times. My most sincere thanks go to Helga Mundt and Sabina Grubba for their tremendous help in administration. I also want to thank Christian Derricks for the technical assistance with computers. They contributed to make my life in Duisburg much easier throughout this time.

I am very grateful to thank Christian Jacobson, Benjamin Zingsem, Juliane Perl, Irene Iglesias, Anna Krämer and Fangzhou Wang for their assistance with experiments during their bachelor thesis degrees and scholarships. In this context, I would like to acknowledge the DAAD (German Academic Exchange Service) though the RISE program.

The “Finkenkrug-crew” is thanked for many enjoyable evenings discussing all sorts of fascinating subjects, not only science related. Therefore, I cannot forget to thank Franziska Scheibel, Thomas Marzi, Dr. Vadim Migunov, Dr. Yu Fu, Dr. Florian Römer, Christian Schöppner, Sabrina Masur, Alexandra Terwey, Kai Wagner, Carola Lottis, and many others (apart from the mentioned above). Thanks as well to all other members of the " AG Farle" group for the stimulating discussions and their cooperative attitude.

My research has been performed in the frame of several projects, where I have had the pleasure of collaborating with other researchers groups and departments. From the institute of materials science of Madrid (ICMM-CSIC), I would like to thank Prof. Dr. Manuel Vázquez, Dr. Cristina Bran and Ester M. Palmero for providing nanowires samples. From the University of Vienna I would like to thank on behalf of Prof. Dr. Josef Fidler and Peter Toson for their assistance with micromagnetic simulations of hysteresis loops of metallic nanowires. From the Aristotle University of Thessaloniki, I thank most warmly to Prof. Dr. Makis Angelakeris, Dr. Konstantinos Simeonidis, Dr. Despina Sakellari, Antonios Makridis and Eirini Mirovali for the fruitful collaboration in the synthesis and characterization of ferrite nanoparticles for biochemical applications. Finally, I would like to thank Prof. Dr. Stephan Barcikowski, Dr. Dongshi Zhang and René Streubel for providing FeMn oxide nanoparticles.

This work has been funded by the European Union's Seventh Framework Programme (FP7), through the REFREEPERMAG Project under grant agreement no. 280670, for

which I am very grateful. Complementary support of the “DAAD” from a bilateral German-Greek IKYDA project is also acknowledged.

And last but certainly not least, I wish to express my deepest appreciation to my family for their love, care, advice and unconditional support even at the cost of being far away from them. Among them I am especially thankful to my parents Rosa and Fernando and my sister Marta, to whom I dedicate this thesis. They encourage me in too many ways to list here. Special thanks to Dennis for his weekly dose of humor, inspiration and understanding along the way. Without their support, I could not have accomplish this PhD. So this thesis is theirs as much as mine.

Thank you all for contributing to my personal and professional development!

List of own publications

1. Concentric $MnFe_2O_4$-rich core/Cr_2O_3-rich shell nanoparticles.

S. Liébana-Viñas, R. Otero-Lorenzo, B. Rivas-Murias, V. Salgueiriño.

J. Phys.: Conference Series, 521, 012002 (2014).

10.1088/1742-6596/521/1/012002

2. Room temperature ferromagnetism in antiferromagnetic cobalt oxide nanooctahedra.

N. Fontaiña-Troitiño, S. Liébana-Viñas, B. Rodríguez-González, Zi-An Li, M. Spasova, M. Farle and V. Salgueiriño.

Nano Letters 14, 640 (2014).

DOI: 10.1021/nl4038533

3. Electrostatic doping as a source for robust ferromagnetism at the interface between antiferromagnetic cobalt oxides.

Z.-A. Li, N. Fontaíña-Trotitiño, A. Kovács, S. Liébana-Viñas, M. Spasova, R.E. Dunin-Borkowski, M. Müller, D. Doennig, R. Pentcheva, M. Farle and V. Salgueiriño.

Scientific Reports, 5, 7997 (2015).

DOI: 10.1038/srep07997

4. Structure-correlated exchange anisotropy in oxidized $Co_{80}Ni_{20}$ nanorods.

S. Liébana-Viñas, U. Wiedwald, A. Elsukova, J. Perl, B. Zingsem, A. S. Semisalova, V. Salgueiriño, M. Spasova and M. Farle.

Chemistry of Materials, 27, 4015–4022 (2015)

DOI: 10.1021/acs.chemmater.5b00976

5. Magnetic hardening of $Fe_{30}Co_{70}$ nanowires.

S. Liébana Viñas, R. Salikhov, C. Bran, E. M. Palmero, M. Vazquez, B. Arvan, X. Yao, P. Toson, J. Fidler, M. Spasova, U. Wiedwald and M. Farle.

Nanotechnology 26, 415704 (2015)

DOI:10.1088/0957-4484/26/41/415704

6. Tuning the magnetism of ferrite nanoparticles.

S. Liébana Viñas, K. Simeonidis, Z.-A. Li, Z. Ma, E. Myrovali, A. Makridis, D. Sakellari, G. Vourlias, U. Wiedwald, M. Spasova, M. Farle, M. Angelakeris.

Journal of Magnetism and Magnetic Materials, in revision (2015).

7. Characterization of the oleic acid/iron oxide nanoparticle interface by magnetic resonance.

S. Masur, T. Marzi, S. Liébana Viñas, Z.-A. Li, R. Meckenstock, M. Farle.

Submitted (2015).

8. Nanoscale mixing and matching in ferrite-based nanoparticles for enhanced magnetic heating efficiency and biocompatibility.

S. Liébana Viñas, K. Simeonidis, Zi-An Li, Z. Ma, E. Myrovali, A. Makridis, D. Sakellari, G. Vourlias, U. Wiedwald, M. Spasova, M. Farle, M. Angelakeris.

In preparation.

9. Eco-friendly magnetic hyperthermia carriers.

K. Simeonidis, A.Makridis, O. Patsia, E. Myrovali, D. Sakellari, O. Patsia, J. Tsiaousis, G. Vourlias, T. Samaras O. Kalogirou, M. Angelakeris, S. Liébana Viñas, Zi-An Li, U. Wiedwald, S. Spasova, M. Farle, M. Tziomaki, K. Topouridou, M. P. Yavropoulou and J. G. Yovos.

In preparation.

10. Inverted AFM/FiM core/shell FeMn/$FeMn_2O_4$ nanoparticles prepared by laser ablation: structural and magnetic characterization.

A. Elsukova, A. Krämer, S. Liébana Viñas, U. Wiedwald, M. Spasova, R. Streubel, S. Barcikowski and M. Farle.

In preparation.

11. Magnetic properties of Fe_3O_4 cubic-shaped nanoparticles; truncated versus with pods grown in the [111] direction.

Sara Liébana Viñas, Benito Rodríguez-González, Michael Farle and V. Salgueiriño.

In preparation.

Conference contributions

1. **Internal meeting of Center for Nanointegration Duisburg-Essen (CENIDE)**

   Duisburg, Germany, 6 November 2012

Title: Colloidal synthesis of magnetic nanoparticles with different shapes

Authors: S. Liebana-Viñas, N. Fontaiña-Troitiño, V. Salgueiriño, M. Farle

Type: Poster presentation (+ 2min oral presentation)

2. **Microscopy Conference (MC)**

   Regensburg, Germany, 25-30 August 2013

Title: High-resolution imaging and spectroscopy of CoO octahedral nanoparticles

Authors: Zi-An Li, Nerio Fontaíña-Troitiño, Sara Liébana-Viñas, Marina Spasova, Verónica Salgueiriño, and Michael Farle

Type: Poster presentation

3. **Joint European Magnetic Symposia (JEMS)**

   Rhodes, Greece, 25-30 August 2013

Title: Correlation of magnetic properties, chemical composition and atomic structure of Fe/Fe-O nanocubes

Authors: Vadim Migunov, Sara Liébana-Viñas, Florian Römer, Anastasia Trunova, Marina Spasova, Michael Farle, Rafal Dunin-Borkowski

Type: Poster presentation

4. **Conference PICO 2013**

   Rhodes, Greece, 25-30 August 2013

Title: High- resolution imaging and spectroscopy of CoO octahedral nanoparticles

Authors: Zi-An Li, Andreas Kovacs, Nerio Fontaíña-Troitiño, Sara Liébana-Viñas, Marina Spasova, Verónica Salgueiriño, Rafal E. Dunin-Borkowski, and Michael Farle

Type: Poster presentation

5. Edgar Lüscher Seminar

Klosters, Switzerland, 1-7 February 2014

Title: Exchange anisotropy in and structural characterization of CoNi nanorods

Authors: S. Liébana Viñas, J. Perl, B. Zingsem, A. Elsukova, M. Spasova, V. Salgueiriño-Maceira, M. Farle.

Type: Poster presentation

6. Spring Meeting of the German Physical Society (DPG)

Dresden, Germany, 30 March – 4 April 2014

Title: Magnetische Eigenschaften von Co80Ni20-nanostabchen.

Authors: Juliane Perl, Sara Liébana Viñas, Benjamin Zingsem, Anna Elsukova, Marina Spasova and Michael Farle

Type: Oral presentation

7. IEEE International Magnetics Conference (Intermag)

Dresden, Germany, 4-8 May 2014

a) Title: Robust Ferromagnetism in Antiferromagnetic Cobalt Oxide Nano - Octahedra

Authors: S. Liebana-Vinas, N. Fontaina-Troitino, Z-A. Li, B. Rodriguez-Gonzalez, M. Spasova, V.Salgueirino, M. Farle

Type: Oral presentation

b) Title: Structural and magnetic characterisation of CoNi nanorods

Authors: Benjamin Zingsem, Sara Liebana Viñas, Juliane Perl, Marina Spasova, Anna Elsukova, Michael Farle

Type: Poster presentation

8. Moscow International Symposium on Magnetism (MISM)

Moscow, Russia, 29 June – 3 July 2014

Title: Exchange bias in oxidized cobalt nickel nanorods

Authors: M. Spasova, S. Liébana-Viñas, J. Perl, A. Elsukova, B. Zingsem, V. Salgueiriño, M. Farle

Type: Oral presentation

9. International Symposium on Spin-Polarized Electron Physics and Nanomagnetism.

Halle, Germany, 10 – 13 July 2014

Title: CoO octahedral with a ferromagnetic interface.

Authors: S. Liébana Viñas, N. Fontaiña Troitiño, B. Rodríguez González, Z-A. Li, M. Spasova, M. Farle, V. Salgueiriño

Type: Poster presentation (invited)

10. Spring Meeting of the German Physical Society (DPG).

Berlin, Germany, 15 – 20 March 2015

Title: Magnetic hardening of FeCo nanowires.

Authors: S. Liébana-Viñas, R. Salikhov, C. Bran, M. Spasova, U. Wiedwald, M. Vazquez, and M. Farle

Type: Oral presentation

11. International Workshop on Magnetic Nanowires and Nanotubes 2015: From 3D Nanostructuring Towards Novel Magnetic Data Storages

Meersburg/Lake Constance, Germany, 17-20 May 2015

Title: Magnetic hardening of FeCo nanowires

Authors: Sara Liébana-Viñas, Ruslan Salikhov, Cristina Bran, Ester M. Palmero, Manuel Vázquez, Peter Toson, Josef Fidler, Marina Spasova, Ulf Wiedwald, and Michael Farle

Type: Oral presentation

12. Complex Magnetic Nanostructures workshop (COMANA)

Aegina, Greece, 2-5 June 2015

Title: Tayloring Exchange Anisotropy in Oxidized CoNi nanorods

Authors: Sara Liébana-Viñas, Ulf Wiedwald, Anna Elsukova, Juliane Perl, Benjamin Zingsem, Anna S. Semisalova, Verónica Salgueiriño, Marina Spasova, and Michael Farle

Type: Poster presentation

13. International Baltic Conference on Magnetism: Focus on biomedical aspects

Svetlogorsk/Kaliningrad, Russia, 30 August-3 September 2015

Title: Magnetism tuning by nanoscale mixing and matching in ferrite nanoparticles

Authors: S. Liébana Viñas, K. Simeonidis, Zi-An Li, E. Myrovali, A. Makridis, D. Sakellari, M. Angelakeris, U. Wiedwald, M. Spasova and M. Farle

Type: Poster presentation

14. XXXI Panhellenic Conference on Solid State Physics and Materials Science

Thessaloniki, Greece, 20-23 September 2015

a) Title: Enhanced magnetic heating efficiency by nanoscale mixing and matching in ferrite-based nanoparticles

Authors: S. Liébana Viñas, K. Simeonidis, Z.-A. Li, Z. Ma, E. Myrovali, A. Makridis, D. Sakellari, M. Angelakeris, U. Wiedwald, M. Spasova, M. Farle

Type: Poster presentation

b) Title: Tuning magnetism in nanostructures by interface design

Authors: Ulf Wiedwald, Sara Liébana-Viñas, Marina Spasova, Ruslan Salikhov, Anna Elsukova, Juliane Perl, Benjamin Zingsem, Anna S. Semisalova, Behnaz Arvan, Xiang Yao, Michael Farle, Verónica Salgueiriño, Cristina Bran, Ester M. Palmero, Manuel Vázquez, Peter Toson, Josef Fidler

Type: Oral presentation (Invited talk)

c) Title: CoO octahedral with a ferromagnetic interface between two antiferromagnets

Authors: M. Spasova, Sara Liébana Viñas, N. Fontaiña Troitiño, Z.-A. Li, V.Salgueiriño, R. Pentcheva, M. Farle

Type: Oral presentation

d) Title: Promising features of bimetallic magnetic nanoparticles allow tuning parameters in magnetic hyperthermia application.

Authors: A. Makridis, K. Simeonidis, E. Myrovali, T. Samaras, O. Kalogirou, M. Angelakeris, S. Liébana Viñas, Z.-A. Li, U. Wiedwald, M. Spasova, M. Farle, M. Tziomaki, K. Topouridou, M. P. Yavropoulou, J. G. Yovos

Type: Poster presentation

Invited talks in other research groups

1. Group of Prof. Dr. Makis Angelakeris

Thessaloniki, Greece, 11 October 2013

Title: Synthesis of magnetic nanoparticles by wet chemistry methods.

2. Group of Dr. Barbara Sacca

Essen, Germany, 11 December 2014

Title: Synthesis and characterization of magnetic nanoparticles.

Curriculum Vitae

The curriculum is not included in the online version for reasons of data protection.

The curriculum is not included in the online version for reasons of data protection.

Declaration of authenticity

I hereby declare that all materials presented in this thesis is the result of my own work, otherwise rigorously cited and specifically acknowledged wherever adapted from different authors.

Sara Liébana Viñas

Signature: Date:

Eklärung

Ich beantrage die Zulassung zur Promotionsprüfung zur Erlangung des Titels ”Dr. rer. nat.”.

Beigefügt sind fünf Ausfertigungen der Dissertation in gebundener Form inklusive der im Zusammenhang entstandenen Veröffentlichung.

Ich habe die eingereichte Dissertation selbständig verfasst, nur due angegebenen Hilfsmittel benutzt und alle wörtlich oder inhaltlich übernommenen Stellen als solche gekennzeichnet.

Die Dissertation wurde nur in diesem Promotionsverfahren eingereicht.

Sara Liébana Viñas

Unterschrift: Datum:

List of relevant publications

1. Room temperature ferromagnetism in antiferromagnetic cobalt oxide nanooctahedra.

N. Fontaiña-Troitiño, S. Liébana-Viñas, B. Rodríguez-González, Zi-An Li, M. Spasova, M. Farle and V. Salgueiriño.

Nano Letters 14, 640 (2014)

DOI: 10.1021/nl4038533

2. Electrostatic doping as a source for robust ferromagnetism at the interface between antiferromagnetic cobalt oxides.

Z.-A. Li, N. Fontaíña-Trotitiño, A. Kovács, S. Liébana-Viñas, M. Spasova, R.E. Dunin-Borkowski, M. Müller, D. Doennig, R. Pentcheva, M. Farle and V. Salgueiriño.

Scientific Reports, 5, 7997 (2015)

DOI: 10.1038/srep07997

3. Structure-correlated exchange anisotropy in oxidized $Co_{80}Ni_{20}$ nanorods.

S. Liébana-Viñas, U. Wiedwald, A. Elsukova, J. Perl, B. Zingsem, A. S. Semisalova, V. Salgueiriño, M. Spasova and M. Farle.

Chemistry of Materials, 27, 4015–4022 (2015)

DOI: 10.1021/acs.chemmater.5b00976

4. Magnetic hardening of $Fe_{30}Co_{70}$ nanowires.

S. Liébana Viñas, R. Salikhov, C. Bran, E. M. Palmero, M. Vazquez, B. Arvan, X. Yao, P. Toson, J. Fidler, M. Spasova, U. Wiedwald and M. Farle.

Nanotechnology 26, 415704 (2015)

DOI:10.1088/0957-4484/26/41/415704